

*TRIAZINE AND IMINE LINKED POROUS
ORGANIC FRAMEWORKS AS PLATFORMS
FOR GAS STORAGE, SEPARATION AND
HETEROGENEOUS CATALYSIS*

Chidharth Krishnaraj

Ghent University

**Center for Ordered Materials,
Organometallics and Catalysis**

Dissertation submitted in fulfilment of the requirements for the degree of

Doctor of Science: Chemistry

January 2021



Promoters

Prof. dr. Pascal Van Der Voort

Prof. dr. Christian V Stevens

Prof. dr. Karen Leus

Department

Chemistry

Green Chemistry and Technology

Chemistry

Members of the Jury

Prof. dr. Arne Thomas

Prof. dr. Damien Debecker

Prof. dr. Klaartje De Buysser

Prof. dr. Veronique Van Speybroeck

Prof. dr. An Verberckmoes

Dr. Himanshu Sekhar Jena

Affiliation

Technische Universität Berlin

Université Catholique de Louvain

Ghent University

Ghent University

Ghent University

Ghent University

Ghent University

Faculty of Sciences

Department of Chemistry

Krijgslaan 281 S3, 9000 Ghent, Belgium

Tel.: +32-9-264.44.49

Fax.: +32-9-264.49.83

This research was funded by BOF GOA2017000303.



© 2021 Ghent University, Department of Chemistry, COMOC-Center for Ordered Materials, Organometallics & Catalysis, Krijgslaan 281-S3, 9000 Gent, Belgium

Alle rechten voorbehouden. Niets uit deze uitgave mag worden gereproduceerd, opgeslagen in een geautomatiseerd gegevensbestand, of openbaar gemaakt, in enige vorm of op enige wijze, hetzij elektronisch, mechanisch, door printouts, kopieën, of op welke manier dan ook, zonder voorafgaande schriftelijke toestemming van de uitgever.

All rights reserved. No part of this publication may be reproduced, stored in a retrieval system or transmitted in any form or by any means, electronic, mechanical, photocopying, recording or otherwise, without prior permission from the publisher.

ACKNOWLEDGEMENTS

First and foremost, I thank my promotor, Prof. Pascal Van Der Voort for choosing me as a PhD student and trusting me with a new research topic in the group. I would like to express my gratitude for guiding me throughout the four years of my PhD. Thank you for providing me enough freedom to develop as an independent researcher and encouraging my ideas.

I want to thank Prof. Karen Leus for helping me both in research and personal life. I remember you as the first person I met when I started my PhD. Thank you for responding to all my queries so quickly. I am glad I could be your first official PhD student and your first soon-to-be postdoc.

Thanks to Prof. Anna Kaczmarek for all the collaborations. You are an inspiration to women in science and I am glad to know you personally.

I also want to thank Prof. Christian Stevens and Prof. Veronique Van Speybroeck for their support through the GOA meetings. Thanks to my collaborators – Prof. Lianne Benning, Helen Freeman, Johannes Schmidt, Nicolas Chaoui, and Jérôme Roeser.

I would like to specially thank Prof. Arne Thomas for accepting me as a visiting researcher in his group. Thanks for being open for discussion at MOF2018. If not for that meeting, I would have missed the chance to work with you. You are one of the smartest persons I have ever met and have inspired me a lot.

I wish to express my thanks to the former colleagues at COMOC – Hannes, Kevin (alpha and beta), Judith, Els, Norini, Xiao, Mei, Shuna, Guangbo. Also, thanks to the current members of COMOC – Jiamin, Chen Hui, Sara, Parviz, Chunhui, Geert, Andreas, Roy, Amrita, Bram. All our conversations, group activities and the time we spent together have been memorable. Further thanks to the members of the department – Tom, Pierre, Kathleen, Katrien, Bart, Pat, Hannes, Jari, Alessio, Natalia, Pieter. Special thanks to Funda for all the random discussions in the BET and coffee room. Thanks to my friends from other groups who are no longer in the department – Dimitri, Tim, Min, Pengshang, Giovanni. Thanks to my friends and colleagues at TU Berlin, Germany – Pradip, Amitava, Jin, Suman, Robert, Julia, Vincent, Sarah, Maria, Christina, Anne. Thanks to my Indian friends (Himanshu, Shalini, Kishu, Vignesh, Ali, Chandu, Renu) at S3 for everything (the food, the movies, the time we spent).

Of course, I am not forgetting you (Jeroen, Laurens and Flore). Thanks for all the fun times during our dinner and games get together. Special mention to Jeroen for the dark jokes, the movies, and discussions about TV series. Thanks, Laurens, for motivating me to run on a regular basis. Flore, we started the PhD together and thanks for being the cheerful person you have always been. Our dart games are unforgettable (team victory for the win :)).

Special thanks to Dr. Himanshu Jena for teaching me everything from the basics of chemistry to advanced topics. Thanks for listening to all my crazy ideas. Our countless discussions on all science, travel, politics, and other things cannot be forgotten. You have been a mentor to me in the lab and a very good friend in personal life. Without your support, it would be difficult for me to imagine my life in Gent.

My friends from outside of the university have also made my time wonderful in these years. Vignesh, Akash and Ravi – my friends from my masters who are still with me in Belgium. Ashish – we have been known each other for more than a decade now. Thanks for making my life fun. Sushree and Aditya for adding spice in my life. Pithchai and Koba – thanks for showing me around Mechelen and for the wonderful food and games. My close friends from outside of Belgium – Ritheesh, Akilesh, Boopathy, Sukumar – thanks for always being there for me to talk whenever I wanted to.

Mom and dad, none of this would have been possible without you. Thank you, papa and mama, for your love and encouragement. You have always believed in me and have been my #1 supporters. I hope that I have grown as the son you wanted me to be. Thanks to my brother Chidhanandh for being there with me from the beginning. You have been the best big brother one could wish for. Also, thanks to my sister-in-law for being the friendly person of the family. Ovia, you have been with me through my happy and sad times. Thanks for being there for me always. Words cannot describe the importance you have in my life.

I would like to sincerely thank my PhD examination committee for spending their valuable time to read and correct my thesis. Finally, I want to thank Ghent University for the funding for my PhD and FWO for the funding for my travel and research stay abroad.

- Chidharth Krishnaraj
Gent, Dec 2020

“The unknown is infinite in both realms of the universe – the big and the small. Be curious to explore the unknown.”

- CK

SCIENTIFIC A1 PUBLICATIONS

As first author/shared first author

1. Strongly Reducing (Diarylamino)benzene based Covalent Organic Framework for Metal-Free Visible Light Photocatalytic H₂O₂ Generation.

C Krishnaraj, HS Jena, L Bourda, A Laemont, P Pachfule, J Roeser, VC Nair, B Sander, SJ Rogge, K Leus, CV Stevens, J A Martens, V Van Speybroeck, E Breynaert, A Thomas, and P Van Der Voort, *Journal of the American Chemical Society* 142(47), **2020**, 20107–20116.

2. A Rigid Urea-Covalent Triazine Framework as a C₂/C₁ and CO₂/CH₄ gas separation material.

C Krishnaraj,¹ HS Jena,¹ F Lecoivre, K Leus, and P Van Der Voort, **2020**, Submitted.

3. Covalent triazine frameworks—a sustainable perspective.

C Krishnaraj, HS Jena, K Leus, P Van Der Voort, *Green Chemistry* 22 (4), **2020**, 1038-1071.

4. Effect of Building Block Transformation in Covalent Triazine-Based Frameworks for Enhanced CO₂ Uptake and Metal-Free Heterogeneous Catalysis.

HS Jena,¹ **C Krishnaraj**,¹ J Schmidt, K Leus, K Van Hecke, P Van Der Voort, *Chemistry—A European Journal* 26 (7), **2020**, 1548-1557.

5. Development of covalent triazine frameworks as heterogeneous catalytic supports.

N Tahir,¹ **C Krishnaraj**,¹ K Leus, P Van Der Voort, *Polymers* 11 (8), **2019**, 1326.

6. Triggering white-light emission in a 2D imine covalent organic framework through lanthanide augmentation.

C Krishnaraj, AM Kaczmarek, HS Jena, K Leus, N Chaoui, J Schmidt, R Van Deun, P Van Der Voort, *ACS Applied Materials & Interfaces* 11 (30), **2019**, 27343-27352.

7. An aliphatic hexene-covalent triazine framework for selective acetylene/methane and ethylene/methane separation.

C Krishnaraj, HS Jena, K Leus, HM Freeman, LG Benning, P Van Der Voort, *Journal of Materials Chemistry A* 7 (21), **2019**, 13188-13196.

8. Catalytic carpets: Pt@ MIL-101@ electrospun PCL, a surprisingly active and robust hydrogenation catalyst.

*K Leus,¹ C Krishnaraj,¹ L Verhoeven, V Cremers, J Dendooven, R K Ramachandra, P Dubruel, P Van Der Voort, **Journal of Catalysis** 360, 2018, 81-88.*

As co-author

9. Luminescent Ratiometric Thermometers Based on a 4f-3d Grafted Covalent Organic Framework to Locally Measure Temperature Gradients During Catalytic Reactions.

*AM Kaczmarek, HS Jena, C Krishnaraj, H Rijckaert, S Veerapandian, A Meijerink, P Van Der Voort, **Angewandte Chemie** 2020.*

10. Regeneration of Hopcalite used for the adsorption plasma catalytic removal of toluene by non-thermal plasma.

*SKP Veerapandian, J-M Giraudon, N De Geyter, Y Onyschchenko, C Krishnaraj, S Sonar, A Löfberg, K Leus, P Van Der Voort, J-F Lamonier, R Morent. **Journal of Hazardous Materials** 402, 2021, 123877.*

11. Illustrating the Role of Quaternary-N of BINOL Covalent Triazine based Frameworks in Oxygen Reduction and Hydrogen Evolution Reactions.

*HS Jena, C Krishnaraj, S Parwaiz, F Lecoivre, J Schmidt, D Pradhan, and P Van Der Voort, **ACS Applied Materials and Interfaces** 12, 40, 2020, 44689-44699.*

12. Amine-containing (nano-) Periodic Mesoporous Organosilica and its application in catalysis, sorption and luminescence.

*AM Kaczmarek, S Abednatanzi, D Esquivel, C Krishnaraj, HS Jena, G Wang, K Leus, R Van Deun, F J Romero-Salguero, P Van Der Voort, **Microporous and Mesoporous Materials** 291, 2020, 109687.*

13. White Light Emission Properties of Defect Engineered Metal–Organic Frameworks by Encapsulation of Eu³⁺ and Tb³⁺.

*HS Jena, AM Kaczmarek, C Krishnaraj, X Feng, K Vijayvergia, H Yildirim, S-N Zhao, R Van Deun, P Van Der Voort, **Crystal Growth & Design** 19 (11), 2019, 6339-6350.*

14. An anionic metal-organic framework as a platform for charge-and size-dependent selective removal of cationic dyes.

SN Zhao, C Krishnaraj, HS Jena, D Poelman, P Van Der Voort, Dyes and Pigments 156, 2018, 332-337.

15. Acetylacetone covalent triazine framework: An efficient carbon capture and storage material and a highly stable heterogeneous catalyst.

HS Jena, C Krishnaraj, G Wang, K Leus, J Schmidt, N Chaoui, P Van Der Voort, Chemistry of Materials 30 (12), 2018, 4102-4111.

16. A fluorine-containing hydrophobic covalent triazine framework with excellent selective CO₂ capture performance.

G Wang, K Leus, HS Jena, C Krishnaraj, S Zhao, H Depauw, N Tahir, Y-Y Liu, P Van Der Voort, Journal of Materials Chemistry A 6 (15), 2018, 6370-6375.

ENGLISH SUMMARY

Covalent Organic Frameworks (COFs) and Covalent Triazine Frameworks (CTFs), introduced in 2005 and 2008 respectively, are porous materials that have shown immense promise in recent years for several applications. They are synthesized by covalently linking organic building blocks to form ordered long-range networks. These materials can be considered as an extension of organic chemistry in higher dimensions. Hence, previously tunable molecular properties can now be translated into larger extended systems. This has rendered COFs and CTFs suitable for several applications ranging from gas storage to energy conversion. However, these materials are still relatively new and show a lot of potential in terms of structural design and advanced applications. In this thesis, several new CTFs and COFs have been synthesized and advancements have been made in gas storage and separation, and heterogeneous thermal and photocatalysis.

Chapter 1 provides a general overview of porous organic materials and delineates how the COFs and CTFs are unique compared to other porous organic materials. An overview of the evolution of COFs and CTFs from their inception to date is discussed. From a design perspective, the reader will be introduced to different synthetic approaches to build these materials. A detailed description on the design requisites and the ensuing elegant chemistry is presented.

In **chapter 2**, the reader will delve into the applications arising from these unique materials. For the scope of the thesis, a strong emphasis is given to the energy and environment based applications that have been achieved till now towards a sustainable development. In the first half, a summary of different COFs and CTFs and their performance in carbon capture and hydrocarbon separation processes have been presented. The latter part of this chapter describes their usage in heterogeneous catalytic processes. A division between the utilization of these materials (i) as supports for catalytically active metals and (ii) as inherent photocatalysts has been made. Finally, the objectives of this thesis have been discussed.

In **chapter 3**, the first reported covalent triazine based porous material for selective C₂/C₁ hydrocarbon separation is described. A series of aliphatic linker based porous materials were synthesized which are thermally stable. The presence of an alkene functionality in the backbone of the porous material provides a platform for higher interaction with unsaturated hydrocarbons, thus increasing the selectivity.

In **chapter 4**, CTFs containing acetylacetone functionalities were developed. In these materials, the conventional usage of nitrogen-rich ligands in porous materials for supporting catalytically active metal species is augmented with oxygen enrichment. These oxygen species can behave as docking sites for catalytically active metal species. As a proof-of-concept, acac-CTFs were used to anchor vanadium metal complexes, which proved to be active for modified Mannich type reactions. Additionally, the polar O and N sites in the CTFs resulted in high CO₂ storage properties.

In **chapter 5**, the acac group in the building block is aromatized into pyrazole and isoxazole units to form two different building blocks. Thus, new sets of pyrazole CTFs and isoxazole CTFs were produced. These materials showed higher CO₂ adsorption in comparison to their acac counterpart. The aromatization also enhanced the basicity in the resulting materials which acted as active metal-free catalysts for the oxidation of benzyl amines to imines.

In **chapter 6**, two new imine COFs were synthesized from (diarylamino)benzene building blocks. The C₄+C₂ combination of the building blocks resulted in a highly crystalline kagome lattice containing dual pores. A thorough structural investigation was performed by a combination of X-ray diffraction, nuclear magnetic resonance, and computational studies. The COFs were photoactive and assisted in the photocatalytic production of hydrogen peroxide through the reduction of molecular oxygen under visible light irradiation.

Finally, the general discussions and conclusions of this thesis are provided in **chapter 7** and an eclectic outlook is provided from a personal standpoint.

DUTCH SUMMARY

Covalent Organic Frameworks (COF's) en Covalent Triazine Frameworks (CTF's), respectievelijk geïntroduceerd in 2005 en 2008, zijn poreuze materialen die de afgelopen jaren een enorm potentieel hebben getoond in verschillende toepassingen. Ze worden gesynthetiseerd door organische bouwstenen covalent te koppelen om zo geordende uitgebreide netwerken te vormen. Deze materialen kunnen worden beschouwd als een uitbreiding van de organische chemie in hogere dimensies. Vandaar dat afstembare moleculaire eigenschappen nu kunnen worden vertaald in langer uitgebreide systemen. Hierdoor zijn COF's en CTF's geschikt voor verschillende toepassingen, variërend van gasopslag tot energieconversie. Deze materialen zijn echter nog relatief nieuw maar vertonen veel potentieel inzake structureel ontwerp en geavanceerde toepassingen. In dit proefschrift zijn verschillende nieuwe CTF's en COF's gesynthetiseerd en zijn vorderingen gemaakt op het gebied van gasopslag en scheiding en heterogene thermische- en fotokatalyse.

Hoofdstuk 1 geeft een algemeen overzicht van poreuze organische materialen en geeft aan hoe de COF's en CTF's uniek zijn in vergelijking met andere poreuze organische materialen. Een overzicht van de evolutie van COF's en CTF's vanaf hun ontstaan tot op heden wordt besproken. Vanuit een ontwikkelingsperspectief zal de lezer kennis maken met verschillende synthetische benaderingen om deze materialen te bouwen. Een gedetailleerde beschrijving van de ontwerpvereisten en de daaruit voortvloeiende elegante chemie wordt gepresenteerd.

In **hoofdstuk 2** gaat de lezer dieper in op de toepassingen die voortkomen uit deze unieke materialen. In dit proefschrift ligt een sterke nadruk op de energie- en milieugerelateerde toepassingen die tot nu toe zijn verwezenlijkt voor een duurzame ontwikkeling. In een eerste deel is een samenvatting gepresenteerd van verschillende COF's en CTF's en hun performantie in koolstofopname- en koolwaterstofscheidingsprocessen. Het laatste deel van dit hoofdstuk beschrijft hun gebruik in heterogene katalytische processen. Er is een onderscheid gemaakt tussen het gebruik van deze materialen (i) als dragers voor katalytisch actieve metalen en (ii) als inherente fotokatalysatoren. Ten slotte worden de doelstellingen van dit proefschrift besproken.

In **hoofdstuk 3** wordt het eerst gerapporteerde covalente poreuze materiaal op triazinebasis voor selectieve C₂ / C₁-koolwaterstofscheiding beschreven. Er werd een reeks thermisch stabiele poreuze materialen gesynthetiseerd op basis van een alifatische

linker. De aanwezigheid van een alkeenfunctionaliteit in de ruggengraat van het poreuze materiaal biedt een platform voor een grotere interactie met onverzadigde koolwaterstoffen, waardoor de selectiviteit toeneemt.

Hoofdstuk 4 beschrijft de ontwikkeling van CTF's die acetylaceton-functionaliteiten bevatten. In deze materialen wordt het conventionele gebruik van stikstofrijke liganden in poreuze materialen, ter verankering van katalytisch actieve metaalsoorten, aangevuld met zuurstofverrijking. Deze zuurstofsoorten kunnen zich gedragen als coördinatieplaatsen voor katalytisch actieve metaalsoorten. Als proof-of-concept werden acac-CTF's gebruikt om vanadiummetaalcomplexen te verankeren, die actief bleken te zijn voor gemodificeerde Mannich-type reacties. Bovendien resulteerden de polaire O- en N-locaties in de CTF's in hoge CO₂-opslagmogelijkheden.

In **hoofdstuk 5** wordt de acac-groep in de bouwsteen gearomatiseerd tot pyrazol- en isoxazol-eenheden om twee verschillende bouwstenen te vormen. Zo werden nieuwe sets van pyrazol-CTF's en isoxazol-CTF's geproduceerd. Deze materialen vertoonden een hogere CO₂-adsorptie in vergelijking met hun acac-tegenhanger. De aromatisering versterkte ook de basiciteit van de resulterende materialen die bijgevolg kunnen fungeren als actieve metaalvrije katalysatoren voor de oxidatie van benzylamines tot imines.

In **hoofdstuk 6** werden twee nieuwe imine-COFs gesynthetiseerd uit (diarylamino)benzeen bouwstenen. De combinatie C₄ + C₂ van de bouwstenen resulteert in een zeer kristallijn kagoomrooster met dubbele poriën. Een grondig structureel onderzoek werd uitgevoerd door een combinatie van x-straaldiffractie, nucleaire magnetische resonantie en computationele studies. De COF's zijn fotoactief en helpen bij de fotokatalytische productie van waterstofperoxide door de reductie van moleculaire zuurstof onder bestraling met zichtbaar licht.

Ten slotte worden een algemene discussie en conclusies van dit proefschrift gegeven in **hoofdstuk 7** en wordt een eclectische kijk gegeven vanuit een persoonlijk standpunt.

CONTENTS

1	POROUS ORGANIC MATERIALS: COVALENT ORGANIC FRAMEWORKS (COFs) AND COVALENT TRIAZINE FRAMEWORKS (CTFs).....	11
	INTRODUCTION	12
1.1.	HYPER CROSS-LINKED POLYMERS (HCP).....	14
1.2.	POLYMERS OF INTRINSIC MICROPOROSITY (PIMs)	14
1.3.	CONJUGATED MICROPOROUS POLYMERS (CMPs).....	14
1.4.	POROUS AROMATIC FRAMEWORKS (PAFs)	15
1.5.	COVALENT ORGANIC FRAMEWORKS (COFs).....	15
1.5.1.	<i>COF design principle</i>	16
1.5.2.	<i>COF linkages</i>	18
1.5.3.	<i>Imine linked COFs</i>	19
1.6.	COVALENT TRIAZINE FRAMEWORKS (CTFs).....	21
1.6.1.	<i>Ionothermal synthesis</i>	23
1.6.2.	<i>Brønsted superacid synthesis</i>	26
1.6.3.	<i>Phosphorus pentoxide (P₂O₅) catalyzed synthesis</i>	28
1.6.4.	<i>Amidine synthesis</i>	28
1.6.5.	<i>Other synthesis methods</i>	30
1.7.	OBJECTIVES: SYNTHETIC OPPORTUNITIES.....	31
1.8.	REFERENCES	31
2	ENERGY AND ENVIRONMENTAL APPLICATIONS OF COFs AND CTFS	36
2.1.	INTRODUCTION.....	37
2.2.	GAS STORAGE AND SEPARATION	37
2.2.1.	<i>Carbon capture</i>	37
2.2.2.	<i>Hydrocarbon separation</i>	46
2.3.	HETEROGENEOUS CATALYSIS.....	50
2.3.1.	<i>Metal based organic transformations</i>	50
2.3.2.	<i>Photocatalysis</i>	56
2.4.	REFERENCES	67
2.5.	OBJECTIVES OF THESIS	74

3 AN ALIPHATIC HEXENE-CTF FOR SELECTIVE C₂/C₁ GAS SEPARATION	76
3.1. INTRODUCTION.....	78
3.2. RESULTS AND DISCUSSION.....	80
3.2.1. <i>Synthesis and Characterization of Hexene-CTFs</i>	80
3.2.2. <i>Structural and morphological analysis</i>	83
3.2.3. <i>Selective olefin adsorption</i>	86
3.2.4. <i>Selective CO₂ adsorption</i>	88
3.3. CONCLUSION	91
3.4. EXPERIMENTAL SECTION.....	92
3.4.1. <i>Instrumentation</i>	92
3.4.2. <i>Synthesis of Hexene-CTFs</i>	93
3.4.3. <i>Bromine addition reaction</i>	93
3.5. REFERENCES.....	93
3.6. SUPPORTING INFORMATION	97
4 ACETYL ACETONE CTF: CARBON CAPTURE MATERIAL AND HIGHLY STABLE HETEROGENEOUS CATALYST	115
4.1. INTRODUCTION.....	117
4.2. RESULTS AND DISCUSSION.....	118
4.2.1. <i>Synthesis and Characterization of acac-CTFs</i>	118
4.2.2. <i>Gas sorption properties</i>	120
4.2.3. <i>Catalytic properties</i>	124
4.3. CONCLUSION	131
4.4. EXPERIMENTAL SECTION	131
4.4.1. <i>Materials and Methods</i>	131
4.5. REFERENCES.....	132
4.6. SUPPORTING INFORMATION	136
5 EFFECT OF BUILDING BLOCK TRANSFORMATION IN CTFs FOR CO₂ UPTAKE AND METAL-FREE HETEROGENEOUS CATALYSIS	145
5.1. INTRODUCTION.....	147
5.2. RESULTS AND DISCUSSION.....	149
5.2.1. <i>Synthesis of CTFs</i>	149
5.2.2. <i>Characterization of CTFs</i>	149
5.2.3. <i>Gas Sorption Properties</i>	153
5.2.4. <i>Catalytic Properties</i>	159

5.3. CONCLUSION	163
5.4. EXPERIMENTAL SECTION	164
5.5. REFERENCES	165
5.6. SUPPORTING INFORMATION.....	169
6 (DIARYLAMINO) BENZENE BASED COF FOR METAL-FREE VISIBLE LIGHT PHOTOCATALYTIC H₂O₂ GENERATION	182
6.1. INTRODUCTION.....	184
6.2. RESULTS AND DISCUSSION	187
6.2.1. <i>Synthesis of COFs</i>	187
6.2.2. <i>Characterization of COFs</i>	187
6.2.3. <i>Photocatalytic studies</i>	192
6.3. CONCLUSION	197
6.4. REFERENCES	197
6.5. SUPPORTING INFORMATION.....	201
7 CONCLUSIONS AND OUTLOOK.....	234
7.1. GAS STORAGE, SEPARATION, AND UTILIZATION.....	236
7.2. HETEROGENEOUS CATALYSIS	237
7.3. PHOTOCATALYSIS	238
7.4. GENERAL OUTLOOK	239
7.5. REFERENCES	241

LIST OF TABLES

TABLE 2. 1. LIST OF REPORTED CTFs FOR CO ₂ ADSORPTION	39
TABLE 2. 2. VARIOUS MATERIALS USED FOR C ₂ /C ₁ HYDROCARBON SEPARATION	47
TABLE 3. 1. THE GAS SELECTIVITIES OF HEXENE-CTFs IN COMPARISON TO SELECTED OTHER POROUS MATERIALS	90
TABLE 4. 1. BET SURFACE AREAS, PORE VOLUMES, CO ₂ AND H ₂ ADSORPTION UPTAKES, CO ₂ ISOSTERIC HEAT OF ADSORPTION (Q_{st}), AND CO ₂ /N ₂ SELECTIVITY OF THE PRESENTED CTFs.....	122
TABLE 4. 2. CATALYTIC ACTIVITY OF V@CATALYSTS FOR MANNICH REACTION.	127
TABLE 4. 3. SUBSTRATE SCOPE FOR MANNICH REACTION USING V@ACAC-CTF.....	130
TABLE 5. 1. BET SURFACE AREAS, PORE VOLUMES, CO ₂ AND H ₂ UPTAKES, CO ₂ ISOSTERIC HEAT OF ADSORPTION (Q_{st}), AND CO ₂ /N ₂ SELECTIVITY OF THE CTFs.....	151
TABLE 5. 2. DISTRIBUTION OF BASICITY AND CORRELATION WITH CO ₂ UPTAKE.....	158
TABLE 5. 3. CATALYTIC TEST USING CTF IN THE AEROBIC OXIDATIVE DIMERIZATION OF BENZYLAMINE TO N-BENZYL-1-PHENYLMETHANIMINE	161
TABLE 6. 1. PHOTOCATALYTIC PRODUCTION OF H ₂ O ₂	194

LIST OF FIGURES

FIGURE 1. 1. MICROSCOPIC VIEW OF PLANT STOMATA	12
FIGURE 1. 2. THREE WAYS TO FORM POROUS MATERIALS (A) PORES FROM DIRECTIONAL POLYMERIZATION OF MONOMERS, (B) PORES DUE TO DEFECTS IN MATERIALS, AND (C) PORES DUE TO IRREGULAR PACKING OF THE MATERIALS.	13
FIGURE 1. 3. GENERAL STEPS FOR SYNTHESIS OF COF. STEP 1: SELECT A TARGET TOPOLOGY, STEP 2: EVALUATE POINTS OF CONNECTION DEPENDING ON THE GEOMETRY, STEP 3: IDENTIFY LINKERS THAT ARE GEOMETRICAL EQUIVALENTS OF THE SUB-STRUCTURE, STEP 4: CONNECT THE LINKERS, AND STEP 5: CHARACTERIZE THE MATERIAL	16
FIGURE 1. 4. BASIC TOPOLOGICAL DIAGRAMS FOR THE DESIGN OF 2D AND 3D COF	17
FIGURE 1. 5. DIFFERENT LINKAGES USED TO SYNTHESIZE COFs (TILL AUGUST 2020)	18
FIGURE 1. 6. SYNTHESIS OF A 2D COF USING C3+C2 LINKERS.....	19
FIGURE 1. 7. A LIST OF SOME OF THE AMINE APPENDED LINKERS USED IN IMINE COF SYNTHESIS.....	20
FIGURE 1. 8. A LIST OF SOME OF THE ALDEHYDE APPENDED LINKERS USED IN IMINE COF SYNTHESIS.....	21
FIGURE 1. 9. DIFFERENT APPROACHES TO FORM TRIAZINES USED IN SYNTHESIS OF CTFs	22
FIGURE 1. 10. (A) TRIMERIZATION OF 1,4-DICYANOBENZENE IN MOLTEN $ZnCl_2$ TO FORM TRIMERS AND OLIGOMERS, FOLLOWED BY AN EXTENDED COVALENT TRIAZINE-BASED FRAMEWORK (CTF-1), (B) EXPERIMENTAL (BLACK) AND CALCULATED (GRAY) PXRD PATTERNS OF CTF-1, AND (C) SCHEMATIC REPRESENTATION OF THE CTF-1 STRUCTURE (C – GRAY, N – BLACK)	24
FIGURE 1. 11. VARIOUS MONOMERS USED TO PREPARE CTFs	25
FIGURE 1. 12. (A) DENSITY FUNCTIONAL THEORY (DFT) OPTIMIZED STRUCTURES FOR THE MONOMERS USED TO SYNTHESIZE THE CTFs, (B) TRIMERIZATION OF BIPHENYL DICARBONITRILE MONOMER USING THE BRONSTED ACID ASSISTED METHOD AT 100°C, AND (C) PHOTOGRAPH OF A DIRECTLY SYNTHESIZED SAMPLE OF THE TRANSPARENT AND FLEXIBLE TRIAZINE-FRAMEWORK-BASED MEMBRANE TFM-1	27

FIGURE 1. 13. (A) SLOW OXIDATION OF ALCOHOL TO PRODUCE ALDEHYDE TO CONTROL THE NUCLEATION RATE FOR THE FORMATION OF A COVALENT TRIAZINE FRAMEWORK, AND (B) DIFFERENT MONOMERS USED TO SHOW THE WIDE APPLICABILITY OF THIS METHOD	29
FIGURE 2. 1. (A) SCHEMATIC ILLUSTRATION OF THE FORMATION OF Tz-DF-CTFs VIA A DUAL STRATEGIC APPROACH, (B) SCHEME OF A PACKED BED ADSORBER FOR Tz-DF-CTFs. (C–E) BREAKTHROUGH CHARACTERISTIC IN THE SEPARATION OF A 15% CO ₂ + 85% N ₂ BINARY MIXTURE AT 298 K, AND (F) COMPARISON OF THE CO ₂ CAPTURE AND N ₂ RECOVERY PRODUCTIVITY AT 298 K.....	43
FIGURE 2. 2. DIFFERENT BINDING CONFIGURATIONS AND THEIR BINDING ENERGIES OF CTF-PO71 WITH (A–C) C ₂ H ₂ AND (D,E) C ₂ H ₄	49
FIGURE 2. 3. POSSIBLE BINDING MODES OF IRIIDIUM COMPLEX ON BIPYRIDINE UNIT. STRUCTURALLY RELAXED ANCHORING MODELS (UPPER ROW) AND THEIR SCHEMATIC FORMULA (LOWER ROW). THE STABILIZATION ENERGIES ARE –444 kJ/MOL (MODEL 1), –414 kJ/MOL (MODEL 2), –439 kJ/MOL (MODEL 3).....	52
FIGURE 2. 4. SEM MICROGRAPHS OF CTF@MONOLITH: (A) BARE CORDIERITE MONOLITH, TOP VIEW; (B–E) CTF-COATED MONOLITH, CROSS-SECTIONAL VIEWS; (F) VIEW ON THE WALL OF A CTF-COATED MONOLITH (LEFT).....	53
FIGURE 2. 5. CONSTRUCTION OF COF-LZU1 AND Pd/COF-LZU1. SCHEMATIC REPRESENTATION FOR THE SYNTHESIS OF COF-LZU1 AND Pd/COF-LZU1 MATERIALS (A). PROPOSED STRUCTURES OF COF-LZU1 (B) AND Pd/COF-LZU1 (C, D) POSSESSING REGULAR MICROPOROUS CHANNELS (DIAMETER OF ~1.8 nm), SIMULATED WITH A 2D ECLIPSED LAYERED-SHEET ARRANGEMENT. C: BLUE, N: RED, AND BROWN SPHERES REPRESENT THE INCORPORATED Pd(OAc) ₂ . H ATOMS ARE OMITTED FOR CLARITY.....	54
FIGURE 2. 6. (A) USE OF A THREE-COMPONENT CONDENSATION SYSTEM TO MODULATE THE NITROGEN CONTENT OF THE 2D IMINE-TYPE COFs. (B) DESIGNED STRATEGIES FOR THE MONOMETALLIC (ROUTE 1) AND BIMETALLIC DOCKING (ROUTE 2). (C) PXRD PATTERNS OF THE X % BPy COFs. (D) OPEN CHANNELS OF THE COFs. (E) PXRD PATTERNS OF THE PdII@X % BPy COFs. (F) PXRD PATTERNS OF THE RhI/PdII@X % BPy COFs. (G) OPEN CHANNELS OF THE METAL LOADED COFs...	55

FIGURE 2. 7. (A) SYNTHESIS OF CTF-T1 AND SULFUR-DOPED CTF-T1, (B) CHARGE DISTRIBUTIONS IN CTF-T1-MC AND CTFS-MC, AND (C) HOMO-LUMO ORBITALS OF CTF-T1-MC AND CTFS-MC.....	59
FIGURE 2. 8. (A) REPRESENTATIVE STRUCTURE OF THE REPEATING UNITS IN THE ASYMMETRIC NETWORK ASY-CTF CONTAINING FOUR DIFFERENT MOLECULAR D-A DOMAINS (M1–M4), (B) ITS SYMMETRIC COUNTERPARTS CTF-TH AND CTF-TH-PH CONTAINING ONLY A SINGLE D-A DOMAIN, AND (C) HOMO AND LUMO LEVELS OF THE FOUR DIFFERENT D-A DOMAINS WITHIN ASY-CTF CALCULATED AT THE B3LYP/6-31G(D) LEVEL.....	60
FIGURE 2. 9. (A) TIME COURSE FOR PHOTOCATALYTIC H ₂ PRODUCTION USING VISIBLE LIGHT FOR FS-COF, A NEAT, NEAR-INFRARED DYE (WS5F) AND A DYE-SENSITIZED COF (FS-COF+WS5F. (B) EQES AT THREE DIFFERENT INCIDENT LIGHT WAVELENGTHS FOR FS-COF AND FS-COF+WS5F. (C) SOLID-STATE UV–VIS SPECTRA FOR FS-COF, WS5F AND FS-COF+WS5F. (D) RELATIVE ENERGY LEVELS AS CALCULATED FOR ASCORBIC ACID, FS-COF AND A NEAR-INFRARED DYE, WS5F; DASHED GREEN AND ORANGE LINES INDICATE POTENTIALS FOR PROTON REDUCTION AND THE TWO-HOLE OXIDATION OF ASCORBIC ACID IN SOLUTION, RESPECTIVELY. (E), (F) PHOTOCATALYTIC H ₂ PRODUCTION USING FS-COF FILMS. PHOTOGRAPHS SHOWING (LEFT TO RIGHT) SOLID FS-COF AND COLLOIDAL DISPERSIONS IN DMF, WATER AND ACETONE, RESPECTIVELY AND FS-COF FILM ON GLASS PRODUCING HYDROGEN.....	62
FIGURE 2. 10. STRUCTURES OF N ₂ -COF AND THE COBALOXIME Co-CATALYSTS.....	64
FIGURE 2. 11. (A) SYNTHESIS OF COF AND Re-COF. (B) SIDE VIEW AND (C) UNIT CELL OF AA STACKING COF. (D) PROPOSED CATALYTIC MECHANISM FOR CO ₂ REDUCTION.....	66
FIGURE 3. 1. N ₂ ADSORPTION (CLOSED SYMBOLS) AND DESORPTION (OPEN SYMBOLS) ISOTHERMS OF ALL HEXENE-CTFs OBTAINED AT 77K.....	81
FIGURE 3. 2. FT-IR SPECTRA OF ALL THE HEXENE-CTFs AND THE TRANS-3-HEXENEDINITRILE MONOMER.....	82
FIGURE 3. 3. TEM IMAGE OF HEXENE-CTF_400_5 SHOWING CRYSTALLINE PATCHES IN AMORPHOUS BULK REGION.....	85

FIGURE 3. 4. TEM IMAGES REVEALING THE DIFFERENT STRUCTURAL ARRANGEMENTS OF A) HEXENE-CTF_400_1, B) HEXENE-CTF_400_10 AND C) HEXENE-CTF_500_10....	85
FIGURE 3. 5. ACETYLENE ADSORPTION (CLOSED SYMBOLS) AND DESORPTION (OPEN SYMBOLS) ISOTHERMS OF ALL HEXENE-CTFS OBTAINED AT 0°C AND 25°C.....	86
FIGURE 3. 6. ETHYLENE ADSORPTION (CLOSED SYMBOLS) AND DESORPTION (OPEN SYMBOLS) ISOTHERMS OF ALL HEXENE-CTFS OBTAINED AT 0°C AND 25°C.....	86
FIGURE 3. 7. CO ₂ ADSORPTION (CLOSED SYMBOLS) AND DESORPTION (OPEN SYMBOLS) ISOTHERMS OF ALL HEXENE-CTFS OBTAINED AT 0°C AND 25°C.....	90
FIGURE 4. 1. FT-IR SPECTRAL COMPARISON BETWEEN ACAC-CTFS OBTAINED AT DIFFERENT REACTION CONDITIONS WITH RESPECT TO THE MONOMER.....	120
FIGURE 4. 2. NITROGEN ADSORPTION/DESORPTION ISOTHERMS OF ACAC-CTFS MEASURED AT 77 K, FILLED AND EMPTY SYMBOLS REPRESENT ADSORPTION AND DESORPTION, RESPECTIVELY.....	121
FIGURE 4. 3. CO ₂ ADSORPTION (CLOSED SYMBOLS) AND DESORPTION (OPEN SYMBOLS) ISOTHERMS OF THE STUDIED ACAC-CTFS MEASURED UP TO 1 BAR AT 273 K AND 298 K.....	122
FIGURE 4. 4. H ₂ ADSORPTION (CLOSED SYMBOLS) AND DESORPTION (OPEN SYMBOLS) ISOTHERMS FOR ACAC-CTFS MEASURED AT 77 K.....	124
FIGURE 4. 5. FT-IR SPECTRA COMPARISON BETWEEN PRISTINE AND ¹³ C CP-MAS ssNMR SPECTRAL COMPARISON BETWEEN (A) PRISTINE ACAC-CTF AND (B) FRESH V@ACAC-CTF CATALYST.....	127
FIGURE 4. 6. DECONVOLUTED XPS N 1S SPECTRA (LEFT) AND O 1S SPECTRA (RIGHT) OF (A) PRISTINE ACAC-CTF (B) V@ACAC-CTF.....	128
FIGURE 4. 7. DECONVOLUTED XPS SPECTRA OF VANADIUM IN THE V 2P REGION FOR V@ACAC-CTF CATALYST.....	129
FIGURE 5. 1. DECONVOLUTED XPS N 1S SPECTRA OF PYZ-CTF-5-400 AND ISOX-CTF-5-400.....	150

FIGURE 5. 2. NITROGEN ADSORPTION/DESORPTION ISOTHERMS OF PYZ-CTFs AND ISOX-CTFs MEASURED AT 77 K, FILLED AND EMPTY SYMBOLS REPRESENT ADSORPTION AND DESORPTION, RESPECTIVELY.....	152
FIGURE 5. 3. CO ₂ ADSORPTION/DESORPTION ISOTHERMS OF PYZ-CTF-5-400 AND ISOX-CTF-5-400 MEASURED AT 1 BAR, FILLED AND EMPTY SYMBOLS REPRESENT ADSORPTION AND DESORPTION, RESPECTIVELY.....	153
FIGURE 5. 4. CO ₂ UPTAKE OF CTF MATERIALS VS THEIR BET SURFACE AREA AND NITROGEN CONTENT PER 1000 M ² /G SURFACE AREA, MEASURED AT 273 K AND 1 BAR.....	155
FIGURE 5. 5. CO ₂ -TPD OF PYZ-CTF, ISOX-CTF, ACAC-CTF AND CTF-1.....	157
FIGURE 5. 6. HYDROGEN ADSORPTION ISOTHERMS OF PYZ-CTF AND ISOX-CTF AT 77K AND 1 BAR.....	158
FIGURE 5. 7. CONVERSION OF 1A USING CTF-1-400 WITH REACTION TIMES USING 1 ATM OF O ₂ . AFTER 12H THE REACTION WAS SPLIT INTO TWO - (I) PURE O ₂ REMOVED AND REACTION CONTINUED (AIR), AND (II) CTF-1-400 WAS FILTERED OUT AND REACTION CONTINUED UNDER PURE (WITHOUT CTF).....	163
FIGURE 6. 1. (A) <i>N,N,N',N'</i> -TETRAMETHYL- <i>P</i> -PHENYLENEDIAMINE (TMPD) AS A TWO-STAGE WURSTER-TYPE REDOX SYSTEM. (B) GENERATION OF HYDROGEN PEROXIDE IN ERYTHROCYTES IN THE PRESENCE OF TMPD.....	184
FIGURE 6. 2. SYNTHESIS OF TAPD-(Me) ₂ AND TAPD-(OMe) ₂ COFs FORMING DUAL PORE KAGOME LATTICE.....	186
FIGURE 6. 3. SOLID-STATE NMR SPECTRA OF TAPD-(Me) ₂ (LEFT COLUMN) AND TAPD-(OMe) ₂ (RIGHT COLUMN). SECTIONS A AND B SHOW ¹ H MAS (35 KHz) NMR SPECTRA AND DECOMPOSITIONS WHICH YIELDED THE CHEMICAL SHIFTS AND FRACTIONS. SECTIONS C AND D SHOW ¹ H DQ-SQ 2D CORRELATIONS INDICATING THE PROXIMITY OF ONE OF THE PHENYL PROTONS TO THE METHYL AND METHOXY PROTONS. SECTIONS E AND F SHOW ¹ H- ¹³ C CP HETCOR 2D CORRELATIONS INDICATING THE PROXIMITY OF ONE TYPE OF CARBON ATOMS AT THE PHENYL RINGS TO THE ATTACHED METHYL AND METHOXY PROTONS. THE ¹³ C { ¹ H} CPMAS SPECTRUM (G) CORRESPONDS TO THE STRUCTURE (H) AND THE SPECTRUM (J) CORRESPONDS TO THE STRUCTURE (I).....	188

FIGURE 6. 4. PXRD PATTERN AND PAWLEY REFINEMENT OF (A) TAPD-(Me) ₂ AND (B) TAPD-(OMe) ₂ COFs, TOP VIEW OF (C) TAPD-(Me) ₂ AND (D) TAPD-(OMe) ₂ COFs SHOWING THE IDEAL ECLIPSED (AA) STRUCTURES. SIDE VIEWS OF (E) TAPD-(Me) ₂ AND (F) TAPD-(OMe) ₂ COFs. *H ATOMS ARE OMITTED FOR CLARITY.....	189
FIGURE 6. 5. COMPARISON BETWEEN THE EXPERIMENTALLY OBSERVED AND MD CALCULATED PXRD PATTERNS FOR TAPD-(Me) ₂ AND TAPD-(OMe) ₂ , AVERAGED OVER THE COURSE OF A 400 PS MD SIMULATION AT 300 K AND 1 BAR USING AN <i>AB INITIO</i> DERIVED SYSTEM-SPECIFIC FORCE FIELDS. THE RESULTING UNIT CELL PARAMETERS AND PEAK POSITIONS HAVE BEEN INDICATED.....	190
FIGURE 6. 6. Ar SORPTION ISOTHERMS AND PORE SIZE DISTRIBUTIONS (INSET) OF TAPD-(Me) ₂ COF AND TAPD-(OMe) ₂ COF.....	191
FIGURE 6. 7. TEM AND SEM IMAGES OF (A, B) TAPD-(Me) ₂ AND (C, D) TAPD-(OMe) ₂ COFs SHOWING CRYSTALLINE DOMAINS AND THE MORPHOLOGY OF COF CRYSTALLITES.....	192
FIGURE 6. 8. (A) SOLID STATE UV-VIS SPECTRA, (B) TAUC PLOT ANALYSES FOR BANDGAP CALCULATIONS, (C) BAND POTENTIAL ALIGNMENTS OF THE COF VS NHE (V) AT PH=0, AND (D) H ₂ O ₂ PRODUCTION PER GRAM CATALYST OVER 5 HOURS OF REACTION TIME OF TAPD-(Me) ₂ AND TAPD-(OMe) ₂ COFs.....	193
FIGURE 7. 1. NUMBER OF PUBLICATIONS IN WEB OF SCIENCE (TILL SEPTEMBER 2020) BASED ON THE KEY WORDS (TOP) “COVALENT ORGANIC FRAMEWORKS” (BOTTOM) “COVALENT TRIAZINE FRAMEWORKS”.....	235

LIST OF ABBREVIATIONS AND ACRONYMS

A

Acac Acetylacetone

B

BET Brunauer-Emmett-Teller

C

CCS Carbon capture and storage

CCU Carbon capture and utilization

CHNS Carbon-hydrogen-nitrogen-sulfur

CMP Conjugated Microporous Polymers

COF Covalent Organic Framework

CTF Covalent Triazine Framework

D

DFT Density Functional Theory

DMF Dimethylformamide

DMSO Dimethyl Sulfoxide

DRIFTS Diffuse reflectance infrared Fourier-transform spectroscopy

E

EDX Energy Dispersive X-ray

EELS Electron Energy Loss Spectroscopy

H

HCP Hyper Cross-linked Polymers

I

IAST Ideal Adsorbed Solution Theory

ICP Inductively coupled plasma

IEA International Energy Agency

IUPAC	International Union of Pure and Applied Chemistry
K	
KAP	Knitting Aromatic Polymers
M	
MOF	Metal-Organic Framework
N	
NMR	Nuclear Magnetic Resonance
O	
OES	Optical emission spectroscopy
P	
PAF	Porous Aromatic Framework
PIM	Polymers of Intrinsic Microporosity
POP	Porous Organic Polymers
PE	Polyethylene
Q	
QSDFT	Quenched Solid-state Density Functional Theory
S	
SDS	Sustainable Development Scenario
SEM	Scanning Electron Microscopy
ss-NMR	Solid-State Nuclear Magnetic Resonance
T	
TAPD	<i>N,N,N',N'</i> -Tetrakis(4-aminophenyl)-1,4-phenylenediamine
TEM	Transmission Electron Microscopy
TGA	Thermogravimetric analysis
THF	Tetrahydrofuran

U

UV Ultra-Violet

X

XPS X-ray Photoelectron Spectroscopy

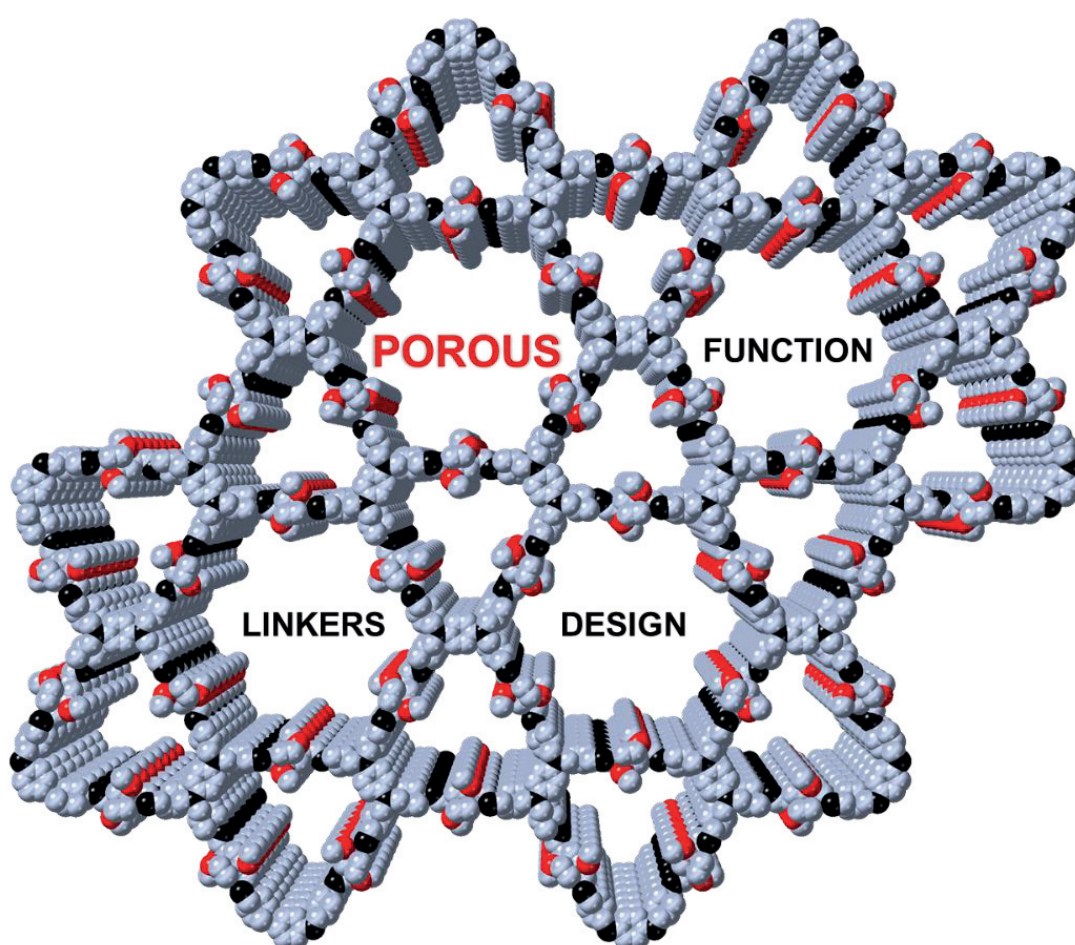
XR(P)D X-ray (powder) diffraction

XRF X-ray fluorescence

Z

ZIF Zeolitic Imidazolate Framework

1 POROUS ORGANIC MATERIALS: COVALENT ORGANIC FRAMEWORKS (COFs) AND COVALENT TRIAZINE FRAMEWORKS (CTFs)



This chapter is based on the published review article:

C Krishnaraj, HS Jena, K Leus, P Van Der Voort. Covalent triazine frameworks – a sustainable perspective. *Green Chemistry* 22 (4), 2020, 1038-1071.

Introduction

A pore can be defined simply as a cavity in an object. From stomata in the plants to hair follicles in mammals, pores have always been existing naturally. Through stomata, plants absorb carbon dioxide and release water vapor and oxygen as part of the global water and carbon cycles (figure 1.1).¹ Hair follicles on the other hand allow the secretion of sebum which lubricates the hair and skin of mammals. In general, porous materials are formed due to inefficient molecular packing occurring from concavities in the components.² The knowledge and design of pores have made a significant impact in the world. For example, porous silicon can effectively emit visible light which has enabled optoelectronics, displays and lasers.³ Other macroscopic pores such as sponges, and textiles have been a part of our daily lives. Apart from the macroscopic pore manipulation, humans have also exploited microscopic pores in materials for various purposes.

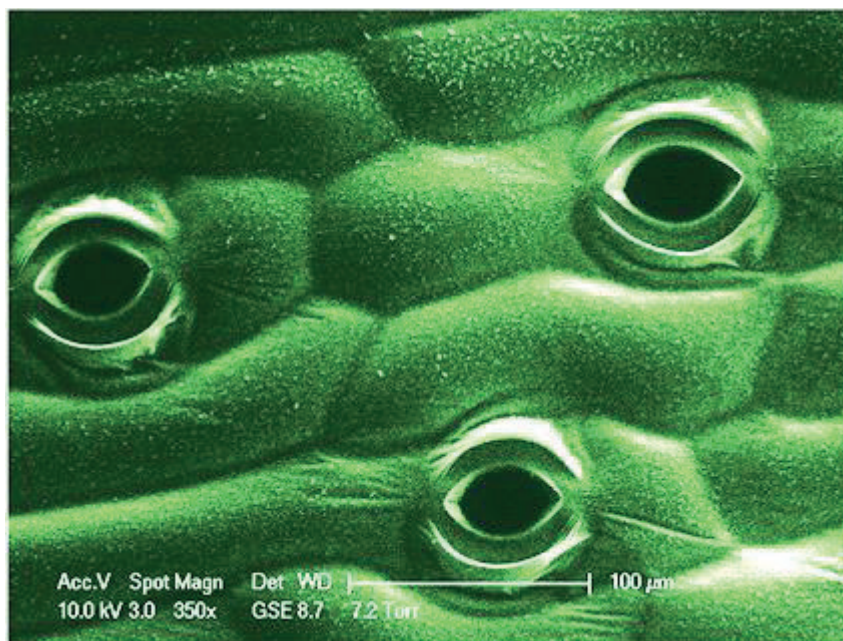


Figure 1. 1. Microscopic view of plant stomata.¹ Reproduced with permission from John Wiley and Sons.

The International Union of Pure and Applied Chemistry (IUPAC)⁴ has classified pores into three main categories:

- (i) Pores with mean diameter greater than 50 nm are called macropores.
- (ii) Pores with mean diameter between 2-50 nm are called mesopores.
- (iii) Pores with mean diameter less than 2 nm are called micropores. When the pore diameter is <0.7 nm they are called ultramicropores.

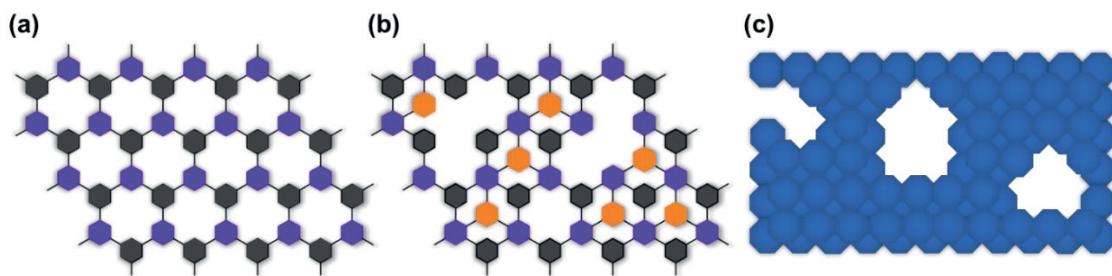


Figure 1. 2. Three ways to form porous materials (a) pores from directional polymerization of monomers, (b) pores due to defects in materials, and (c) pores due to irregular packing of the materials.

This classification was based on the nitrogen physisorption isotherms analyzed at 77K. A nanopore includes all the above pores but with an upper limit of ~100 nm. There are different types of pores based on their connection pathways in the material and their morphology. Based on the availability of the pores to an external fluid, pores can be classified as (a) closed pores, (b) blind or dead-end open pores, (c) through open pores. Based on their morphology they can be (a) cylindrical (through or blind), (b) ink-bottle, (c) funnel, and (d) slit-shaped. Another important term is the roughness of the external surface of the material. The convention is that a rough surface is non-porous unless it has irregularities that are deeper than their width.

Porous materials can be formed mainly through three ways (figure 1.2).

- (a) Pores formed inherently from crystalline structures, e.g., Metal-organic frameworks (MOFs), Covalent organic frameworks (COFs), Zeolites. These are highly regular networks with pores of molecular dimensions.
- (b) Pores formed through selective removal of certain elements from an original structure, e.g., defective MOFs, porous metal oxides.
- (c) Pores formed by aggregation or loose packing of the materials, e.g., ceramics. These pores are highly dependent on the initial material synthesis and treatment.

Porous materials containing such pores provide an internal surface area that can be utilized for several applications. Though there are several types of porous materials based on organic and inorganic moieties, the focus of this dissertation is on porous organic materials, more specifically porous solids. Porous organic materials are built using purely organic (hydrocarbon) building blocks linked through covalent bonds.⁵ These solid

materials can be classified as hyper cross-linked polymers (HCPs)⁶, polymers of intrinsic microporosity (PIMs)⁷, conjugated microporous polymers (CMPs)⁸, porous aromatic frameworks (PAFs)⁹, covalent organic frameworks (COFs)¹⁰ and covalent triazine frameworks (CTFs).¹¹ CTFs are a special class of material and can also be considered a sub-class of COFs or PAFs (based on the observed crystalline or amorphous features). Due to such an extensive list of porous organic materials, a brief introduction is provided for HCPs, PIMs, CMPs and PAFs. Keeping in the mind the focus of this dissertation, the discussion is further extended on COFs and CTFs.

1.1. Hyper Cross-linked Polymers (HCP)

The synthesis of HCPs is based on fast kinetics to form strong linkages in a highly cross-linked network predominantly containing porosity.⁶ HCPs are based mainly on Friedel-Crafts chemistry which produce amorphous polymers with low densities, high surface areas and microporosities. Mainly, three types of synthesis routes are used to make HCPs – post cross-linking of polymers, direct one-step polycondensation, and using external cross-linkers. High degree of cross-linking allows high stability to the materials and can be achieved with mild reaction conditions and cheap starting products. The HCP chemistry allows easy scale-up of the polymers with good reproducibility. Knitting aromatic polymers (KAPs) are a classic example of HCPs.⁶

1.2. Polymers of Intrinsic Microporosity (PIMs)

PIMs are comprised of macromolecules developed mainly from polybenzodioxin linkages. They are amorphous microporous polymers formed by interclasped aromatic rings put together like a chain with contorted sites which restricts efficient packing.⁷ Porosity is obtained in the bulk of the material due to this inefficient packing rather than interconnected bonds within the material. Initially the synthesis was based on phthalocyanine-forming reaction of a bis(phthalonitrile) monomer aided by a metal ion template. PIMs are generally soluble in organic solvents and this solubility allowed the processing of PIMs into films for membrane applications. They lack designed framework but do possess microporosity based on polymer chain flexibility.

1.3. Conjugated Microporous Polymers (CMPs)

CMPs are amorphous covalently linked polymers that allow the material network extension in a π -conjugated order.⁸ These are different from other materials due to the

availability of unique π -conjugation and porosity. The building units vary from phenyl units to heterocyclic aromatic units. Different covalent reactions⁸ such as Suzuki coupling, Sonogashira-Hagihara reaction, Phenazine ring fusion, Friedel-Crafts arylation etc. have been used to synthesize CMPs. Due to the availability of diverse π units in the network, CMPs have been used in heterogeneous catalysis, light harvesting and electric energy storage applications. CMPs are insoluble and amorphous in nature which makes their structural characterization hard.

1.4. Porous Aromatic Frameworks (PAFs)

PAFs are open framework materials which are amorphous and rich in benzene rings. The first PAF (PAF-1) was synthesized using Yamamoto type Ullmann coupling reaction of tetrakis(4-bromophenyl)methane and showed high BET surface area of 5600 m² g⁻¹.⁹ PAF-1 was formed through irreversible coupling reaction which creates strong C-C covalent bonds thus forming highly stable framework which is resistant to harsh chemical treatments. PAFs can be built from diverse building units due to the availability of several coupling reactions. This also allows the tuning of functionality at a molecular level. However due to the lack of crystallinity, their structure cannot be resolved using X-ray diffraction methodologies. Though other characterization techniques have been employed to study these materials.

1.5. Covalent Organic Frameworks (COFs)

COFs are a class of crystalline porous organic polymers which were firstly developed by Yaghi and co-workers in 2005.¹² They are synthesized by using organic building units coupled with strong covalent bonds. Hence COFs in general have permanent porosity and highly ordered structures. A great advantage of these materials is that their structure can be accurately predetermined based on the geometry of the building blocks and the type of covalent bond applied to couple the building blocks. This concept of reticular chemistry provides a platform for precise functionalization at molecular resolution in these materials. This allows unique conformations and morphologies that creates confined molecular space and interface to interact with photons, excitons, electrons, holes, spins, ions, and molecules.

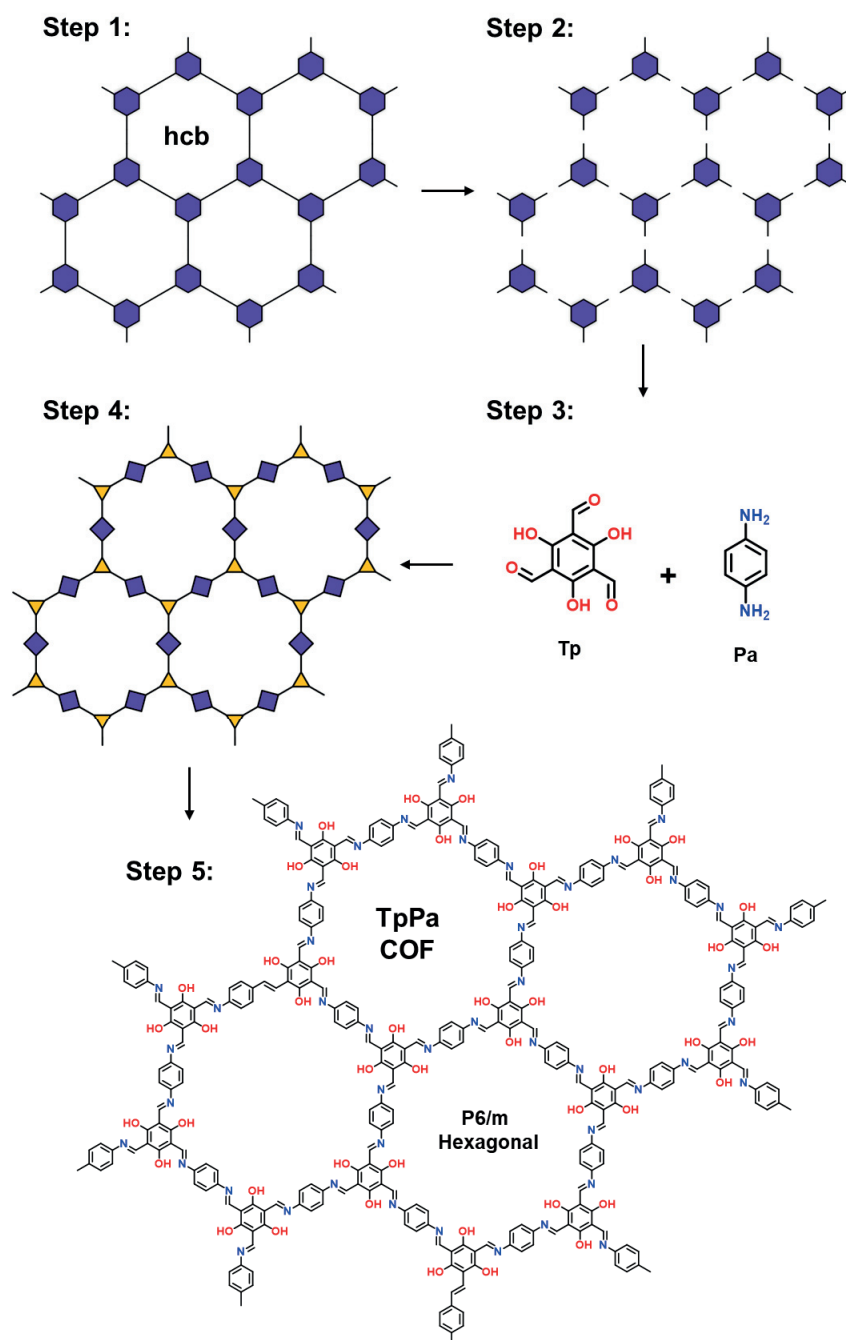


Figure 1. 3. General steps for synthesis of COF. Step 1: Select a target topology, Step 2: Evaluate points of connection depending on the geometry, Step 3: Identify linkers that are geometrical equivalents of the sub-structure, Step 4: Connect the linkers, and Step 5: Characterize the material.¹³

1.5.1. COF design principle

A COF is comprised of mainly two components: linkers (building blocks) and linkages (covalent bonds formed between the building blocks). The general approach for reticular synthesis of COFs is shown in figure 1.3.¹³ In step 1, the desired topology is targeted and

deconstructed into fundamental sub-structures. Step 2 involves evaluation of their points of connection and their geometry. In step 3, the geometrical equivalents of these sub-structures are identified in organic molecules which can be used as linkers. Generally, rigid linkers are chosen to obtain unaltered directional polymerization to reach a thermodynamically stable material. Step 4 consists of stitching up these linkers through covalent linkages by identifying the synthetic conditions leading to a crystalline COF. These conditions are obtained by balancing the thermodynamics (microscopic reversibility of the linkages) and the kinetics (rate of the reaction) of the COF formation. Step 5 involves the characterization of COF through X-ray or electron diffraction techniques. By having a knowledge on the topologies of the desired target, theoretical X-ray diffraction patterns can be simulated and matched with the experimental patterns.

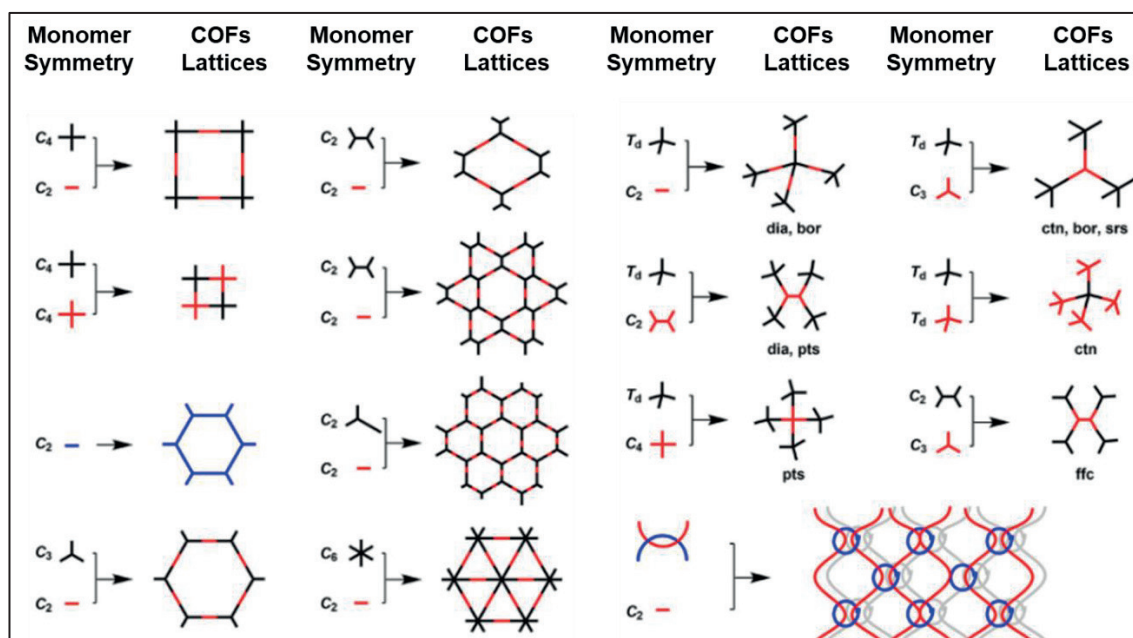


Figure 1. 4. Basic topological diagrams for the design of 2D and 3D COF.¹⁴ Reproduced with permission from American Chemical Society.

For the choice of any COF lattice, the monomer symmetry is essential. Based on the monomer symmetry, several COF lattices have been reported. A general scheme of the basic topological diagrams for the design of 2D and 3D COFs is given in figure 1.4.¹⁴ By combining linkers with different geometry, one can obtain a COF structure with long range order. For example, $C_3 + C_2$ linker will give rise to a hexagonal COF, whereas $C_6 + C_2$ will give rise to a trigonal COF. Based on the target topology and application, a judicial decision can be taken on the choice of the monomers.

1.5.2. COF linkages

The notion behind COF started with utilization of dynamic reversibility of certain chemical reactions which could allow the material to self-correct and produce a thermodynamically stable and crystalline material. Until now, several types of reversible linkages have been utilized for the formation of COFs as shown in figure 1.5.¹⁵ In addition, certain exceptions to this rule have also resulted in formation of crystalline materials through irreversible reactions, by focusing on other intermolecular interactions. Based on these reactions, several 2D and 3D COFs have been reported so far. Though the library of linkers for 2D COFs are diverse, the 3D COFs are limited due to low availability of 3D directional linkers.¹⁶ On the other hand, though limited, only 3D COFs have been transformed into single crystals.¹⁷ Hence on a synthetic viewpoint, a universal method to synthesize crystalline COFs is not available and often, trial and error methods are used to identify ideal growth conditions.

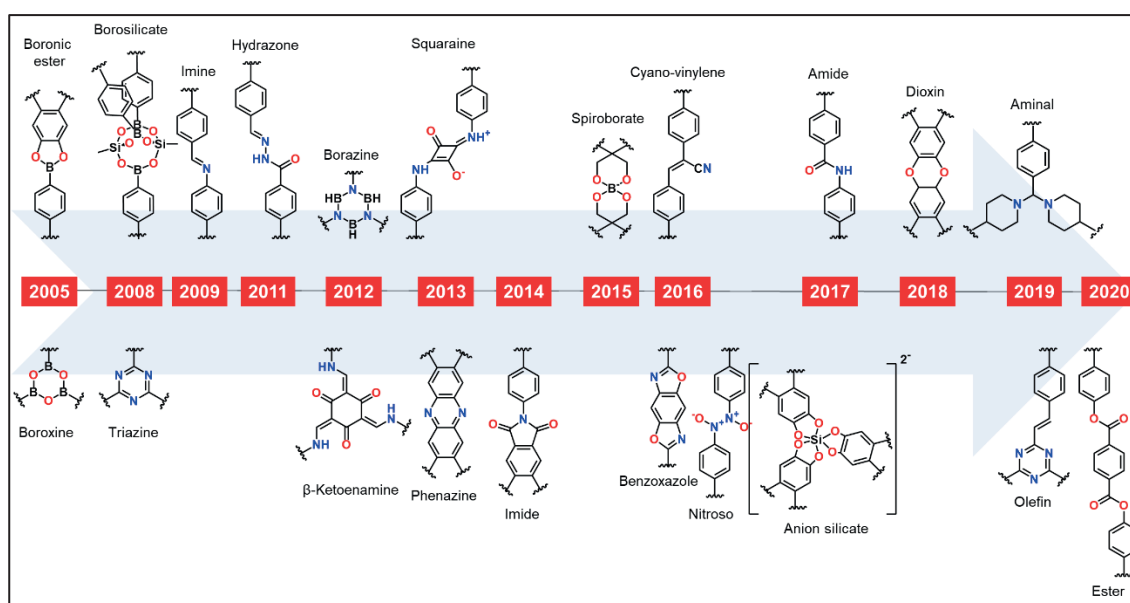


Figure 1. 5. Different linkages used to synthesize COFs (till August 2020).

Since the inception of COF in 2005, the number of linkages to produce COFs has been increasing a lot lately. The most widely studied linkages in terms of number of published reports are imine (2009)¹⁸ and triazine (2008).¹⁹ This is due to their high stability and applicability in several research fields. Moreover, there is a diverse availability of linkers to make these COFs. However, even after several reports on these materials, the research continues due to their unexplored potential in different types of applications (discussed in Chapter 2).

1.5.3. Imine linked COFs

Imine COFs are synthesized by utilizing the dynamic reversible formation of imine ($C=N$) bonds. For this, monomers with amine ($-NH_2$) and aldehyde ($-CHO$) groups are required. Based on the desired topologies, the linkers are designed with proper geometries to form an extended crystalline network. For example, a C3 linker with three aldehyde groups at 120° angles to each other and a C2 linker with two amine groups at 180° angle to each other can be used to make a hexagonal COF (figure 1.6).²⁰ The most used conditions to form imine COFs are by dissolving stoichiometric amounts of the monomers in a mixture of mesitylene/dioxane or o-dichlorobenzene/butanol along with diluted acetic acid in an ampule. Three cycles of freeze-pump-thaw is performed to remove any dissolved gases and make the synthesis conditions inert. The ampule is then vacuum sealed and placed in an oven at 120°C for three days. After three days, a precipitate is observed at the bottom of the ampule. The precipitate is filtered and washed with common organic solvents such as acetone, ethanol, tetrahydrofuran etc. Sometimes a Soxhlet extraction is performed to remove unreacted linkers or partially reacted intermediates from the end-product. Before further usage for application or characterization, the COF is activated under vacuum at 90°C or 120°C . Sometimes supercritical CO_2 activation is required to avoid pore collapse of the COFs during vacuum activation. The cleaning and activation procedure can be altered according to the requirement.

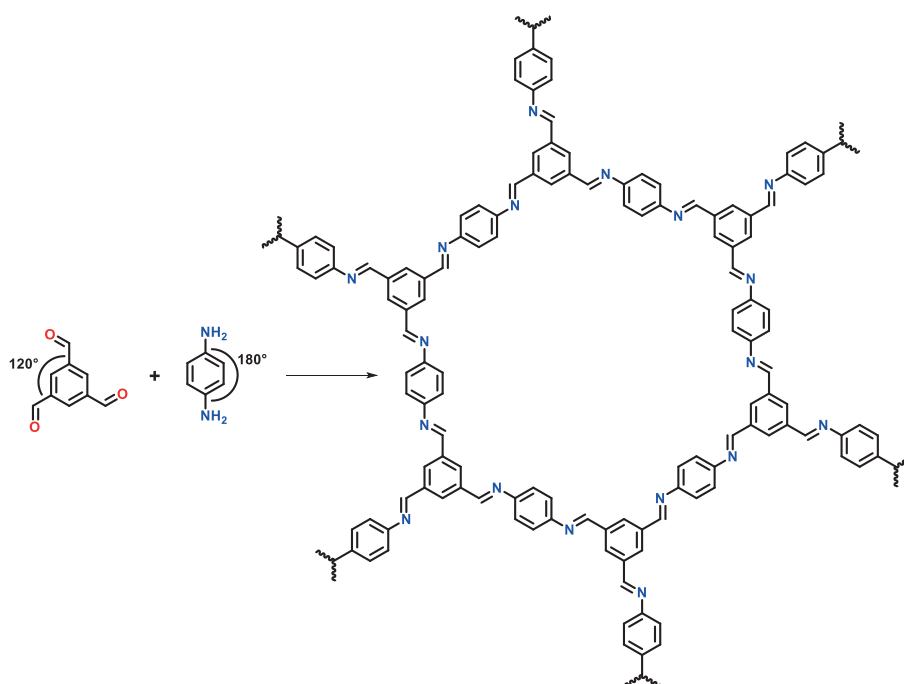


Figure 1. 6. Synthesis of a 2D COF using C3+C2 linkers.

As discussed earlier, one of the main advantages of imine COFs is the availability of several linkers. A list of some of the linkers used for producing imine COFs is given in figures 1.7 and 1.8.¹⁴ This has resulted in several crystalline and porous organic materials which have been used for a diverse array of applications such as gas storage and separation, metal-based catalysis, metal-free catalysis, optoelectronics, photodynamic therapy, thermometry, metal sorption, waste-water treatment, photocatalysis, electrocatalysis.^{14,15}

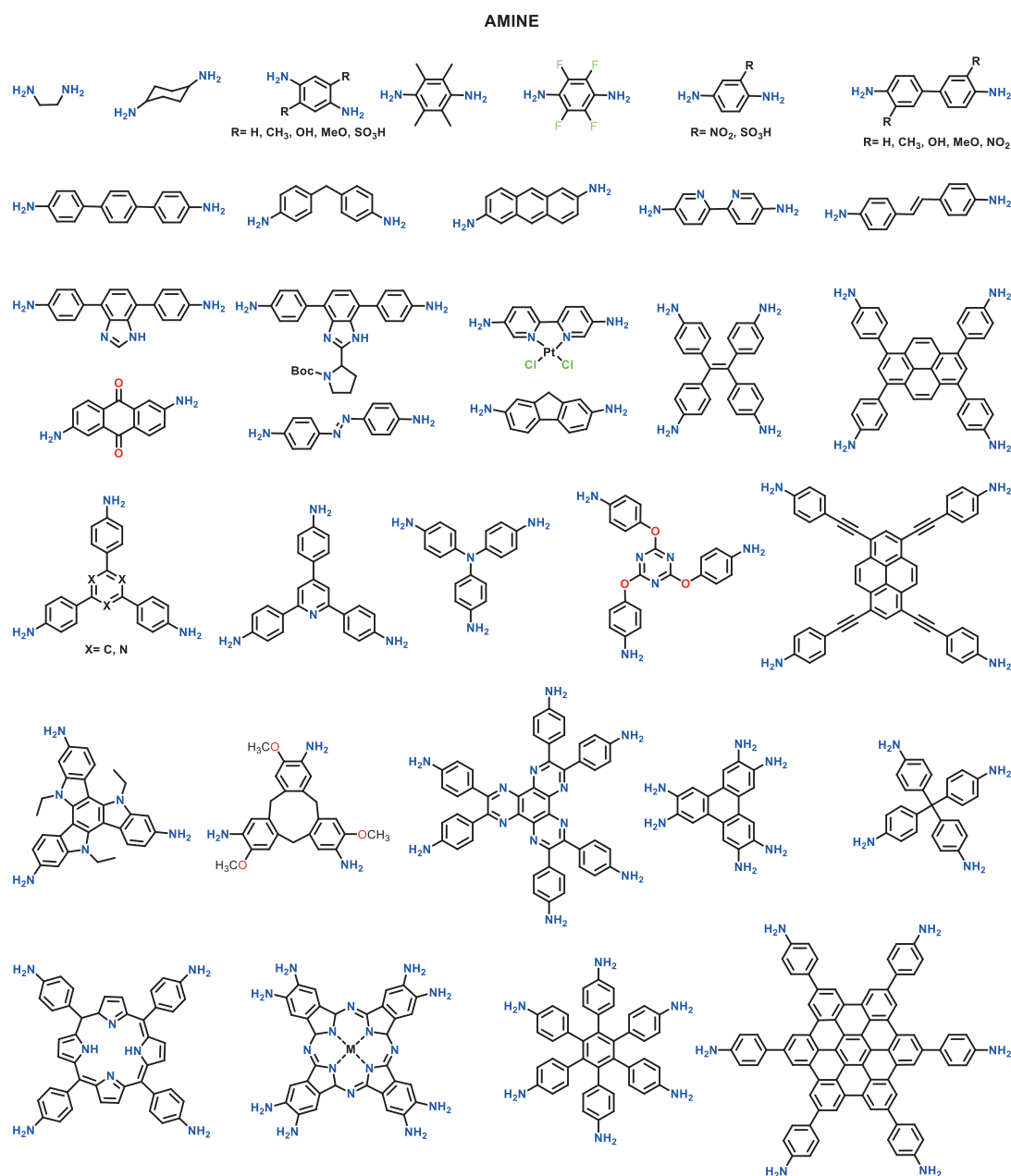


Figure 1. 7. A list of some of the amine appended linkers used in imine COF synthesis.¹⁴

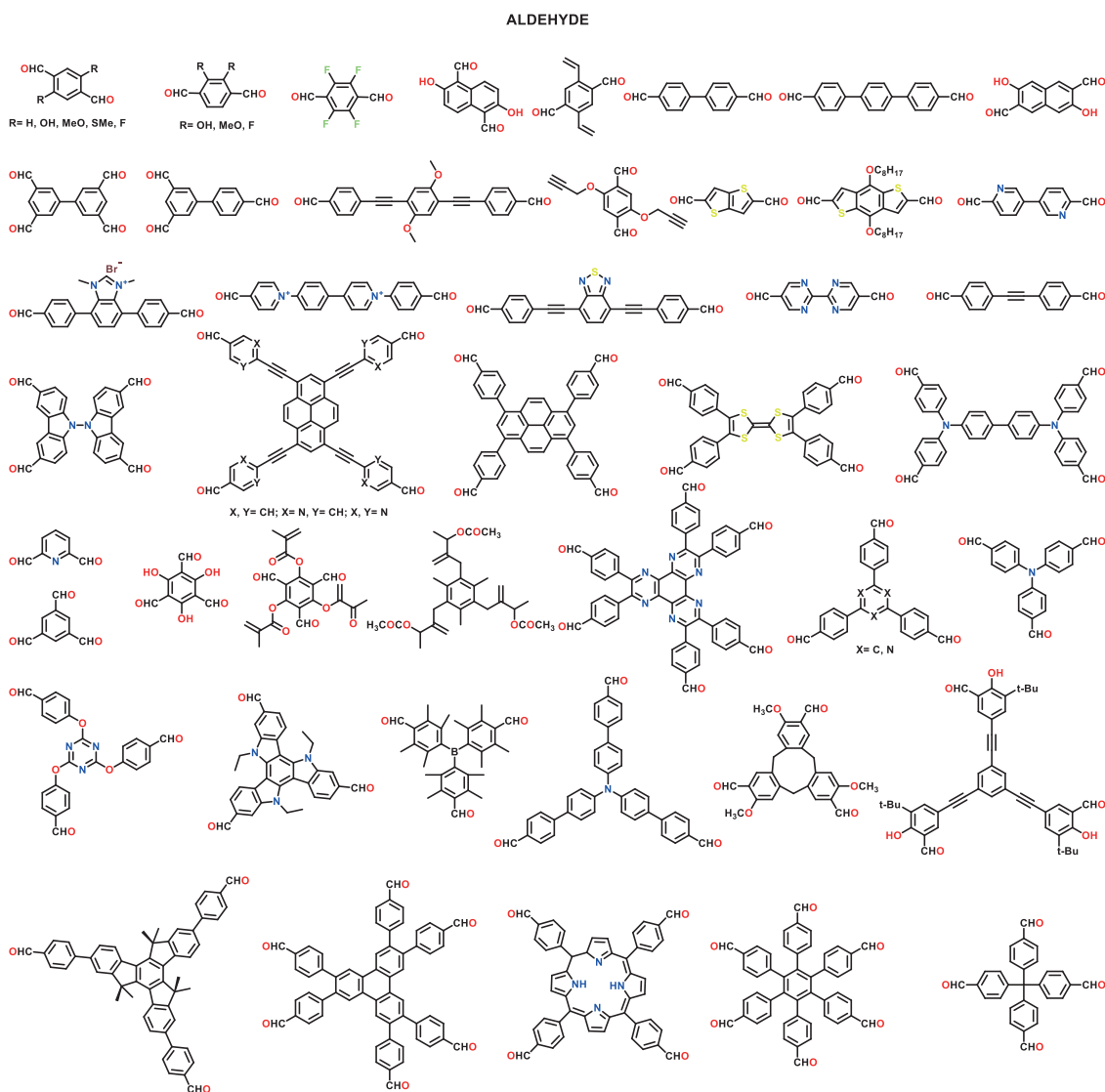


Figure 1. 8. A list of some of the aldehyde appended linkers used in imine COF synthesis.¹⁴

1.6. Covalent Triazine Frameworks (CTFs)

CTF is a porous material constructed particularly by using a triazine ring formation reaction as the covalent linkage between organic building units to form an extended porous framework (figure 1.9).¹⁵ Polymerization of aromatic nitriles was first reported in 1962 by W. G. Toland.²¹ Different metal (copper, manganese, and cobalt) salts were used as catalysts for the trimerization of benzonitrile, orthophthalonitrile, isophthalonitrile and terephthalonitrile to their respective 1,3,5-triazine derivatives, by heating them in the temperature range of 200–400 °C. This idea was further expanded by H. A. Vogel²² in 1972 and G. H. Miller²³ in 1973, employing di-, tri- and tetra-nitrile containing monomers to polymerize at high temperatures (410–550 °C) in the presence of a metal chloride

catalyst. The produced polymers were converted into highly stable and insoluble polymeric materials under the influence of heat and pressure. However, at that time the term covalent triazine framework was not coined and the characterization of the material was limited mainly to elemental and infrared analyses. No in-depth analysis was carried out to determine the crystalline and porous properties of these materials. In 2008, A. Thomas and M. Antonietti introduced the term CTF and expanded the synthesis of these materials as covalent organic frameworks with crystallinity, tunable functionalities, and permanent porosities.¹⁹ This allowed the development of high nitrogen containing ordered porous materials having high thermal (up to 500°C) and chemical stability (10M H₂SO₄ and 10M NaOH). CTF-1 was the first covalent triazine framework prepared through the trimerization of 1,4-dicyanobenzene at 400 °C using an ionothermal synthesis route, wherein, molten ZnCl₂ acted as both the solvent and the catalyst.

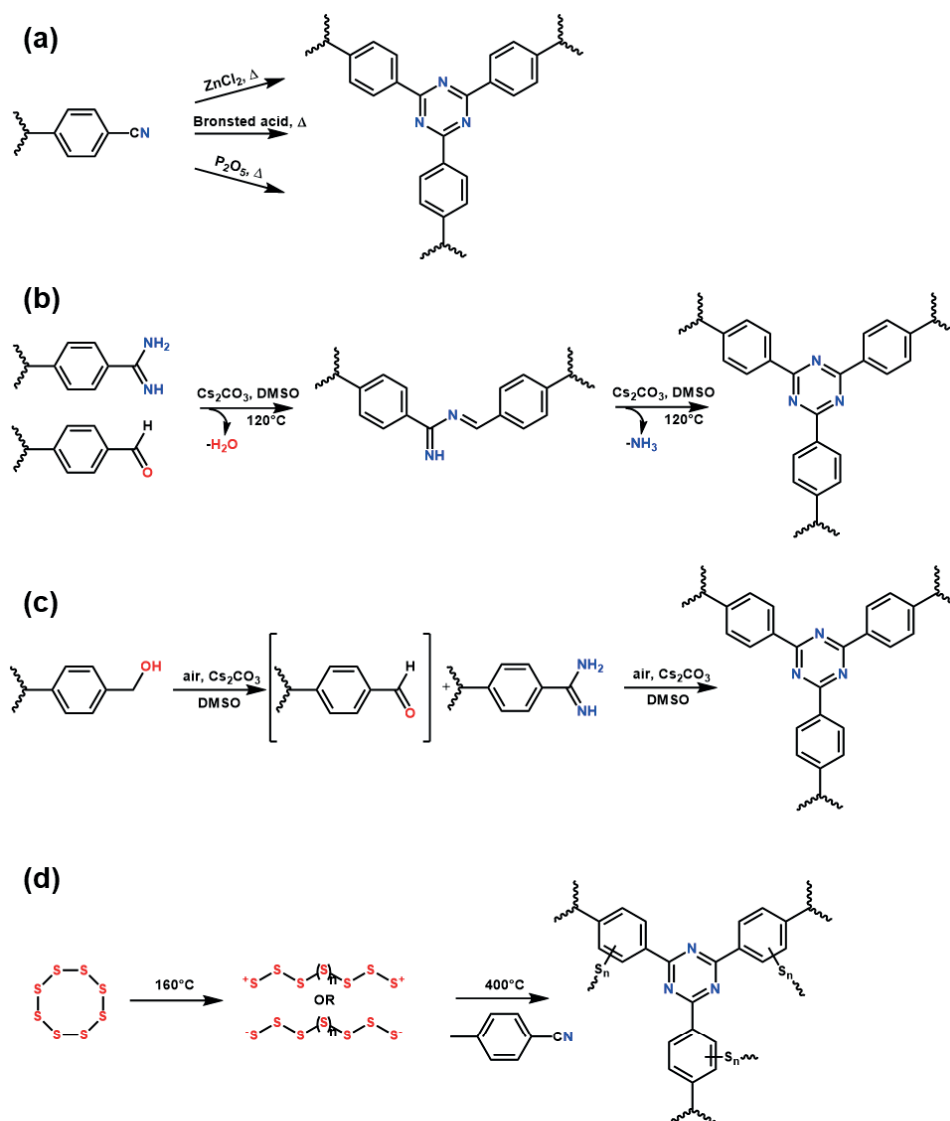


Figure 1. 9. Different approaches to form triazines used in synthesis of CTFs.¹⁵

CTFs show promising properties and can compete with current state-of-the-art materials for several applications. These materials exhibit a long-term stability and are not prone to atmospheric deterioration.^{24, 25} The strong covalent linkage (C=N), high intrinsic nitrogen content and the ability to add heteroatoms in the structure provide a base for several potential applications such as heterogeneous catalysis, gas storage and separation, dye adsorption etc. Ideally to be able to produce a crystalline covalent organic framework, a dynamic reversible covalent linkage is required as it provides the possibility of self-correction in the materials to restrict defect formation. However, by doing so, a dual-edged sword situation is created as the covalent linkages are also susceptible to instability. For example, boronate ester COFs are highly crystalline materials, but exhibit a limited stability in comparison to CTFs.²⁶ Several strategies have been introduced such as keto–enol tautomerization,²⁷ high stacking interaction^{28, 29} and post modification³⁰ to produce stable COFs. CTFs show high stabilities even in the presence of strong acids (10M H₂SO₄) and bases (10M NaOH),³¹ giving them an edge over several other porous materials and a strong potential to be used in industrial applications. Particularly, they can be recycled and reused easily which allows them to be a strong candidate in terms of sustainable materials.

1.6.1. Ionothermal synthesis

The concept of ionothermal synthesis was first introduced in 2004 by R. E. Morris et al.,³² for the synthesis of zeolites using ionic liquids and eutectic mixtures as solvent and structural template. This is a different strategy compared to the standard hydrothermal preparation, which takes place in a predominantly molecular solvent. Ionothermal synthesis opened several possibilities for the preparation of zeolites and other related porous solids. The first reported CTF was synthesized using this ionothermal synthesis route (figure 1.10).^{19, 25} ZnCl₂ at high temperatures become molten and act as ionic liquids which can dissolve aromatic dinitrile monomers. In addition, ZnCl₂, being a Lewis acid in nature catalyzes the trimerization of nitriles into triazines. The trimerization of a nitrile into a triazine is a sufficiently reversible reaction at high temperatures and hence this reaction allows the formation of an extended porous network. Typically, various molar ratios of the aromatic dinitrile monomer and ZnCl₂ are transferred into an ampoule, which is thoroughly evacuated under vacuum, sealed, and heated at 400 °C for 40–48 h.²⁵ The resulting black monolith is purified by the following general cleaning steps with H₂O,

HCl (to remove Zn and Cl residues) and THF (to remove unreacted organic moieties). The final grounded product is in the form of a black powder.

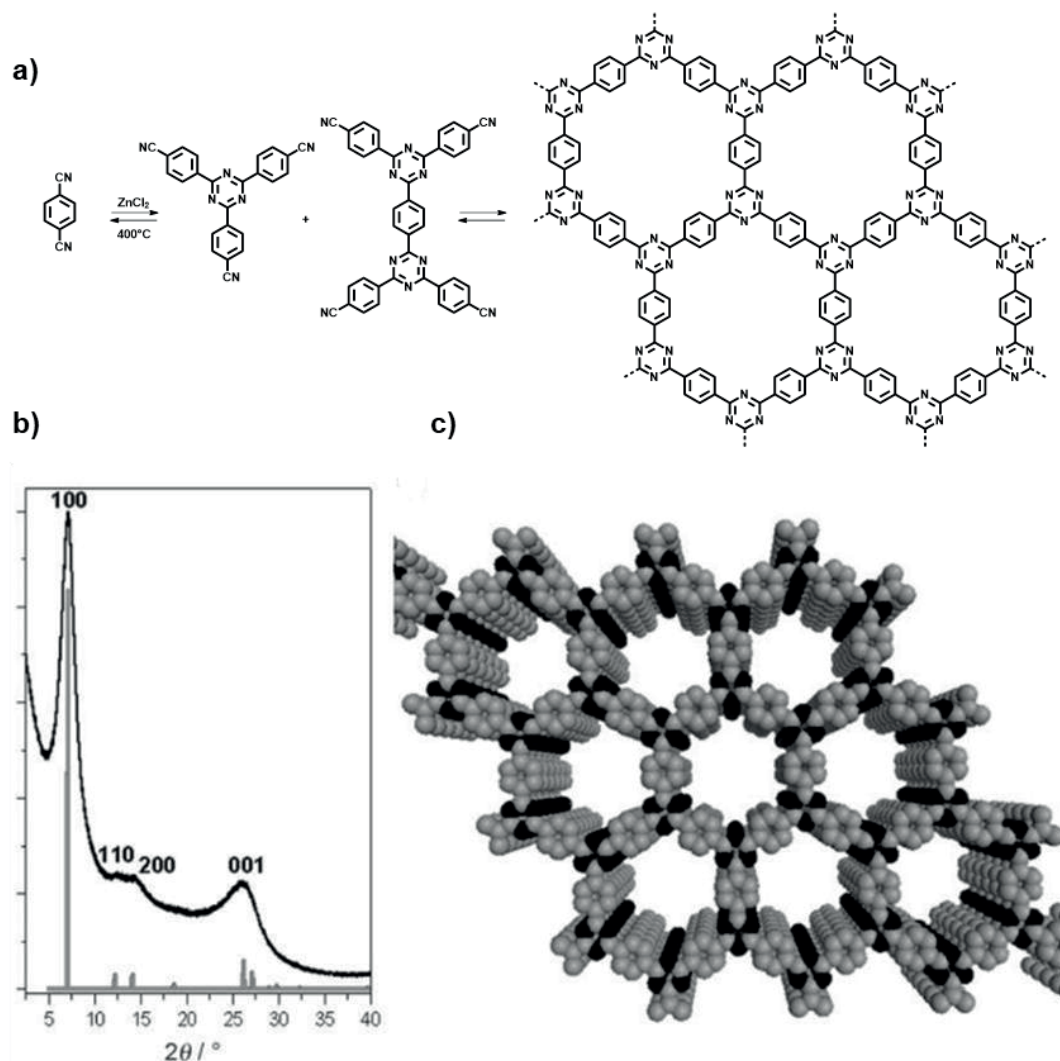


Figure 1. 10. (a) Trimerization of 1,4-dicyanobenzene in molten ZnCl₂ to form trimers and oligomers, followed by an extended covalent triazine-based framework (CTF-1), (b) Experimental (black) and calculated (gray) PXRD patterns of CTF-1, and (c) schematic representation of the CTF-1 structure (C – gray, N – black).¹⁹ Reproduced with permission from John Wiley and Sons.

Most of the obtained CTFs using this method have been reported as amorphous materials and only CTF-0,³³ CTF-1¹⁹ and CTF-2³⁴ were obtained as crystalline materials. The crystallinity depends to a high extent on the planarity of the applied monomers and contorted monomers usually result in amorphous characteristics. Another cause for the amorphous nature of CTFs is the harsh reaction conditions, as the high reaction temperature causes carbonization of the material. In addition, the applied high

temperatures can produce uncontrollable side reactions, cleavage of nitrile groups, defective pore enlargement, pore wall collapse and interpenetration.^{35, 36} The effect of the synthesis temperature and carbonization has been studied by Antonietti et al.²⁴ and Gascon et al.³⁵ In general, a higher synthesis temperature results in an increased surface area and average pore volume of the CTFs. However, this also comes with the expense of a decreased nitrogen content, modification of the monomer functionality, increased defects and loss of crystallinity. Nonetheless, this has also proved to be beneficial for catalysis by allowing higher substrate diffusion and improving gas storage in several CTFs.

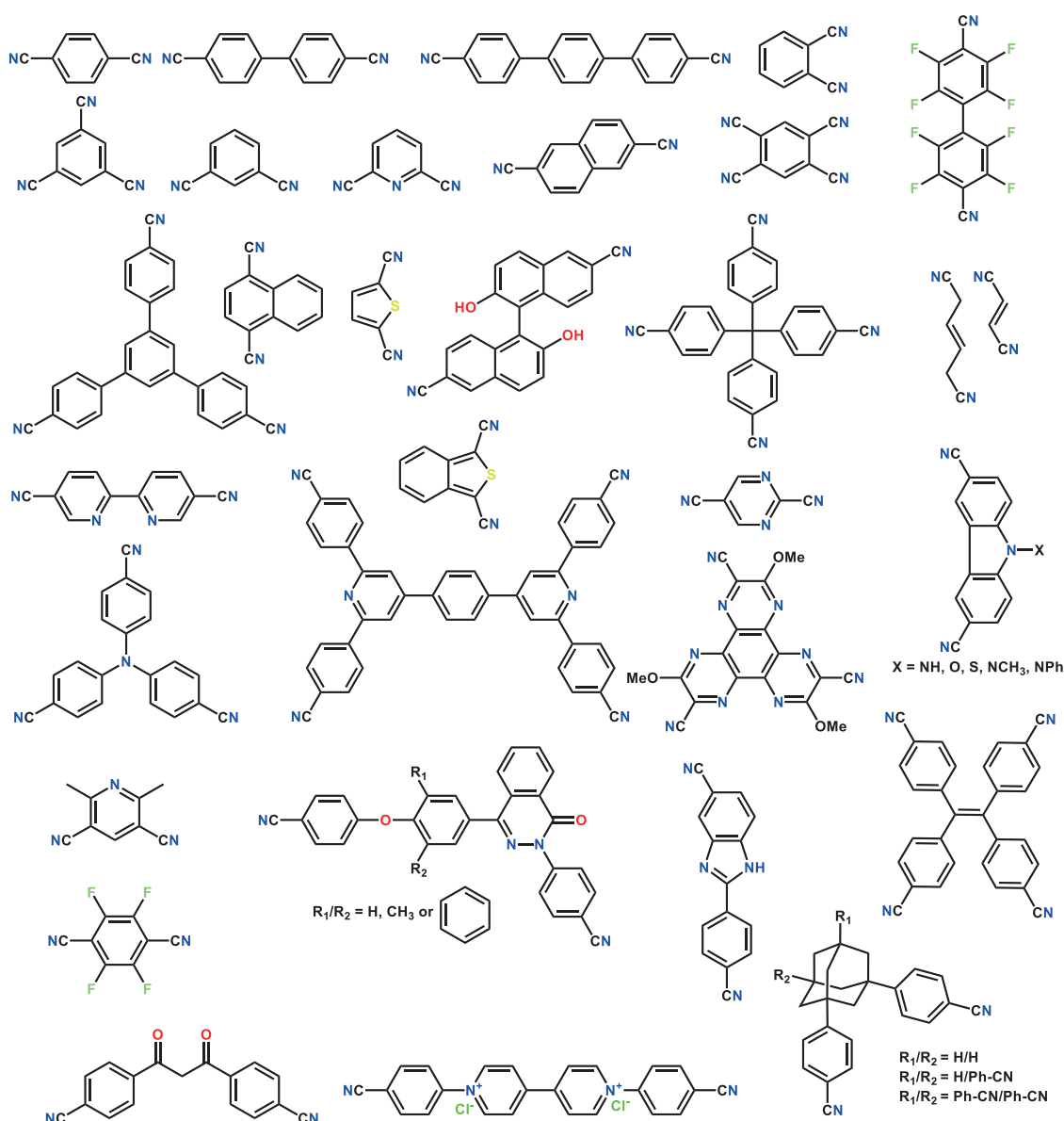


Figure 1. 11. Various monomers used to prepare CTFs.

Apart from the intrinsic nitrogen content from the triazine units, additional nitrogen groups have been added into the framework by modifying the functional group of the dinitrile monomer. Such nitrogen-rich frameworks have been constructed using pyridine, pyrimidine, dimethylpyridine (lutidine), bipyridine and phenylenebis-pyridine containing dinitrile linkers (figure 1.11).³⁷⁻³⁹ This increase in nitrogen content has shown to be beneficial for several applications including CO₂ storage (due to enhanced interaction between N and the CO₂ molecules) and heterogeneous catalysis (since N can donate a lone pair electron for stabilizing the homogeneous metal/metal complexes). In addition, several monomers containing additional heteroatoms have also been utilized for constructing CTFs through this method. These include thiophene,⁴⁰ tetraphenylthiophene,⁴¹ perfluorinated,⁴²⁻⁴⁴ phthalazinone,⁴⁵ and hexaazatriphenylene⁴⁶ based CTFs. Moreover, charged CTFs such as imidazolium^{47, 48} and viologen⁴⁹ cations have also been reported. In addition, a tetracyanoquinodimethane containing conductive CTF⁵⁰ was also synthesized which showed excellent specific capacitances (380 F g⁻¹). Overall, the ionothermal synthesis route paves way for inclusion of a variety of functionalities into the CTF which can be tuned according to the desired application.

1.6.2. Brønsted superacid synthesis

Way back in 1941, A. H. Cook and D. G. Jones had synthesized triazine containing materials using chlorosulfonic acid for the trimerization of aromatic nitriles.⁵¹ The idea of forming aromatic polymers containing the s-triazine ring using aromatic dinitriles was reported in 1966. In this report, D. R. Anderson, and J. M. Holovka used chlorosulfonic acid along with heat to achieve the trimerization.⁵² Additionally, H. A. Vogel in 1972 used trifluoromethane sulfonic acid (triflic acid, CF₃SO₃H) to form triazine based polymers at low temperatures.²² However, the characterization of these polymers was limited during that time and their porous characteristics were not studied. In 2012, Cooper et al. reported the Brønsted acid synthesis of CTFs. Trifluoromethane sulfonic acid was employed as a catalyst to trimerize aromatic nitriles at room temperature and also under microwave conditions. This method exhibited significant advantages in comparison to the ZnCl₂ method – (i) milder synthetic conditions, (ii) no carbonization, (iii) easy cleaning steps, (iv) avoid residual ZnCl₂ in the materials, and (v) produce photoactive materials. In addition, due to the milder synthesis conditions, this approach was also applied to produce porous CTF membranes by obtaining thin films of the acidic nitrile solution onto flat glass discs (figure 1.12).⁵³ The resulting membranes also exhibited

permanent porosities which enabled efficient CO₂/N₂ separation. However, there are some inherent disadvantages of this acid assisted method such as the high cost of the catalyst, lower activity towards heteroatomic nitrile monomers and the difficulty of handling the reaction due to the involved corrosive and eye irritating carcinogenic chemicals.

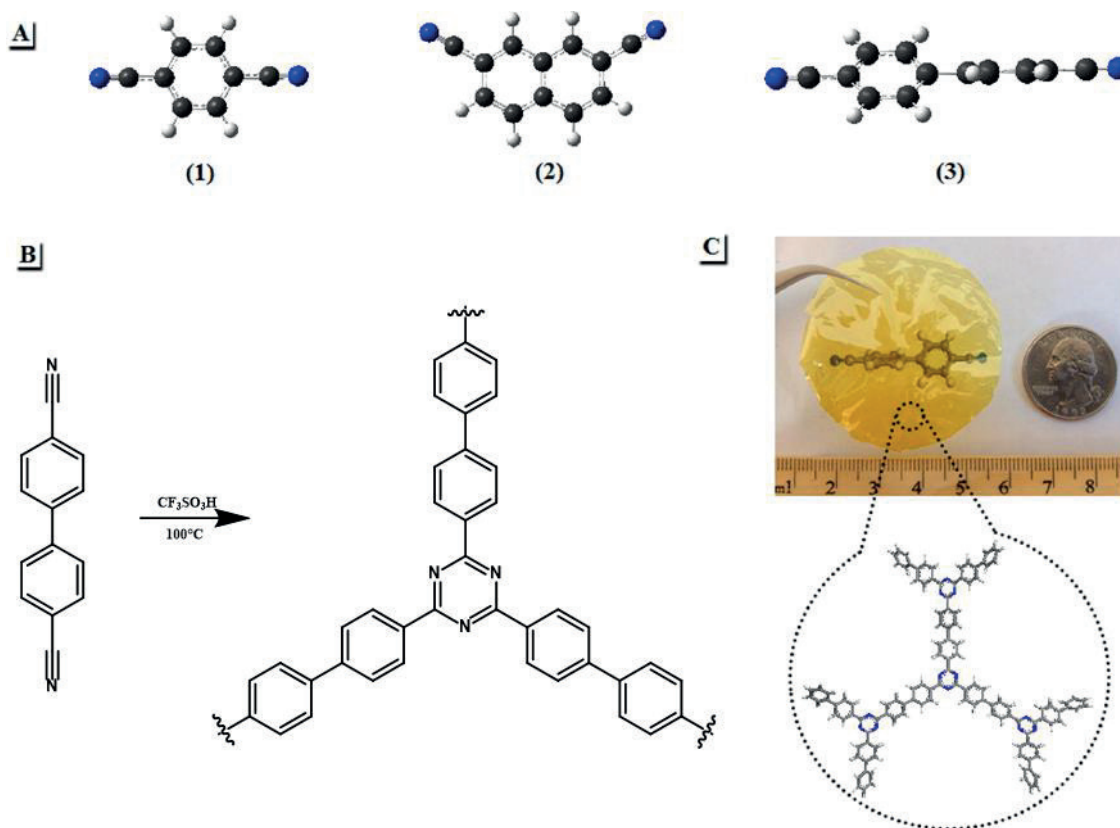


Figure 1. 12. (a) Density Functional Theory (DFT) optimized structures for the monomers used to synthesize the CTFs, (b) Trimerization of biphenyl dicarbonitrile monomer using the Brønsted acid assisted method at 100°C, and (c) Photograph of a directly synthesized sample of the transparent and flexible triazine-framework-based membrane TFM-1.⁵³ Reproduced with permission from American Chemical Society.

In terms of crystallinity, the Brønsted acid method was not able to produce highly crystalline CTFs. Only a few semi-crystalline CTFs were produced by Cooper et al. under microwave assisted conditions. These CTFs are porous but lack long-range order required to make crystalline frameworks. However, Xu et al. used the interfacial polymerization technique to synthesize single-layer/few-layer triazine-based two-dimensional polymer (2DP) analogous to CTF-1 with an AB stacking structure.⁵⁴ Dichloromethane and triflic acid were used to obtain the 2DP with a typical lateral size of several micrometers, which allows its processing into mechanically strong layered free-standing films with a high

specific surface area. Dichloromethane and triflic acid are immiscible and hence provide a perfect platform for the formation of an interfacial layer, where dichloromethane contains the dissolved monomer and at the interface the trimerization is catalyzed by triflic acid. Xu et al. further expanded the work to produce the same CTF-1 in millimeter-sized crystalline lamellar structure, from which micrometer-sized few-layer 2DP sheets could be exfoliated via a micromechanical cleavage or liquid sonication.⁵⁵ The site-specific adsorption of triflic acid during the synthesis was described to be responsible for the AB stacking configuration. Though the produced materials are crystalline, the upscaling of this procedure remains a limitation.

1.6.3. Phosphorus pentoxide (P_2O_5) catalyzed synthesis

G. H. Miller in 1973 also reported the use of phosphorus pentoxide, phosphorus trichloride, phosphorus pentachloride, arsenic trichloride, arsenic pentachloride, hydrochloric acid, hydrofluoric acid, fluorosulfonic acid and chlorosulfonic acid as catalysts for the preparation of curable polymeric compositions of aromatic polynitriles at 410–550 °C.²³ In addition, P_2O_5 can also convert amides $[(C=O)-NH_2]$ into nitriles. Baek et al. used this strategy in which P_2O_5 was used as a sequential catalyst to first convert aromatic amides into nitriles followed by the conversion of nitriles into triazines by applying heat.⁵⁶ A highly crystalline pCTF-1 was produced with a surface area up to 2034.1 m² g⁻¹ and a total pore volume of 1.04 cm³ g⁻¹. This method can also be used to directly convert polynitriles into their corresponding CTFs, thus expanding the monomer scope for producing CTFs. This also overcomes the disadvantage of $ZnCl_2$ residue removal from the typical ionothermal synthesis route.

1.6.4. Amidine synthesis

Recently, Tan et al. (2017) developed a milder synthetic procedure for the development of CTFs using a condensation reaction between an aldehyde and an amidine dihydrochloride involving a Schiff base formation followed by a Michael addition.⁵⁷ 1,4-Benzene-dialdehyde, 4,4'-biphenyl-dialdehyde, tris(4-formyl-phenyl)-amine, and tris(4-formylbiphenyl)-amine were reacted with terephthalamidine dihydrochloride at 120 °C to produce CTF-HUST-1, CTF-HUST-2, CTF-HUST-3 and CTF-HUST-4, respectively. In contrast to the CTFs produced using the Brønsted acid method, these CTFs always had layered structures. However, the CTFs showed no long-range ordering and were amorphous in nature.

Later on, an in-situ oxidation strategy was developed by the same group to synthesize crystalline CTFs (figure 1.13).⁵⁸ Here the overall reaction was slowed down by performing two reactions in one-pot – (i) production of an aldehyde by oxidation of alcohol and (ii) condensation reaction between the produced aldehyde with an amidine dihydrochloride to form triazine. In essence, the slow production of aldehyde allows the formation of a crystalline CTF by reducing the entire reaction speed and controlling the nucleation rate. The CTFs produced through this method had very good long-range order and displayed high crystallinity. Additionally, this method expands the monomer scope for the CTF synthesis as a wide range of alcohols, which are easily available, can be used for this reaction. Moreover, this method provides a platform for the large-scale production of CTFs. In another approach, Jin and Tan et al. (2019) tuned the feeding rate of the aldehyde monomers to control the nucleation and crystal growth which in turn resulted in an enhanced crystallinity.⁵⁹ In these methods, a drawback regarding green chemistry is the usage of dimethylsulfoxide (DMSO) as an oxidant, which is not a benign solvent. Further work on this field is required which could lead to the development of CTFs using a safer alternative following the principles of green chemistry.

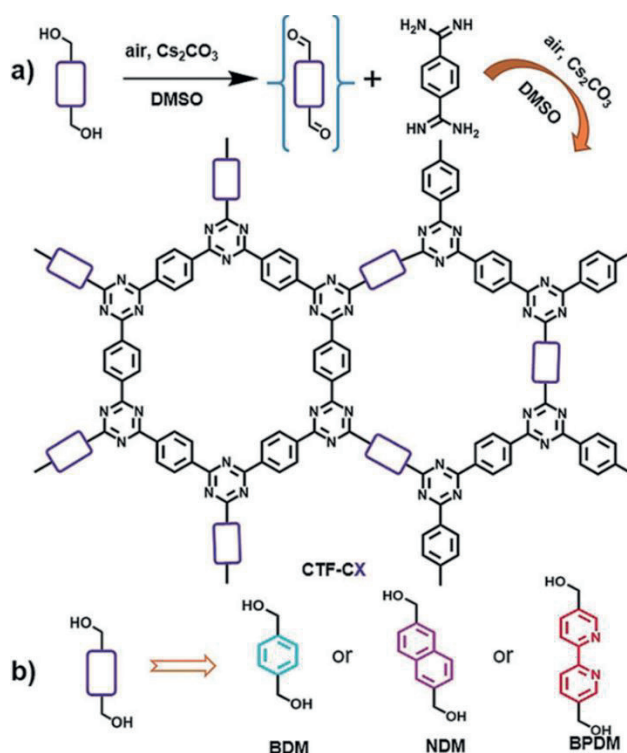


Figure 1. 13. (a) Slow oxidation of alcohol to produce aldehyde to control the nucleation rate for the formation of a covalent triazine framework, and (b) Different monomers used to show the wide applicability of this method.⁵⁸ Reproduced with permission from John Wiley and Sons.

1.6.5. Other synthesis methods

Though several triazine based polymers^{41, 60} and triazine containing COFs¹⁴ have been reported, in this thesis we are considering a COF formed particularly by the formation of a triazine unit creating the covalent bond. An alternative synthesis route for this instead of the standard trimerization was developed by the group of Coskun, where a sulfur-mediated route is used without any additional catalysts or solvents (figure 1.9).⁶¹ S-CTF-1 was formed through an in-situ vulcanization with elemental sulfur. A high sulfur content (62 wt%) was obtained in the reported S-CTF-1 which is analogous to the CTF-1 structure. Due to this chemical impregnation of sulfur, S-CTF-1 was shown to be an excellent cathode material for Li-S batteries. However, this method also utilizes high synthesis temperatures (400 °C) and hence cannot avoid partial carbonization. In addition, the applicability of these materials in a wide range of applications is limited due to the presence of large amounts of sulfur in the micropores.

Recently vinylene (–CH=CH–) linked triazine containing covalent organic frameworks were synthesized by reversible aldol condensation reaction.⁶² Trimethyltriazine is used as an electron deficient core where the methyl protons are acidic and react with aldehyde to create the covalent linkage. The extended network formation has been achieved through both base-catalyzed as well as acid-catalyzed route. These are synthesized in relatively milder conditions and yield highly stable as well as crystalline materials which can be characterized easily. Moreover, these materials can be tuned as required based on the largely available functional aldehyde linkers. These materials are at their emergence and are yet to be explored in detail for sustainable applications. These have the potential to overcome the synthesis and characterization limitations of existing CTFs.

Some of the CTFs reported in literature are crystalline whereas most of them are amorphous but consist of the triazine unit formed by nitrile trimerization. Since COFs are described as porous organic materials which are crystalline, CTFs cannot be placed directly under COFs, but should have their own category. Some CTFs which are crystalline can be recognized as COFs, but the amorphous counterparts should be considered under porous organic polymers or porous aromatic frameworks. Nonetheless, the CTFs are also studied intensively due to several advantages that it provides over other crystalline but less stable COFs.

1.7. Objectives: Synthetic Opportunities

It is clear from above discussion that imine COFs and CTFs can ideally replace state-of-the-art porous materials in future due to the advantages they provide. Since the inception of COFs, several imine COFs and CTFs have already been reported based on novel linkers and have been utilized in different applications. However, their potential has not yet been realized fully and there lie umpteen number of opportunities just based on the design criteria. Modification of functional groups in the linkers can modify the chemical properties of the end-product. For example, having more fluorine groups in the linkers can enhance the hydrophobicity of the COFs, which can be used for oil/water separation. Also, the length of the linkers can be modified to tune the pore volume and surface area of the materials which is essential in industrial gas separations. Often the topological structure of the materials is also important for applications such as optoelectronics and energy storage.

One of the main objectives targeted in this thesis is to design novel COFs and CTFs for applications in energy storage and catalysis. These applications are discussed in detail in the following chapter. From a design perspective there are a lot of opportunities yet to be explored in COFs and CTFs. Altering molecular functionalities through the variation of the building blocks can lead to interesting properties. Moreover, new topologies can be developed in COFs by following reticular chemistry principles.

1.8. References

- (1) J. E. McGregor, A. M. Donald, *Journal of Microscopy* 2010, 239, 135-141.
- (2) L. Tan, B. Tan, *Chem. Soc. Rev.* 2017, 46, 3322–3356.
- (3) P. C. Searson, J. M. Macaulay, S. M. J. Prokes, *Electrochem. Soc.* 1992, 139, 3373–3377.
- (4) J. Rouquerol, D. Avnir, C. W. Fairbridge, D. H. Everett, J. H. Haynes, N. Pernicone, J. D. F. Ramsay, K. S. W. Sing, K. K. Unger, *Pure Appl. Chem.* 1994, 66, 1739–1758.
- (5) S. Das, P. Heasman, T. Ben, S. Qiu, *Chem. Rev.* 2017, 117, 1515–1563.
- (6) L. Tan, B. Tan, *Chem. Soc. Rev.* 2017, 46, 3322–3356.
- (7) N. B. Mc Keown, P. M. Budd, *Chem. Soc. Rev.* 2006, 35, 675–683.

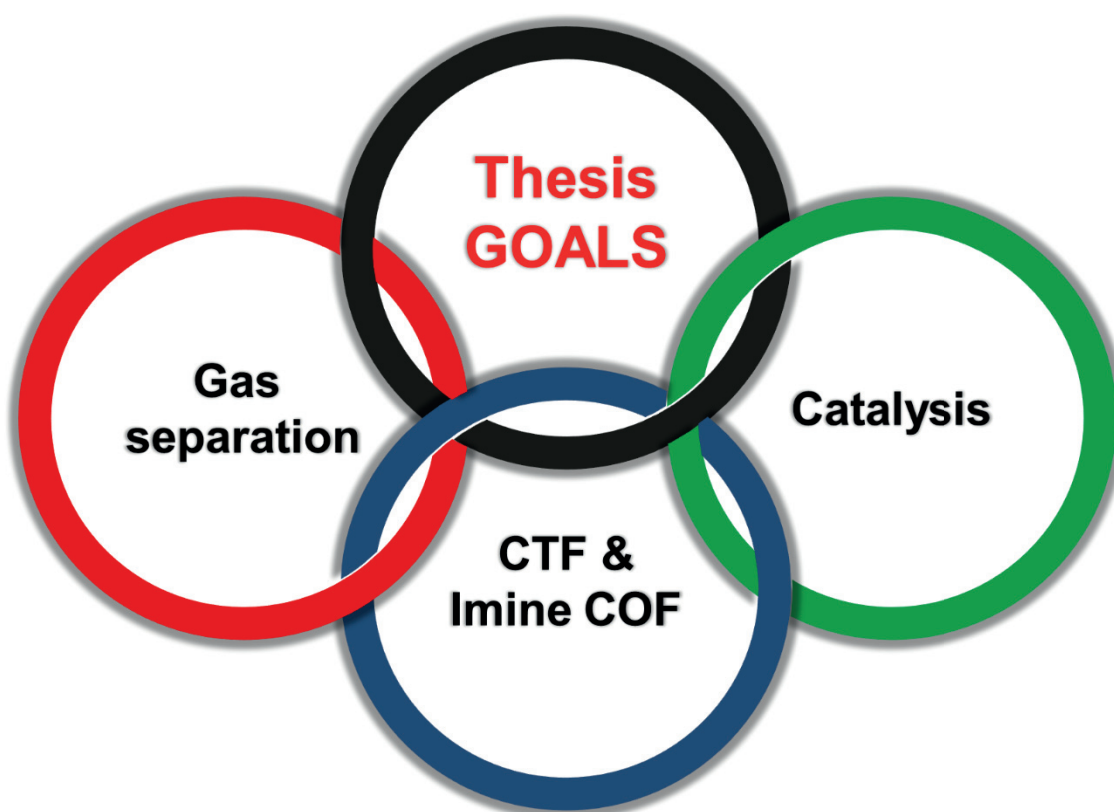
- (8) Y. Xu, S. Jin, H. Xu, A. Nagai, D. Jiang, *Chem. Soc. Rev.* 2013, 42, 8012–8031.
- (9) T. Ben, S. Qiu, *CrystEngComm* 2013, 15, 17–26.
- (10) N. Huang, P. Wang, D. Jiang, *Nat. Rev. Mater.* 2016, 1.
- (11) M. Liu, L. Guo, S. Jin, B. Tan, *J. Mater. Chem. A* 2019, 7, 5153–5172.
- (12) N. W. Ockwig, A. P. Cote, M. O. Keffe, A. J. Matzger, O. M. Yaghi, *Science* 2005, 310, 1166–1171.
- (13) C. S. Diercks, O. M. Yaghi, *Science* 2017, 355.
- (14) K. Geng, T. He, R. Liu, S. Dalapati, K. T. Tan, Z. Li, S. Tao, Y. Gong, Q. Jiang, D. Jiang, *Chem. Rev.* 2020, 120, 8814–8933.
- (15) C. Krishnaraj, H. S. Jena, K. Leus, P. Van Der Voort, *Green Chem.* 2020, 22, 1038–1071.
- (16) X. Guan, F. Chen, Q. Fang, S. Qiu, *Chem. Soc. Rev.* 2020, 49, 1357–1384.
- (17) T. Ma, E. A. Kapustin, S. X. Yin, L. Liang, Z. Zhou, J. Niu, L. Li, Y. Wang, J. Su, J. Li, X. Wang, W. D. Wang, W. Wang, J. Sun, O. M. Yaghi, *Science*. 2018, 361, 48–52.
- (18) F. J. Uribe-Romo, J. R. Hunt, H. Furukawa, C. Klöck, M. O’Keeffe, O. M. Yaghi, *J. Am. Chem. Soc.* 2009, 131, 4570–4571.
- (19) P. Kuhn, M. Antonietti, A. Thomas, *Angew. Chemie - Int. Ed.* 2008, 47, 3450–3453.
- (20) S. Y. Ding, J. Gao, Q. Wang, Y. Zhang, W. G. Song, C. Y. Su, W. Wang, *J. Am. Chem. Soc.* 2011, 133, 19816–19822.
- (21) W. G. Toland, Polymerization of aromatic nitriles, USA Patent 3060179, 1962.
- (22) H. A. Vogel, US Patent 3654192, 1972.
- (23) G. Miller, US Patent 3775380, 1973.
- (24) M. Liu, L. Guo, S. Jin and B. Tan, *J. Mater. Chem. A* 2019, 7, 5153–5172.
- (25) P. Kuhn, A. Forget, D. Su, A. Thomas and M. Antonietti, *J. Am. Chem. Soc.* 2008, 130, 13333–13337.
- (26) H. Li, H. Li, Q. Dai, H. Li and J.-L. Bredas, *Adv. Theory Simul* 2018, 1, 1700015.

- (27) S. Kandambeth, A. Mallick, B. Lukose, M. V. Mane, T. Heine and R. Banerjee, *J. Am. Chem. Soc.* 2012, 134, 19524–19527.
- (28) F. Haase, K. Gottschling, L. Stegbauer, L. S. Germann, R. Gutzler, V. Duppel, V. S. Vyas, K. Kern, R. E. Dinnebier and B. V. Lotsch, *Mater. Chem. Front.* 2017, 1, 1354–1361.
- (29) A. Halder, M. Ghosh, M. A. Khayum, S. Bera, M. Addicoat, H. S. Sasmal, S. Karak, S. Kurungot and R. Banerjee, *J. Am. Chem. Soc.* 2018, 140, 10941–10945.
- (30) F. Haase, E. Troschke, G. Savasci, T. Banerjee, V. Duppel, S. Dörfler, M. M. J. Grundei, A. M. Burow, C. Ochsenfeld, S. Kaskel and B. V. Lotsch, *Nat. Commun.* 2018, 9, 2600.
- (31) Y. Zhang and S. Jin, *Polymers* 2019, 11, 31.
- (32) E. R. Cooper, C. D. Andrews, P. S. Wheatley, P. B. Webb, P. Wormald and R. E. Morris, *Nature* 2004, 430, 1012–1016.
- (33) P. Katekomol, J. Roeser, M. Bojdys, J. Weber and A. Thomas, *Chem. Mater.* 2013, 25, 1542–1548.
- (34) M. J. Bojdys, J. Jeromenok, A. Thomas and M. Antonietti, *Adv. Mater.* 2010, 22, 2202–2205.
- (35) D. Y. Osadchii, A. I. Olivos-Suarez, A. V. Bavykina and J. Gascon, *Langmuir* 2017, 33, 14278–14285.
- (36) S. Kuecken, J. Schmidt, L. Zhi and A. Thomas, *J. Mater. Chem. A* 2015, 3, 24422–24427.
- (37) A. V. Bavykina, A. I. Olivos-Suarez, D. Osadchii, R. Valecha, R. Franz, M. Makkee, F. Kapteijn and J. Gascon, *ACS Appl. Mater. Interfaces* 2017, 9, 26060–26065.
- (38) S. Hug, L. Stegbauer, H. Oh, M. Hirscher and B. V. Lotsch, *Chem. Mater.* 2015, 27, 8001–8010.
- (39) S. Mukherjee, M. Das, A. Manna, R. Krishna and S. Das, *J. Mater. Chem. A* 2019, 7, 1055–1068.
- (40) K. Wang, Y. Tang, Q. Jiang, Y. Lan, H. Huang, D. Liu and C. Zhong, *J. Energy Chem.* 2017, 26, 902–908.

- (41) T. Geng, W. Zhang, Z. Zhu, G. Chen, L. Ma, S. Ye and Q. Niu, *Polym. Chem.* 2018, 9, 777–784.
- (42) Y. Zhao, K. X. Yao, B. Teng, T. Zhang and Y. Han, *Energy Environ. Sci.* 2013, 6, 3684–3692.
- (43) S. H. Je, H. J. Kim, J. Kim, J. W. Choi and A. Coskun, *Adv. Funct. Mater.* 2017, 27, 1703947.
- (44) G. Wang, K. Leus, H. S. Jena, C. Krishnaraj, S. Zhao, H. Depauw, N. Tahir, Y.-Y. Liu and P. Van Der Voort, *J. Mater. Chem. A* 2018, 6, 6370–6375.
- (45) K. Yuan, C. Liu, L. Zong, G. Yu, S. Cheng, J. Wang, Z. Wang and X. Jian, *ACS Appl. Mater. Interfaces* 2017, 9, 13201–13212.
- (46) X. Zhu, C. Tian, G. M. Veith, C. W. Abney, J. Dehaudt and S. Dai, *J. Am. Chem. Soc.* 2016, 138, 11497–11500.
- (47) T. T. Liu, R. Xu, J. D. Yi, J. Liang, X. S. Wang, P. C. Shi, Y. B. Huang and R. Cao, *ChemCatChem* 2018, 10, 2036–2040.
- (48) K. Park, K. Lee, H. Kim, V. Ganesan, K. Cho, S. K. Jeong and S. Yoon, *J. Mater. Chem. A* 2017, 5, 8576–8582.
- (49) O. Buyukcakil, S. H. Je, S. N. Talapaneni, D. Kim and A. Coskun, *ACS Appl. Mater. Interfaces* 2017, 9, 7209–7216.
- (50) Y. Li, S. Zheng, X. Liu, P. Li, L. Sun, R. Yang, S. Wang, Z.-S. Wu, X. Bao and W.-Q. Deng, *Angew. Chem., Int. Ed.* 2018, 57, 7992–7996.
- (51) A. H. Cook and D. G. Jones, *J. Chem. Soc.* 1941, 184–187.
- (52) D. R. Anderson and J. M. Holovka, *J. Polym. Sci., Part A-1: Polym. Chem.* 1966, 4, 1689–1702.
- (53) X. Zhu, C. Tian, S. M. Mahurin, S.-H. Chai, C. Wang, S. Brown, G. M. Veith, H. Luo, H. Liu and S. Dai, *J. Am. Chem. Soc.* 2012, 134, 10478–10484.
- (54) J. Liu, W. Zan, K. Li, Y. Yang, F. Bu and Y. Xu, *J. Am. Chem. Soc.* 2017, 139, 11666–11669.
- (55) J. Liu, P. Lyu, Y. Zhang, P. Nachtigall and Y. Xu, *Adv. Mater.* 2018, 30, 1705401.
- (56) S. Y. Yu, J. Mahmood, H. J. Noh, J. M. Seo, S. M. Jung, S. H. Shin, Y. K. Im, I. Y. Jeon and J. B. Baek, *Angew. Chem., Int. Ed.* 2018, 57, 8438–8442.

- (57) K. Wang, L. M. Yang, X. Wang, L. Guo, G. Cheng, C. Zhang, S. Jin, B. Tan and A. Cooper, *Angew. Chem., Int. Ed.* 2017, 56, 14149–14153.
- (58) M. Liu, Q. Huang, S. Wang, Z. Li, B. Li, S. Jin and B. Tan, *Angew. Chem. Int. Ed.* 2018, 57, 11968–11972.
- (59) M. Liu, K. Jiang, X. Ding, S. Wang, C. Zhang, J. Liu, Z. Zhan, G. Cheng, B. Li, H. Chen, S. Jin and B. Tan, *Adv. Mater.* 2019, 31, 1807865.
- (60) J. Sun, C. Tessier and R. Holm, *Inorg. Chem.* 2007, 46, 2691–2699.
- (61) S. N. Talapaneni, T. H. Hwang, S. H. Je, O. Buyukcakir, J. W. Choi and A. Coskun, *Angew. Chem.* 2016, 128, 3158–3163.
- (62) A. Acharjya, P. Pachfule, J. Roeser, F.-J. Schmitt, A. Thomas, *Angew. Chem.* 2019, 58, 14865-14870.

2 ENERGY AND ENVIRONMENTAL APPLICATIONS OF COFs AND CTFs



This chapter is based on the published review articles:

C Krishnaraj, HS Jena, K Leus, P Van Der Voort. Covalent triazine frameworks – a sustainable perspective. **Green Chemistry** 22 (4), **2020**, 1038-1071.

N Tahir,¹ **C Krishnaraj**,¹ K Leus, P Van Der Voort. Development of covalent triazine frameworks as heterogeneous catalytic supports. **Polymers** 11 (8), **2019**, 1326.

2.1. Introduction

In the previous chapter, an introduction towards the design of COFs and CTFs was provided. In this chapter, more detailed attention is given towards the established applications of imine COFs and CTFs. These materials have been used for gas adsorption and storage, gas separation, catalysis, proton conduction, energy storage, photocatalysis, photoluminescence, photovoltaics, enantioseparation, drug delivery, iodine adsorption and pollutant removal.¹ In the scope of this dissertation, the focus will be on gas capture and separation, metal based and metal-free heterogeneous catalysis using imine COFs and CTFs.

2.2. Gas storage and separation

COFs and CTFs exhibit high surface areas and permanent porosities and based on the synthesis method these properties can also be tuned as desired. It has been previously shown that ultramicropores are essential for selective gas storage applications.²⁻⁴ In addition, various functionalities can be incorporated into the structure based on the selected building unit for its synthesis. Hence these tunable properties in COFs and CTFs enable their utilization as microporous gas adsorbents which can also be selective to desired gases based on the introduced functionalities. In the following sections, the development of imine COFs and CTFs in terms of gas storage and separation is discussed.

2.2.1. Carbon capture

Recently, the global warming crisis has been gaining a lot of attention due to the threat it poses to the world. Economic and social development are essential for everyone; however, these developments have come with a high price. Human activities have led to an increase in the global warming. Greenhouse effect, emission from industries, and transport related emissions have all led to an increased carbon footprint. The U.S. National Oceanic and Atmospheric Administration (NOAA) has shown that the global carbon dioxide (CO₂) concentration in the atmosphere has increased from 315 ppm to 414.38 ppm in July 2020.⁵ CO₂ is regarded as the main anthropogenic greenhouse gas and is widely accepted as the primary contributor to global warming.⁶ The burning of fossil fuels (e.g. coal, petroleum and natural gas) accounts for approximately 86% of the greenhouse gas emissions.⁷ Recently, there is an increased awareness in the world about this issue and several countries and institutions are making attempts to restrict these emissions.⁸ As a solution, the transition towards alternative clean energy sources such as

solar or hydrogen fuels are being promoted.⁹ However, these are long-term goals and their realization requires more research and in addition more investments for practical implementation.

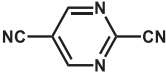

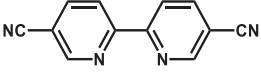
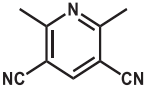

An alternative remediation of the existing problems would be to restrict and reduce the atmospheric CO₂ concentration. Researchers propose carbon capture and storage (CCS) and carbon capture and utilization (CCU) as a promising solution.^{10, 11} An essential part of this solution is to capture and separate CO₂. Approximately 70% of the costs of CCS and CCU is associated with the post-combustion flue gas CO₂ separation. Flue gas consists of 15-16% CO₂, 73-77% N₂ and other minor components such as H₂O, CO, SO_x and NO_x.¹² The usage of porous materials to capture CO₂ in an efficient, eco-friendly and low-cost manner is important. Currently, amine scrubbing is used to capture CO₂ gas from flue gas mixture. However, this consumes higher energy for regeneration. The use of physical adsorbents can provide a cheaper way to selectively capture CO₂ in an effective manner.¹³

Typically, several types of inorganic sorbent materials are used for selective CO₂ capture. Metal-organic materials with coordinately saturated metal centers and periodically arrayed hexafluorosilicate (SiF₆²⁻) anions were synthesized with different types of metal ions and tested for CO₂ capture and separation.¹⁴ The highest CO₂ uptake was obtained as 5.4 mmol/g at 1 bar and 298K for SiFSIX-2-Cu-i. Moreover, a selectivity of 140 was obtained for CO₂/N₂ (90/10) mixture. Zeolitic imidazolate frameworks (ZIFs) are a subset of MOFs which have been studied for selective CO₂ capture. For example, Nanosized ZIF-8 and ZIF-8-derived nitrogen functionalized microporous carbon materials after acid treatment showed upto 3.5 mmol/g CO₂ uptake at 1 bar and 298K.¹⁵ A CO₂/N₂ selectivity of 79 was observed for the best material in this series. The commercially available zeolite sorbent (Zeolite 13X) shows upto 5 mmol/g CO₂ uptake at 1 bar and 298K and a selectivity of 500 over CO₂/N₂ (90/10) mixture.¹⁶

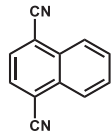
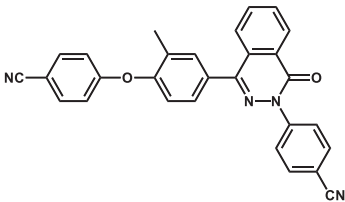
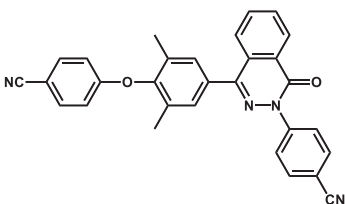
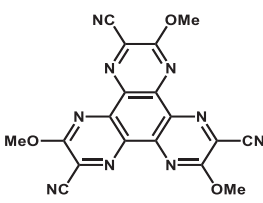
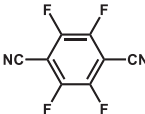
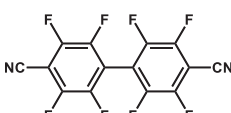
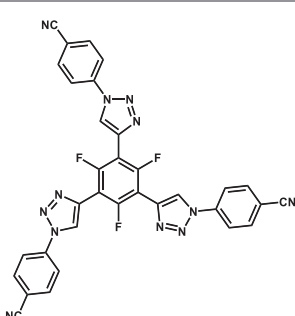
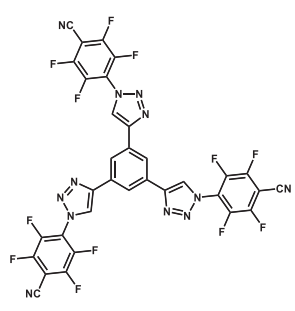
CTFs have proven to be promising platforms for CO₂ capture, storage and utilization due to their tunable pore sizes, surface areas and functionalities based on the choice of the monomer. Lotsch et al. reported on a series of nitrogen rich CTFs as high-performance materials for selective carbon capture and storage.¹⁷ Based on a comparison between several CTFs, they found that the micropore volume plays a vital role in the maximum CO₂ uptake and the presence of nitrogen has a secondary effect to enhance the CO₂ adsorption performance. The selectivity of CO₂ over N₂ was largely attributed to the

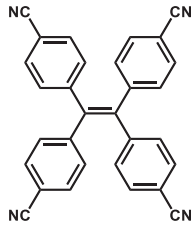
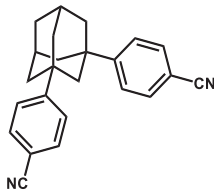
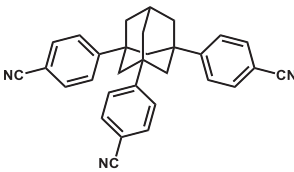
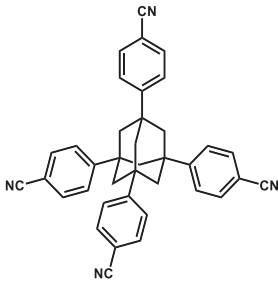
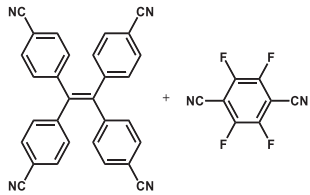
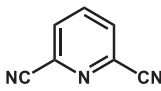
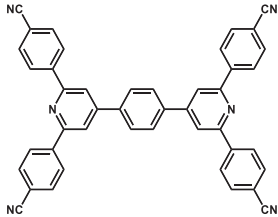
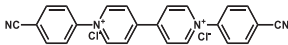
nitrogen content. Considering the importance of the micropore volume, Zhong et al. targeted CTFs with ultramicropores in addition to a high nitrogen content.¹⁸ Particularly, a short monomer, fumaronitrile (FUM) was used to construct CTF-FUM-350 which had 0.52 nm ultramicropores and exhibited a high CO₂/N₂ (102.4) and CO₂/CH₄ (20.5) selectivity at room temperature (298 K). However, the overall uptake was only around 2.57 mmol/g at 298 K. In terms of chemical functionalities, the incorporation of preferential CO₂-philic groups such as nitrogen, oxygen, fluorine etc., induce strong electrostatic interactions between the porous material surface and the CO₂ molecules. In this regard, Jian et al. reported on a series of N-heterocyclic phthalazinone linkers to synthesize ether-linked phthalazinone-based CTFs (PHCTFs).¹⁹ These PHCTFs had electron-rich N/O atoms and particularly PHCTF-5 exhibited a high CO₂/N₂ selectivity of 138. Dai et al. reported on an *in situ* doping strategy for the synthesis of hexaazatriphenylene-based conjugated triazine frameworks. HAT-CTF-450/600 material showed an exceptionally high CO₂ uptake of 6.3 mmol/g at 273 K and 1 bar²⁰ due to the synergistic effects of ultrananoporosity and rich N/O co-doped sites. Another important feature to note is that this material can adsorb 3 mmol/g at 0.15 bar and 273 K. This pressure is more relevant for the practical carbon adsorption from flue gas which contains ~15% CO₂ at a total pressure of 1 bar.

Table 2. 1. List of reported CTFs for CO₂ adsorption.

Material	Structure	BET area	CO ₂ uptake (mmol/g)		CO ₂ /N ₂ selectivity	Ref
			273 K	298 K		
pym-CTF600		689	3.34	2.15	126	17
CTF1-600		2557	4.36	2.21	26	17
bipy-CTF600		2479	5.58	2.95	37	17
lut-CTF500		1680	5.04	2.58	27	17
CTF-FUM-350		230	3.5	2.5	102.4	18

Triazine and Imine Linked Porous Organic Frameworks as Platforms for Gas Storage, Separation and Heterogeneous Catalysis

CTF-DCN-500		735	2.7	1.7	37	18
PHCTF-4		1270	2.3	1.5	35	19
PHCTF-5		1015	2.2	1.3	138	19
HAT-CTF-450/600		1090	6.3	4.8 (297 K)	160	20
FCTF-1-600		1535	5.53	3.41	19	23
F-DCBP-CTF-1		1574	5.98	3.82	31	24
df-TzCTF600		1720	6.79	4.60	21	25
Tz-df-CTF600		1754	7.65	5.08	21.1	26

PCTF-1		2235	3.28	2.02	14	27
PCTF-3		641	2.19	1.45	25	27
PCTF-4		1090	2.32	1.63	26	27
PCTF-5		1183	2.61	1.62	32	27
MM-2		1360	4.80	3.16	23	28
CTF-py ^{HT}		3040	5.97	4.22	29	29
CTF-20-400		1458	3.48	2.09	19	30
cCTF-500		1247	3.02	1.81	-	31

*For the annotation of the material, the annotation used in the literature was applied.

Inclusion of fluorine in a porous material has proven to promote CO₂ adsorption since fluorine is highly electronegative and enhances the electrostatic interaction. In addition, C-F bonds increase the hydrophobicity of the material which enables easier usage under humid conditions.²¹ Also, since F groups are larger in size compared to H, its presence can effectively reduce the micropore size of the porous material thus facilitating a better kinetic selectivity.²² Han et al. reported the first perfluorinated CTF (FCTF-1) synthesized using tetrafluoroterephthalonitrile as a building block for selective CO₂ capture.²³ The FCTF-1-600 material showed a high CO₂ uptake of 5.53 mmol/g at 273 K and 1 bar and a CO₂/N₂ selectivity of 152 under kinetic flow conditions. In addition to this, Van Der Voort et al. reported on F-DCBP-CTF material synthesized using 2,2',3,3',5,5',6,6'-octafluoro-4,4'-biphenyldicarbonitrile as a monomer.²⁴ Though defluorination occurred during the synthesis of the CTFs, the F-DCBP-CTF-1 still showed a remarkable CO₂ uptake of 5.98 mmol/g at 273 K and 1 bar. The synergistic effects of the polar C-F bonds and rich CO₂-philic N sites assisted in the adsorption process. In addition, it was shown that the overall hydrophobicity of the material increased in comparison to the DCBP-CTF material (analogous material to F-DCBP-CTF; DCBP linker consists of H instead of F). Very recently, Das et al. reported on 1,2,3-triazole functionalized CTFs which showed 6.79 mmol/g CO₂ uptake at 273 K and 1 bar.²⁵ The presence of ultra-micropores (0.45-0.9 Å) and various CO₂-philic sites such as triazolic, triazine and pyrrolic N-species were responsible for this high CO₂ uptake capacity. The same group also reported on a triazole-substituted perfluorinated aromatic nitrile based CTF (Tz-PFCN) which showed the highest CO₂ uptake (7.65 mmol/g at 273 K and 1 bar) so far.²⁶ They used a dual approach to incorporate both the thermally sacrificial fluorine functionality to create microporosity and multi-N-containing triazole functionality for increasing the CO₂ affinity. They also tested the material for their breakthrough performance which demonstrated the potential applicability of these materials for real-time applications (Figure 2.1).

Janiak et al. showed that the CTFs prepared using an ionothermal method resulted in a higher surface area, porosity and micropore volume than the CTFs prepared using triflic acid.²⁷ In addition, the CO₂ uptake was also affected by the synthesis temperature and ZnCl₂ equivalents. They also used a mixed linkers approach for the preparation of CTFs. It was noted that a higher CO₂ accessible micropore volume and a higher micropore volume fraction ($V_{0.1}/V_{tot} = 82\%$) improved the CO₂ uptake to 4.8 mmol/g at 273 K and 1 bar.²⁸ Giambastiani et al. reported on N-doped CTFs (CTF-py) which showed a CO₂ uptake of 2.03 mmol/g and 5.08 mmol/g at 0.1 bar and 1 bar (273 K) respectively.²⁹ In

addition, CTF-py^{HT} (CTF-pyridine High Temperature) synthesized at high temperature (two treatments at 400°C and 750°C) showed a CO₂ uptake of 5.97 mmol/g at 1 bar (273 K). Van Der Voort et al. synthesized CTFs using N-heteroaromatic building blocks in the presence of 20 molar equivalents of ZnCl₂ as catalyst.³⁰ The resulting CTFs showed a CO₂ adsorption capacity of 3.48 mmol/g at 273 K and 1 bar with a high CO₂/N₂ selectivity of 36 at 298 K.

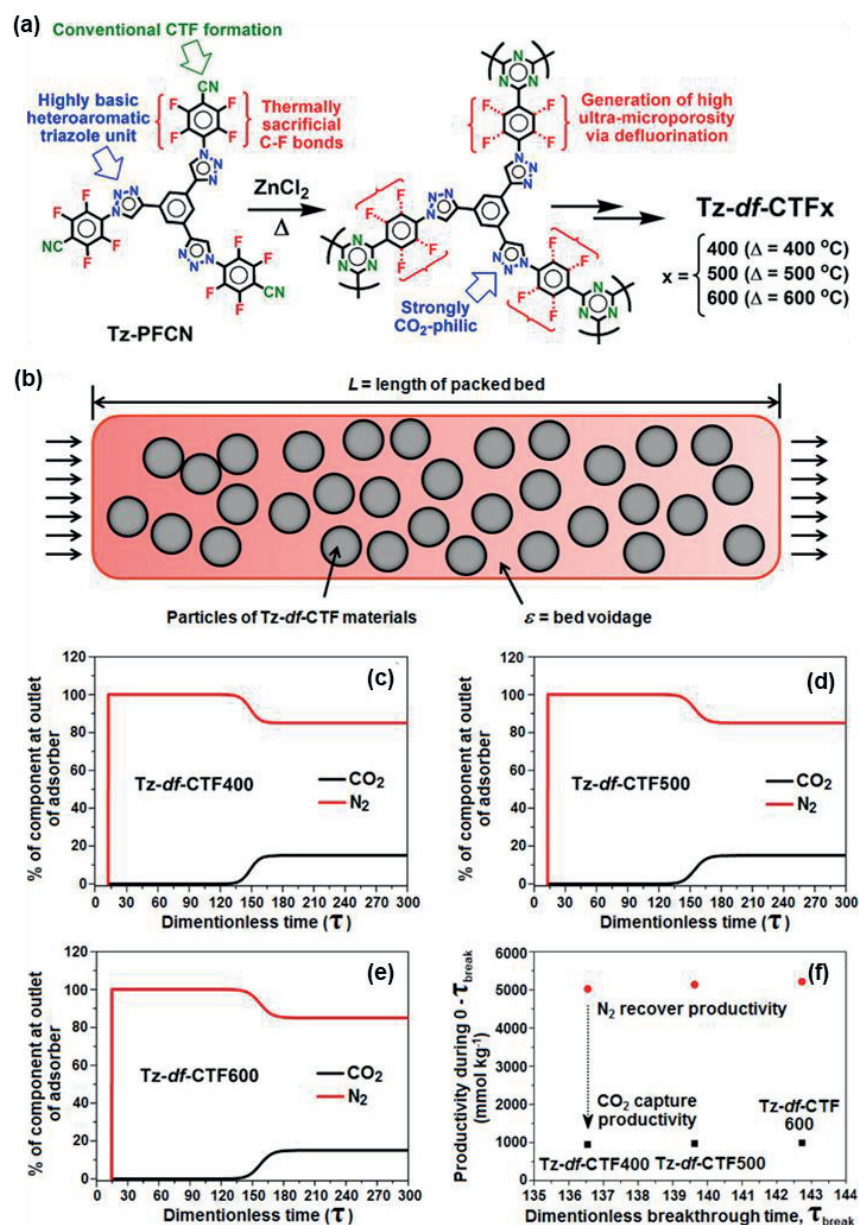


Figure 2. 1. (a) Schematic illustration of the formation of Tz-df-CTFs via a dual strategic approach, (b) Scheme of a packed bed adsorber for Tz-df-CTFs. (c–e) Breakthrough characteristic in the separation of a 15% CO₂ + 85% N₂ binary mixture at 298 K, and (f) Comparison of the CO₂ capture and N₂ recovery productivity at 298 K.²⁶ Reproduced with permission from American Chemical Society.

Besides using heteroatom doping strategy, the use of charged building blocks in the porous materials can also improve the CO₂ uptake. This was demonstrated by Coskun et al. who reported on the first charged covalent triazine framework (cCTF) prepared from dicationic viologen derivatives.³¹ The inclusion of ionic functionalities in the materials improved their CO₂ affinity to 3 mmol/g at 273 K and 1 bar. Around the same time, Yoon et al. reported on 1,3-bis(pyridyl) imidazolium based CTFs (bpim-CTFs). An uptake of 3.31 mmol/g CO₂ was obtained at 288 K and 1 bar with a CO₂/N₂ selectivity up to 32.³² Another strategy implemented by Coskun et al. is to activate the CTF using a base (KOH) treatment at 700°C.³³ This thermochemical activation allowed for a 2.2 fold increase of CO₂ uptake from 2.7 mmol/g to 6 mmol/g at 273 K and 1 bar.

CO₂ adsorption of imine-based COFs was investigated for the first time in 2012.³⁴ Banerjee et al. reported two 2D COFs (TpPa-1 and TpPa-2), which were constructed from 1,3,5-triformylphloroglucinol (Tp) with *p*-phenylenediamine (Pa-1) and 2,5-dimethyl-*p*-phenylenediamine (Pa-2), respectively.³⁴ Both the COFs showed strong chemical stability in acid (9N HCl) and boiling water due to irreversible proton tautomerism from the enol-imine (OH) to the keto-enamine form. The CO₂ uptake of TpPa-1 and TpPa-2 was measured to be 3.5 and 2.8 mmol/g at 273 K and 1 bar, respectively. This synthetic strategy was further extended by employing different diamine monomers such as benzidine (BD) to synthesize TpBD COFs.³⁵ The CO₂ uptake of TpBD from the solvothermal method was 1.9 mmol/g at 273 K and 1 bar. Other COFs with similar starting monomers having different functional groups were also reported.³⁶ The order of CO₂ capacity at 273 K and 1 bar was TpPa-1 (3.5 mmol/g) > TpPa-NO₂ (3.2 mmol/g) > TpPa-2 (2.8 mmol/g) > TpBD-(NO₂)₂ (2.3 mmol/g) > TpBD (1.8 mmol/g) > TpBDMe₂ (1.6 mmol/g) > TpPa-F₄ (1.5 mmol/g) > TpBD-(OMe)₂ (1.2 mmol/g). Altering the synthesis method of COFs can also affect the gas uptake capacities. For example, TpPa-1 synthesized using microwave-assisted solvothermal method showed higher surface area and better crystallinity than the conventional solvothermally synthesized TpPa-1 COF.³⁷ Moreover, the CO₂ uptake of TpPa-COF (MW) at 273 K and 1 bar was 4.9 mmol/g CO₂ with the Q_{st} of 34.1 kJ mol⁻¹ at zero coverage. This is higher than the conventional TpPa-1. The presence of abundant N-H sites on the pores of the TpPa (MW) COF can interact more favorably with polarizable CO₂ through hydrogen bonding interactions. This resulted in a CO₂/N₂ adsorption selectivity of 32 at 273 K, calculated from the Henry law.

Another strategy to improve the stability and crystallinity of COFs was through the introduction of –OH functionalities adjacent to the imine (–C=N–) centers in COFs and thereby creating intramolecular O–H···N=C hydrogen bonding interactions.³⁸ An example of this strategy was shown through DhaTph COF containing –OH groups. DhaTph COF showed higher crystallinity, stability and porosity compared to the DmaTph COF which had –OMe groups in place of –OH groups and lacked intramolecular hydrogen bonding interactions. The DhaTph COF showed a CO₂ uptake 2.9 mmol/g at 273 K and 1 bar, while DmaTph showed lower CO₂ uptake of 1.6 mmol/g. This was attributed to the higher crystallinity and order present in the DhaTph COF.

Nitrogen-rich COFs are good candidates for CO₂ capture due to the enhanced interaction affinity of nitrogen atoms to CO₂. To this end, two triangular starting monomers of 2,4,6-tris(4-aminophenyl)-1,3,5-triazine and 1,3,5-triformylbenzene were used to synthesize a nitrogen-rich COF (N-COF).³⁹ Due to the nitrogen rich environment on the pore walls the CO₂ uptake capacity of the N-COF was 2.7 mmol/g at 1 bar and 273 K, and 1.3 mmol/g at 1 bar and 298 K. Recently, imine and β -ketoenamine COFs were synthesized from C3-symmetric aldehyde (1,3,5-tris(4-aminophenyl)benzene (TAPB) and 1,3,5-tris(4'-amino-3',5'-isopropylphenyl) benzene (iPrTAPB)) and amine (tris(4'-formylphenyl)benzene (TFPB) and 1,3,5-triformyl-phloroglucinol (TFP)).⁴⁰ The CO₂ uptake capacities in the four COFs follow the order of TAPB-TFP (4.1 mmol/g) > iPrTAPB-TFP (2.4 mmol/g) > TAPB-TFPB (0.9 mmol/g) > iPrTAPB-TFPB (0.7 mmol/g) at 273 K and 1 bar pressure. Steric hindrance of the isopropyl groups and increased basicity of the amine groups in comparison to the imine groups were linked to these differences in the CO₂ uptake. El-Kaderi et al. reported a mesoporous imine linked COF (ILCOF-1) built using 1,3,6,8-tetrakis(4'-formylphenyl)-pyrene and *p*-phenylenediamine. ILCOF-1 showed very high surface area of 2723 m² g⁻¹ with an average pore size of 2.3 nm. ILCOF-1 adsorbed 1.4 mmol/g CO₂ at 273 K and 1 bar pressure. The Q_{st} value calculated using Clausius-Clapeyron equation at low coverage was 18.3 kJ mol⁻¹. The high-pressure CO₂ sorption measurement of ILCOF-1 showed 29.3 mmol/g uptake at 298 K and 40 bar pressure. The nitrogen-functionalization on the pore walls was correlated with to the N···CO₂ interactions for binding CO₂.

Integration of functional groups on the channel walls can create a good platform for increasing molecular interactions with CO₂. Jiang et al. utilized a ring opening reaction to convert a conventional 2D COF ([HO] x% –H₂P–COFs) with low CO₂ uptake into a high CO₂ adsorbing COF ([HO₂C] x% –H₂P–COFs).⁴¹ The [HO] x% –H₂P–COFs

displayed low CO₂ adsorption capacity between 1-1.4 mmol/g at 273 K and 1 bar, while the [HO₂C] x% -H₂P-COFs showed 2.8 and 2.2 fold increase in CO₂ uptake compared to their corresponding parent COFs (for example, up to 3.9 mmol/g at 273 K and 1 bar for [HO₂C] 100% -H₂P-COF was obtained). The selectivity for [HO₂C] 100% -H₂P-COF at 15/85 CO₂/N₂ flue gas mixture, 298 K and 0.001 bar was 323, which is 18 times more than the [HO] 100% -H₂P-COF and comparable to that of MgMOF-74. The [HO₂C] 100% -H₂P-COF exhibited a selectivity of 77 at 298 K and 1 bar pressure, while [HO] 100% -H₂P-COF showed only a selectivity of 8. In addition, while using flue gas mixture, [HO₂C] 100% -H₂P-COF showed 0.5 mmol/g CO₂ uptake at 1 bar, which was over 3 times more than the [HO] 100% -H₂P-COF.

Compared with the CTFs, the imine-based COFs have much better crystallinity and structural regularity, which are beneficial to precisely tune the order pore size. On the other hand, the chemical and thermal stability of CTFs is higher than the imine-COFs. This allows the trade-off over the crystallinity in CTFs. Eventually, the most important aspect is CO₂ uptake capacity/selectivity along with sufficient stability, which is easier to achieve through CTFs synthesized using ionothermal synthesis conditions.

2.2.2. Hydrocarbon separation

Hydrocarbons are produced from petroleum or natural gas processing.⁴² Petroleum is a mixture of several chemicals and varies in its composition between 50-97 wt% of hydrocarbons. Natural gas has the major component as methane and other minor components like ethane, propane, and butanes.⁴² In the production of chemical feedstocks and fuels, hydrocarbon mixtures (such as propene-propane) are separated into different component fractions on large scale. However, these separations demand high energy and additional costs associated with the setups. Mainly, petroleum is divided into fractions of butanes, gasoline, naphtha, kerosene etc., based on their differences in boiling points. Hence this type of separation of the petroleum components is energy intensive. An alternative to this would be the use of porous adsorbents which can selectively adsorb one or more of any desired hydrocarbons and sequentially allow other components to pass through. This would be less energy consuming than the conventional distillation-based setups. However, the challenging part is the design of selective porous adsorbents.

One of the most industrially important hydrocarbons is methane (CH₄).⁴³ Methane is attributed with the lowest carbon amount and least CO₂ emission per unit energy.

Methane is obtained as the major component in natural gas, but natural gas contains several minor impurities such as ethane, propane, butanes etc. Conventional cryogenic distillation method requires high pressure and low temperatures which is not very energy efficient. Liang et al. reported on a series of bisbenzimidazole-functionalized covalent triazine frameworks (CTF-BIBs) synthesized through the ionothermal synthesis route.¹⁴⁵ The CTF-BIBs exhibited selective separation of C₂H₆/CH₄ (20.4) and C₃H₈/CH₄ (386.6). The high C₃H₈/CH₄ selectivity of CTF-BIB-1 is due to the ultrahigh C₃H₈ adsorption and increased affinity compared to CH₄. In addition, CTF-BIB-1 displayed excellent separation in industrial fixed bed adsorbents by transient breakthrough simulations for an equimolar CO₂/C₃H₈/C₂H₆/CH₄ mixture. The breakthrough times sequence was C₃H₈>C₂H₆>CO₂>CH₄ which is decided according to the hierarchy of the corresponding adsorption strengths.

Table 2. 2. Various materials used for C₂/C₁ hydrocarbon separation.

Material	Temp.	C ₂ H ₂ uptake (mmol/g)	C ₂ H ₄ uptake (mmol/g)	C ₂ H ₂ /CH ₄ selectivity	C ₂ H ₄ /CH ₄ selectivity	Ref
MOF [Mn(INA) ₂]·MeOH	273 K	3.69	59.7	515	64	116
MOF [Mn(INA) ₂]·MeOH	298 K	2.66	2.08	385	29	116
Zn-F-TRZ	273 K	1.88	0.97	255.9	68.3	117
Zn-F-ATRZ	273 K	1.43	0.97	215.3	35.1	117
Zn-F-DATRZ	273 K	0.48	0.61	15.1	219.0	117
NAC-600	298 K	4.60	5.70	24.2	31.9	118
NAC-700	298 K	6.39	6.41	47.1	45.1	118
NAC-800	298 K	5.28	4.49	26.5	19.4	118
UTSA-33a	296 K	-	-	13.8	11.1	119
UTSA-33a	273 K	-	-	16.1	14.7	119

ZJU-61a	298 K	6.02	4.00	74.4	49.5	120
ZJU-61a	273 K	6.96	5.34	115.3	87.6	120
UTSA-10a	296 K	1.85	1.29	8.1	4.6	121
HOF-BTB	295 K	2.87	2.32	7.8	7.9	122
HOF-BTB	273 K	4.95	3.80	9.5	9.3	122
Wet ZIF-8	273 K	-	-	-	5.56	123
Solid ZIF-67	273 K	-	-	-	3.1	124
UTSA-50	296 K	3.80	-	68	-	125
$\text{Zn}_4(\text{OH})_2(1,2,4\text{-btc})_2$	295 K	2.22	-	14.7	-	126

Alkenes are generally not present in petroleum but are found in the distilled fractions due to the cracking process during distillation.⁴² In addition, they are also produced from different raw materials and are used for making polymers.

Polyethylene is one of the most used common mega products (plastic) and is employed in packaging, one time use products etc. Polyethylene is produced using ethylene (C_2H_4) as the starting monomer. Nearly 25 trillion tons of ethylene are generated every year and the highest cost of production is due to the separation of ethylene from other hydrocarbons.⁴⁴ The starting C_2H_4 must be of high-end grade with excellent purity to obtain high degree of polymerization. Often trace amount of acetylene (C_2H_2) is present in the feed gas, which can terminate ethylene polymerization by catalytic poisoning. Conventional methods to overcome this problem include catalytic conversion of acetylene to ethylene by utilization of precious metal (Pd or Ag) catalysts with H_2 for reduction.^{45, 46} However, this adds extra cost in the overall process due to high catalyst costs and other instrumental setups. Porous adsorbent based separation processes provide an alternative way to reduce the overall cost. To this end, Ding et al., used an organic pigment molecule (Pigment Orange-71 (PO71)) to synthesize CTF-PO71.⁴⁷ This was the first report on the use of an organic porous material that is capable of separating C_2H_2 and

C_2H_4 gases. At 1 bar pressure, the CTF-PO71 adsorbed 2.8 mmol/g and 1.9 mmol/g of C_2H_2 at 273 K and 298 K, respectively. On the other hand, the adsorption capacity for C_2H_4 is lower under same conditions. This difference in adsorption capacity shows potential of gas separation. The theoretical separation factor based on the equilibrium adsorption values and calculated using ideal adsorbed solution theory (IAST) was 2.8-1.8 (Figure 2.2). The presence of the functional sites provided different electrostatic potentials on the pore surface and hence created a strong interaction between C_2H_2 and the CTF-PO71 material. The preferential adsorption of C_2H_2 over C_2H_4 , besides the low cost of the monomer and high stability of the CTF-PO71 material demonstrates its potential for practical implementation.

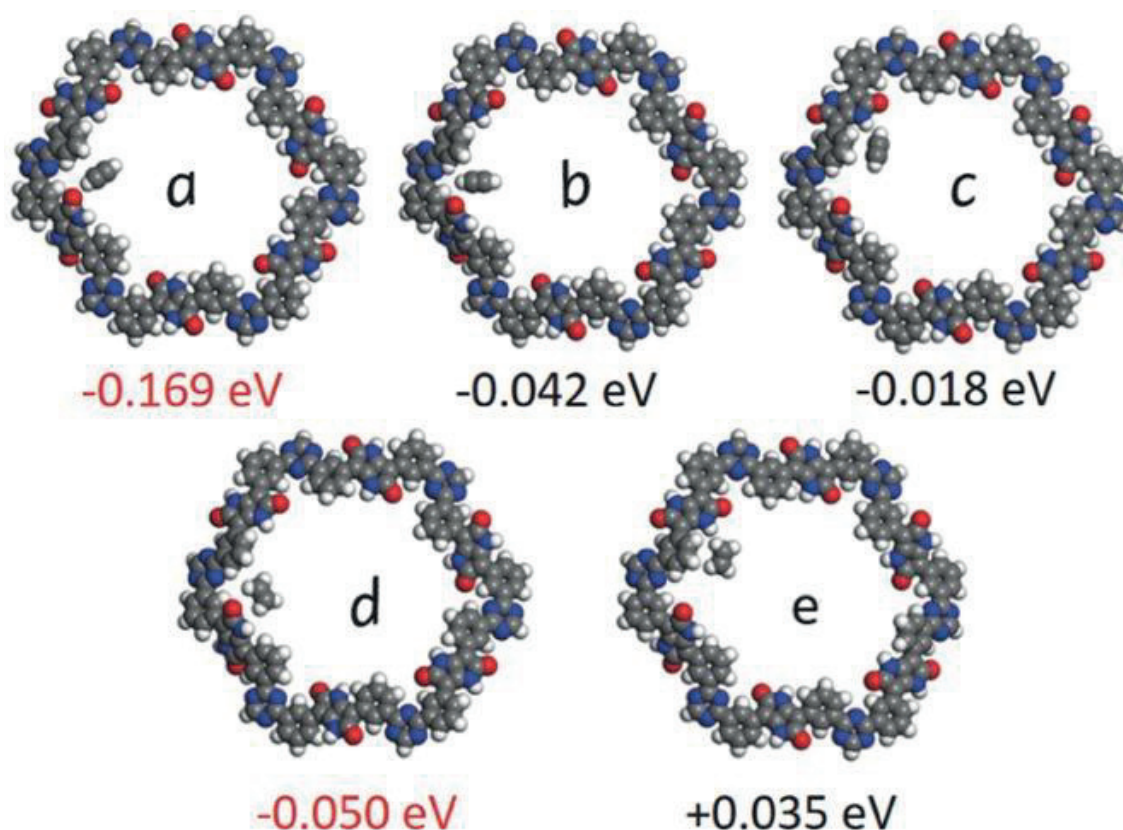


Figure 2. 2. Different binding configurations and their binding energies of CTF-PO71 with (a–c) C_2H_2 and (d,e) C_2H_4 .⁴⁷ Reproduced with permission from John Wiley and Sons.

Another industrially important hydrocarbon is acetylene (C_2H_2) by itself. Acetylene is generally obtained as a byproduct of natural gas and petroleum processing.⁴⁸ Other methods of producing acetylene include oxidative and non-oxidative coupling of methane into ethane, ethylene, and acetylene.⁴⁹ Often these processes contain methane as impurities due to incomplete conversion. Hence, there is a requirement of separating

methane from the end-product. There are large differences in the physical properties of methane and C2 hydrocarbons which can be utilized to make selective adsorbents.

2.3. Heterogeneous catalysis

Applying heterogeneous catalysts is one way to improve a chemical process as it provides several advantages over homogeneous catalysts such as easy recovery, reusability, and potential in continuous flow processes.⁵¹ Imine-COFs and CTFs provide a perfect platform for heterogeneous catalysis as they have high surface areas, an ordered pore distribution, tunable surface properties and high stability. Furthermore, the functionality of these materials can be tuned to use them as a support for active homogeneous catalysts or to use them as a metal-free organocatalyst. A wide range of organic transformations have already been reported using imine-COF and CTF based heterogeneous catalysts. For clarity, this section is divided into metal based organic transformation, photocatalysis, electrocatalysis and organocatalysis. Some of these sections do overlap each other but in general they can be differentiated based on the reaction conditions.

2.3.1. Metal based organic transformations

Homogeneous catalysts are well known and have proven to be highly effective. However, they are limited by several issues such as catalyst recovery, deactivation, aggregation, attrition etc. To overcome these issues, porous materials are often used as supports to anchor either metal complexes or metal nanoparticles. This provides a higher stability to the catalysts and promotes the substrate and product diffusion due to the inherent porous properties. The overall downstream processing is cost effective if a heterogeneous catalyst is utilized.⁵¹

2.3.1.1. Application of CTFs in Metal based organic transformations

In 2009, soon after the first reports on CTFs, Schüth et al. developed a Pt based catalyst using 2,6-dicyanopyridine (DCP) as the monomer to construct the CTF. The N-rich sites in the CTF were used to anchor Pt precursor by pre- and post-modification approaches.⁵² The performance of the resulting Pt-CTF/K₂[PtCl₄]-CTF was compared with the homogeneous Periana catalyst (Pt on a bipyrimidine complex) for methane oxidation to methanol using SO₃ in concentrated sulfuric acid. High turnover numbers (TON) around 300 were obtained using the CTF based catalysts even after five recycling steps. The presence of N-heterocyclic moieties on the CTF surface was utilized for the stabilization

of Pd nanoparticles by Thomas et al.⁵³ The Pd/CTF thus formed was compared with the commercially available activated carbon (AC) for glycerol oxidation. The Pd/CTF catalysts showed a longer lifetime due to the high N content stabilizing the Pd nanoparticles and was more selective towards glycerate than Pd/AC. Prati et al. studied the influence of the size confinement effect of CTFs on the stabilization of Pd nanoparticles.⁵⁴ Their results showed that 2.6 nm PdHx particles were stabilized within the CTF pores. Due to the high N content, CTFs are basic in nature and hence they can be utilized as a replacement for a base used in several catalytic reactions. Palkovits et al. reported on several Ru supported CTFs for the base-free oxidation of 5-hydroxymethylfurfural to 2,5-furandicarboxylic acid in water.⁵⁵ However, DMSO was required to wash the material and the reactivation required harsh conditions (350°C, H₂ flow). As discussed earlier, it is well known that the CO₂ emission have created several global threats and its remediation through CCS and CCU is very important. Within this context, Zhang et al. demonstrated that CTFs could be used as an effective material for both the capture and conversion of CO₂.⁵⁶ They demonstrated in first instance that the di(4-cyanophenyl)ethyne based CTF (CTF-DCE) can adsorb 4.3 mmol/g CO₂ at 273 K and 1 bar. In a following step, Ag nanoparticles were embedded into the CTF matrix which was used afterwards as a catalyst for the direct carboxylation of terminal alkynes using CO₂. The applied mild reaction conditions and good reusability of these materials show promise in their use for synthetic chemistry.

Though CTFs have inherent triazine units in their framework, the presence of a polydentate ligand in the structure can enable further stability for the anchored metal complexes. To demonstrate this, Yoon et al. utilized 2,2'-Bipyridine-5,5'-dicarbonitrile as a monomer to produce the corresponding CTF which was used as a support for the [IrCp*Cl₂]₂ complex.⁵⁷ The resulting air stable heterogeneous catalyst was used for the conversion of CO₂ to formate through hydrogenation. A high turnover number (5000) and turnover frequency (5300 h⁻¹) was obtained. Later on, the same group reported on the use of the bpy-CTF (bipyridine-CTF) for the anchoring of bimetallic complexes (Al and Co complexes) to produce a recyclable heterogenized catalyst [bpy-CTF-Al(OTf)₂][Co(CO)₄].⁵⁸ Al(OTf)₃ was first immobilized on the CTF and a subsequent exchange of the [OTf]⁻ anion with the [Co(CO)₄]⁻ anion was performed. The resulting bimetallic CTF based catalyst was able to efficiently convert propylene oxide to β -butyrolactone with 90% selectivity. Van Der Voort et al. also performed an extensive computational and experimental study regarding the coordination environment of the

bpy- CTF (Figure 2.3).⁵⁹ In this work, an Ir(I) complex was anchored on the bpy-CTF which was utilized for the borylation of arenes and heteroarenes using B₂Pin₂ as the borylating agent. Gascon et al. used a mixed linker strategy to create a bidentate N ligand system in a CTF to anchor Ir(III)Cp* using 4,4'-dicyanobiphenyl and 2,6-dicyanopyridine.⁶⁰ The presence of 2,6-dicyanopyridine moieties in the framework ensures strong coordination sites for the metal complexation whereas the dicyanobiphenyl promotes molecular diffusion due to its enlarged pore size (mesoporosity). The air stable Ir/CTF was used to produce hydrogen (60 mol/L/h) from formic acid.

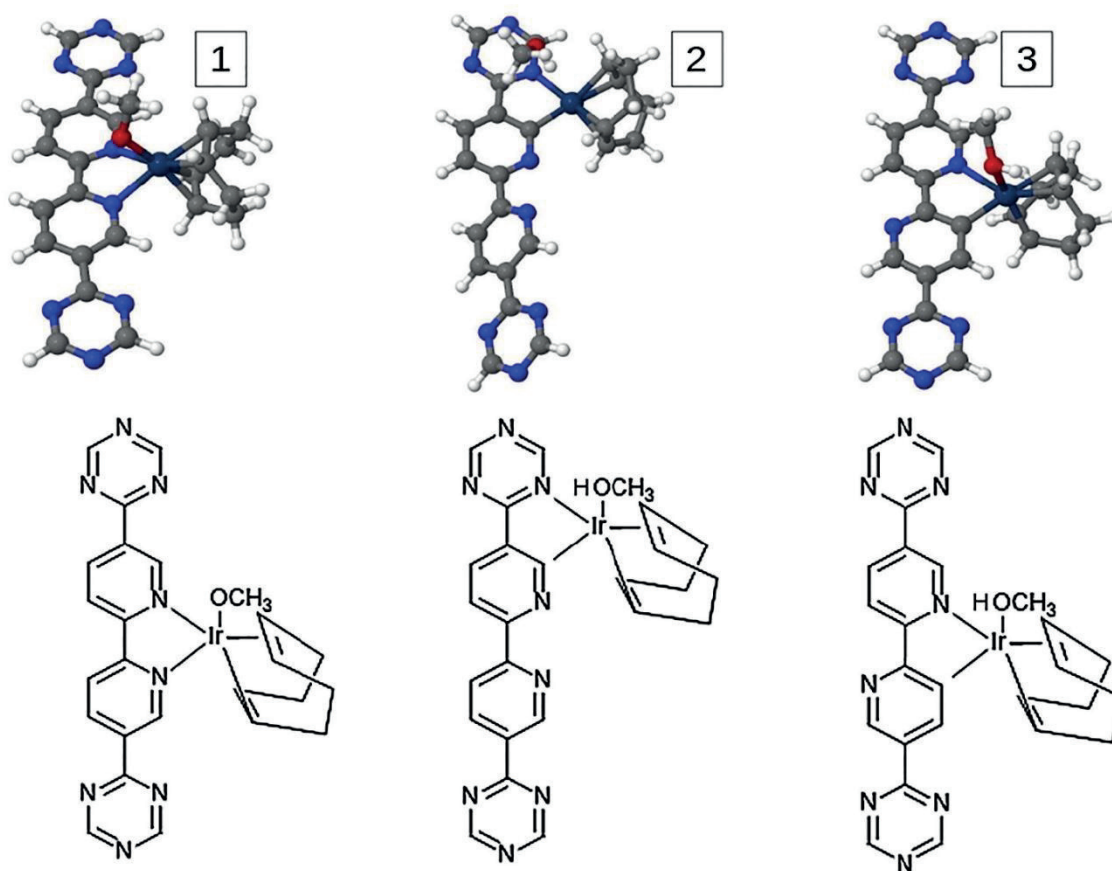


Figure 2. 3. Possible binding modes of Iridium complex on bipyridine unit. Structurally relaxed anchoring models (upper row) and their schematic formula (lower row). The stabilization energies are -444 kJ/mol (model 1), -414 kJ/mol (model 2), -439 kJ/mol (model 3).⁵⁹ Reproduced with permission from Elsevier.

Most of the metal based catalytic transformations using CTFs are based on the presence of N sites in the CTF. However, several other coordination sites can also be designed in CTFs for metal complexation. Yoon et al. reported on an ionic-liquid-based heterogenized cobalt catalyst, [imidazolium-CTF][Co(CO)₄] for the direct ring-opening carbonylation of propylene oxide to methyl 3-hydroxybutyrate with 86% selectivity.³²

The $\text{Co}(\text{CO})_4^-$ complex was successfully loaded onto the CTF through exchange with the Br^- present in the framework. Yoon et al. also developed an N-heterocyclic carbene (NHC) based CTF which could be used as a support for an Ir(III) complex.⁶¹ Due to the strong σ -donating and poor π -accepting characteristics of the NHC ligand, the Ir-NHC complex could efficiently catalyze the conversion of CO_2 to formate via hydrogenation. A high TOF (16000 h^{-1}) and TON (24300) was achieved. These results demonstrate that there are various possibilities of utilizing functionalized CTFs for efficient metal coordination.

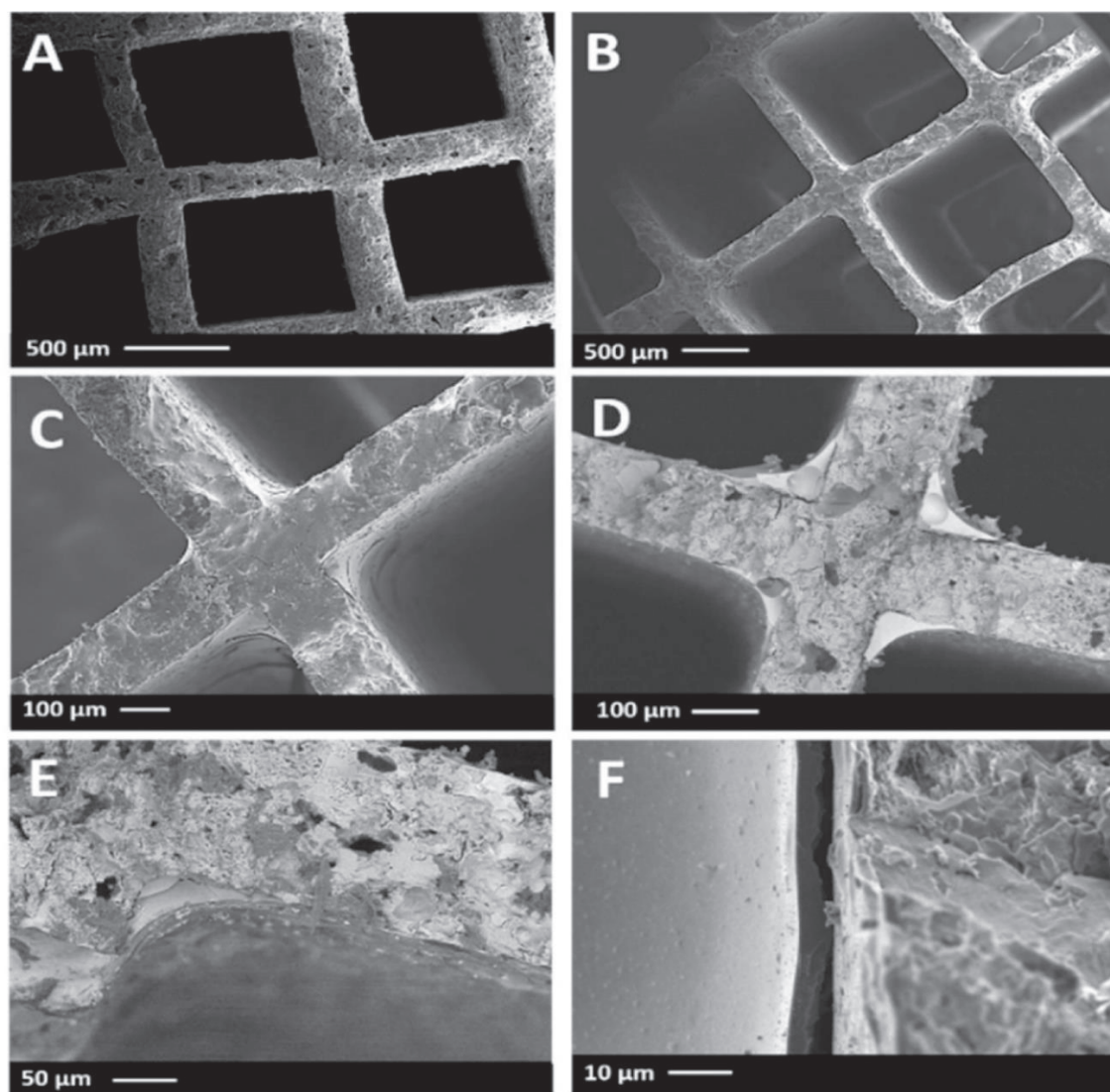


Figure 2. 4. SEM micrographs of CTF@monolith: (a) bare cordierite monolith, top view; (b–e) CTF-coated monolith, cross-sectional views; (f) view on the wall of a CTF-coated monolith (left).⁶³ Reproduced with permission from American Chemical Society.

However, the use of CTFs in their powder form is not ideal for practical usage due to their size limitation which would result in attrition and aggregation during the catalytic

process. To solve this issue Gascon et al. used a one-step method to produce rigid and easy-to handle CTF-based spheres prepared by a phase inversion method using polyimide Matrimid as a binder.⁶² The resulting spheres were porous which could be loaded with Ir(III)Cp* by post-modification for the hydrogenation of CO₂ to produce formic acid. One drawback of this process was that the porosity could not be completely preserved upon formulation. Furthermore, they also developed monoliths coated with CTF particles which were then postmodified with Ir and Pt complexes (Figure 2.4).⁶³ These monoliths could be effectively utilized in the formic acid dehydrogenation and methane oxidation. These methods can be seen as a first step towards the practical implementation of CTFs in organic transformations.

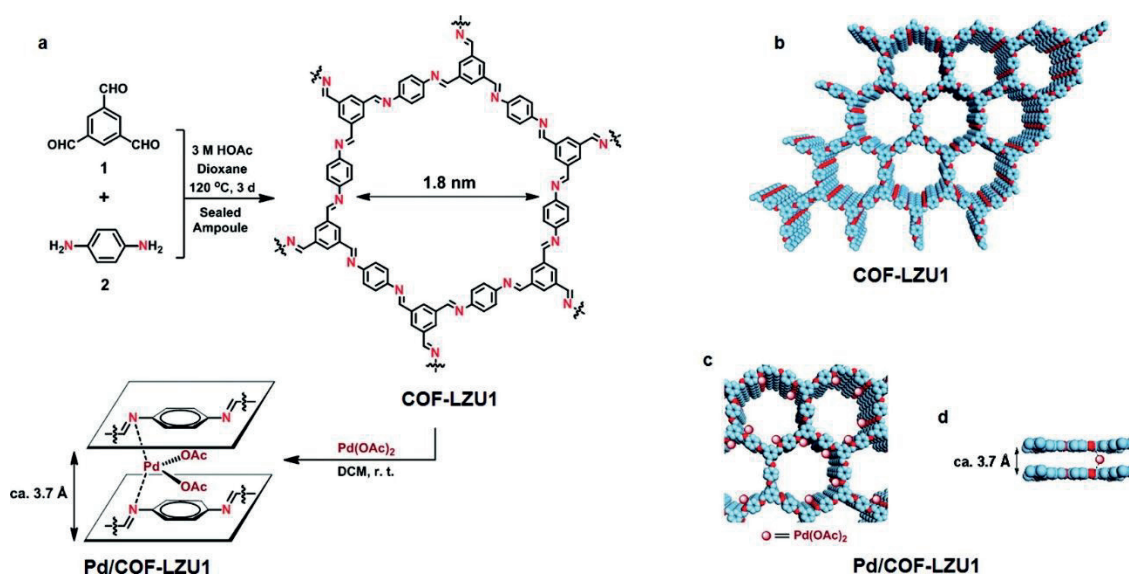


Figure 2. 5. Construction of COF-LZU1 and Pd/COF-LZU1. Schematic representation for the synthesis of COF-LZU1 and Pd/COF-LZU1 materials (a). Proposed structures of COF-LZU1 (b) and Pd/COF-LZU1 (c, d) possessing regular microporous channels (diameter of ~1.8 nm), simulated with a 2D eclipsed layered-sheet arrangement. C: blue, N: red, and brown spheres represent the incorporated Pd(OAc)₂. H atoms are omitted for clarity.⁶⁴ Reproduced with permission from American Chemical Society.

2.3.1.2. Application of COFs in Metal based organic transformations

The first example of the use of imine-COF in metal based organic transformation was in 2011, where Pd(II) was anchored onto COF-LZU for performing Suzuki-Miyaura coupling reaction.⁶⁴ The nitrogen rich imine sites in the COF were responsible for strong coordination of Pd (Figure 2.5.). Following this, an immense growth in the number of reports using COFs as platform for metal coordination has been reported. A 3D COF-300

was also used for phosphine-free Suzuki-Miyaura, Heck and Sonogashira cross-coupling reactions.⁶⁵ A low Pd loading of 0.1 mol% was used to perform the overall reaction within the range of 20-120 minutes with yields of >90% for a wide substrate scope. On the other hand, the commercial Pd/C afforded around 55% yield under same conditions with higher Pd content (0.2 mol%). X-ray photoelectron spectroscopy (XPS) and high-resolution transmission electron microscopy (HRTEM) analysis revealed the formation of Pd0 nanoparticles during the reaction. A series of 2,2'-bipyridine COFs have also shown a high catalytic reactivity for the Heck coupling reactions. The amount of bipyridine sites for Pd coordination could be easily controlled in these COFs.⁶⁶

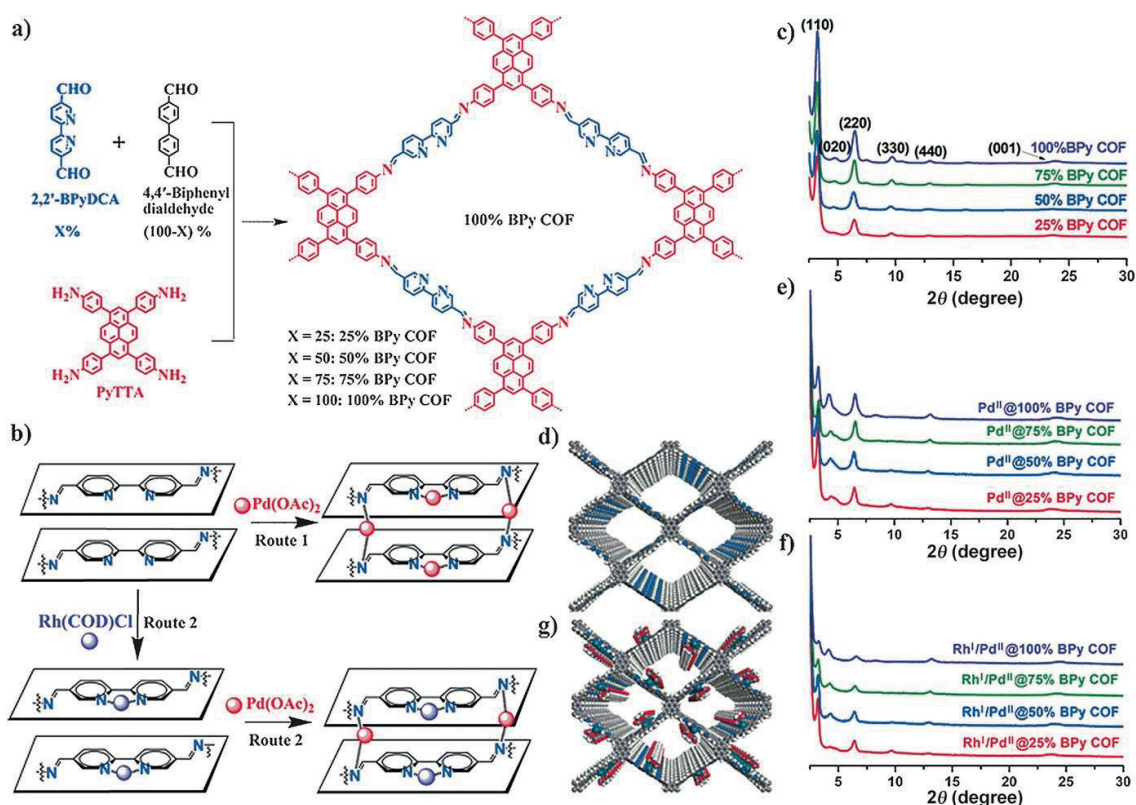


Figure 2. 6. (a) Use of a three-component condensation system to modulate the nitrogen content of the 2D imine-type COFs. (b) Designed strategies for the monometallic (Route 1) and bimetallic docking (Route 2). (c) PXRD patterns of the X % BPy COFs. (d) Open channels of the COFs. (e) PXRD patterns of the PdII@X % BPy COFs. (f) PXRD patterns of the RhI/PdII@X % BPy COFs. (g) Open channels of the metal loaded COFs.⁶⁷ Reproduced with permission from John Wiley and Sons.

The nitrogen content of COFs could be varied by using nitrogen rich linkers such as bipyridine. Several pyrene-bipyridine-biphenyl containing COFs with varying bipyridine units were synthesized for creating metal docking sites.⁶⁷ In addition to the inherent bipyridine sites, the imine nitrogen also can coordinate to the metals. Using this strategy,

Gao et al., reported a series of bimetallic Rh/Pd BPyCOF (Figure 2.6.). These were used in a one-pot cascade reaction system.⁶⁷ Rh(I) catalyzed the addition of phenylboronic acid to benzaldehyde to produce diphenylmethanol. Further Pd(II) catalyzed the oxidation of diphenylmethanol to generate benzophenone. Similar approach was used to create a Mn/Pd bimetallic COF system for Heck-epoxidation tandem reaction.⁶⁸ In this case, Pd catalyzed the Heck coupling and further on Mn catalyzed the epoxidation step. Yields >90% were obtained for the tandem reaction with the bimetallic COF, whereas with single metal COF only either of the half reactions could be catalyzed.

Apart from nitrogen rich sites for metal coordination, other heteroatoms can also be utilized. Acetylacetone (acac) consists of two oxygen atoms which is well-known for anchoring transition-metal ions.⁶⁹ To this end, TAPT-2,3-DHTA COF was synthesized by the condensation reaction of 2,3-dihydroxy terephthalaldehyde and 1,3,5-tris(4-aminophenyl) triazine.⁷⁰ Further it was impregnated with vanadium ions to produce VO-TAPD-2,3-DHTA COF. This was employed in Prins reaction and sulfide oxidation. Excellent catalytic activity was observed for the synthesis of nopol and a range of sulfides oxidation was achieved without significant losses to the structure. In another report, vanadium docked COF was utilized as an effective heterogeneous catalyst for modified Mannich-type reaction.⁷¹ High yields of up to 99% was obtained for a wide substrate scope. Moreover, there was no significant loss of catalytic activity over 5 catalytic cycles showing the recyclability of such COFs in heterogeneous catalysis applications.

2.3.2. Photocatalysis

It is a given that photocatalysis is clean, sustainable and overall a green process. Plants use sunlight to fix atmospheric CO₂ and produce carbohydrates and oxygen through photosynthesis. For several years already, researchers have been focused on the development of artificial photosynthetic processes where the basic principles of natural photosynthesis are utilized to synthesize fine chemicals. Several researchers have reported the usage of UV light for direct excitation of molecules.⁷²⁻⁷⁴ However, the ideal green solution would be to directly use visible light for activating the reaction. Sensitizers which transfer electrons from an excited state to the molecule are usually applied.⁷⁵ Several homogeneous sensitizers have been utilized in various organic transformations.⁷⁶⁻⁸⁰ The earliest report on heterogeneous photocatalyst was in 1972 by Fujishima and Honda.⁸¹ By then electrolysis of water had been studied well and a potential difference of more than 1.23 V is required for this process. This potential is equal to the energy of

radiation with ~ 1000 nm wavelength. Hence, they used a photo-electrochemical cell where the photo energy provided the required potential difference for the electrochemical decomposition of water. A semiconducting n-type TiO_2 electrode was used for this purpose. Since then, several semiconductors have been applied as photocatalysts and the use of organic polymers as photocatalysts have also attracted significant attention.

2.3.2.1. Application of CTFs in photocatalysis

The high thermochemical stability, inherent triazine content and tunable functional groups of CTFs can be utilized to create highly efficient photocatalysts. For instance, CTF-1 comprising of benzene and triazine units is an intrinsically donor-acceptor containing porous material and has a bandgap of 2.42 eV.⁸² Benzene is an electron donor with an electron affinity of -1.15 eV whereas the triazine moiety is an electron acceptor with an electron affinity of +0.46 eV.⁸³ The study on the density of states of triazine-based frameworks using first-principles calculations confirmed their behavior as organic semiconductors. In addition to this, the functional groups present on the monomers can also be tuned to incorporate other donor or acceptor units.⁸² Hence, CTFs are considered as promising candidates for several photocatalytic processes such as photocatalytic water splitting for the production of H_2 or O_2 , photocatalytic degradation of pollutants, photocatalytic CO_2 reduction etc. One must however take into account that the CTFs produced through the ionothermal synthesis at elevated temperatures ($>400^\circ\text{C}$) are highly carbonized and black in color. This renders their photocatalytic application potential almost inefficient.

One possible way to overcome this problem is by lowering the synthesis temperature. But this results into an incomplete trimerization and reduced long-range order in the obtained materials. However, Lotsch et al. were able to synthesize phenyl-triazine oligomers at lower synthesis temperatures instead of CTFs ($300\text{--}350^\circ\text{C}$).⁸⁴ This resulted in a photocatalytically active material which showed hydrogen evolution rates of $1076\ \mu\text{mol/h/g}$. However, long synthesis times (>150 h) were required to obtain a certain degree of polymerization. On the other hand, Thomas et al. used a shorter reaction time and a higher temperature (400°C) to avoid partial carbonization.⁸⁵ To obtain a porous and photoactive material, both the Bronsted acid and Lewis acid methods were combined. First trifluoromethanesulfonic acid was used to form a pre-CTF (amorphous polymer) which was then treated with ZnCl_2 in open crucibles at a high temperature. In this way an average hydrogen evolution rate of $1072\ \mu\text{mol/h/g}$ under visible light (>420 nm) using Pt as a cocatalyst was obtained.

Apart from the ZnCl_2 method, researchers have focused on the development of CTFs under mild conditions to produce photoactive CTFs. As an example, Wu et al. used CTF-T1, synthesized using the bronsted acid method, and Pt nanoparticles were dispersed in its framework.⁸⁶ Under visible light irradiation (wavelength=420nm), CTF-T1 exhibited a lower photocatalytic H_2 evolution activity compared to g- C_3N_4 (graphitic carbon nitride) during the first two runs but showed a higher activity than g- C_3N_4 in the fifth run. Janiak et al. used a tetra(4-cyanophenyl)ethylene monomer to synthesize PCTF-8 applying the Bronsted acid method which showed a high thermal stability ($>400^\circ\text{C}$) and a high photoluminescence performance.⁸⁷ The PCTF-8 material showed only an average H_2 evolution value of $2370 \mu\text{mol/g}$ due to lack of long-range order. However, it was sensitive towards the detection of nitroaromatic analytes with trinitrophenol quenching *ca.* 71% of the fluorescence emission intensity. Cooper et al. studied the effect of the spacer length in CTFs on the photocatalytic H_2 evolution activity both computationally and experimentally.⁸⁸ A decrease in the optical gap was observed in the UV-vis spectra upon increasing the phenylene spacer length. The observed trend in the activity for the CTF series and the origin of maximum in the hydrogen evolution rate for CTF-2 (Dicyanobiphenyl linker) was due to a combination of the thermodynamic driving force and the optical gap.

Post-modification of CTFs with other materials could not only help in increasing the photoactivity but can also increase the stability of the otherwise labile materials by acting as a strong support.⁸⁹ It is well known that the noble metal free MoS_2 quantum dots can be an excellent photocatalyst. Particularly, for H_2 evolution, the sulfur edges of the MoS_2 crystal layers enable the activity and the quantum confinement can result in higher surfaces and edges of the material. However, MoS_2 quantum dots require harsh preparation conditions and hence the use of a microporous CTF for confining the MoS_2 to produce quantum dots is a promising approach. Wu et al. used an *in situ* photodeposition method to synthesize MoS_2 /CTF composites.⁹⁰ The interactions between the MoS_2 and the CTFs allowed an interfacial charge transfer and separation and the obtained H_2 evolution rates were higher than for the MoS_2 /g C_3N_4 materials. Cao et al. used Rhenium modified CTF-Py for efficient photocatalytic reduction of CO_2 to CO .⁹¹ A solid-gas system was used to avoid Re leaching and deactivation due to dimerization leading to a stable heterogeneous catalyst.

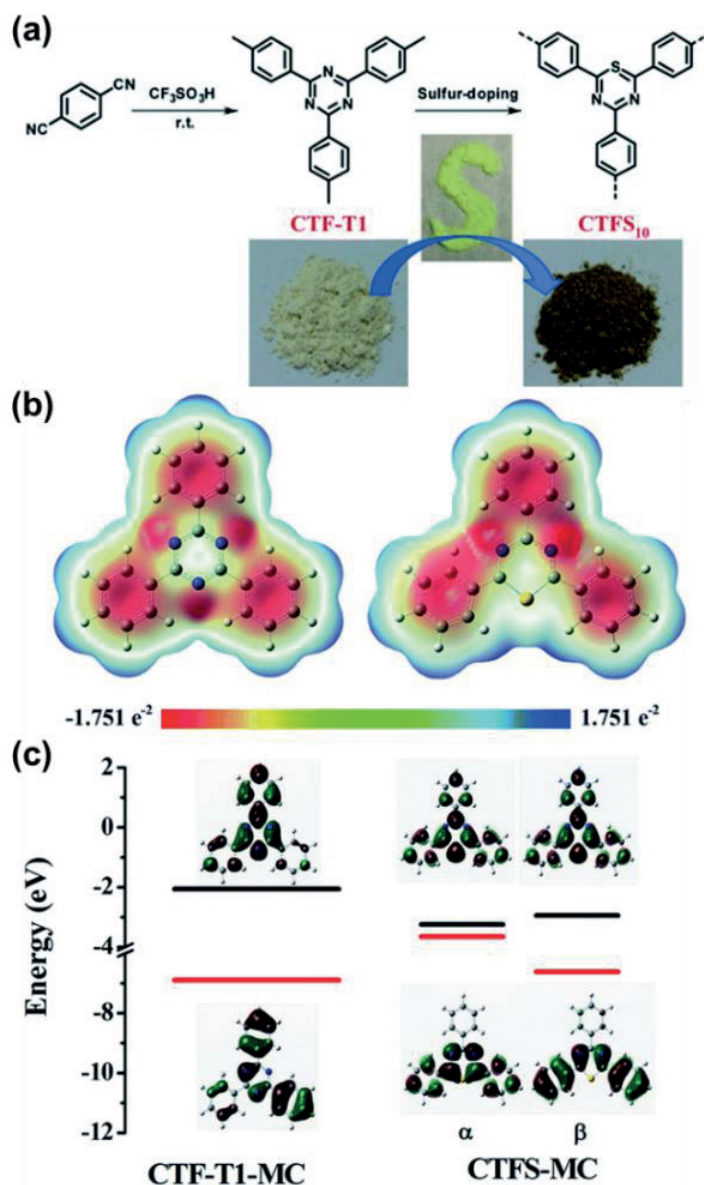


Figure 2. 7. (a) Synthesis of CTF-T1 and sulfur-doped CTF-T1, (b) Charge distributions in CTF-T1-MC and CTFS-MC, and (c) HOMO-LUMO orbitals of CTF-T1-MC and CTFS-MC.⁹² Reproduced with permission from Royal Society of Chemistry.

It is well known that heteroatom doping can modify the photocatalytic activity of a photoactive material. Su et al. used a sulfur heteroatom doping approach (Figure 2.7) to improve the photocatalytic H_2 evolution rate in comparison to the pristine CTF and $\text{g-C}_3\text{N}_4$.⁹² Wu et al. applied a chemical doping approach to introduce phosphorus groups into the framework of CTF-1 which enhanced the optical and electronic property by promoting generation, separation and transfer of electron-hole pairs in the material. For the photocatalytic H_2 evolution, the P doped CTF (PCTF-1) showed a higher H_2 evolution rate compared to the pristine CTF-1 and P-doped $\text{g-C}_3\text{N}_4$.⁹³ Recently, Tan et al. synthesized a series of donor-acceptor CTFs with N, S and O containing fluorene

analogues as electron donors and triazine units as electron acceptors.⁹⁴ The photocurrent intensity of the synthesized CTFs was in the order of CTF-N>CTF-S>CTF-O or in other words, CTF-N showed the best performance (538 $\mu\text{mol/h}$ H_2 evolution rate). The CTFs obtained according to the low temperature amidine method also can be used for photocatalysis as they are not carbonized. For example, the CTF-HUSTs synthesized by Tan et al. showed 2647 $\mu\text{mol/h/g}$ H_2 evolution rate under visible light.⁹⁵

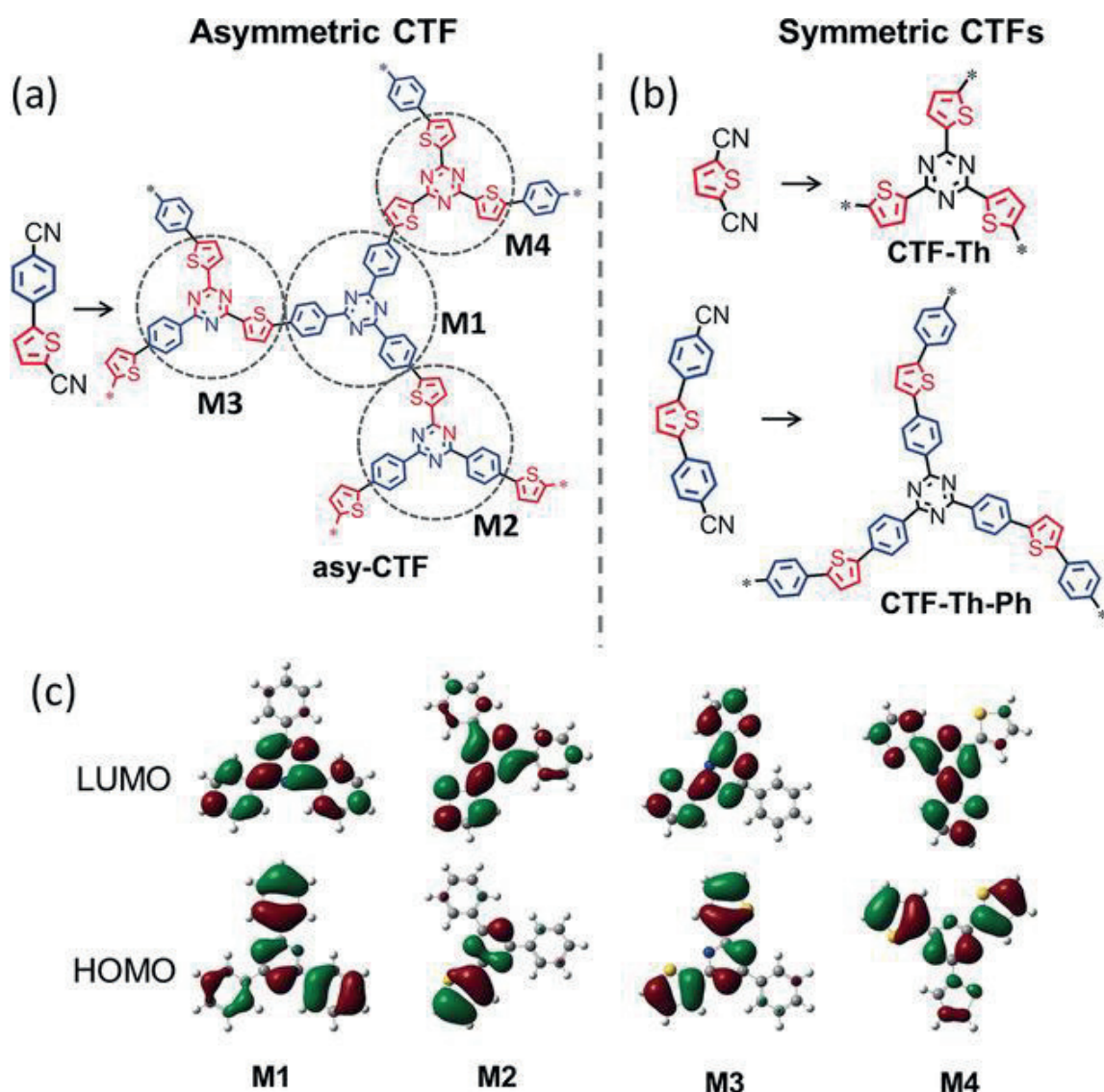


Figure 2. 8. (a) Representative structure of the repeating units in the asymmetric network asy-CTF containing four different molecular D-A domains (M1–M4), (b) its symmetric counterparts CTF-Th and CTF-Th-Ph containing only a single D-A domain, and (c) HOMO and LUMO levels of the four different D-A domains within asy-CTF calculated at the B3LYP/6-31G(d) level.⁹⁶ Reproduced with permission from John Wiley and Sons.

Zhang et al. employed a simple design strategy to produce an asymmetric CTF (asy-CTF) using the Bronsted acid assisted method and 5-(4-cyanophenyl)thiophene-2-carbonitrile as a building block (Figure 2.8).⁹⁶ In addition, they compared it to two symmetric CTFs with thiophene (CTF-Th) and phenylthiophene (CTF-Th-Ph) units for the synthesis of 1,2,3-triphenylphosphindole 1-oxide. The asy-CTF had four different molecular donor-acceptor domains in the framework which led to higher charge separation, electron transfer, and sufficient photoredox potential. In general, the asy-CTF material showed a superior performance for the photosynthesis of 1,2,3-triphenylphosphindole 1-oxide in comparison to the CTF-Th and CTF-Th-Ph materials.

2.3.2.2. Application of COFs in photocatalysis

Lotsch et al. reported a photoactive hydrazine based COF (TFPT-COF) synthesized by condensation of 2,5-diethoxyterephthalohydrazide (DETH) and 1,3,5-tris(4-formylphenyl)triazine (TFPT).⁹⁷ This was employed in photocatalytic hydrogen evolution reaction under visible light irradiation and produced H₂ from water with a hydrogen evolution rate (HER) of 1970 $\mu\text{mol/h/g}$ in the presence of platinum nanoparticles and a sacrificial agent of triethanolamine (TEOA). Following this, they also reported a series of azine COFs with different nitrogen numbers (N_x-COFs, $x = 0-3$) in the central aryl ring which exhibited differences in crystallinity and porosity.⁹⁸ An enhanced amount of H₂ production was observed with the increase in the nitrogen atoms in the central aryl ring. Hydrogen evolution rates of 23, 90, 438 and 1703 $\mu\text{mol/h/g}$ were obtained for N₀-COF, N₁-COF, N₂-COF and N₃-COF, respectively. Increased surface area and improved charge migration efficiency corresponding to the number of nitrogen atoms was linked to the increased photocatalytic activity. Sun et al. synthesized a series of β -ketoenamine-based COFs, namely TpPa-COF-X ($X = -(\text{CH}_3)_2, -\text{CH}_3, -\text{H}$ and $-\text{NO}_2$) to understand the effect of functional groups on the photocatalytic properties of COFs.⁹⁹ TpPa-COF- $(\text{CH}_3)_2$ exhibited an HER of 8.33 mmol/h/g, which is 2.7-times, 5.3-times and 38-times higher than that of TpPa-COF-CH₃ (3.07 mmol/h/g), TpPa-COF-H (1.56 mmol/h/g) and TpPa-COF-NO₂ (0.22 mmol/h/g), respectively. The outcome of this comparative study indicated that the presence of electron donating groups in the COF structure enhances the charge separation efficiency and correspondingly increases the HER.

By incorporating sulfone groups in the COF structure, Cooper et al. designed S-COF and FS-COF which showed the highest HER up to date amongst COFs.¹⁰⁰ By using Pt as the co-catalyst and ascorbic acid as the electron donor, S-COF and FS-COF exhibited an HER

of 4.44 and 10.1 mmol/h/g, respectively. Furthermore, by using a dye-sensitized version of the COF, 16.3 mmol/h/g HER was obtained (Figure 2.9). To show the importance of crystallinity in charge transfer in COF structures, amorphous analog FS-COF was synthesized, namely FS-P which showed only 1.12 mmol/h/g HER. Moreover, a sulfone-free TP-COF showed 1.60 mmol/g/h HER which indicated the important role of sulfone groups in hydrogen production. Experimental and theoretical studies showed that the increased planarity of the building blocks can lower the optical band gaps of the COFs, thus increasing their light absorption ability and excited-state lifetime. In addition, sulfone groups increased the hydrophilicity or wettability of the COF which is relevant to the photocatalytic conditions as water is the main substrate used for hydrogen production.

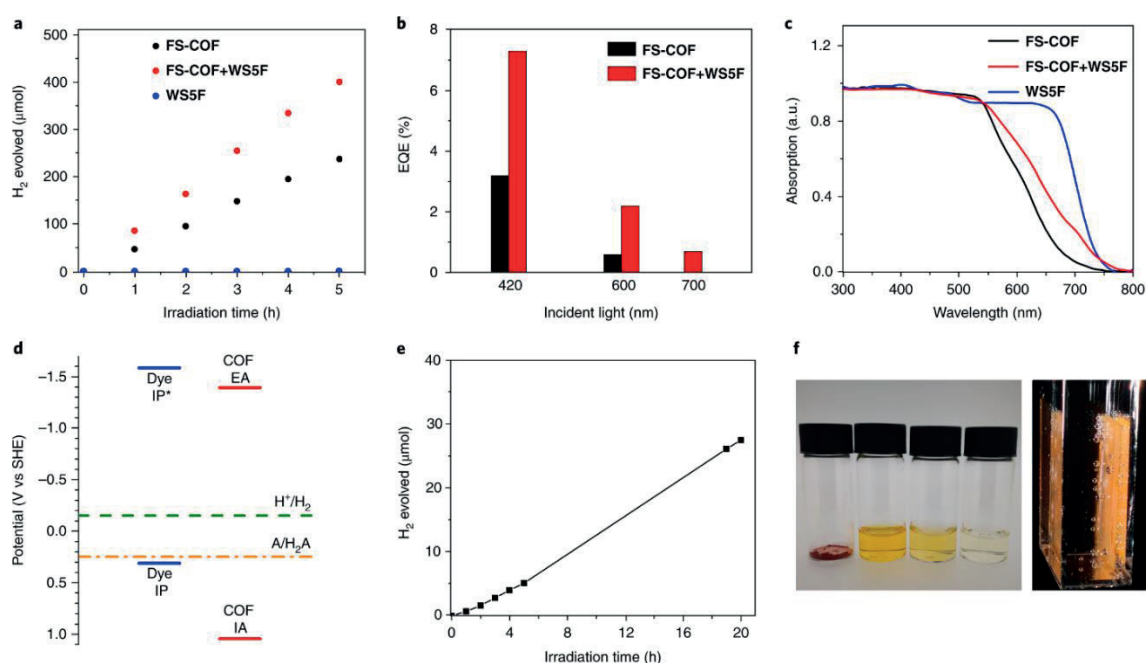


Figure 2. 9. (a) Time course for photocatalytic H₂ production using visible light for FS-COF, a neat, near-infrared dye (WS5F) and a dye-sensitized COF (FS-COF+WS5F). (b) EQEs at three different incident light wavelengths for FS-COF and FS-COF+WS5F. (c) Solid-state UV-vis spectra for FS-COF, WS5F and FS-COF+WS5F. (d) Relative energy levels as calculated for ascorbic acid, FS-COF and a near-infrared dye, WS5F; dashed green and orange lines indicate potentials for proton reduction and the two-hole oxidation of ascorbic acid in solution, respectively. (e), (f) Photocatalytic H₂ production using FS-COF films. photographs showing (left to right) solid FS-COF and colloidal dispersions in DMF, water and acetone, respectively and FS-COF film on glass producing hydrogen.¹⁰⁰ Reproduced with permission from Springer Nature.

Thomas et al. designed two highly crystalline acetylene ($-C\equiv C-$) and diacetylene ($-C\equiv C-C\equiv C-$) functionalized β -ketoenamine COFs (TP-EDDA-COF and TP-BDDA-COF, respectively) for their application in photocatalytic hydrogen evolution.¹⁰¹ By using Pt co-catalyst the experimental results showed that the diacetylene moieties had an important role on the photocatalytic performance of the COFs as the photocatalytic activity of TP-BDDA-COF (324 $\mu\text{mol/h/g}$) was much higher than that of TP-EDDA-COF (30 $\mu\text{mol/h/g}$). In addition, experiments with deuterated water showed that the produced hydrogen is indeed from water splitting.

The excellent crystallinity, tunable porosity, and functional groups in COFs in addition to tailorable semiconducting properties makes them suitable platform to obtain composite materials which could further boost the photocatalytic activities. In 2014, Banerjee et al. synthesized TpPa-2-COF as a stable scaffold for supporting cadmium sulfide (CdS) nanoparticles to produce a CdS-COF composite, which was studied for hydrogen evolution through photocatalysis.¹⁰² Among several hybrids, the one with 10 wt% COF, CdS-COF (90:10) showed a steep hydrogen production of 3678 $\mu\text{mol/h/g}$ which was significantly higher than the bulk CdS particles (124 $\mu\text{mol/h/g}$). The dense π conjugated back bone, high surface area and the heterojunction was correlated with the stabilization of the generated photo electron hole pairs. For the first time, Yu *et al.* reported the use of a thioether-functionalized TTR-COF for photocatalytic hydrogen evolution from seawater.¹⁰³ The thioether functionality showed selective affinity towards Au ions and thus the adsorbed Au ions were beneficial for the separation and migration of the photoexcited electron-hole pairs generated in the COF. Apart from using distilled water, it would be beneficial if water splitting could be achieved in naturally occurring water. Zhang et al. introduced MoS_2 into TpPa-1-COF to synthesize a $\text{MoS}_2/\text{TpPa-1-COF}$ hybrid for improving visible-light driven hydrogen evolution.¹⁰⁴

Graphitic carbon nitride ($\text{g-C}_3\text{N}_4$) has been established as one of the most promising photocatalytic platform for visible-light driven hydrogen evolution. Yan et al. synthesized a COF altered with $\text{g-C}_3\text{N}_4$ to create a composite material, termed as CN-COF, with imine bond linked between the COF and carbon nitride interface.¹⁰⁵ Remarkably, the hybrid composite exhibited a superior HER of 10.1 mmol/g/h. This was attributed to the strong visible-light absorption and the efficient charge separation and migration of the photogenerated electron-hole pairs. Recently, Lan et al. covalently anchored different amounts of $\text{NH}_2\text{-UiO-66}$ onto the surface of TpPa-1-COF to produce a MOF/COF composite.¹⁰⁶ This hybrid material exhibited efficient photocatalytic hydrogen evolution

N₃-COF), which were employed as photocatalysts for photocatalytic reduction of CO₂ to CH₃OH in the presence of H₂O under visible-light irradiation without the use of any additional sacrificial agents. 13.7 $\mu\text{mol/g}$ and 8.6 $\mu\text{mol/g}$ methanol were formed using N₃-COF and ACOF-1 respectively.¹⁰⁹ Theoretical calculations using the density functional theory (DFT) showed that the HOMO and LUMO electronic distributions of N₃-COF are well separated which favored intramolecular charge transfer. Huang et al. worked on a newly designed photoactive triazine-based COF as a photosensitizer and impregnated Re(bpy)(CO)₃Cl as a CO₂ reduction molecular catalyst.¹¹⁰ The Re-COF was then employed for photocatalytic CO₂ reduction, showing $\sim 15 \text{ mmol CO g}^{-1}$ production during 20 h (Figure 2.11). Triethanolamine was used as a sacrificial reducing agent, resulting in a TON of 48, which was 22-times better than its homogeneous counterpart. This increased activity was mainly correlated to the high electron transfer from COFs to Re(bpy)(CO)₃Cl and inhibition of charge recombination in the Re-COF.

In the past few years, other earth-abundant redox valence transition metals, including cobalt and nickel complexes, have been employed for photocatalytic reduction of CO₂ in homogeneous systems.¹¹¹ Zou et al. synthesized pyridine-based COF with Ni single sites (Ni-TpBpy) as a photocatalyst for selective photocatalytic reduction of CO₂ to CO. In this system, electrons are transferred from the photosensitizer to Ni sites for CO evolution under visible-light irradiation.¹¹² The obtained Ni-TpBpym exhibited an activity of 4057 $\mu\text{mol/g}$ of CO production in 5 h with a CO selectivity of 96% over H₂. Also, the photocatalyst showed stable reusability over 3 cycles.

Recently, Lan et al. worked on a series of transition metal ion anchored on COFs (DQTP COF-M, M = Co, Ni, Zn) for photocatalytic CO₂ reduction.¹¹³ Among the obtained materials, DQTP COF-Co and DQTP COF-Zn exhibited the best CO and formic acid evolution rate of 1020 $\mu\text{mol/h/g}$ and 152.5 $\mu\text{mol/h/g}$, respectively. A “two-pathway” mechanism for photocatalytic CO₂ reduction in the COFs was proposed. Selective CO or formic acid production was dependent on the type and confined region around the metal ions. An electron-rich coordination environment weakened and broke the C–O bond and –COOH intermediate to CO was observed. On the other hand, an electron-deficient coordination environment enhanced the C–O bond force to form HCOOH. Following this work, they designed a set of porphyrin–tetrathiafulvalene(TTF)-based COFs (TTCOF-M, M = 2H, Zn, Ni, Cu) for photocatalytic reduction of CO₂ without additional photosensitizers, sacrificial agents and noble metal co-catalysts.¹¹⁴ Among all the obtained TTCOFs, TTCOF-Zn exhibited the highest CO production rate of 2.06

$\mu\text{mol/h/g}$ with 100% selectivity and high recyclability. The proposed mechanism involves photoinduced electron transfer (PET) from the electron-rich TTF unit (HOMO center) to the electron-deficient TAPP unit (LUMO center) after photon absorption from visible light irradiation. Subsequently, the excited electrons move to the catalytically active metallic sites (Zn or Cu in TAPP) and are further used for photocatalytic CO_2 reduction. Simultaneously, the photogenerated holes in TTF oxidize H_2O to O_2 to ensure that the catalytic system gains electrons from H_2O for charge balance.

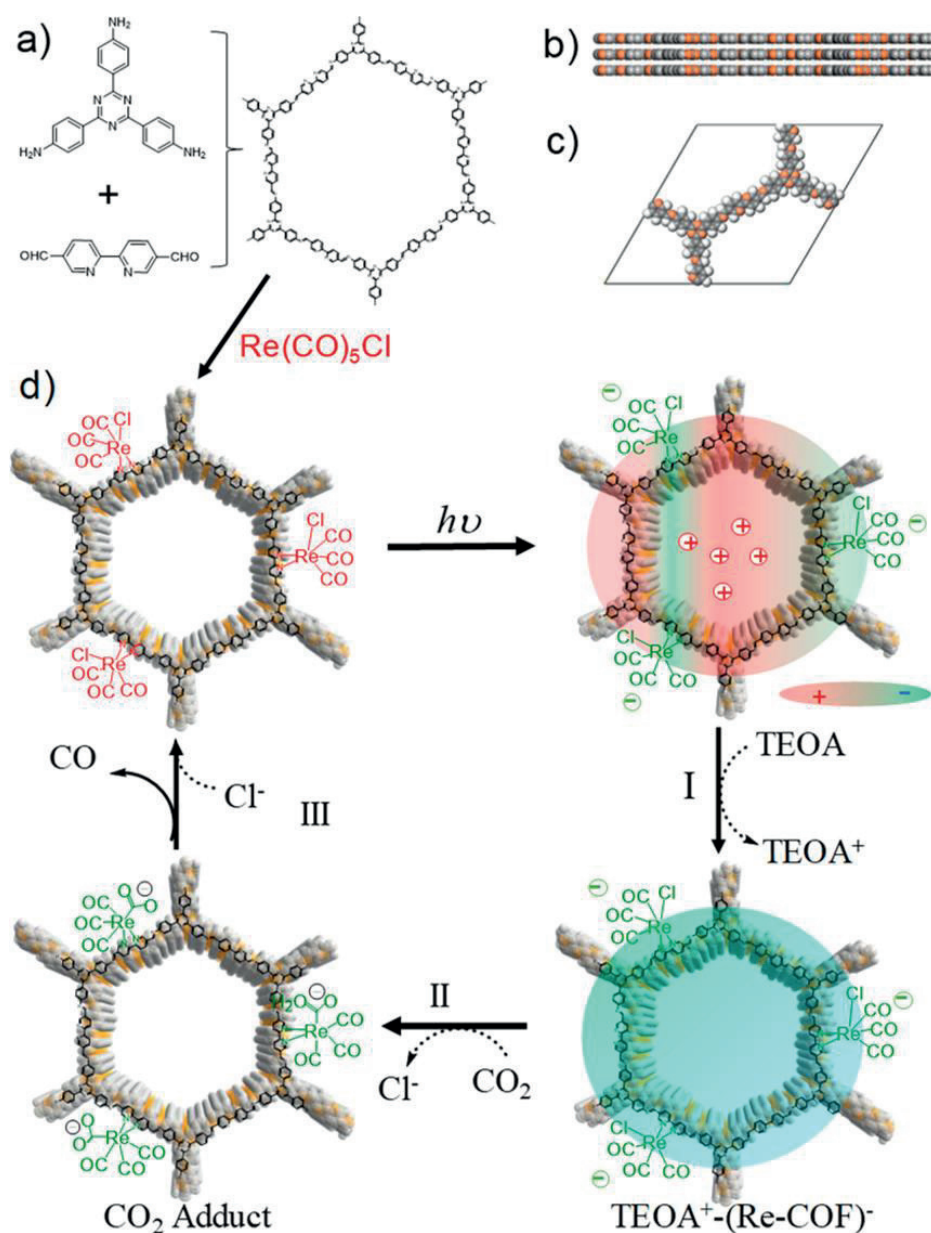


Figure 2. 11. (a) Synthesis of COF and Re-COF. (b) Side View and (c) Unit Cell of AA Stacking COF. (d) Proposed Catalytic Mechanism for CO_2 Reduction.¹¹⁰ Reproduced with permission from American Chemical Society.

2.4. References

- (1) Geng, K.; He, T.; Liu, R.; Dalapati, S.; Tan, K. T.; Li, Z.; Tao, S.; Gong, Y.; Jiang, Q.; Jiang, D. *Chem. Rev.* 2020, 120, 16, 8814–8933.
- (2) H. Furukawa and O. M. Yaghi, *J. Am. Chem. Soc.*, 2009, 131, 8875–8883.
- (3) T. S. Blankenship II, N. Balahmar and R. Mokaya, *Nat. Commun.*, 2017, 8, 1545.
- (4) H. S. Scott, N. Ogiwara, K.-J. Chen, D. G. Madden, T. Pham, K. Forrest, B. Space, S. Horike, J. J. Perry IV, S. Kitagawa and M. J. Zaworotko, *Chem. Sci.*, 2016, 7, 5470–5476.
- (5) <https://www.esrl.noaa.gov/gmd/ccgg/trends/>.
- (6) N. Mac Dowell, P. S. Fennell, N. Shah and G. C. Maitland, *Nat. Clim. Change*, 2017, 7, 243.
- (7) F. Perera, *Int. J. Environ. Res. Public Health*, 2018, 15, 16.
- (8) J. Zheng and S. Suh, *Nat. Clim. Change*, 2019, 9, 374–378.
- (9) S. Chu, Y. Cui and N. Liu, *Nat. Mater.*, 2017, 16, 16.
- (10) M. Bui, C. S. Adjiman, A. Bardow, E. J. Anthony, A. Boston, S. Brown, P. S. Fennell, S. Fuss, A. Galindo, L. A. Hackett, J. P. Hallett, H. J. Herzog, G. Jackson, J. Kemper, S. Krevor, G. C. Maitland, M. Matuszewski, I. S. Metcalfe, C. Petit, G. Puxty, J. Reimer, D. M. Reiner, E. S. Rubin, S. A. Scott, N. Shah, B. Smit, J. P. M. Trusler, P. Webley, J. Wilcox and N. Mac Dowell, *Energy Environ. Sci.*, 2018, 11, 1062–1176.
- (11) R. M. Cuéllar-Franca and A. Azapagic, *J. CO₂ Util.*, 2015, 9, 82–102.
- (12) K. Sumida, D. L. Rogow, J. A. Mason, T. M. McDonald, E. D. Bloch, Z. R. Herm, T.-H. Bae and J. R. Long, *Chem. Rev.*, 2012, 112, 724–781.
- (13) C. A. Trickett, A. Helal, B. A. Al-Maythaly, Z. H. Yamani, K. E. Cordova and O. M. Yaghi, *Nat. Rev. Mater.*, 2017, 2, 17045.
- (14) J. W. To, J. He, J. Mei, R. Haghpanah, Z. Chen, T. Kurosawa, S. Chen, W. G. Bae, L. Pan, J. B. Tok, J. Wilcox and Z. Bao, *J. Am. Chem. Soc.*, 2016, 138, 1001–1009.
- (15) O. Shekhah, Y. Belmabkhout, Z. Chen, V. Guillerm, A. Cairns, K. Adil and M. Eddaoudi, *Nat. Commun.*, 2014, 5, 4228.
- (16) Y. Belmabkhout, V. Guillerm and M. Eddaoudi, *Chem. Eng. J.*, 2016, 296, 386–397.
- (17) S. Hug, L. Stegbauer, H. Oh, M. Hirscher and B. V. Lotsch, *Chem. Mater.*, 2015, 27, 8001–8010.

- (18) K. Wang, H. Huang, D. Liu, C. Wang, J. Li and C. Zhong, *Environ. Sci. Technol.*, 2016, 50, 4869–4876.
- (19) K. Yuan, C. Liu, L. Zong, G. Yu, S. Cheng, J. Wang, Z. Wang and X. Jian, *ACS Appl. Mater. Interfaces*, 2017, 9, 13201–13212.
- (20) X. Zhu, C. Tian, G. M. Veith, C. W. Abney, J. Dehaudt and S. Dai, *J. Am. Chem. Soc.*, 2016, 138, 11497–11500.
- (21) R. Berger, G. Resnati, P. Metrangolo, E. Weber and J. Hulliger, *Chem. Soc. Rev.*, 2011, 40, 3496–3508.
- (22) Z.-Z. Yang, Y. Zhao, H. Zhang, B. Yu, Z. Ma, G. Ji and Z. Liu, *Chem. Commun.*, 2014, 50, 13910–13913.
- (23) Y. Zhao, K. X. Yao, B. Teng, T. Zhang and Y. Han, *Energy Environ. Sci.*, 2013, 6, 3684–3692.
- (24) G. Wang, K. Leus, H. S. Jena, C. Krishnaraj, S. Zhao, H. Depauw, N. Tahir, Y.-Y. Liu and P. Van Der Voort, *J. Mater. Chem. A*, 2018, 6, 6370–6375.
- (25) S. Mukherjee, M. Das, A. Manna, R. Krishna and S. Das, *J. Mater. Chem. A*, 2019, 7, 1055–1068.
- (26) S. Mukherjee, M. Das, A. Manna, R. Krishna and S. Das, *Chem. Mater.*, 2019, 31, 3929–3940.
- (27) Bhunia, I. Boldog, A. Möller and C. Janiak, *J. Mater. Chem. A*, 2013, 1, 14990–14999.
- (28) S. Dey, A. Bhunia, H. Breitzke, P. B. Groszewicz, G. Buntkowsky and C. Janiak, *J. Mater. Chem. A*, 2017, 5, 3609–3620.
- (29) G. Tuci, M. Pilaski, H. Ba, A. Rossin, L. Luconi, S. Caporali, C. Pham-Huu, R. Palkovits and G. Giambastiani, *Adv. Funct. Mater.*, 2017, 27, 1605672.
- (30) G. Wang, K. Leus, S. Zhao and P. Van Der Voort, *ACS Appl. Mater. Interfaces*, 2017, 10, 1244–1249.
- (31) O. Buyukcakil, S. H. Je, S. N. Talapaneni, D. Kim and A. Coskun, *ACS Appl. Mater. Interfaces*, 2017, 9, 7209–7216.
- (32) K. Park, K. Lee, H. Kim, V. Ganesan, K. Cho, S. K. Jeong and S. Yoon, *J. Mater. Chem. A*, 2017, 5, 8576–8582.
- (33) Y. J. Lee, S. N. Talapaneni and A. Coskun, *ACS Appl. Mater. Interfaces*, 2017, 9, 30679–30685.
- (34) S. Kandambeth, A. Mallick, B. Lukose, M. V. Mane, T. Heine, R. Banerjee, *J. Am. Chem. Soc.* 2012, 134, 19524.

- (35) B. P. Biswal, S. Chandra, S. Kandambeth, B. Lukose, T. Heine, R. Banerjee, *J. Am. Chem. Soc.* 2013, 135, 5328.
- (36) S. Chandra, S. Kandambeth, B. P. Biswal, B. Lukose, S. M. Kunjir, M. Chaudhary, R. Babarao, T. Heine, R. Banerjee, *J. Am. Chem. Soc.* 2013, 135, 17853.
- (37) H. Wei, S. Chai, N. Hu, Z. Yang, L. Wei, L. Wang, *Chem. Commun.* 2015, 51, 12178.
- (38) S. Kandambeth, D. B. Shinde, M. K. Panda, B. Lukose, T. Heine, R. Banerjee, *Angew. Chem. Int. Ed.* 2013, 52, 13052.
- (39) Q. Gao, L. Bai, X. Zhang, P. Wang, P. Li, Y. Zeng, R. Zou, Y. Zhao, *Chin. J. Chem.* 2015, 33, 90.
- (40) D. Kaleeswaran, P. Vishnoi, R. Murugavel, *J. Mater. Chem. C* 2015, 3, 7159.
- (41) N. Huang, X. Chen, R. Krishna, D. Jiang, *Angew. Chem. Int. Ed.* 2015, 54, 2986.
- (42) Leffler, W. L. *Petroleum Refining in Nontechnical Language*, 4th ed.; Penwell: Tulsa, 2008.
- (43) Y. He, W. Zhou, G. Qian, B. Chen, *Chem. Soc. Rev.*, 2014, 43, 5657-5678.
- (44) van Miltenburg, W. Zhu, F. Kapteijn, J. A. Moulijn, *Chem. Eng. Res. Des.* 2006, 84, 350.
- (45) Y.-F. He, J.-T. Feng, Y.-Y. Du, D.-Q. Li, *ACS Catal.* 2012, 2, 1703.
- (46) J. Hu, Q. Yang, L. Yang, Z. Zhang, B. Su, Z. Bao, Q. Ren, H. Xing, S. Dai, *ACS Catal.* 2015, 5, 6724.
- (47) Y. Lu, J. He, Y. Chen, H. Wang, Y. Zhao, Y. Han and Y. Ding, *Macromol. Rapid Commun.*, 2018, 39, 1700468.
- (48) P. Passler, W. Hefner, K. Bucki, H. Meinass, A. Meiswinkel, H.-J. Wernicke, G. Ebersberg, R. Müller, J. Bässler, H. Behringer, D. Mayer, *Acetylene. Ullman's Encyclopedia of Industrial Chemistry; Electronic Release; Wiley-VCH: Weinheim*, 2012.
- (49) K. Griesbaum, A. Behr, D. Biedenkapp, H.-W. Voges, D. Garbe, C. Paetz, G. Collin, D. Mayer, H. Höke, *Hydrocarbons. Ullman's Encyclopedia of Industrial Chemistry; Electronic Release; Wiley-VCH: Weinheim*, 2012.
- (50) Z. R. Herm, E. D. Bloch, J. R. Long, *Chem. Mater.* 2014, 26, 323–338.
- (51) C. Copéret, M. Chabanas, R. Petroff Saint-Arroman and J.-M. Basset, *Angew. Chem., Int. Ed.*, 2003, 42, 156–181.
- (52) R. Palkovits, M. Antonietti, P. Kuhn, A. Thomas and F. Schüth, *Angew. Chem., Int. Ed.*, 2009, 48, 6909–6912.

- (53) C. E. Chan-Thaw, A. Villa, P. Katekomol, D. Su, A. Thomas and L. Prati, *Nano Lett.*, 2010, 10, 537–541.
- (54) C. E. Chan-Thaw, A. Villa, D. Wang, V. D. Santo, A. Orbelli Biroli, G. M. Veith, A. Thomas and L. Prati, *ChemCatChem*, 2015, 7, 2149–2154.
- (55) J. Artz and R. Palkovits, *ChemSusChem*, 2015, 8, 3832–3838.
- (56) Q.-Q. Dang, C.-Y. Liu, X.-M. Wang and X.-M. Zhang, *ACS Appl. Mater. Interfaces*, 2018, 10, 27972–27978.
- (57) K. Park, G. H. Gunasekar, N. Prakash, K.-D. Jung and S. Yoon, *ChemSusChem*, 2015, 8, 3410–3413.
- (58) S. Rajendiran, P. Natarajan and S. Yoon, *RSC Adv.*, 2017, 7, 4635–4638.
- (59) N. Tahir, F. Muniz-Miranda, J. Everaert, P. Tack, T. Heugebaert, K. Leus, L. Vincze, C. V. Stevens, V. Van Speybroeck and P. Van Der Voort, *J. Catal.*, 2019, 371, 135–143.
- (60) V. Bavykina, M. G. Goesten, F. Kapteijn, M. Makkee and J. Gascon, *ChemSusChem*, 2015, 8, 809–812.
- (61) G. H. Gunasekar, K. Park, V. Ganesan, K. Lee, N.-K. Kim, K.-D. Jung and S. Yoon, *Chem. Mater.*, 2017, 29, 6740–6748.
- (62) V. Bavykina, E. Rozhko, M. G. Goesten, T. Wezendonk, B. Seoane, F. Kapteijn, M. Makkee and J. Gascon, *ChemCatChem*, 2016, 8, 2217–2221.
- (63) V. Bavykina, A. I. Olivos-Suarez, D. Osadchii, R. Valecha, R. Franz, M. Makkee, F. Kapteijn and J. Gascon, *ACS Appl. Mater. Interfaces*, 2017, 9, 26060–26065.
- (64) S. Y. Ding, J. Gao, Q. Wang, Y. Zhang, W. G. Song, C. Y. Su, W. Wang, *J. Am. Chem. Soc.* 2011, 133 (49), 19816–19822.
- (65) R. S. B. Gonçalves, A.B. V. de Oliveira, H. C. Sindra, B. S. Archanjo, M. E. Mendoza, L. S. A. Carneiro, C. D. Buarque, P. M. Esteves, *ChemCatChem* 2016, 8(4), 743-750.
- (66) J. Zhang, Y. Peng, W. Leng, Y. Gao, F. Xu, J. Chai, *Chinese Journal of Catalysis*, 2016, 37(4), 468-475.
- (67) W. Leng, Y. Peng, J. Zhang, H. Lu, X. Feng, R. Ge, B. Dong, B. Wang, X. Hu, Y. Gao, *Chemistry – A European Journal*, 2016, 22(27), 9087-9091.
- (68) W. Leng, R. Ge, B. Dong, C. Wang, Y. Gao, *RSC Adv.*, 2016, 6, 37403-37406.
- (69) W. P. Schaefer, *Inorg. Chem.* 1965, 4, 5, 642–648.
- (70) H. Vardhan, G. Verma, S. Ramani, A. Nafady, A. M. Al-Enizi, Y. Pan, Z. Yang, H. Yang, S. Ma, *ACS Appl. Mater. Interfaces* 2019, 11, 3, 3070–3079.

- (71) H. Vardhan, L. Hou, E. Yee, A. Nafady, M. A. Al-Abdrabalnabi, A. M. Al-Enizi, Y. Pan, Z. Yang, S. Ma, *ACS Sustainable Chem. Eng.* 2019, 7, 5, 4878–4888.
- (72) V. Balzani, A. Credi and M. Venturi, *Chem. Soc. Rev.*, 2009, 38, 1542–1550.
- (73) Gomes Silva, R. Juárez, T. Marino, R. Molinari and H. García, *J. Am. Chem. Soc.*, 2011, 133, 595–602.
- (74) M. Kaczmarek, Y.-Y. Liu, C. Wang, B. Laforce, L. Vincze, P. Van Der Voort and R. Van Deun, *Dalton Trans.*, 2017, 46, 12717–12723.
- (75) J. Schneider, M. Matsuoka, M. Takeuchi, J. Zhang, Y. Horiuchi, M. Anpo and D. W. Bahnemann, *Chem. Rev.*, 2014, 114, 9919–9986.
- (76) X. Li, S. Cui, D. Wang, Y. Zhou, H. Zhou, Y. Hu, J.-g. Liu, Y. Long, W. Wu, J. Hua and H. Tian, *ChemSusChem*, 2014, 7, 2879–2888.
- (77) C.-P. Lee, R. Y.-Y. Lin, L.-Y. Lin, C.-T. Li, T.-C. Chu, S.-S. Sun, J. T. Lin and K.-C. Ho, *RSC Adv.*, 2015, 5, 23810–23825.
- (78) N. Duvva, U. Chilakamarthi and L. Giribabu, *Sustainable Energy Fuels*, 2017, 1, 678–688.
- (79) X. Wang, S. Goeb, Z. Ji, N. A. Pogulaichenko and F. N. Castellano, *Inorg. Chem.*, 2011, 50, 705–707.
- (80) K. Prier, D. A. Rankic and D. W. C. MacMillan, *Chem. Rev.*, 2013, 113, 5322–5363.
- (81) Fujishima and K. Honda, *Nature*, 1972, 238, 37–38.
- (82) X. Jiang, P. Wang and J. Zhao, *J. Mater. Chem. A*, 2015, 3, 7750–7758.
- (83) K. Sakaushi and M. Antonietti, *Acc. Chem. Res.*, 2015, 48, 1591–1600.
- (84) K. Schwinghammer, S. Hug, M. B. Mesch, J. Senker and B. V. Lotsch, *Energy Environ. Sci.*, 2015, 8, 3345–3353.
- (85) S. Kuecken, A. Acharjya, L. Zhi, M. Schwarze, R. Schomäcker and A. Thomas, *Chem. Commun.*, 2017, 53, 5854–5857.
- (86) J. Bi, W. Fang, L. Li, J. Wang, S. Liang, Y. He, M. Liu and L. Wu, *Macromol. Rapid Commun.*, 2015, 36, 1799–1805.
- (87) Bhunia, D. Esquivel, S. Dey, R. Fernández-Terán, Y. Goto, S. Inagaki, P. Van Der Voort and C. Janiak, *J. Mater. Chem. A*, 2016, 4, 13450–13457.
- (88) B. Meier, R. S. Sprick, A. Monti, P. Guiglion, J.-S. M. Lee, M. A. Zwijnenburg and A. I. Cooper, *Polymer*, 2017, 126, 283–290.
- (89) Parzinger, B. Miller, B. Blaschke, J. A. Garrido, J. W. Ager, A. Holleitner and U. Wurstbauer, *ACS Nano*, 2015, 9, 11302–11309.

- (90) Q. Jiang, L. Sun, J. Bi, S. Liang, L. Li, Y. Yu and L. Wu, *ChemSusChem*, 2018, 11, 1108–1113.
- (91) R. Xu, X.-S. Wang, H. Zhao, H. Lin, Y.-B. Huang and R. Cao, *Catal. Sci. Technol.*, 2018, 8, 2224–2230.
- (92) L. Li, W. Fang, P. Zhang, J. Bi, Y. He, J. Wang and W. Su, *J. Mater. Chem. A*, 2016, 4, 12402–12406.
- (93) Z. Cheng, W. Fang, T. Zhao, S. Fang, J. Bi, S. Liang, L. Li, Y. Yu and L. Wu, *ACS Appl. Mater. Interfaces*, 2018, 10, 41415–41421.
- (94) L. Guo, Y. Niu, H. Xu, Q. Li, S. Razzaque, Q. Huang, S. Jin and B. Tan, *J. Mater. Chem. A*, 2018, 6, 19775–19781.
- (95) K. Wang, L. M. Yang, X. Wang, L. Guo, G. Cheng, C. Zhang, S. Jin, B. Tan and A. Cooper, *Angew. Chem., Int. Ed.*, 2017, 56, 14149–14153.
- (96) W. Huang, J. Byun, I. Rörich, C. Ramanan, P. W. M. Blom, H. Lu, D. Wang, L. Caire da Silva, R. Li, L. Wang, K. Landfester and K. A. I. Zhang, *Angew. Chem., Int. Ed.*, 2018, 57, 8316–8320.
- (97) L. Stegbauer, K. Schwinghammer and B. V. Lotsch, *Chem. Sci.*, 2014, 5, 2789 — 2793.
- (98) V. S. Vyas, F. Haase, L. Stegbauer, G. Savasci, F. Podjaski, C. Ochsenfeld and B. V. Lotsch, *Nat. Commun.*, 2015, 6, 8508.
- (99) J.-L. Sheng, H. Dong, X.-B. Meng, H.-L. Tang, Y.-H. Yao, D.-Q. Liu, L.-L. Bai, F.-M. Zhang, J.-Z. Wei and X.-J. Sun, *ChemCatChem*, 2019, 11, 2313 — 2319.
- (100) T. Banerjee and B. V. Lotsch, *Nat. Chem.*, 2018, 10, 1175 — 1177.
- (101) P. Pachfule, A. Acharjya, J. Roeser, T. Langenhahn, M. Schwarze, R. Schomäcker, A. Thomas and J. Schmidt, *J. Am. Chem. Soc.*, 2018, 140, 1423 — 1427.
- (102) J. Thote, H. B. Aiyappa, A. Deshpande, D. DíazDíaz, S. Kurungot and R. Banerjee, *Chem.–Eur. J.*, 2014, 20, 15961 — 15965.
- (103) L. Y. Li, Z. M. Zhou, L. Y. Li, Z. Y. Zhuang, J. H. Bi, J. H. Chen, Y. Yu and J. G. Yu, *ACS Sustainable Chem. Eng.*, 2019, 7, 18574 — 18581.
- (104) M.-Y. Gao, C.-C. Li, H.-L. Tang, X.-J. Sun, H. Dong and F.-M. Zhang, *J. Mater. Chem. A*, 2019, 7, 20193 — 20200.
- (105) M. Luo, Q. Yang, K. Liu, H. Cao and H. Yan, *Chem. Commun.*, 2019, 55, 5829 — 5832.
- (106) F.-M. Zhang, J.-L. Sheng, Z.-D. Yang, X.-J. Sun, H.-L. Tang, M. Lu, H. Dong, F.-C. Shen, J. Liu and Y.-Q. Lan, *Angew. Chem., Int. Ed.*, 2018, 57, 12106 — 12110.

- (107) T. Banerjee, F. Haase, G. Savasci, K. Gottschling, C. Ochsenfeld and B. V. Lotsch, *J. Am. Chem. Soc.*, 2017, 139, 16228 —16234.
- (108) B. P. Biswal, H. A. Vignolo-González, T. Banerjee, L. Grunenberg, G. Savasci, K. Gottschling, J. Nuss, C. Ochsenfeld and B. V. Lotsch, *J. Am. Chem. Soc.*, 2019, 141, 11082 —11092.
- (109) Y. Fu, X. Zhu, L. Huang, X. Zhang, F. Zhang and W. Zhu, *Appl. Catal., B*, 2018, 239, 46 —51.
- (110) S. Yang, W. Hu, X. Zhang, P. He, B. Pattengale, C. Liu, M. Cendejas, I. Hermans, X. Zhang, J. Zhang and J. Huang, *J. Am. Chem. Soc.*, 2018, 140, 14614 —14618.
- (111) Wang *ChemSusChem*, 2017, 10, 4393 —4402.
- (112) W. Zhong, R. Sa, L. Li, Y. He, L. Li, J. Bi, Z. Zhuang, Y. Yu and Z. Zou, *J. Am. Chem. Soc.*, 2019, 141, 7615 —7621.
- (113) M. Lu, Q. Li, J. Liu, F.-M. Zhang, L. Zhang, J.-L. Wang, Z.-H. Kang and Y.-Q. Lan, *Appl. Catal., B*, 2019, 254, 624 —633.
- (114) M. Lu, J. Liu, Q. Li, M. Zhang, M. Liu, J. L. Wang, D. Q. Yuan and Y. Q. Lan, *Angew. Chem., Int. Ed.*, 2019, 58, 12392 —12397.
- (115) Y. Song, Q. Sun, B. Aguila, S. Ma, *Advanced Science*, 2018, 6(2), 1801410.
- (116) R.-G. Lin, L. Libo, R.-B. Lin, H. Arman, B. Chen, *CrystEngComm*, 2017, 19, 6896-6901.
- (117) H.-P. Li, S.-N. Li, H.-M. Sun, M.-C. Hu, Y.-C. Jiang, Q.-G. Zhai, *Cryst. Growth Des.*, 2018, 18, 3229-3235.
- (118) J. Wang, R. Krishna, T. Yang, S. Deng, *J. Mater. Chem. A*, 2016, 4, 13957-13966.
- (119) M. C. Das, H. Xu, S. Xiang, Z. Zhang, H. D. Arman, G. Qian, B. Chen, *Chemistry-A European Journal*, 2011, 14, 7817-7822.
- (120) X. Duan, Q. Zhang, J. Cai, Y. Cui, C. Wu, Y. Yang, G. Qian, *Microporous and mesoporous materials*, 2014, 190, 32-37.
- (121) Y. He, C. Song, Y. Ling, C. Wu, R. Krishna, B. Chen, *APL Materials*, 2014, 2, 124102.
- (122) X.-X. Zhang, P. Xiao, C.-H. Zhan, B. Liu, R.-Q. Zhong, L.-Y. Yang, C.-Y. Sun, H. Liu, Y. Pan, G.-J. Chen, N. Li, *Ind. Eng. Chem. Res.*, 2015, 54, 43, 7890-7898.
- (123) Y. Pan, C. Jia, B. Liu, Z. Zhang, X. Tong, H. Li, Z. Li, R. Ssebadduka, C. Sun, L. Yang, G. Chen, *Fluid Phase Equilibria*, 2016, 414, 14-22.
- (124) T.-U. Yoon, S. B. Baek, D. Kim, E.-J. Kim, W.-G. Lee, B. K. Sing, M. S. Lah, Y.-S. Bae, K. S. Kim, *Chem. Commun.*, 2018, 54, 9360-9363.

- (125) H. Xu, Y. He, Z. Zhang, S. Xiang, J. Cai, Y. Cui, Y. Yang, G. Qian, B. Chen, J. Mater. Chem. A, 2013, 1, 77-81.
- (126) Z. Zhang, S. Xiang, X. Rao, Q. Zheng, F. R. Fronczek, G. Qian, B. Chen, Chem. Commun., 2010, 46, 7205-7207.

2.5. Objectives of thesis

The field of Covalent Triazine Frameworks and Covalent Organic Frameworks has seen a rapid development in the recent years, but still can be considered to be at its infancy due to the available potential which is not yet explored. Particularly from the perspective of energy and environmental applications these advanced materials show huge promise. In this thesis the focus is on development of novel CTFs and COFs for application in gas storage, separation, and heterogeneous catalysis (metal based and photocatalysis). Detailed attention is given towards the synthesis and characterization of these materials as these are essential in understanding the role of chemical functionalities and structure of these porous materials for the corresponding application. Compared to traditional gas adsorbents such as activated carbons, zeolites, and MOFs, both CTFs and COFs can be advantageous as there is a molecular control over the incorporated functionalities and in addition, they are metal-free.

For gas storage and separation, the first strategy is to increase the polar functionalities in the material to increase adsorbate-adsorbent interactions. For this, nitrogen and oxygen containing building blocks are ideal as they are polar in nature and have been utilized in other porous materials for improving gas separation selectivity (e.g., CO₂/N₂). The second strategy is to optimize the pore volume and surface area to influence the kinetic parameters of the gas storage and separation. The building block size, synthesis temperature and catalyst content can be varied to tune the material to the desired structural properties.

The second part of applications using the CTFs and COFs are classified as heterogeneous catalysis. These materials can be used either as catalyst supports or as catalysts themselves. To act as catalyst supports, the materials must have strong chelating ligands to stabilize homogeneous catalytic complexes. Moreover, the materials must also be sufficiently porous (large surface areas, pore volumes) to allow substrate diffusion. In CTFs, nitrogen containing building blocks have been widely explored as catalytic

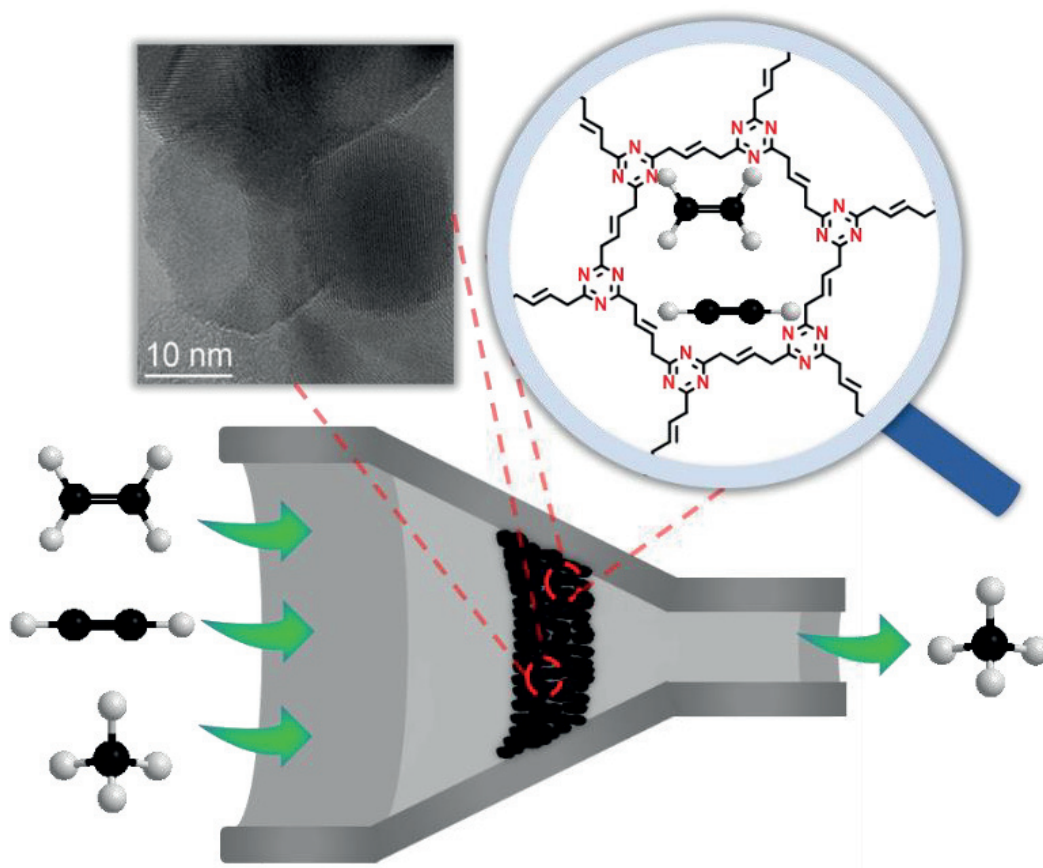
supports for metal complexes. Hence, the target in this thesis is to find new building blocks for coordinating metal complexes.

Apart from being catalytic supports, COFs and CTFs can also be used as organocatalysts due to the presence of catalytic active sites. CTFs made using ionothermal synthesis contain several defective nitrogen sites which have been previously found in N-doped activated carbons and N-doped graphene. Such sites have shown promising catalytic activity for oxidation reactions. Hence, the use of CTFs in such reactions have been explored in this thesis.

COFs are synthesized using a milder condition and do not get carbonized. Hence, they most often retain the photoactivity even after formation of longer networks. Upon light irradiation, certain COFs can generate charge carriers (electron-hole pairs). Especially, the formation of conjugated COFs can be useful for charge transfer and separation. The separated photoelectrons can be used for reduction reactions and the separated photoholes can be used for oxidation reactions. Several COFs have been shown to be photocatalytically active for reactions such as hydrogen evolution, CO₂ reduction, and oxidative hydroxylation. In this thesis, we extend this rapidly developing field by incorporating novel functionalities into the COF structure to perform photoreduction reactions.

Finally, in chapter 7, the most important results obtained in this thesis are highlighted and discussed. A general outlook about COFs and CTFs is provided, including perspectives on designing novel structures, especially for the purpose of environmental applications. Suggestions over translating these fundamental studies towards practical and realistic applications are provided.

3 AN ALIPHATIC HEXENE-CTF FOR SELECTIVE C₂/C₁ GAS SEPARATION



The results of this chapter were published in:

C Krishnaraj, HS Jena, K Leus, HM Freeman, LG Benning, P Van Der Voort. An aliphatic hexene-covalent triazine framework for selective acetylene/methane and ethylene/methane separation. **Journal of Materials Chemistry A** 7 (21), 2019, 13188-13196.

Abstract

In this chapter, a novel hexene-covalent triazine framework (Hexene-CTF) was prepared from trans-3-Hexenedinitrile (an aliphatic olefin type monomer) for high-performance acetylene/methane and ethylene/methane separation. The porosity, surface area, and ordering of the materials were varied by changing the synthesis conditions. The materials were characterized thoroughly by surface area analysis as well as transmission and scanning electron microscopy (TEM and SEM) measurements. The number of double bonds present within the CTF materials was determined by a bromine addition reaction. A high uptake of acetylene (3.85 mmol/g at 0°C and 1 bar) was obtained. The presence of unsaturated double bonds in the Hexene-CTF enhanced the interaction of the framework with the unsaturated double bond and triple bond of ethylene and acetylene respectively due to stronger π - π interactions. On the contrary, the saturated methane gas was not efficiently adsorbed, which resulted in a higher C₂/C₁ selectivity. The calculated isosteric heat of adsorption showed a direct correlation between the gas uptake and the ordering in the Hexene-CTF at low pressure regimes. This is the first example of a porous organic polymer which is capable of C₂/C₁ hydrocarbon separation.

3.1. Introduction

C2 hydrocarbons such as acetylene (C_2H_2) and ethylene (C_2H_4) are important raw materials in the petrochemical industries.¹ C_2H_2 gas is used worldwide for several applications including portable blowtorch², processing polymeric films³, and synthesis of Vitamin A.⁴ It is produced by cracking of petroleum^{5,6} and generally contains methane (CH_4) as a C1 hydrocarbon by-product.^{5,6} C_2H_4 is another important raw material for several consumer products such as polyethylene, ethylene oxide, ethylene dichloride and ethylbenzene.⁷ It is produced through industrial-scale steam cracking of gaseous (ethane, propane, or butane) or liquid feedstocks (naphtha), where larger hydrocarbons are broken to smaller ones and unsaturation is introduced.^{8,9} However, several side products such as methane, propene, raw pyrolysis gasoline (RPG), hydrogen, and buta-1,3-diene are also produced. Particularly, with propane or a naphtha feedstock, a 2:3 or 1:2 ratio of methane:ethylene is produced respectively.^{8,9} Conventionally a cryogenic distillation method is used for such small C2/C1 hydrocarbon separation which is based on the difference in boiling points or vapor pressures.^{10,11} Consequently, these processes consume a lot of energy and there is a constant search to develop new methods for olefin/paraffin separation.¹² Alternatively, microporous adsorbents¹³ which can (i) selectively separate acetylene and ethylene from methane at room temperature and, (ii) are energy and cost-effective can be used.

Several microporous adsorbents have been used for such C2/C1 separation. In particular, Metal-Organic Frameworks (MOFs) have been studied for acetylene/methane separation. MOFs contain metal ions or metal clusters that are connected by rigid organic linkers to form an extended framework.¹⁴ Among the MOF based adsorbents, the FJ1-H8 material has been reported to exhibit the highest gravimetric acetylene uptake of 9.46 mmol/g at 22°C and 1 atm.¹⁵ Cu-TDPAT also shows high acetylene uptake of 7.5 mmol/g at 22°C and 1 atm with good selectivity over CH_4 (127.1).¹⁶ Additionally, ZJU-198a material was reported to have a very high C_2H_2/CH_4 selectivity of 497.9 and 391.1 at 0°C and 25°C respectively.¹⁷ However, for the latter material, in comparison to other MOFs, the acetylene uptake was rather moderate (~3.78 mmol/g at 296 K and 1 atm). In the case of ethylene/methane separation, an adsorption-hydration method was employed by Zhang et al. (2015) in a wet ZIF-8 material as a strategy to separate C_2H_4/CH_4 gas mixtures where the highest selectivity obtained was 5.56.¹⁸ More recently, a ZIF-67/water-ethylene glycol slurry was used by Pan et al. (2016) to recover C_2H_4 from C_2H_4/CH_4 mixtures.¹⁹ The

selectivity coefficients at 10°C for ethylene glycol, water, and solid ZIF-67 were 3.7, 4.7, and 3.1 respectively. This was increased to 6.3 using ZIF-67/water-ethylene glycol slurry through the absorption-adsorption hybrid method, yet the selectivity coefficient at room temperature was only 3.6. In general, MOFs display high gas uptakes and selectivities due to the presence of the metal in the framework, which exhibits a strong interaction with the adsorbed gas molecules.^{20,21} However, the upscaling of such functionalized MOFs is expensive as it depends on specially functionalized or complex organic and metallic components. MOFs also require toxic chemicals like dimethyl formamide (DMF) for synthesis.^{22,23} In addition, most well-known MOFs tend to be sensitive to atmospheric conditions.²⁴ As gas separation applications often occur under harsh conditions (for example: flue gas separation)²⁵ usage of specialized MOFs is not preferred due to stability problems.

Recently, Covalent Organic Frameworks (COFs) have been used for various gas adsorption and storage applications.^{26,27} These light-weight alternative materials follow reticular construction principles that allow prediction of the structure beforehand. This enables tunable pore size and functionalities of the porous materials with strong covalent bonds that keep the materials both mechanically and chemically stable. Among COFs, particularly, Covalent Triazine Frameworks (CTFs) are widely studied materials for applications in gas adsorption and storage, catalysis, and chromatography.²⁸ In general, they are prepared through an ionothermal synthesis route using the trimerization of dinitrile monomers to form triazine rings.²⁹ A careful selection of monomers allows us to design any desired functionalities into the backbone of the framework. Several CTFs have been used for selective adsorption of CO₂ and CH₄.³⁰ However, the adsorption of acetylene and ethylene has only been reported using CTF-PO7131 that was synthesized from the Pigment Orange 71. The acetylene/ethylene separation was attributed to the pyrrolo-pyrrole aromatic unit in the framework. Due to the advantage of high surface area, porosity, and control over the functionality, CTFs provide a good platform for olefin adsorption. In addition, CTFs are highly stable both thermally and chemically.^{31,32}

Two dimensional CTFs are made using rigid aromatic units to provide stability and good π - π interaction for stacking into sheets.³⁴ Unsaturated aliphatic linkers could also provide good π - π interactions for the extended framework formation. However, the potential of such linkers to form COF structures has not been explored in detail. Ethylene dimer (C₂H₂)₂ has large dispersion energy,³⁵ which can be utilized in a CTF structure. Additionally, the formation of triazine rings can provide extra support to form stable

structures.³⁶ Recently, FUM-CTF was reported to selectively adsorb CO₂ because of the presence of ultramicropores and high nitrogen content.³⁰ The FUM-CTF material, which exhibited a high thermal and chemical stability, was made using fumaronitrile (aliphatic linker) as the monomer. Here, we propose the strategical design of a novel CTF (Hexene-CTF) using trans-3-hexenedinitrile as the monomer. The scope of this work is to obtain an olefin functionalized CTF that can selectively adsorb acetylene and ethylene over methane and provide enough stability for the framework formation. The additional benefits of a robust structure and higher nitrogen content allows olefin functionalized CTFs to be a good choice for selective acetylene and ethylene adsorption. Moreover, the commercial availability and cheap cost of the monomers allows an inexpensive alternative for the synthesis of a C₂H₂ and C₂H₄ selective microporous adsorbent.

3.2. Results and discussion

3.2.1. Synthesis and Characterization of Hexene-CTFs

The preparation of Hexene-CTF was carried out using the ionothermal synthesis approach in which trans-3-Hexenedinitrile was mixed with ZnCl₂ in quartz ampoules at different temperatures and different monomer to ZnCl₂ ratios (see the detailed procedure in the section 3.4). A continuous reversible trimerization of the nitrile groups occurs in the presence of molten ZnCl₂ at high temperatures which serves as a Lewis acid catalyst and as a solvent. An additional increase in temperature causes the reorganization of the trimerized moieties into an extended framework which in principle is thermodynamically stable at the highest synthesis temperature.^{29,32} A series of Hexene-CTF materials (scheme 3.1) was synthesized by varying the temperature (400°C and 500°C) and the molar ratio of the linker to ZnCl₂ (1:1, 1:5 and 1:10). In the following, the resulting polymers are named as Hexene-CTF_x_y, where x = synthesis temperature and y = ZnCl₂ molar equivalents. The products were obtained as black monoliths which were crushed into powders for efficient cleaning using distilled water, 1M HCl (reflux) and tetrahydrofuran (THF). Thereafter, the materials were activated at 120°C under vacuum overnight prior to further analysis. The obtained yields were always >80%.

Scheme 3.1. Idealized representation of the formation of Hexene-CTF through the trimerization of trans-3-hexenedinitrile.

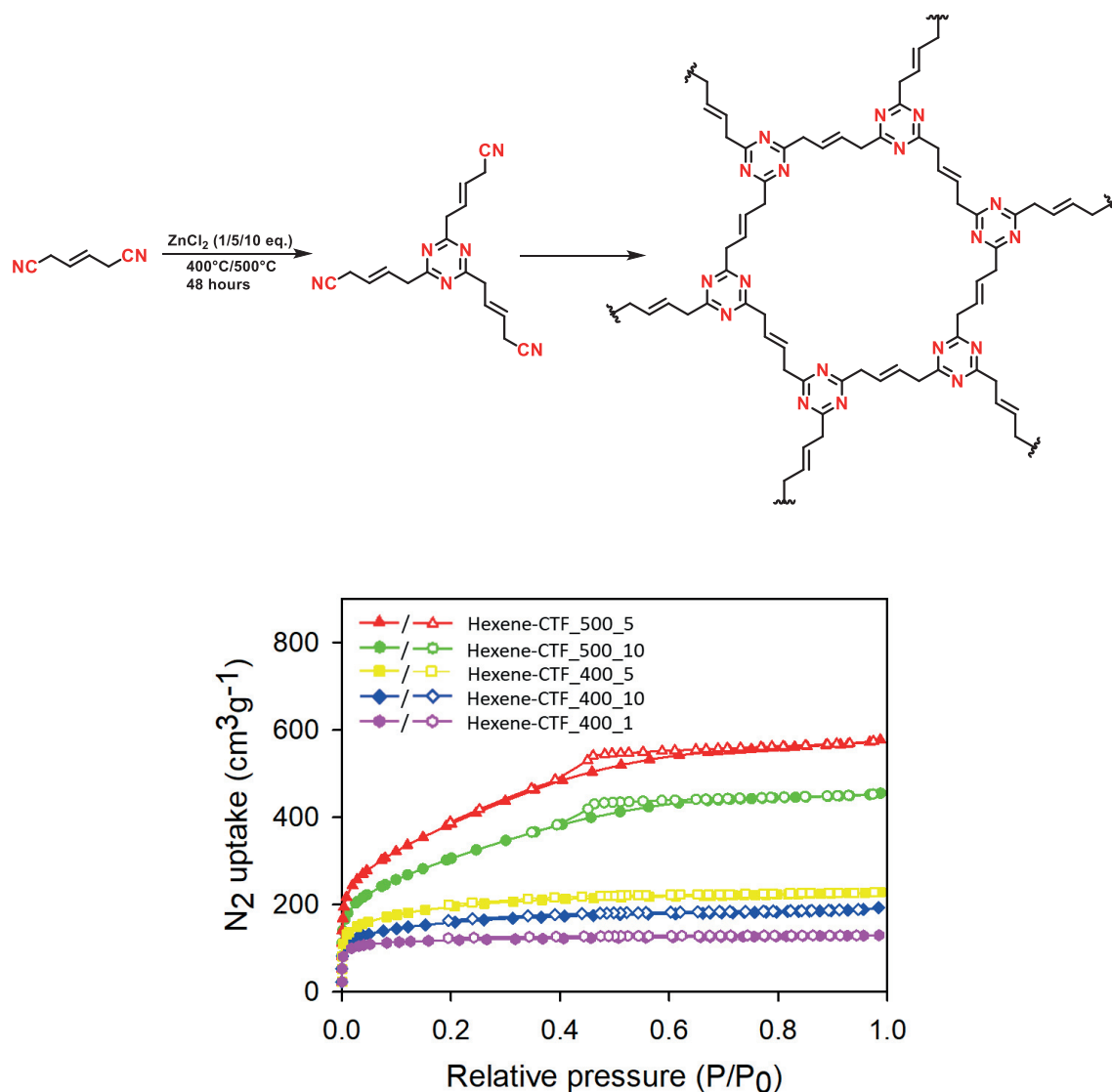


Figure 3. 1. N₂ adsorption (closed symbols) and desorption (open symbols) isotherms of all Hexene-CTFs obtained at 77K.

The N₂ adsorption-desorption (Figure 3.1) isotherms of all the Hexene-CTF materials represent a Type I isotherm, which is typical for microporous materials and is a common feature of several CTFs.^{37,38,39} Materials synthesized at 400°C are purely microporous. However, at higher synthesis temperatures (500°C), a hysteresis was observed which indicates the presence of mesoporosity. This is a common phenomenon observed in CTFs, where higher temperatures cause corrosive fragmentation of the walls on top of the micropores due to thermal decomposition.³² This results in the conversion of some of the micropores into mesopores (Figure S3.1). Table S3.1 lists the surface area and porosity characteristics of the produced Hexene-CTF series. The obtained surface areas were

proportional to the synthesis temperatures. The monomer to ZnCl_2 ratio of 1:5 resulted in a higher surface area at both 400°C and 500°C. Increasing the ZnCl_2 up to 10 eq. reduced the surface area and increased the amorphous content. In addition, the elemental analysis results (Table S3.2) correspond well to the N_2 uptake isotherms showing higher surface area in the materials synthesized at higher temperatures. The increase in the carbon content at higher synthesis temperature is caused by the C-C bond carbonization and C-H bond activation with H_2 evolution causing thermal decomposition of the materials.⁴⁰ Additionally, a decrease in the nitrogen content was observed at higher synthesis temperature due to the homolytic cleavage of -CN as previously reported for other CTFs.^{28,29,32,40} For a particular synthesis temperature, the dependence of the carbon content on the monomer to ZnCl_2 ratio also corresponded to their surface areas, with higher C contents being associated with lower surface areas. The successful trimerization of the nitrile groups was confirmed through Fourier transform infra-red (FTIR) analysis (Figure 3.2) as evidenced by the typical triazine peaks around 1360 cm^{-1} and 1550 cm^{-1} .^{41,42} Additionally, the FTIR spectra of the monomer does not contain these peaks suggesting that the framework consisted of triazine rings in all the materials. Furthermore, the -CN peak at 2226 cm^{-1} was completely attenuated corresponding to the absence of monomeric impurities and ensuring the complete conversion into triazine units.⁴³

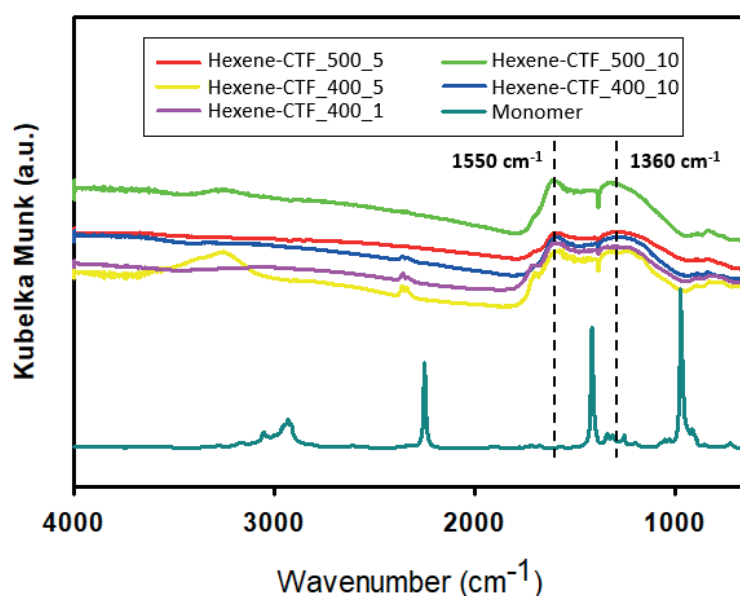


Figure 3. 2. FT-IR spectra of all the Hexene-CTFs and the trans-3-hexenedinitrile monomer.

3.2.2. Structural and morphological analysis

Powder X-ray diffraction (PXRD) measurements were performed to characterize the materials' phase and nature. All the CTFs showed characteristics of amorphous materials with a broad diffraction band at $2\theta = 26^\circ$, which can be assigned to a two-dimensional sheet stacking (Figure S3.2). This is a common feature observed in CTFs where due to the harsh synthesis conditions, the materials are mostly amorphous.^{40,41,42} Interestingly, the diffraction for the Hexene-CTF_400_10 is broader whereas for the Hexene-CTF_400_1 it is relatively sharper and more intense. This indicates that the higher ZnCl₂ content increases the amorphous nature. Previously, it was observed that a 1:1 ratio of monomer:ZnCl₂ was optimal for complete trimerization, but when the ZnCl₂ content was increased, an enhanced surface area was observed.³² However, we noticed that there is a kind of trade-off between the order and the surface area of the material.

To explore this in more detail, TEM was used. In general, for all the Hexene-CTF materials several clusters displaying layered crystalline features dispersed amongst a larger amorphous region were seen (Figure 3.3). The clusters can be correlated to the hexagonal stacking of the 2D sheets. As expected, a higher number of crystalline clusters were observed for the Hexene-CTF_400_1 in comparison to Hexene-CTF_400_10 (Figure 3.4 and Figure S3.4). This is linked to the lower ZnCl₂ content that likely reduced nucleation and hence during growth led to fewer defects in the framework. The plane spacing showed an average of 0.34 nm for Hexene-CTF_400_1 and 0.35 nm for Hexene-CTF_400_10 corresponding to the broad PXRD peak around $2\theta = 26^\circ$. However, we also noticed several regions with a plane spacing of ~ 0.25 nm (Figure S3.5). This is likely due to the flexible nature of the aliphatic monomer causing distortion in the structure at high synthesis temperatures. Furthermore, a lower synthesis temperature ensured fewer carbonization defects, whereas at 500°C, the Hexene-CTF_500_10 exhibited a spaghetti-like network of lattice fringes within an amorphous bulk (Figure 3.4c and Figure S3.4c). Additionally, electron energy loss spectroscopy (EELS) measurements of the carbon K-edge of the materials confirmed the presence of a majority amorphous bulk. Furthermore, zinc was not detectable in the materials through TEM-EDX (Energy Dispersive X-ray spectroscopy) measurements (Figure S3.6). To study the influence of the synthesis temperature on the morphology of the materials, SEM measurements were collected (Figure S3.4). The average particle size is largest for Hexene-CTF_400_1, which has been shown to contain more crystalline clusters compared to other Hexene-CTFs made at higher temperatures and higher ZnCl₂ equivalents. For the higher synthesis temperature

(Hexene-CTF_500_10), the average particle size decreases, which can be related to the increase in amorphous characteristics caused by defects at higher synthesis temperatures. This matches the trends in the surface area measurements, PXRD patterns, and TEM analysis.

Bromine addition is a common technique used to estimate the degree of olefin unsaturation. Bromine gas is highly reactive towards the double bonds and forms C-Br bond easily. From the quantified increase in the mass of the CTF after the bromination one can easily estimate the total number of accessible double bonds in the CTF material. For an ideal structure having no defects, the total bromine content should be 1.51 g/g. For the Hexene-CTF_400_10 only 3.91 mmol/g or 0.62 g/g bromine reacted, which means that only 41% of the double bonds are accessible after the CTF formation (Table S3.2). This is probably due to the harsh synthetic conditions in which partial carbonization occurs. Overall, the degree of unsaturation follows the order: Hexene-CTF_400_1 (46%) > Hexene-CTF_400_5 (44%) > Hexene-CTF_400_10 (41%) > Hexene-CTF_500_5 (39.7%) > Hexene-CTF_500_10 (39%). The elemental analysis results and bromine number details are given in Table S3.2. For comparing the carbonization in all the materials with the ideal theoretical material, C/N ratio is calculated. The theoretical C/N ratio of an ideal material is 2.57. Generally, the higher the C/N ratio, the higher the degree of carbonization. There is a significant decrease in the nitrogen content during the material synthesis, which can also be compared with the loss of double bonds calculated from bromination results (Table S3.2). From the table, it is quite clear that the degree of carbonization increases with an increase in temperature and amount of ZnCl₂, which is a common phenomenon in all CTF materials. The degree of carbonization was calculated using the elemental analysis using the following general formula to compensate for the residue formed (Equation S3.1). In the ¹³C CP-MAS NMR spectra, for both Hexene-CTF_400_5 and Br-Hexene-CTF_400_5, only a broad peak at 100-155 ppm was observed due to carbonization (Figure S3.3). The broad peak includes both set of sp³ and triazine C. However, Hexene-CTF_400_5 showed a small hump (A) at 147 ppm which corresponds to the sp² carbon ethylene bridge. As expected, this does not appear for the brominated (Br-Hexene-CTF_400_5) where all the sp² carbon is converted to sp³ carbon by bromine addition.

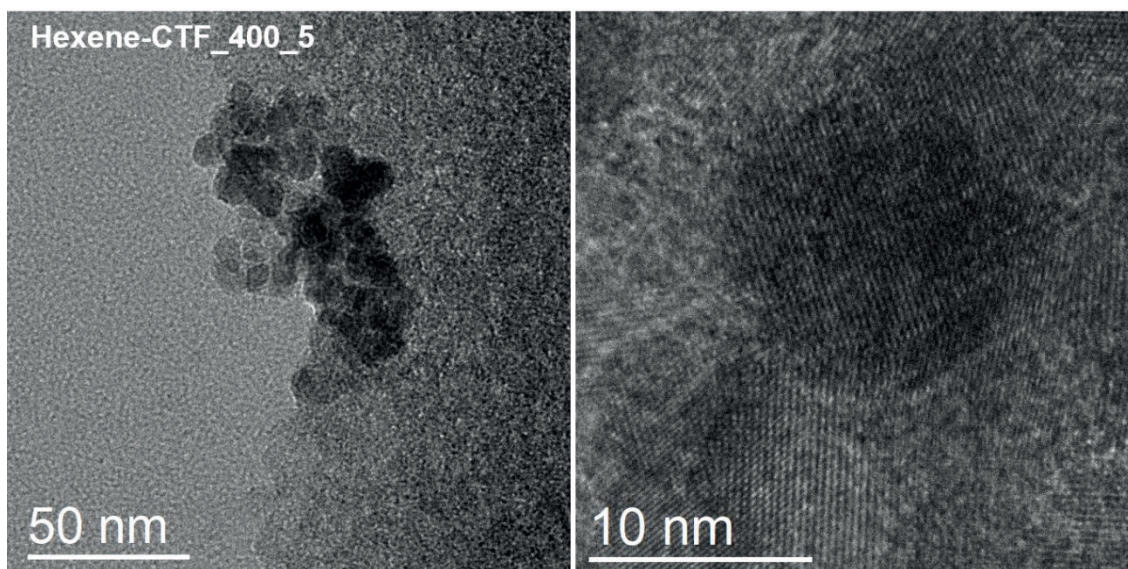


Figure 3. 3. TEM image of Hexene-CTF_400_5 showing crystalline patches in amorphous bulk region.

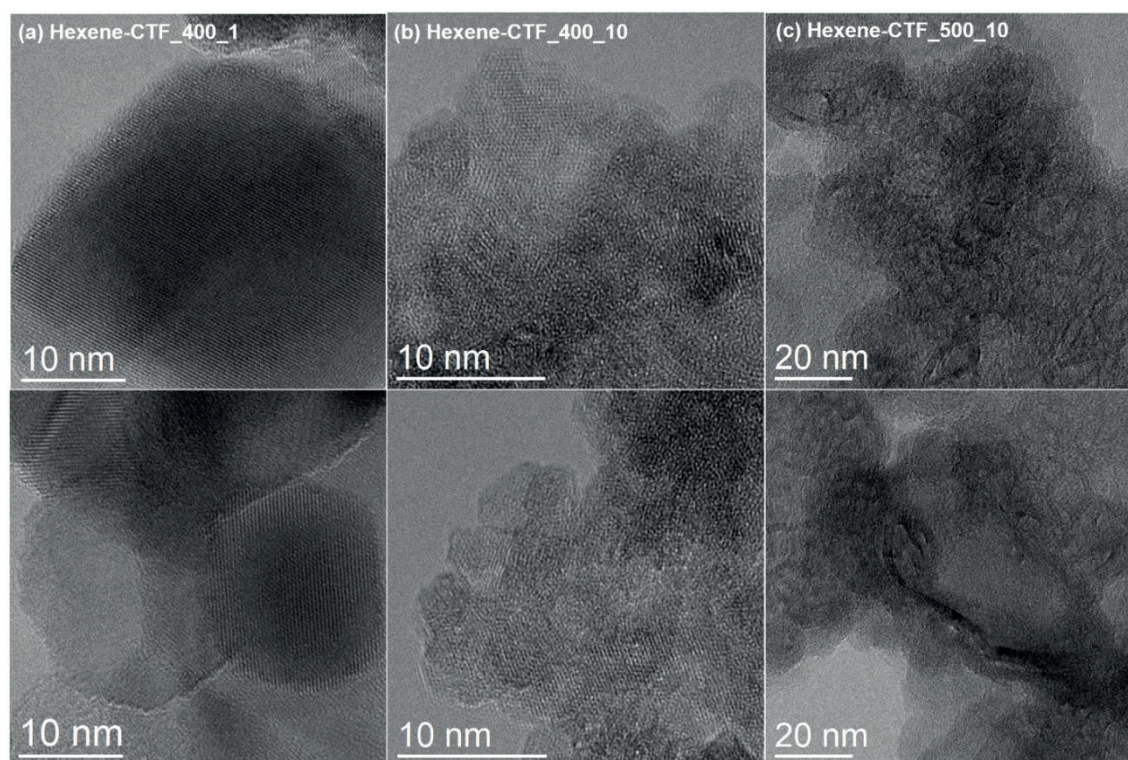


Figure 3. 4. TEM images revealing the different structural arrangements of a) Hexene-CTF_400_1, b) Hexene-CTF_400_10 and c) Hexene-CTF_500_10.

The physicochemical stability of the Hexene-CTFs as studied by thermogravimetric analysis (TGA) under dynamic N₂ flow revealed that all the CTFs high thermal stabilities from 425°C to 500°C after which they started to decompose (Figure S3.7). The materials are insoluble in common organic solvents such as acetone, methanol, ethanol,

dichloromethane, tetrahydrofuran, dimethylformamide, dimethyl sulfoxide, diethyl ether, and chloroform. In addition, the stability of the Hexene-CTF_500_5 was tested in boiling water for 3 days. The N₂ adsorption measurement after this treatment showed that the porosity of the material was retained (Figure S3.8).

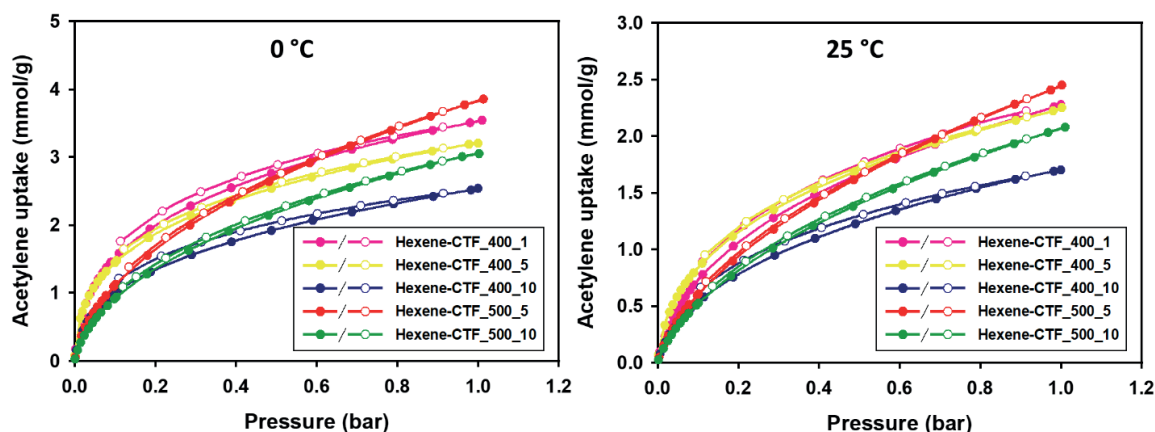


Figure 3. 5. Acetylene adsorption (closed symbols) and desorption (open symbols) isotherms of all Hexene-CTFs obtained at 0°C and 25°C.

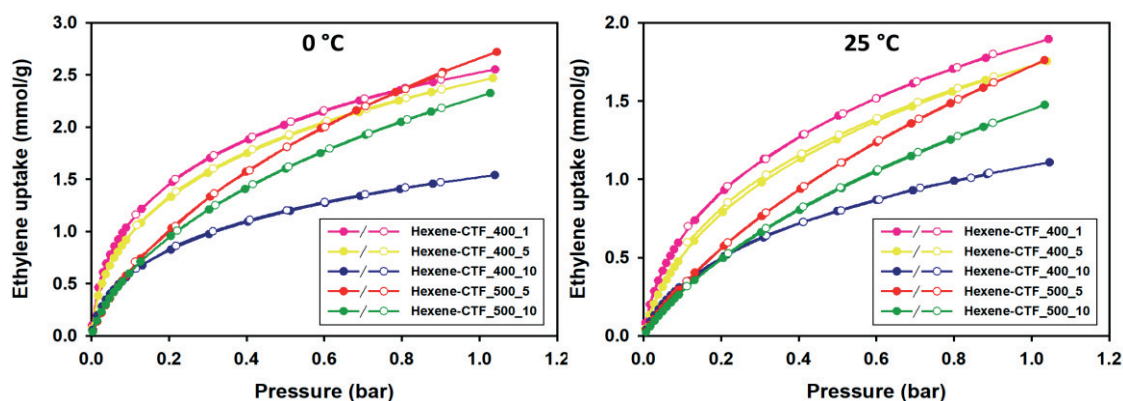


Figure 3. 6. Ethylene adsorption (closed symbols) and desorption (open symbols) isotherms of all Hexene-CTFs obtained at 0°C and 25°C.

3.2.3. Selective olefin adsorption

We studied the targeted adsorption of C₂H₂ and C₂H₄ on the Hexene-CTFs by utilizing the presence of inherent olefin functionalities in the CTFs (Table S3.4, Figures 3.5 and 3.6). The highest C₂H₂ uptake of 3.85 mmol/g was obtained using the Hexene-CTF_500_5 at 0°C and 1 bar. The second highest C₂H₂ uptake was 3.54 mmol/g using Hexene-CTF-400_1 at 0°C and 1 bar. Even though the surface area of Hexene-CTF_400_1 is much lower than Hexene-CTF_500_5, the C₂H₂ uptake is quite close. This

can be attributed to the higher ordering in Hexene-CTF_400_1, resulting in an enhanced interaction of the C_2H_2 gas molecules with the framework. Particularly, in the lower pressure regime, where the adsorption is dominated by the interaction between the chemical moieties rather than the physical adsorption alone, the Hexene-CTFs synthesized at 400°C outperforms the Hexene-CTFs synthesized at 500°C. This is also can be corroborated by the degree of unsaturation retained in the CTFs as a function of temperature. Hexene-CTF_400_1 retained 46% of the double bonds (estimated by the bromine number, Table S3.2), after the harsh synthesis conditions, which is a higher content compared to Hexene-CTF_500_5 (39.7% double bonds) in which more carbonization occurs. The same trend is also observed for the C_2H_4 adsorption for which Hexene-CTF_400_1 exhibits a higher C_2H_4 uptake in the low-pressure regime in comparison to Hexene-CTF_500_5. The unsaturated gases and the olefin functionalities present within the CTF framework exhibit π - π interactions which results in a higher C2 gas uptake compared to C1 gas. We cannot rule out the partial contribution of other physisorption based interactions during the gas uptake in these materials. However, the variation in the ordering of the materials and the resulting olefin gas uptake values prove that the π - π interaction between C_2H_2/C_2H_4 molecules and the alkene functionality of Hexene-CTF is a more dominant factor than others. To prove the role of the double bonds in the gas adsorption, we performed the gas adsorption measurements on the brominated Hexene-CTF. The brominated Hexene-CTF does not have any double bonds remaining and as expected, the overall acetylene and ethylene uptake went down significantly (Figure S3.16). This experiment proves that the presence of double bonds is the main cause for higher acetylene and ethylene uptake.

The selectivity over CH_4 was estimated using the ratio of the initial slopes in the Henry regime (<0.05 bar) of the adsorption isotherms (Table 3.1 and Figures S3.9-S3.12). These initial slopes were obtained by a linear fit. In Table 3.1 the estimated C_2H_2/CH_4 and C_2H_4/CH_4 selectivities of the Hexene-CTF family are presented. In general, the selectivities for the Hexene-CTFs vary between 14.5-24.5 (C_2H_2/CH_4) and 9.4-14.8 (C_2H_4/CH_4). There is apparently no direct correlation with the applied synthesis conditions. The CH_4 -alkene π -H interaction is weaker in comparison to the CH_4 -aromatic π -H interaction,⁴⁴ which is beneficial for a higher selectivity. In a purely aromatic CTF, the π -H interaction influences the C2/C1 selectivity negatively, whereas the presence of aliphatic olefin components helps by having a reduced interaction with CH_4 and thus increases the C2/C1 selectivity. Noteworthy is that the alkene functionality- CH_4

interaction cannot be termed as a π -H interaction, however, the presence of both benzene and ethylene groups can result in π -H interactions.⁴⁴ Unlike the C₂H₄-aromatic unit interaction, the C₂H₄-aliphatic π - π interaction is dominated by dispersion energy.³⁵ To better understand the adsorption properties of the Hexene-CTF for C₂H₄, the isosteric heats of adsorption (Q_{st}) were calculated using the Clausius-Clapeyron equation for the isotherms measured at 0°C and 25°C.

$$Q_{st} = RT^2 \left[\frac{\partial \ln P}{\partial T} \right]_N$$

Where, T is the temperature, R is the universal gas constant and P is the pressure for given quantity of gas adsorbed (N). The Q_{st} values range from 26-47 kJ/mol for C₂H₂ (Figure S3.13) and 24-37 kJ/mol for C₂H₄ (Figure S3.14), which is significantly higher than several other reported porous materials. Especially, the CTF-PO71 material showed a good C₂H₂/C₂H₄ selectivity but had lower Q_{st} values than Hexene-CTFs.³¹ The obtained values highlight the importance of introducing olefin functionalities in the Hexene-CTFs, which provides efficient π - π complexation between the framework and the adsorbed unsaturated gas molecules. In addition, the Q_{st} for methane is lower and ranges from 14-21 kJ/mol (Figure S3.15), which validates the selective adsorption of C₂H₂ and C₂H₄ over CH₄. The Q_{st} values are higher for the Hexene-CTFs made at 400°C and a decrease for Hexene-CTFs made at 500°C due to a higher number of defects caused in the framework by the higher reaction temperature. Such a difference is also seen in previous cases of CTFs for CO₂ adsorption. The selectivities are in the mid-range compared to several other porous materials. Mostly MOFs have been studied for such separations and the presence of metals in these materials plays a major role in the selectivity. However, some of these materials have lower overall gas uptake¹⁷ and are also less stable than CTFs. Here we present for the first time the use of a metal-free adsorbent having inherent aliphatic functional groups for such C2/C1 separation. Furthermore, this is the first report of using COFs for C₂H₂/CH₄ and C₂H₄/CH₄ selectivity studies.

3.2.4. Selective CO₂ adsorption

In addition to the C2/C1 separation, we also examined the materials for their CO₂ uptake. The CO₂ adsorption/desorption isotherms were recorded at 0°C and 25°C up to 1 bar (Figure 3.7). The detailed uptake values are given in Table S3.4. Upon comparison of these values with respect to the synthesis conditions, the Hexene-CTF_400_1 shows the highest CO₂ uptake of 2.66 mmol/g (0°C, 1 bar) and 1.72 mmol/g (25°C, 1 bar). These

uptakes are amongst the average when compared to previously reported CTFs.²⁷ This is due to a lower N content than most other CTFs which is essential for increasing the interaction with CO₂. The highest uptake for the Hexene-CTF was also observed for the material synthesized at 400°C. This is in contradiction with most of the reported CTFs for CO₂ adsorption, where the CTF made at higher synthesis temperature usually shows the highest CO₂ uptake because of a higher surface area (dispersion or Van der Waal interactions) dominating the overall adsorption.³⁰ However, in the case of Hexene-CTFs, the CO₂ adsorption is more related to the presence of the functional groups. Based on the elemental analysis (Table S3.2), the Hexene-CTF_400_1 has the highest N content resulting in a higher CO₂ uptake. This further emphasizes the importance of having a large N content for CO₂ interaction. The amount of ZnCl₂ used for the synthesis also influenced the CO₂ adsorption. More specifically, an increase in the ZnCl₂ equivalents decreased the overall CO₂ uptake. We attribute this to be a result of some residual Zn present in the materials which could not be removed even after extensive washing. The Zn residue decreases the surface area and blocks the interaction sites with CO₂. The Clausius-Clapeyron equation was used to calculate the isosteric heat of adsorption (Q_{st}) of CO₂ using the isotherms at 0°C and 25°C (Figure S3.17). The highest Q_{st} of 32.2 is calculated for Hexene-CTF_400_1 and it supports the corresponding highest CO₂ uptake amongst the Hexene-CTF family. The liquefaction heat of bulk CO₂ is 17 kJ/mol⁴² and the Q_{st} values for the Hexene-CTFs are much higher (~27-32 kJ/mol). These values are also higher than those for activated carbon at low CO₂ pressure (17.8 kJ/mol) and are well above the Q_{st} values of several CTFs.³⁰ The isosteric heat of adsorption values of the materials were observed to be directly related to the micropore volumes of the materials. For comparing the series of materials, micropore volume/total pore volume ratio (V_{micro}/V_{tot}) was calculated (Table S3.1). It was noted that Hexene-CTF_400_1 shows the highest micropore volume to the total pore volume ratio and correspondingly shows higher gas-framework interaction. The order of V_{micro}/V_{tot} in the materials is Hexene-CTF_400_1 > Hexene-CTF_400_5 > Hexene-CTF_400_10 > Hexene-CTF_500_5 = Hexene-CTF_500_10 and corresponding order of interaction (Q_{st}) was observed for C₂H₂, CO₂ and CH₄. Overall, a higher micropore volume content result in higher gas-framework interaction.

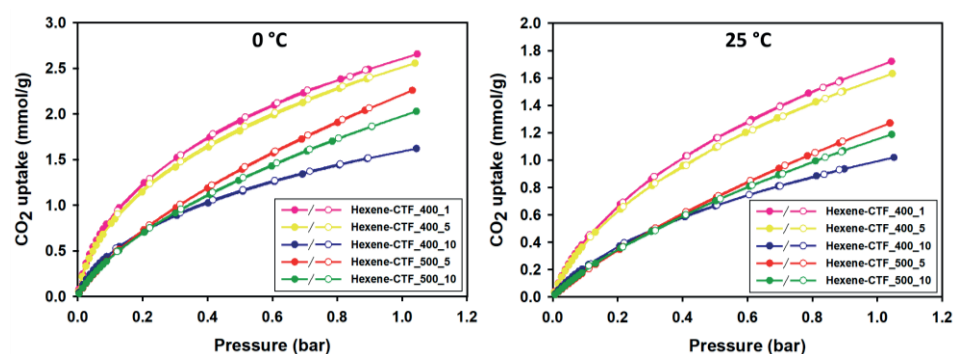


Figure 3. 7. CO₂ adsorption (closed symbols) and desorption (open symbols) isotherms of all Hexene-CTFs obtained at 0°C and 25°C.

Table 3. 1. The gas selectivities of Hexene-CTFs in comparison to selected other porous materials

Material description	Temperature (°C)	C ₂ H ₂ /CH ₄	C ₂ H ₄ /CH ₄	CO ₂ /N ₂	CO ₂ /CH ₄
Hexene-CTF_400_10	25	22.3	13.6	82.5	7.5
	0	21.8	13.2	67.9	9.8
Hexene-CTF_400_5	25	18.9	10.3	44.5	7.8
	0	20.6	10.8	45.6	8.3
Hexene-CTF_400_1	25	14.5	12.8	44.8	8.0
	0	16.3	11.8	44.6	8.6
Hexene-CTF_500_10	25	22.8	11.3	25.2	7.0
	0	24.5	14.8	29.6	9.6
Hexene-CTF_500_5	25	19.4	9.4	25.8	5.3
	0	19.9	10.0	29.2	6.6
UTSA-33a ⁴⁵	23	13.8	11.1	-	-
	0	16.1	14.7	-	-
ZJU-61a ⁴⁶	25	74.4	49.5	-	-
	0	115.3	87.6	-	-
UTSA-10a ⁴⁷	23	8.1	4.6	-	-

HOF-BTB ⁴⁸	25	7.8	7.9	-	-
	0	9.5	9.3	-	-
Wet ZIF-8 ¹⁸	0	-	5.56	-	-
ZIF-67/water-ethylene glycol slurry ¹⁹	0	-	10	-	-
Solid ZIF-67 ¹⁹	0	-	3.1	-	-
FUM-CTF ³⁰	25	-	-	102.4	20.5

The selectivity of the CTFs for CO₂ over CH₄ and N₂ was also studied as it is an important factor for carbon capture and storage (Figures S3.19-S3.22).^{26,27} The selectivity of all the materials is presented in Table 3.1. The CO₂/N₂ selectivity was calculated using the slopes ratio in the Henry regime of the CO₂ (<0.05 bar) and N₂ (<0.1 bar) adsorption isotherms. For porous materials like MOFs and porous organic frameworks (POFs), this is a common method to estimate the gas separation performance; the CO₂/N₂ selectivity is among the top 15% for several porous organic polymers.³⁰ As expected the selectivity is higher for the materials synthesized at 400°C than at 500°C due to the higher number of functional groups remaining in the material. From this study, it can be concluded that for Hexene-CTFs, the synthesis temperature has a role in the selectivity of CO₂ over N₂ with 400°C to be the better one. However, the employed amount of ZnCl₂ has negligible effects on the selectivity. In addition, Hexene-CTF performs well in comparison to several other porous organic polymers in terms of CO₂/CH₄ selectivity.³⁰

3.3. Conclusion

In conclusion, for the first time, a family of aliphatic olefin functionalized covalent triazine framework materials were synthesized using the ionothermal synthesis method. The Hexene-CTFs showed tunable textural and porous properties that is a result of varying synthesis temperature and monomer:ZnCl₂ ratio. The surface areas for the materials synthesized at 500°C were higher than for the materials synthesized at 400°C due to an increase in the number of defects causing mesoporosity in addition to the expected microporosity. High-resolution imaging of the material revealed that Hexene-CTFs consisted of clusters of crystalline regions embedded in an amorphous bulk. The

size of these crystalline regions depended on the synthesis temperatures and the employed ZnCl_2 equivalents. The Hexene-CTF_400_1 showed the largest crystalline clusters due to the usage of a lower amount of ZnCl_2 and a lower synthesis temperature, whereas the Hexene-CTF_500_10 was characterized by spaghetti-like lattice planes. The C_2H_2 , C_2H_4 , and CO_2 gas adsorption revealed that the adsorption performance depended more on the materials' structural order than the surface area. In the low-pressure regime, the higher ordered crystalline CTFs showed higher adsorption of C_2H_2 , C_2H_4 and CO_2 even though it had the least surface area due to higher availability of functional groups in the framework. This also had an influence on the selectivity over CH_4 (for C_2H_2 , C_2H_4 , and CO_2) and N_2 (for CO_2). Though the general uptake for CO_2 is average compared to several other CTFs, the selectivities are among the highest in comparison to several other porous organic polymers. Furthermore, this is the first time where the concept of using aliphatic unsaturated functional groups in the framework of a COF is used to adsorb unsaturated gases selectively by utilizing higher π - π interaction. This notion can be extended to design intricate COFs which can further improve the adsorption properties.

3.4. Experimental Section

3.4.1. Instrumentation

The chemicals were purchased from Sigma-Aldrich and used without further purifications unless mentioned otherwise. Elemental analyses (C/H/N/O) were performed on a Thermo Scientific Flash 2000 CHNS-O analyzer equipped with a TCD detector. N_2 adsorption isotherms were obtained from a Belsorp Mini apparatus at 77K. Fourier transform infrared spectroscopy (FT-IR) was carried out in a Thermo Nicolet 6700 FTIR spectrometer equipped with a nitrogen-cooled MCT detector and a KBr beam splitter for the region of 4000-650 cm^{-1} . X-Ray powder diffraction (XRPD) measurements were done on a Thermo Scientific ARL X'Tra diffractometer, operated at 40 kV, 30 mA using $\text{Cu K}\alpha$ radiation ($\lambda = 1.5406 \text{ \AA}$). Carbon dioxide (CO_2), Ethylene (C_2H_4), Acetylene (C_2H_2), Methane (CH_4), and Nitrogen (N_2) gas adsorption isotherms were collected using a Quantachrome iSorb-HP gas sorption analyzer. Thermogravimetric analysis (TGA) was performed on a Netzsch STA-449 F3 Jupiter-simultaneous TG-DSC analyzer within a temperature range of 20-800°C, under a N_2 atmosphere and heating rate of 2°C/min. 1800-2700 scans were further accumulated with a 4 s recycle delay. Scanning electron microscopy (SEM) images were taken on a FEI Quanta 200 FEG microscope with 4 nm

resolution operating at 30 kV. Transmission electron microscopy (TEM) images were acquired on a FEI Tecnai G2 F20 X-Twin FEG TEM operated at 200 kV and equipped with a Gatan Imaging Filter (GIF) Tridiem™. The zinc loading was determined by an Inductively Coupled Plasma (ICP) measurement Optima 8000 atomic Emission Spectrometer (ICP-OES).

3.4.2. Synthesis of Hexene-CTFs

The targeted Hexene-CTF materials were synthesized using the monomer, trans-3-hexenedinitrile under ionothermal conditions. In general, trans-3-hexenedinitrile (106 mg, 1 mmol) was charged in an ampoule with 1/5/10 equivalents of ZnCl₂ in a glovebox. The ampoule was then evacuated, flame-sealed, and slowly heated to the desired temperature (400°C /500°C) with a heating rate of 1°C/min for 48 hours in a Nabertherm furnace oven. Once the oven was cooled to room temperature, the ampoules were opened, and the crude material was grounded and washed with distilled water (stirring for 12 hours) to remove unreacted ZnCl₂. Then it was refluxed with 0.1 M HCl and THF for 12 hours each to remove water and unreacted linker/organic impurities. The final product was activated at 120°C under vacuum for 24 hours.

3.4.3. Bromine addition reaction

In general, to quantify the number of double bonds present in the Hexene-CTFs, 100 mg of the CTF was weighed in a dry Schlenk flask and treated with an excess amount of bromine gas under an inert atmosphere. The accessible unsaturated olefin bonds in the material were brominated whereas the unreacted bromine was eliminated by heating the material at 120°C under vacuum.³³ After removal of unreacted bromine gas, the increase in the mass of the CTF was calculated to estimate the amount of bromine reacted to the CTF.

3.5. References

- (1) O. Colten, Industrial & Engineering Chemistry, 1959, 51(9), 983-984.
- (2) L. A. Falligant, U.S. Patent 2683484, 1954.
- (3) A. Moshonov, Y. Avny, Journal of Applied Polymer Science, 1980, 25, 771-781.
- (4) G. Parker, L. Smith, I. Baxendale, Tetrahedron, 2016, 72, 1645-1652.
- (5) S. P. Robinson, U.S. Patent 2482438, 1949.

- (6) H. A. Dutcher, U.S. Patent 2582016, 1946.
- (7) Beyond the Ethylene Steam Cracker, www.acs.org/content/acs/en/pressroom/cutting-edge-chemistry/beyond-the-ethylene-steam-cracker.html, (accessed Nov 5, 2018).
- (8) Ethene (Ethylene), www.essentialchemicalindustry.org/chemicals/ethene.html, (accessed Nov 5, 2018).
- (9) Cracking and related refinery processes, www.essentialchemicalindustry.org/processes/cracking-isomerisation-and-reforming.html#steam_cracking, (accessed Nov 5, 2018).
- (10) E. A. Kaufman, J. A. Moss, J. L. Jr. Pickering, U.S. Patent 5372009, 1994.
- (11) P. F. Keusenkothen, F. Hershkowitz, WO2012/0099679A1, 2012.
- (12) C. Millet, P. Bourgeois, G. Kraus, J.-P. Gabillard, U.S. Patent 6270557B1, 2001.
- (13) L. Zhang, X. Cui, H. Xing, Y. Yang, Y. Cui, B. Chen, G. Qian, RSC Advances, 2017, 7, 20795-20800.
- (14) M. Eddaoudi, D. Moler, H. Li, B. Chen, T. Reineke, M. O'Keeffe, O. Yaghi, Accounts of Chemical Research, 2001, 34, 319-330.
- (15) J. Pang, F. Jiang, M. Wu, C. Liu, K. Su, W. Lu, D. Yuan, M. Hong, Nature Communications, 2015, 6.
- (16) K. Liu, D. Ma, B. Li, Y. Li, K. Yao, Z. Zhang, Y. Han, Z. Shi, J. Mater. Chem. A, 2014, 2, 15823-15828.
- (17) L. Zhang, X. Cui, H. Xing, Y. Yang, Y. Cui, B. Chen, G. Qian, RSC Advances, 2017, 7, 20795-20800.
- (18) X. Zhang, P. Xiao, C. Zhan, B. Liu, R. Zhong, L. Yang, C. Sun, H. Liu, Y. Pan, G. Chen, Industrial & Engineering Chemistry Research, 2015, 54, 7890-7898.
- (19) Y. Pan, C. Jia, B. Liu, Z. Zhang, X. Tong, H. Li, Z. Li, R. Ssebadduka, C. Sun, L. Yang, Fluid Phase Equilibria, 2016, 414, 14-22.
- (20) S. Xiang, W. Zhou, J. Gallegos, Y. Liu, B. Chen, Journal of the American Chemical Society, 2009, 131, 12415-12419.
- (21) Y. Zhang, B. Li, R. Krishna, Z. Wu, D. Ma, Z. Shi, T. Pham, K. Forrest, B. Space, S. Ma, Chemical Communications, 2015, 51, 2714-2717.

- (22) Y. Khabzina, J. Dhainaut, M. Ahlhelm, H. Richter, H. Reinsch, N. Stock, D. Farrusseng, *Industrial & Engineering Chemistry Research*, 2018, 57, 8200-8208.
- (23) H. Reinsch, *European Journal of Inorganic Chemistry*, 2016, 4290-4299.
- (24) K. Leus, T. Bogaerts, J. De Decker, H. Depauw, K. Hendrickx, H. Vrielinck, V. Van Speybroeck, P. Van Der Voort, *Microporous and Mesoporous Materials*, 2016, 226, 110-116.
- (25) D. Aaron, C. Tsouris, *Separation Science and Technology*, 2005, 40, 321-348.
- (26) L. Zhu, Y. Zhang, *Molecules*, 2017, 22, 1149.
- (27) Y. Zeng, R. Zou, Y. Zhao, *Advanced Materials*, 2016, 28, 2855-2873.
- (28) K. Sakaushi, M. Antonietti, *Accounts of Chemical Research*, 2015, 48, 1591-1600.
- (29) P. Kuhn, M. Antonietti, A. Thomas, *Angewandte Chemie International Edition*, 2008, 47, 3450-3453.
- (30) K. Wang, H. Huang, D. Liu, C. Wang, J. Li, C. Zhong, *Environmental Science & Technology*, 2016, 50, 4869-4876.
- (31) Y. Lu, J. He, Y. Chen, H. Wang, Y. Zhao, Y. Han, Y. Ding, *Macromolecular Rapid Communications*, 2017, 39, 1700468.
- (32) P. Kuhn, A. Forget, D. Su, A. Thomas, M. Antonietti, *Journal of the American Chemical Society*, 2008, 130, 13333-13337.
- (33) S. Clerick, E. De Canck, K. Hendrickx, V. Van Speybroeck, P. Van Der Voort, *Green Chemistry*, 2016, 18, 6035-6045.
- (34) W. Zhao, L. Xia, X. Liu, *CrystEngComm*, 2018, 20, 1613-1634.
- (35) K. Kim, S. Karthikeyan, N. Singh, *Journal of Chemical Theory and Computation*, 2011, 7, 3471-3477.
- (36) K. Schwinghammer, S. Hug, M. Mesch, J. Senker, B. Lotsch, *Energy & Environmental Science*, 2015, 8, 3345-3353.
- (37) P. Katekomol, J. Roeser, M. Bojdys, J. Weber, A. Thomas, *Chemistry of Materials*, 2013, 25, 1542-1548.
- (38) S. Dey, A. Bhunia, H. Breitzke, P. Groszewicz, G. Buntkowsky, C. Janiak, *Journal of Materials Chemistry A*, 2017, 5, 3609-3620.

- (39) S. Dey, A. Bhunia, I. Boldog, C. Janiak, *Microporous and Mesoporous Materials* 2017, 241, 303-315.
- (40) D. Osadchii, A. Olivos-Suarez, A. Bavykina, J. Gascon, *Langmuir*, 2017, 33, 14278-14285.
- (41) G. Wang, K. Leus, H. Jena, C. Krishnaraj, S. Zhao, H. Depauw, N. Tahir, Y. Liu, P. Van Der Voort, *Journal of Materials Chemistry A*, 2018, 6, 6370-6375.
- (42) H. Jena, C. Krishnaraj, G. Wang, K. Leus, J. Schmidt, N. Chaoui, P. Van Der Voort, *Chemistry of Materials*, 2018, 30, 4102-4111.
- (43) G. Wang, K. Leus, S. Zhao, P. Van Der Voort, *ACS Applied Materials & Interfaces*, 2017, 10, 1244-1249.
- (44) P. Tarakeshwar, H. Choi, K. Kim, *Journal of the American Chemical Society*, 2001, 123, 3323-3331.
- (45) M. Das, H. Xu, S. Xiang, Z. Zhang, H. Arman, G. Qian, B. Chen, *Chemistry - A European Journal*, 2011, 17, 7817-7822.
- (46) X. Duan, Q. Zhang, J. Cai, Y. Cui, C. Wu, Y. Yang, G. Qian, *Microporous and Mesoporous Materials*, 2014, 190, 32-37.
- (47) Y. He, C. Song, Y. Ling, C. Wu, R. Krishna, B. Chen, *APL Materials*, 2014, 2, 124102.
- (48) T. Yoon, S. Baek, D. Kim, E. Kim, W. Lee, B. Singh, M. Lah, Y. Bae, K. Kim, *Chemical Communications*, 2018, 54, 9360-9363.

3.6. Supporting Information

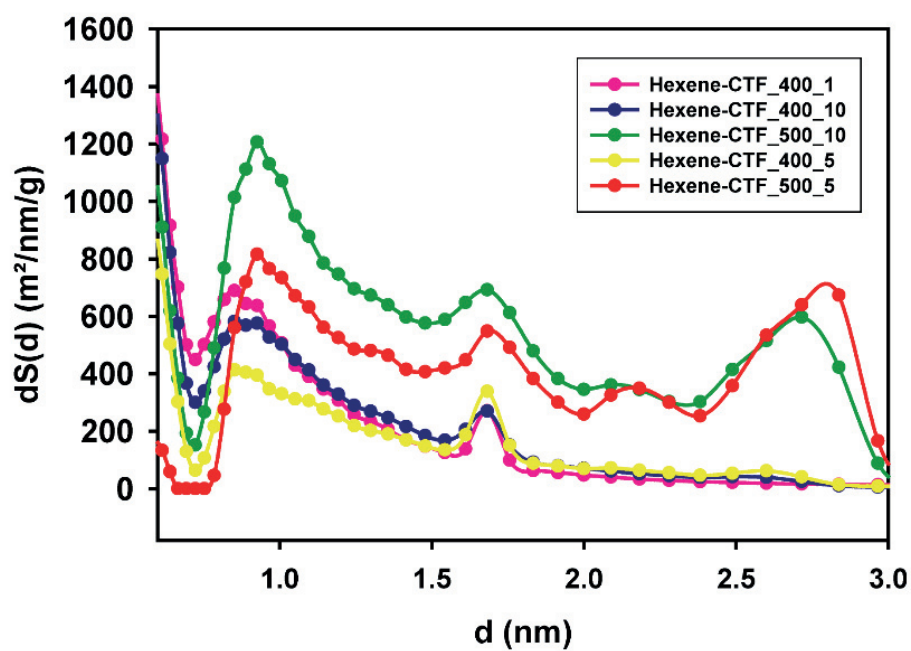


Figure S3.1. Pore size distribution of Hexene-CTF_400_10 and Hexene-CTF_500_10.

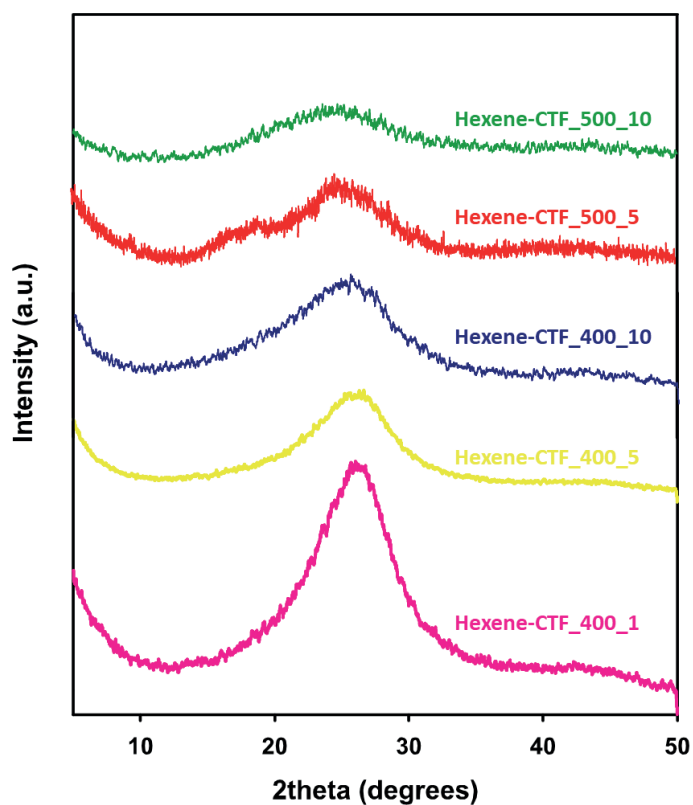


Figure S3.2. Powder X-Ray Diffraction (PXRD) patterns of all Hexene-CTFs.

Table S3.1. Porous properties of Hexene-CTFs.

Material description	^a S.A. _{BET} (m ² g ⁻¹)	^b V _{micro} (cm ³ g ⁻¹)	^c V _{tot} (cm ³ g ⁻¹)	V _{micro} /V _{tot} (%)
Hexene-CTF_400_10	499	0.2802	0.298	94.02
Hexene-CTF_400_5	579	0.3239	0.3413	94.90
Hexene-CTF_400_1	356	0.1965	0.2005	98.00
Hexene-CTF_500_10	1016	0.6437	0.6925	92.95
Hexene-CTF_500_5	1375	0.8293	0.8922	92.95

^a BET surface area was calculated over the relative pressure range of 0.05–0.3 at 77 K. ^b V_{micro}, micropore volume was calculated by N₂ adsorption isotherms using the t-plot method. ^c V_{tot}, total pore volume was calculated at P/P₀ = 0.98.

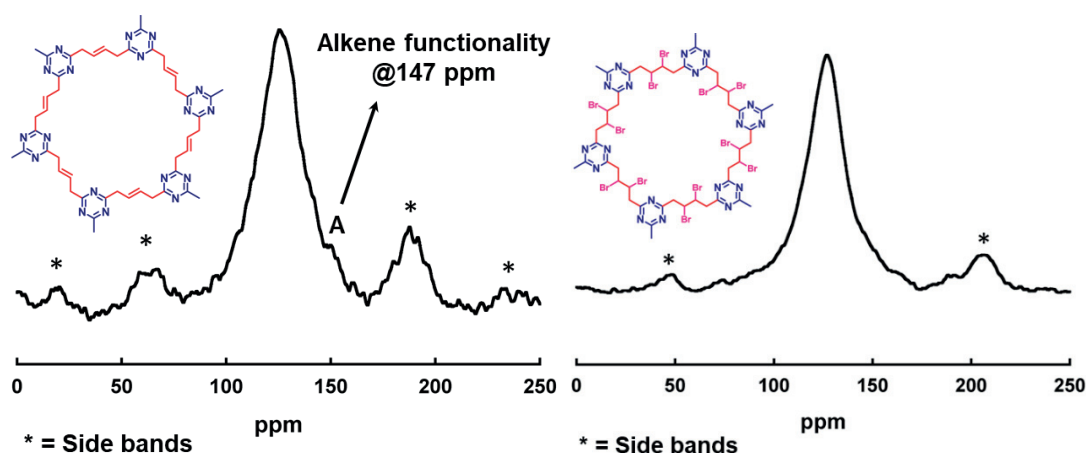


Figure S3.3. ¹³C CP-MAS NMR spectra of Hexene-CTF_400_5 (left) and Br-Hexene-CTF_400_5 (right).

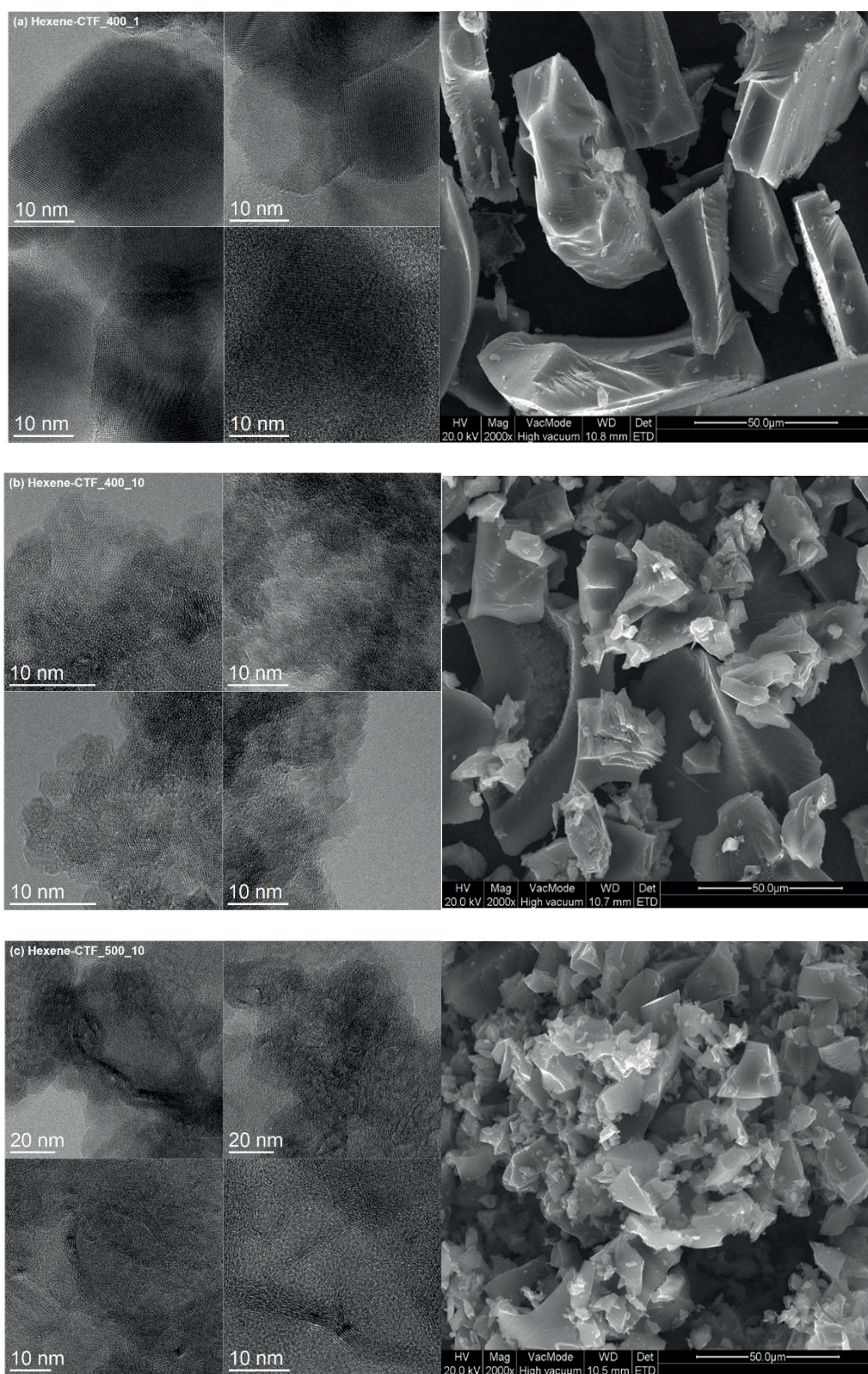


Figure S3.4. HR-TEM and SEM images of (a) Hexene-CTF_400_1, (b) Hexene-CTF_400_10 and (c) Hexene-CTF_500_10.

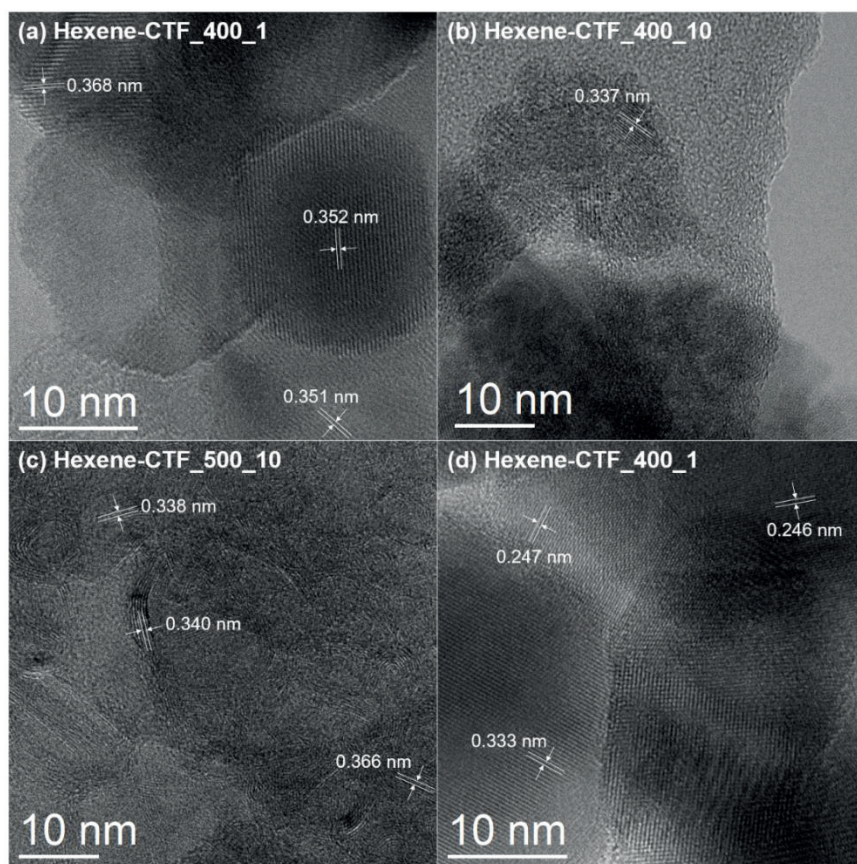


Figure S3.5. HR-TEM image of Hexene-CTF_400_1 showing two different plane-spacing.

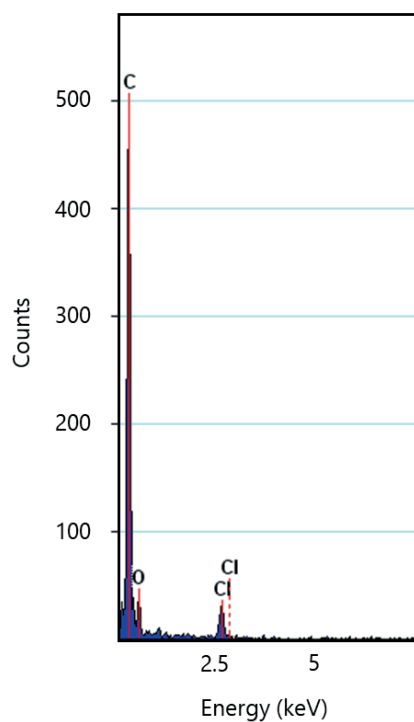
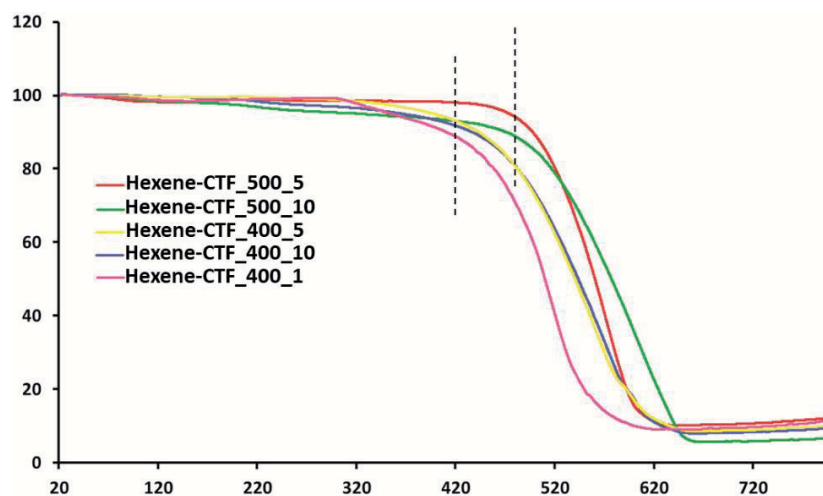


Figure S3.6. TEM-EDX of Hexene-CTF_400_1.

Equation S3.1.

$$\text{Degree of carbonization} = \left\{ \left[\frac{C\%}{(C\% + N\% + H\%)} \right] * 100 \right\} - \text{Theoretical } C\%$$

**Figure S3.7.** Thermogravimetric analysis (TGA) of all Hexene-CTFs .**Table S3.2.** Elemental analysis (C/H/N) and Bromine number of all Hexene-CTFs.

Material description	C (wt. %)	H (wt. %)	N (wt. %)	Residue (wt. %)	Br number double bonds	C/N ratio	Excess carbon content (carbonization %)
Hexene-CTF_400_10	70.9	1.9	8.8	18.3	0.62 g/g (41%)	8.05	14.7
Hexene-CTF_400_5	68.9	2.6	9.5	19	0.67 g/g (44%)	7.25	17.2
Hexene-CTF_400_1	66.1	2.8	11.1	20	0.69 g/g (46%)	5.95	18.8
Hexene-CTF_500_10	73.7	1.5	8.4	16.4	0.59 g/g (39%)	8.77	19.5
Hexene-CTF_500_5	70.7	1.5	8.7	19.1	0.60 g/g (39.7%)	8.12	20.3
Theoretical	67.9	5.7	26.4	-	1.51 g/g (100%)	2.57	-

Table S3.3. Zinc content in the CTF materials determined using ICP-OES analysis.

Material	Zn content (mg/g)
Hexene-CTF_400_1	24
Hexene-CTF_400_5	22.7
Hexene-CTF_400_10	26
Hexene-CTF_500_5	33.4
Hexene-CTF_500_10	22.2

Even after rigorous washing steps, Zn could not be removed completely. The amount of Zn was estimated from ICP-OES analysis (Table S3).

The rest of the residue could possibly be due to the excess chlorine from ZnCl_2 . However, it was not possible to detect Cl content from ICP-OES due to instrumental limitations. In addition, certain unavoidable oxygen impurities (ZnO , surface OH, etc...) could account for the residue.

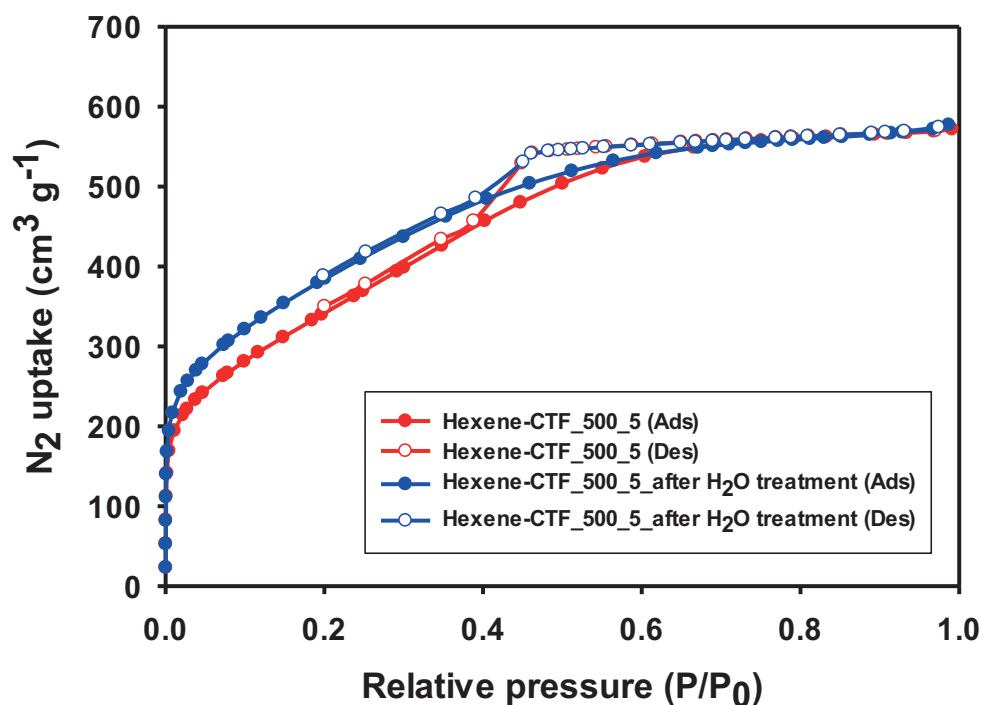


Figure S3.8. N_2 sorption isotherms of Hexene-CTF_500_5 before and after boiling water treatment.

Table S3.4. CO₂, N₂, CH₄, C₂H₄ and C₂H₂ gas uptakes by Hexene-CTFs at 25°C and 0°C at 1 bar.

Material description	Temp (°C)	CO₂ (mmol/g)	N₂ (mmol/g)	CH₄ (mmol/g)	C₂H₄ (mmol/g)	C₂H₂ (mmol/g)
Hexene-CTF_400_10	25	1.02	0.048	0.25	1.12	1.69
	0	1.62	0.091	0.4	1.54	2.54
Hexene-CTF_400_5	25	1.63	0.13	0.45	1.75	2.24
	0	2.56	0.21	0.72	2.47	3.19
Hexene-CTF_400_1	25	1.72	0.13	0.46	1.89	2.28
	0	2.66	0.24	0.74	2.55	3.54
Hexene-CTF_500_10	25	1.18	0.09	0.28	1.48	2.08
	0	2.03	0.16	0.43	2.33	3.05
Hexene-CTF_500_5	25	1.27	0.11	0.36	1.76	2.45
	0	2.26	0.17	0.61	2.72	3.85

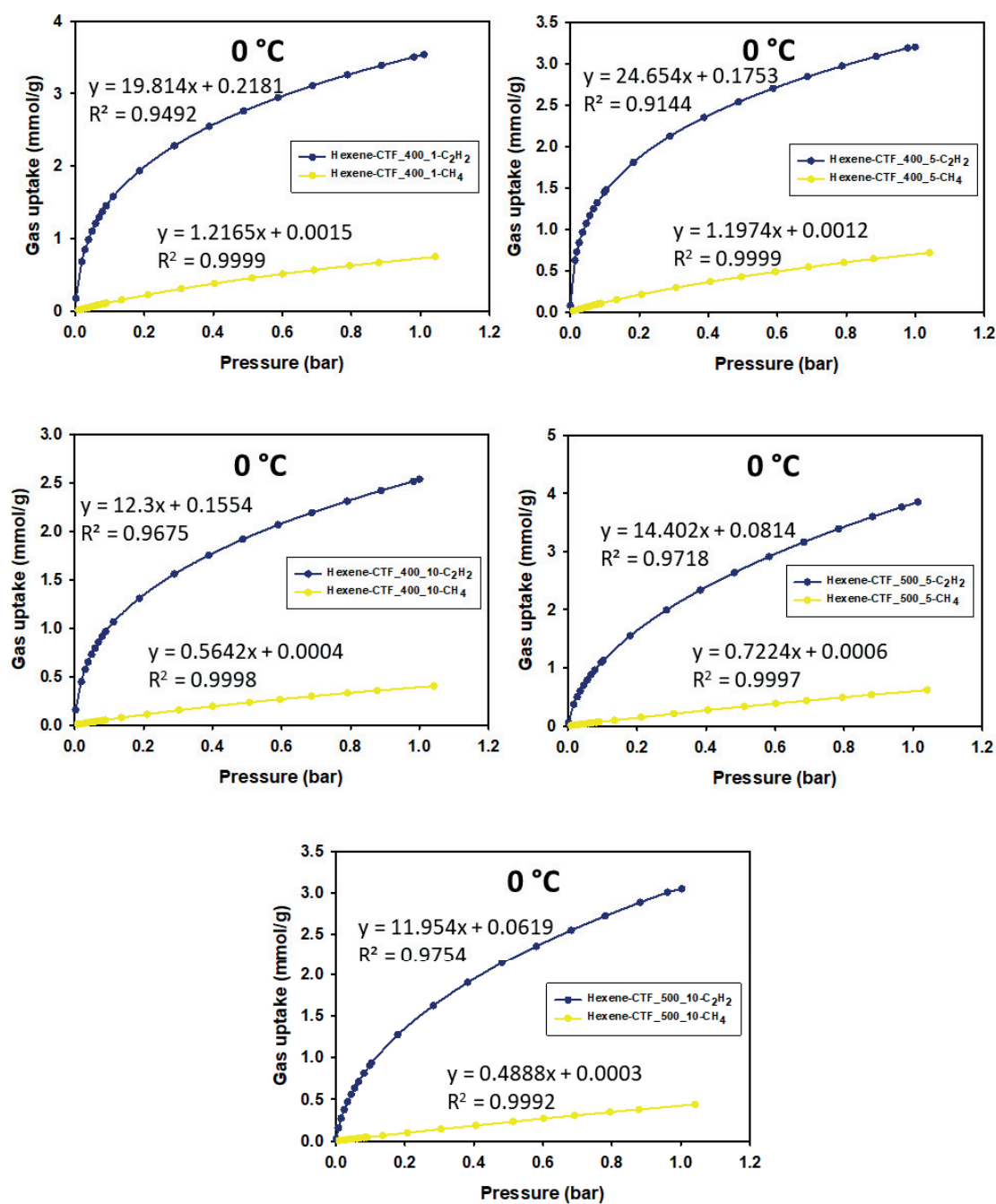


Figure S3.9. $\text{C}_2\text{H}_2/\text{CH}_4$ selectivity estimated using the ratio of the initial slopes in the Henry regime of the adsorption isotherms at 0 °C.

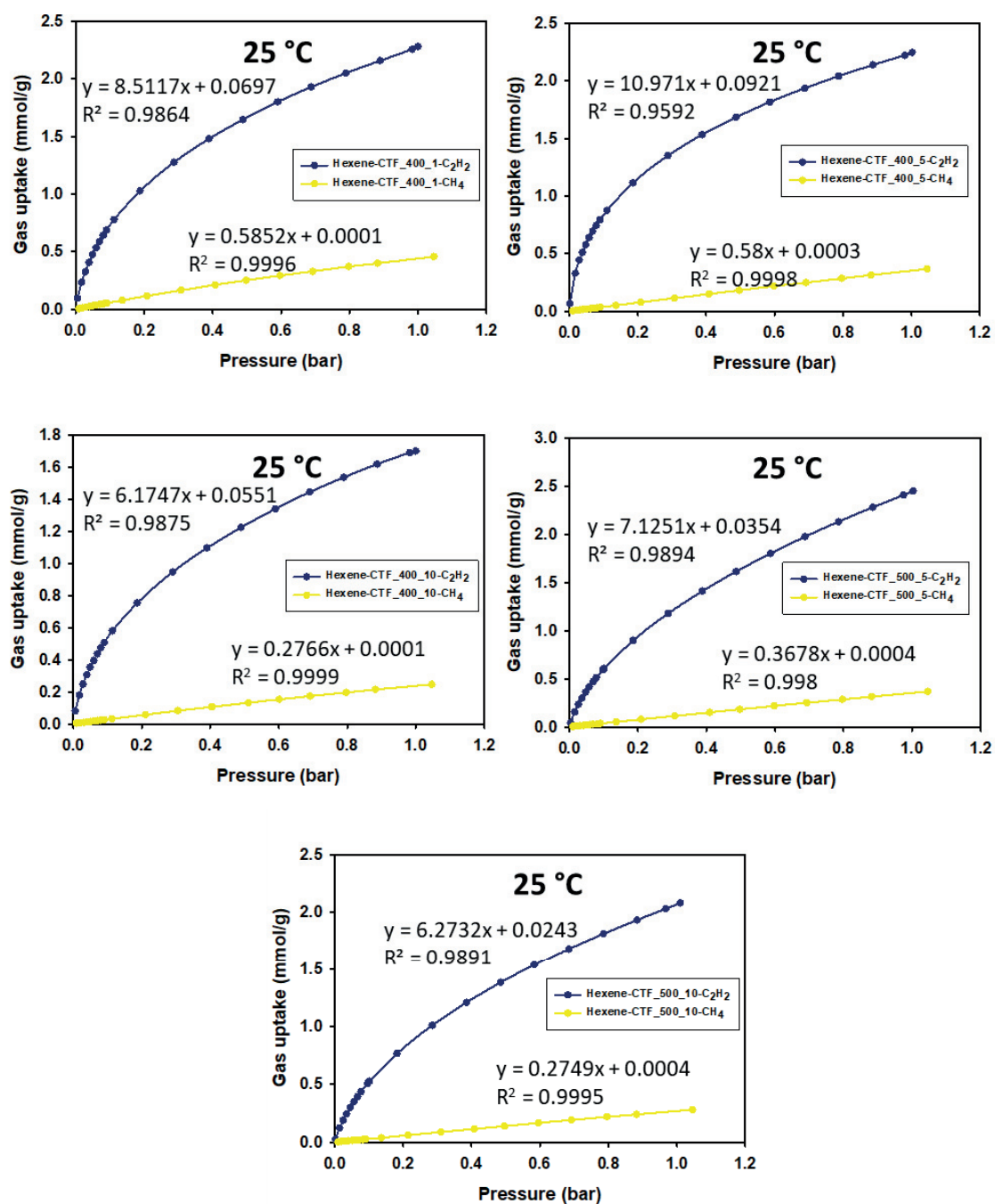


Figure S3.10. C₂H₂/CH₄ selectivity estimated using the ratio of the initial slopes in the Henry regime of the adsorption isotherms at 25 °C.

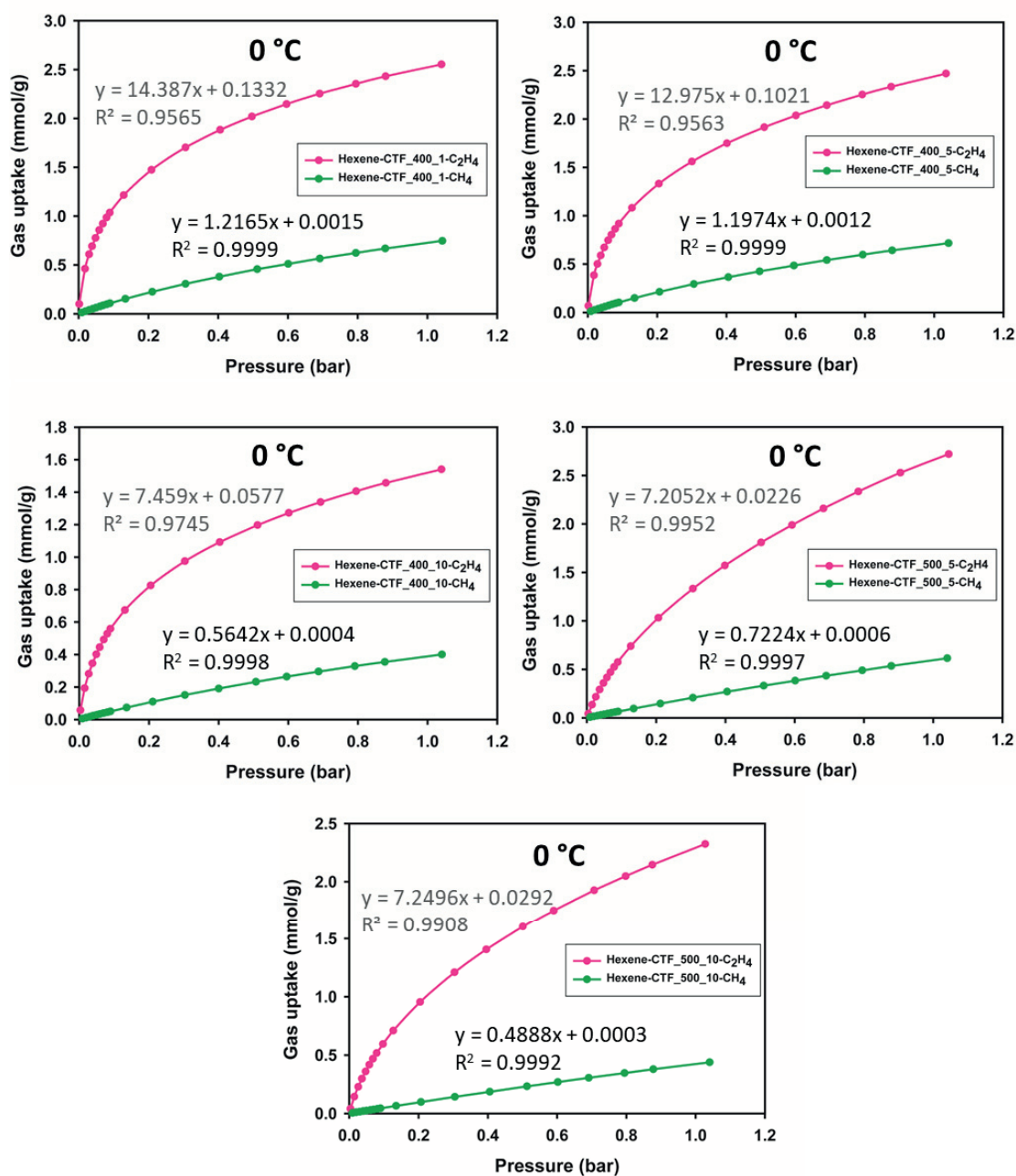


Figure S3.11. C₂H₄/CH₄ selectivity estimated using the ratio of the initial slopes in the Henry regime of the adsorption isotherms at 0 °C.

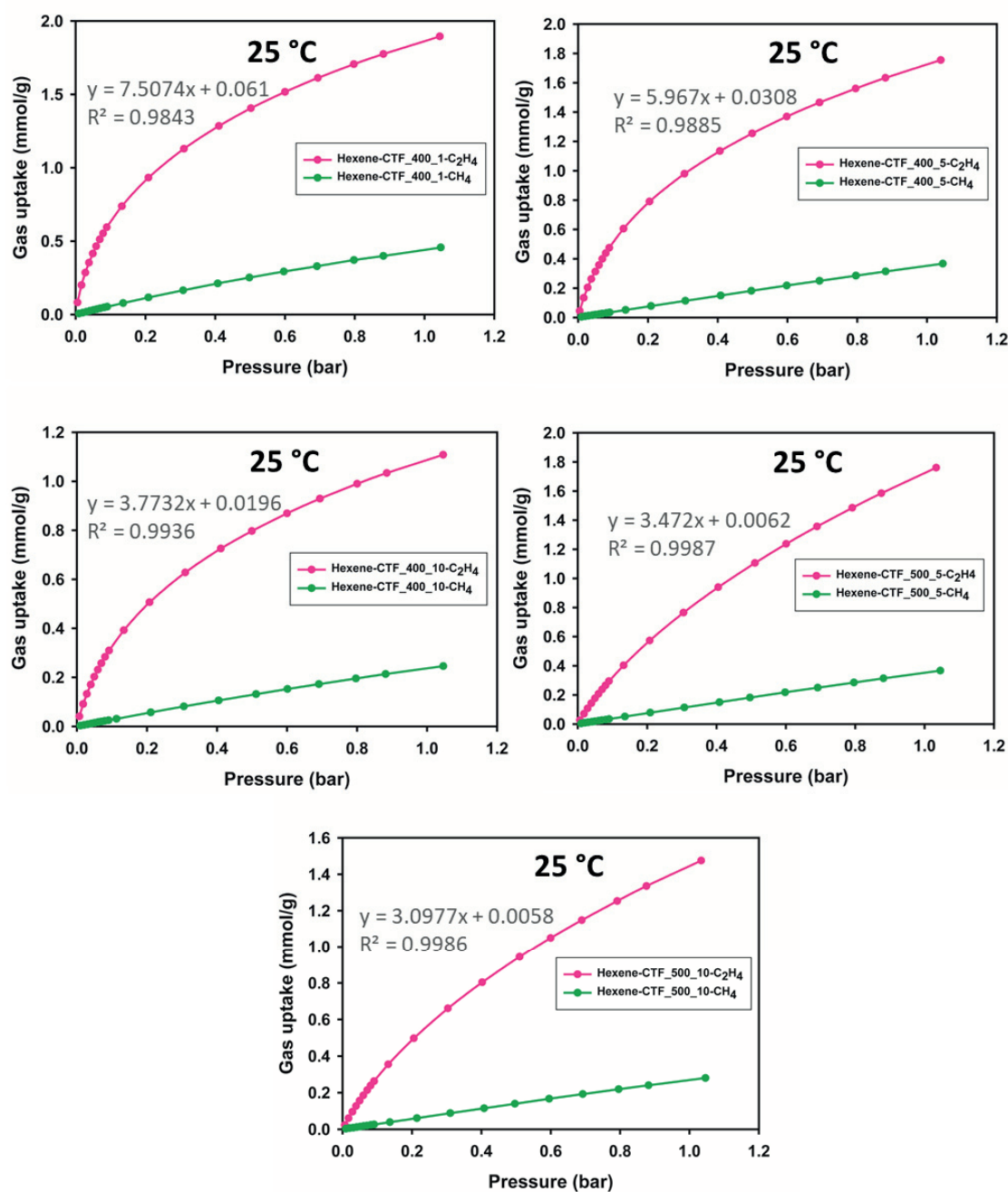


Figure S3.12. C_2H_4/CH_4 selectivity estimated using the ratio of the initial slopes in the Henry regime of the adsorption isotherms at 25°C.

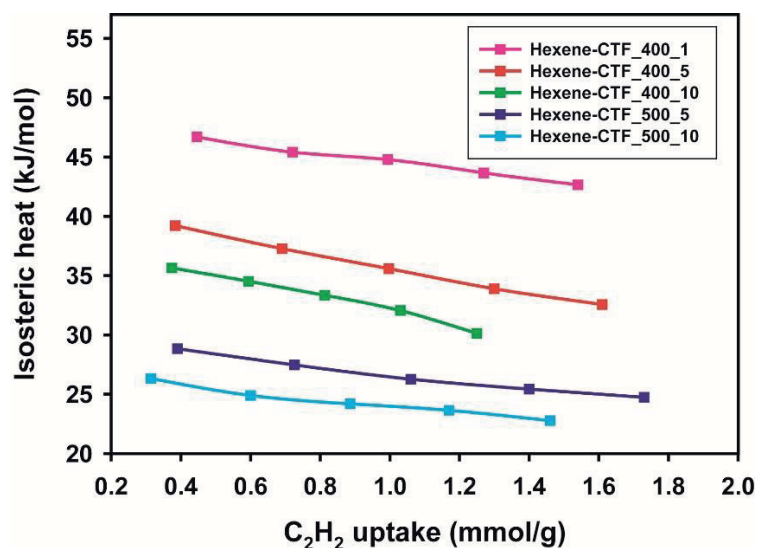


Figure S3.13. Isosteric heat of adsorption (Q_{st}) of C₂H₂ for all Hexene-CTFs.

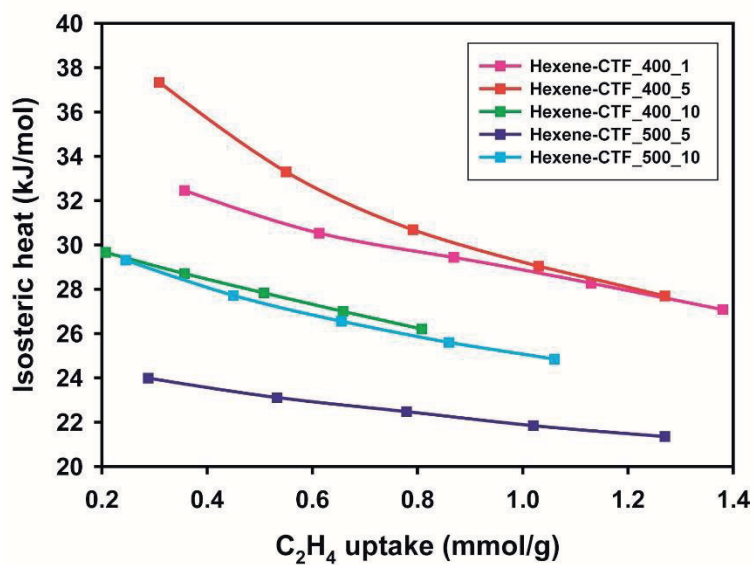


Figure S3.14. Isosteric heat of adsorption (Q_{st}) of C₂H₄ for all Hexene-CTFs.

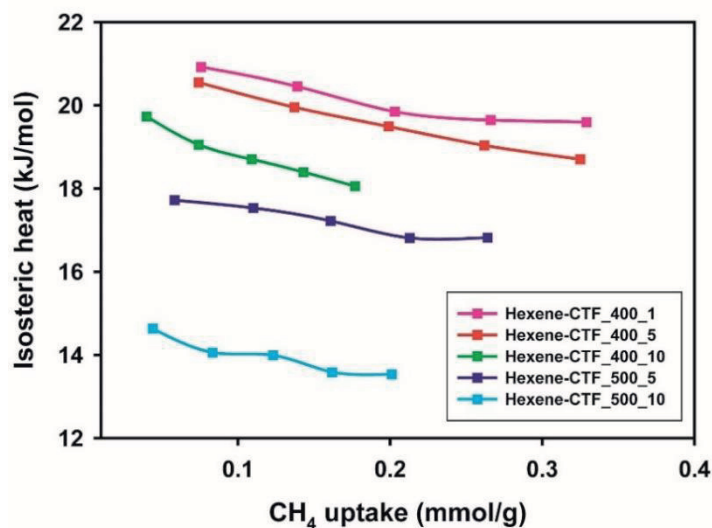


Figure S3.15. Isosteric heat of adsorption (Q_{st}) of CH₄ for all Hexene-CTFs.

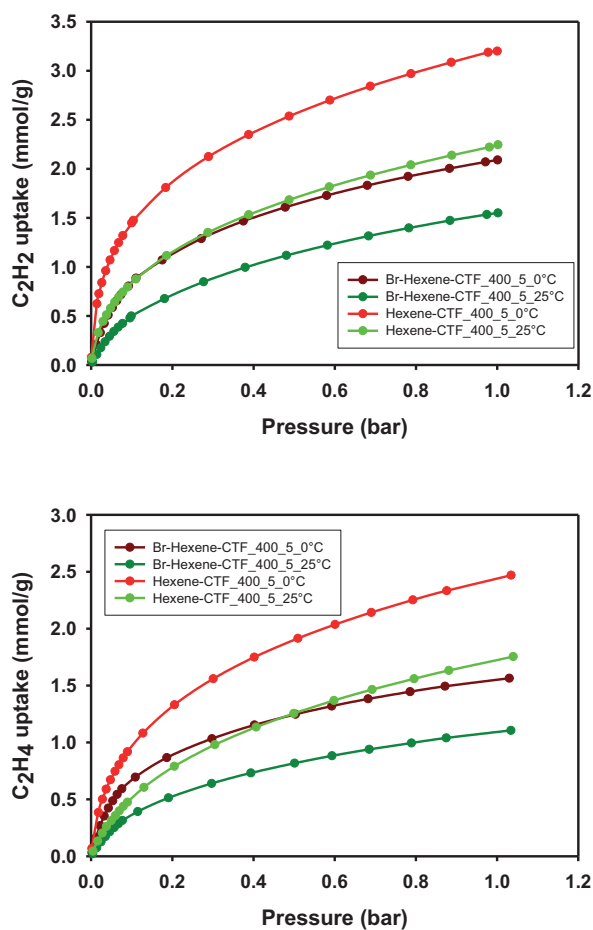


Figure S3.16. C₂H₂ (top) and C₂H₄ (bottom) uptake isotherms of Br-Hexene-CTF_400_5 and Hexene-CTF_400_5 at 0°C and 25°C. Note: The mass of Bromine is subtracted (according to the bromine number) in order to compare the pure CTFs by excluding the effect of overall increased mass due to Bromine.

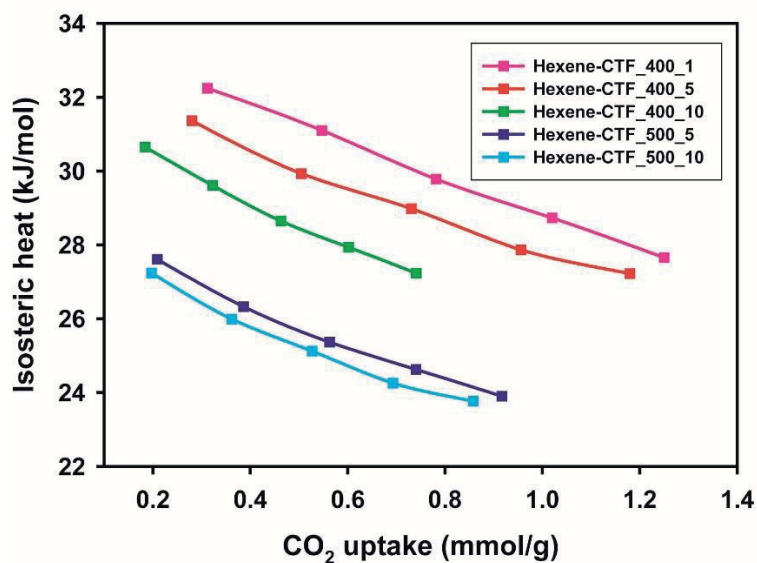


Figure S3.17. Isosteric heat of adsorption (Q_{st}) of CO₂ for all Hexene-CTFs.

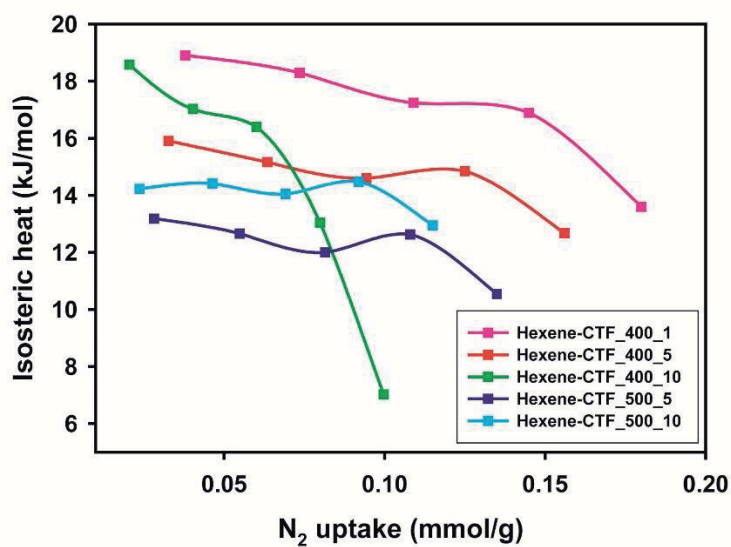


Figure S3.18. Isosteric heat of adsorption (Q_{st}) of N₂ for all Hexene-CTFs.

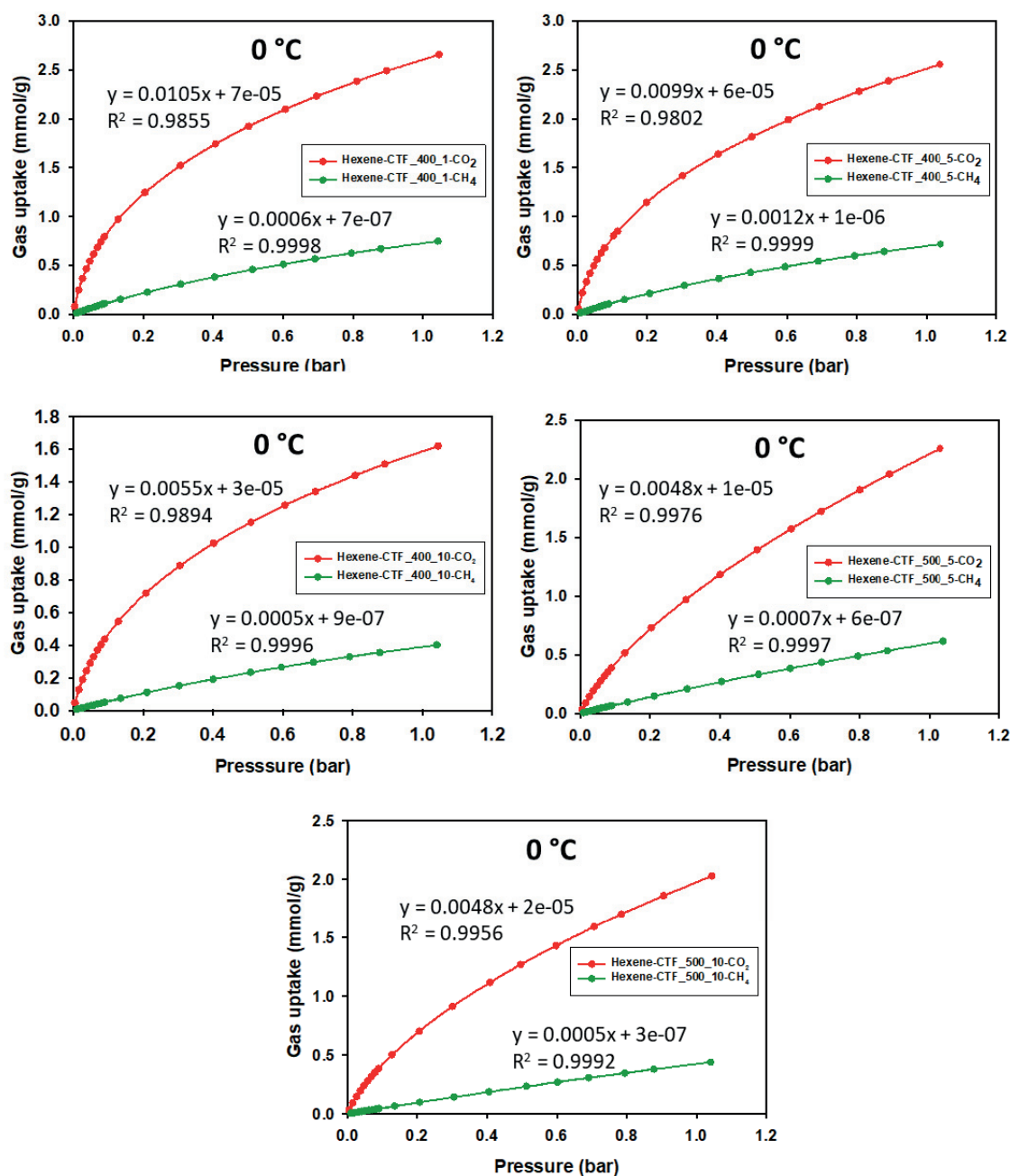


Figure S3.19. CO₂/CH₄ selectivity estimated using the ratio of the initial slopes in the Henry regime of the adsorption isotherms at 0°C.

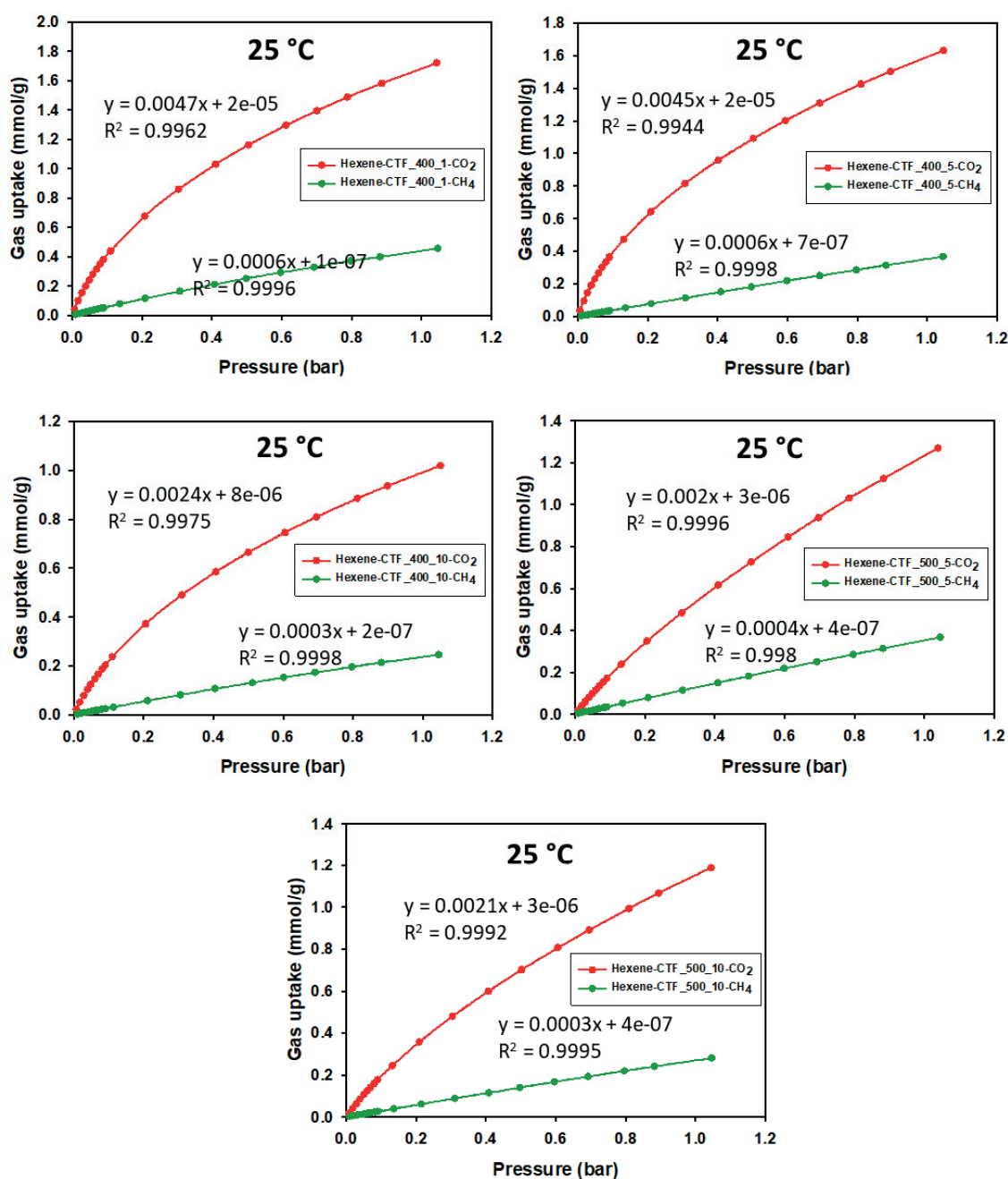


Figure S3.20. CO₂/CH₄ selectivity estimated using the ratio of the initial slopes in the Henry regime of the adsorption isotherms at 25 °C.

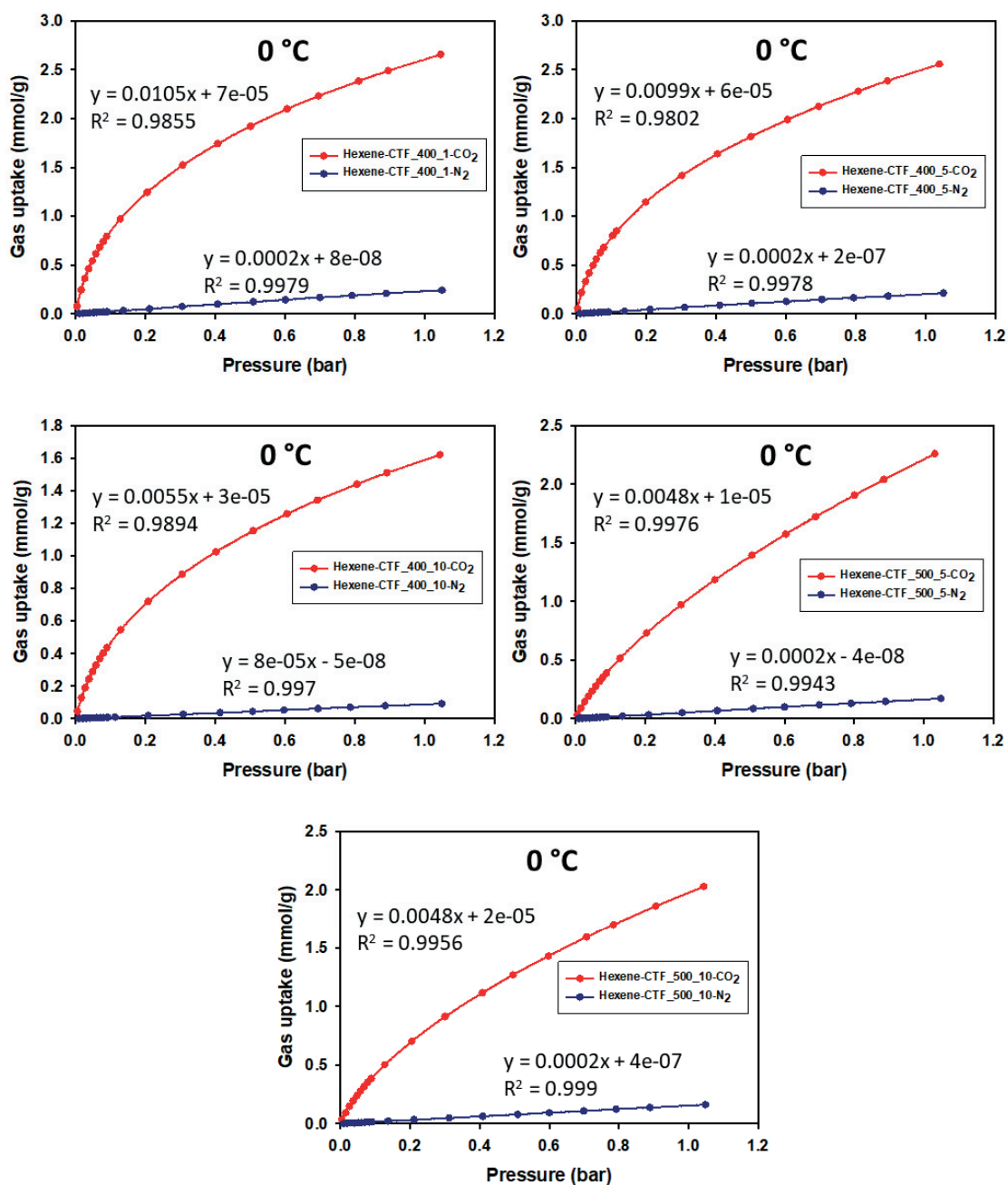


Figure S3.21. CO₂/N₂ selectivity estimated using the ratio of the initial slopes in the Henry regime of the adsorption isotherms at 0 °C.

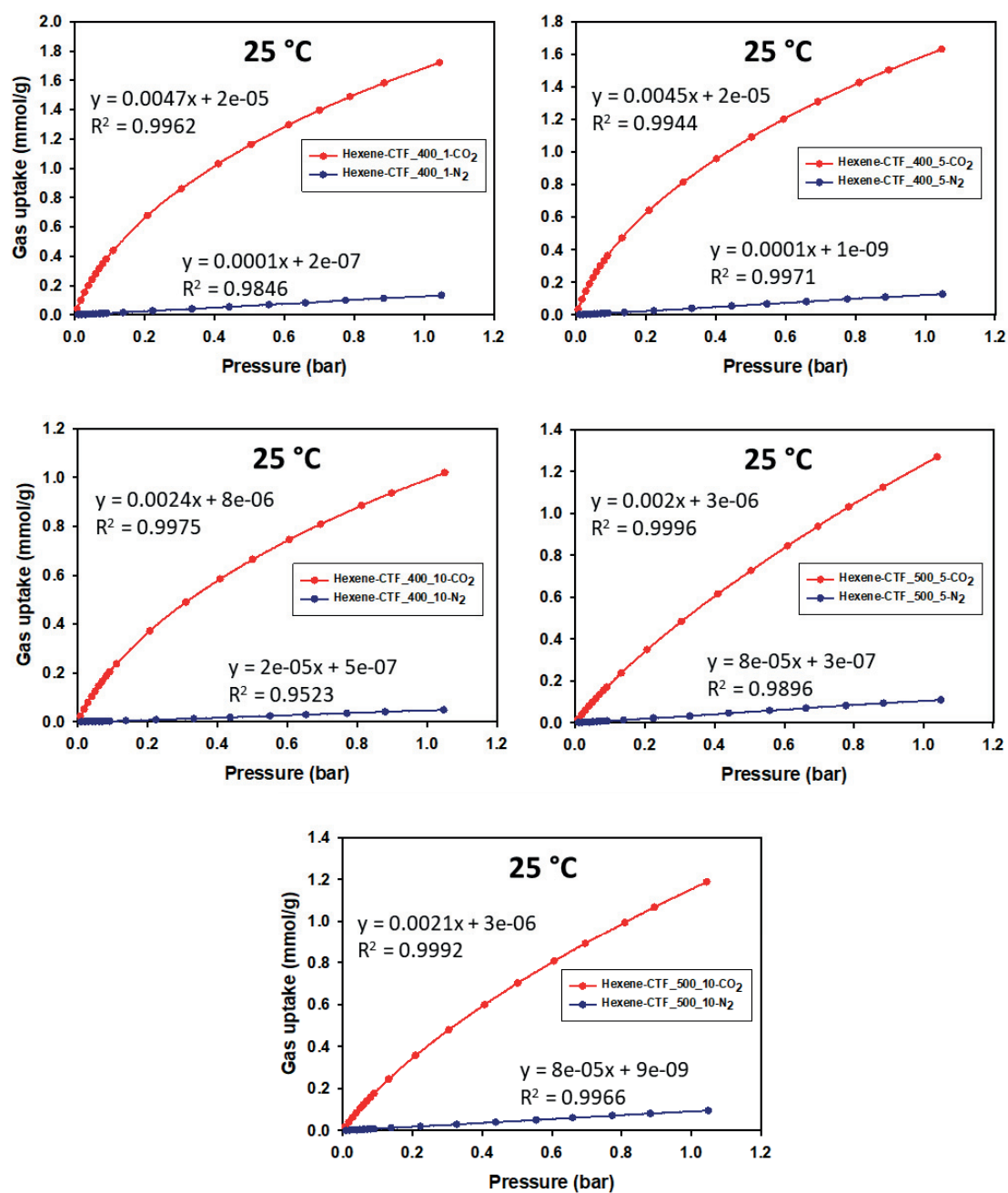
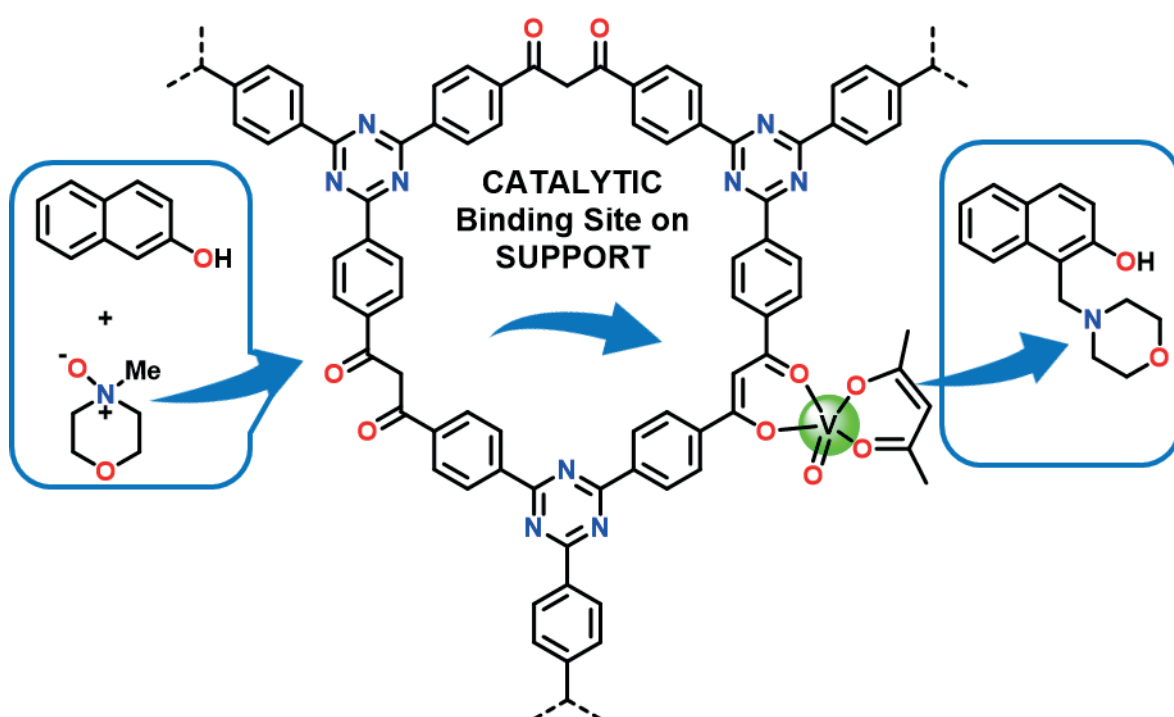


Figure S3.22. CO₂/N₂ selectivity estimated using the ratio of the initial slopes in the Henry regime of the adsorption isotherms at 25°C.

4 ACETYL ACETONE CTF: CARBON CAPTURE MATERIAL AND HIGHLY STABLE HETEROGENEOUS CATALYST



The results of this chapter were published in:

HS Jena, **C Krishnaraj**, G-B Wang, K Leus, J Schmidt, N Chaoui, P Van Der Voort, Acetyl acetone covalent triazine framework: an efficient carbon capture and storage material and highly stable heterogeneous catalyst, Chem. Mater. 2018, 30, 12, 4102-4111.

Abstract

We present, for the first time, Covalent Triazine Frameworks functionalized with acetyl acetate group (acac-CTFs). They are obtained from the polymerization of 4,4'-malonyldibenzonitrile under ionothermal conditions and exhibit BET surface areas up to 1626 m²/g. The materials show excellent CO₂ uptake (3.30 mmol/g at 273 K and 1 bar), H₂ storage capacity (1.53 wt% at 77 K and 1 bar) and a good CO₂/N₂ selectivity (up to 46 at 298 K). The enhanced CO₂ uptake value and good selectivity are due to the presence of dual polar sites (N and O) throughout the material. Also, acac-CTF was used to anchor VO(acac)₂ as a heterogeneous catalyst. The V@acacCTF showed outstanding reactivity and reusability for the modified Mannich-type reaction with a higher turnover number than the homogeneous catalyst. The higher reactivity and reusability of the catalyst comes from the coordination of the vanadyl ions to the acetyl acetate groups present in the material. The strong metalation is confirmed from Fourier Transform Infrared analysis, ¹³C MAS NMR spectral analysis and X-ray photoelectron spectroscopy measurement. Detailed characterization of the V@acac-CTF reveals that electron donation from O[^]O of the acetyl acetate group to VO(acac)₂, combined with the high surface area of acac-CTF, is responsible for the stabilization of the catalyst. Overall, this contribution highlights the necessity of stable catalytic binding sites on heterogeneous supports to fabricate greener catalysts for sustainable chemistry.

4.1. Introduction

Engineering new porous materials with exceptional porosities and active binding sites has been one of the most exciting research domains in chemistry.^{1,2} This research area is still growing rapidly, aiming at the optimization of their primary applications in gas storage/separation, catalysis, sensing, drug delivery, and energy conversions.³⁻¹¹ Metal Organic Frameworks (MOFs) and Porous Organic Frameworks/Polymers (POFs/POPs) are attracting particular attention because of their high porosity, comprised of a uniform and tunable pore size, easy incorporation of diverse guest molecules and introduction of a wide range of chemical functionalities by post-synthesis treatment.³⁻¹¹ Furthermore, designing MOFs and Covalent Organic Frameworks (COFs) with active homogeneous catalytic sites would offer new opportunities in the field of heterogeneous catalysis.¹²⁻¹⁵ Among COFs, Covalent Triazine Frameworks (CTFs)¹⁶⁻²⁰ are high performance materials with intrinsic repetitive triazine moieties, high surface areas, and importantly, low framework densities. In general, CTFs are synthesized from nitrile containing monomers *via* either the ionothermal route using molten ZnCl_2 ^{17,18} or by $\text{CF}_3\text{SO}_3\text{H}$ catalyzed^{19,20} trimerization reactions. These materials have been used as smart candidates for carbon capture and storage as well as heterogeneous catalysis.²¹⁻²⁶ Among CTFs, hexaazatriphenylene-based conjugated CTF²⁵ (HAT CTF 450/600) showed the highest CO_2 uptake value of 6.3 mmol/g at 273 K and 1 bar and bipyridine-CTF²³ synthesized at 600°C showed the highest H_2 storage of 2.12 wt% at 77 K and 1 bar.

In heterogeneous catalysis, CTFs have been used as solid support for oxidation,²⁷⁻³⁰ hydrogenation,³¹⁻³⁴ hydrolysis of ammonia borane,³⁵ carbonylation³⁶, etc. Moreover, designing new CTFs with active binding sites ($\text{N}^{\wedge}\text{N}$, $\text{N}^{\wedge}\text{O}$, $\text{O}^{\wedge}\text{O}$, etc) can produce efficient heterogeneous supports for more sustainable and environmentally friendly catalytic reactions. In this direction, CTFs containing pyridine, 2,2'-bipyridine and N-Heterocyclic Carbene (NHC) based functional ligands have been developed and used as catalytic supports for transition and noble metal complexes.²⁷⁻³⁸

Apart from these, acetyl acetone (acac) based homogeneous transition metal complexes have shown significant catalytic performance in a wide variety of organic transformation as well.³⁹⁻⁴¹ Notably, only a few acac-functionalized heterogeneous systems like silica and periodic mesoporous organosilica (PMO) have shown significant reactivity and reusability for the cross-coupling reaction, hydroxylation, click reaction, Glaser-type coupling, and alcohol oxidation.⁴²⁻⁴⁵

However, none of the Porous Organic Frameworks (POFs)/ Porous Organic Polymers (POPs) have been functionalized with acac groups yet. Therefore, in this chapter acac group was incorporated into a CTF backbone to design a robust acac-CTF supported transition metal catalyst for sustainable catalysis.

Following this rationale, acetyl acetone functionalized CTFs from 4,4'-malonyldibenzonitrile⁴⁶ were synthesized. As a proof of concept, the acac-CTF supported VO(acac)₂ complex (V@acac-CTF; Scheme 4.1) efficiently catalyzed the modified Mannich reaction with a higher turnover number (TON) than Uang *et al.*,⁴⁰ protocol where VO(acac)₂ was used as a homogenous catalyst. The catalyst is reusable for at least four reaction cycles without any loss in reactivity. This is the first example of an acac-functionalized POF employed as carbon capture and storage material and catalytic support for transition-metal complex to perform an organic transformation.

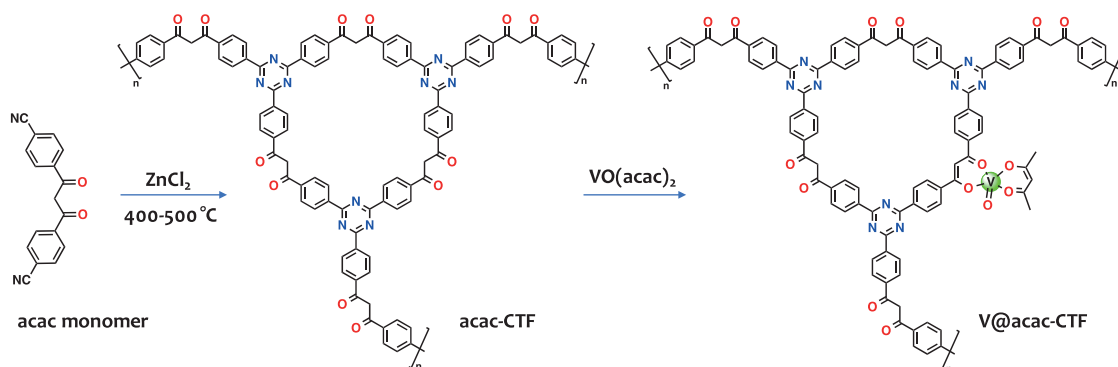
4.2. Results and discussion

4.2.1. Synthesis and Characterization of acac-CTFs

For the synthesis of the targeted acac-CTF materials, the nitrile linker, 4,4'-malonyldibenzonitrile, was synthesized by following the procedure reported by Carlucci *et al.*⁴⁶ To obtain a family of acac-functionalized CTF materials with different structural properties such as specific surface area, total pore volume, and pore structure, synthesis was undertaken at 400 °C and 500 °C using 1:5 and 1:10 molar ratio of the linker to ZnCl₂. All CTFs were synthesized in molten ZnCl₂ serving as both solvent and Lewis acid catalyst during the reaction. For the synthesis, an ampoule was charged with the monomer (500 mg, 1.8 mmol) and 5/10 equivalents of anhydrous ZnCl₂ in a glovebox (Table S4.1). Subsequently, respective ampoules were evacuated, flame-sealed, and slowly heated to the desired temperatures (400/500 °C) with the heating step of 1 °C/min for 48 h in a Nabertherm furnace oven. After the oven had cooled to room temperature, the ampoules were opened and the crude material was grounded and refluxed in water for 6 h to remove unreacted ZnCl₂, as well as filtered and thoroughly washed using distilled water. Afterward, to remove the unreacted linker and other organic impurities from the obtained materials, the black powder was stirred in HCl (1 M) overnight followed by successive washing with water until neutral pH was reached. A final wash with tetrahydrofuran was necessary to remove the water. The materials were dried and activated at 150 °C under vacuum overnight before further analysis. For more simplicity, the obtained acac

functionalized CTFs were denoted as acac-CTF-5-400, acac-CTF-10-400, acac-CTF-5-500 and acac-CTF-10-500 (acac-CTF-molar equivalent of ZnCl_2 -synthesis temperature) (Table S4.1). Among them, acac-CTF-10-500 showed the highest Brunauer-Emmett-Teller (BET) surface area of $1626 \text{ m}^2/\text{g}$ (Table 4.1).

Scheme 4.1. Schematic representation of the synthesis of acac-CTF supported $\text{VO}(\text{acac})_2$ complex, V@acac-CTF .



To ensure the presence of an acac functional group even after the harsh CTF synthesis, FT-IR measurements were performed on all four acac-CTF materials. Notably, a sharp band at 1710 cm^{-1} ($-\text{C}(\text{O})$) and 3060 cm^{-1} ($=\text{C}-\text{H}$) in acac-CTF-5-400 and acac-CTF-10-400 confirmed the presence of acac functional group, even after CTF synthesis (Figure 4.1).³⁹⁻⁴² However, in case of acac-CTF-5-500 and acac-CTF-10-500, broad bands were observed at those same places. This occurs due to the materials' carbonization at high synthesis temperatures as noted in several cases of CTFs.^{15,16} Additionally, the absence of $-\text{CN}$ band (2226 cm^{-1}) and presence 1590 cm^{-1} ($-\text{C}=\text{N}$; triazine) confirmed the complete trimerization of nitrile group to triazine ring ensuring the successful CTF formations.

To study the materials' phase and nature, powder X-ray diffraction (PXRD) measurement was undertaken (Figure S4.1). Based on these measurements, all the acac-CTF materials were found to be amorphous with a broad peak at $2\theta = 24^\circ$, indicating graphitic like two-dimensional layer formation.^{15,16} This is common for CTFs where two-dimensional sheets are stacked on top of each other at an average d -spacing of 3.7 \AA . Elemental analysis was carried out to confirm the percentage of C, N, H, and O in the materials. The obtained results indicate a lower H, N, and O content and a higher C content than the theoretical values (Table S4.2), probably due to the materials' partial carbonization.^{17,18} As expected, there might be a mixture of keto-enol tautomer formation during the CTF synthesis and of the material undergoes partial carbonization due to relatively unstable enol isomers

resulting in only 50% ideal structure (Scheme S4.1). Notably, in the case of acac-CTF-10-400, a higher C/N ratio was observed, confirming the higher nitrile cleavages and triazine ring decomposition during the trimerization process.^{17,18} Additionally, the observed lower C/O ratio in acac-CTF-10-400 suggests lower decomposition of acac functional groups and the corresponding presence of more acac functional groups in the final product.⁴⁷ The physiochemical stability of the obtained CTFs was confirmed by TGA under N₂ atmosphere (Figure S4.2). All the CTFs are stable up to 500 °C and start to decompose at higher temperatures.

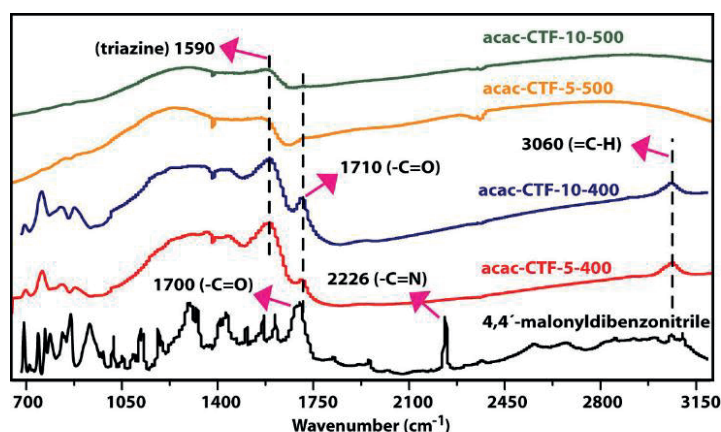


Figure 4. 1. FT-IR spectral comparison between acac-CTFs obtained at different reaction conditions with respect to the monomer.

4.2.2. Gas sorption properties

The permanent porosity and surface area properties of all the obtained acac-CTFs were explored using N₂ sorption measurements at 77 K (Figure 4.2). Before the measurement, all materials were activated at 150 °C overnight and under vacuum. The obtained plot consists of two types of isotherms (type-I, (P/P₀; <0.5 bar) and type-II (P/P₀; >0.5 bar)) like most of the reported CTFs.^{17,18, 48, 49} The steep increase observed of N₂ uptake from a region of low relative pressure confirms the materials' microporous nature whereas the presence of hysteresis from P/P₀ > 0.5 bar indicates mesopores. The observed mesopores are due to the presence of relatively large pores of size 2.5 nm (Scheme S4.2). Besides, at 500 °C corrosive fragmentation of the walls on top of the micropores cannot be ruled out which might be another reason for observed mesopores. As expected, with a temperature increase and additional ZnCl₂, the BET surface areas, total pore volumes (V_{tot}), and micropore volumes (V_{micro}) of the materials were increased (Table 4.1). Hence,

acac-CTF-10-500 showed the highest BET surface area and pore volume which is possibly due to more defects in the structure.

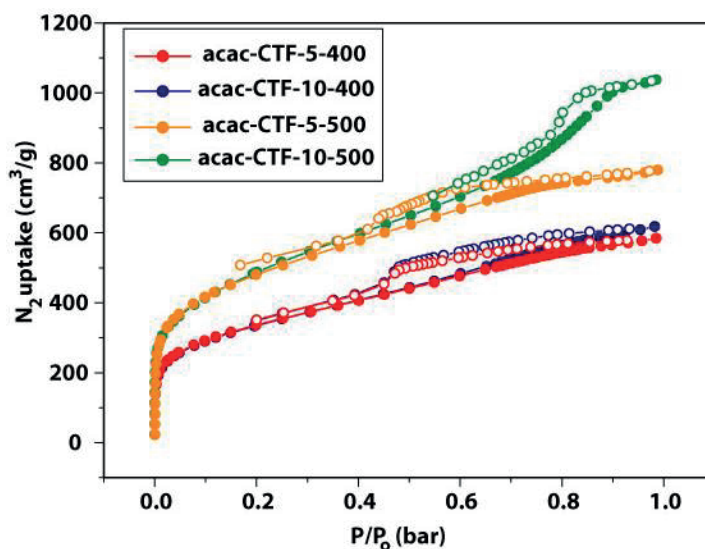


Figure 4. 2. Nitrogen adsorption/desorption isotherms of acac-CTFs measured at 77 K, filled and empty symbols represent adsorption and desorption, respectively.

Notably, acac-CTF-5-500 exhibited the highest number of micropores ($V_{\text{micro}}/V_{\text{tot}}$) with respect to the material's total pore. Additionally, the materials' polar functional groups (N-/O-), high surface area as well as their high microporous to mesoporous nature prompted us to further explore their gas sorption/storage properties at atmospheric pressure (1 bar) and their selectivity for CO₂ over N₂.

To explore the gas sorption properties of these materials, CO₂ adsorption/desorption isotherms were recorded at 273 K and 298 K, both at 1 bar (Figure 4. 3). The uptake values at both temperatures are included in Table 4.1. On comparing these values with respect to the synthesis temperatures, acac-CTFs obtained at 500 °C shows more CO₂ uptake than 400 °C.

However, the amount of ZnCl₂ used was not linearly related with the uptake amount. The acac-CTF-5-500 showed the best uptake value (3.30 mmol/g at 273 K and 1.97 mmol/g at 298 K). This might be due to a higher amount of dual polar sites (N and O; and higher number of $V_{\text{micro}}/V_{\text{tot}}$ present in the materials (Table 4.1).²⁵ Although the obtained best value is lower than HAT CTF (450/600)²⁵, it is higher than several CTFs measured at 273K [CTF-1 (2.47 mmol/g),²³ CTF-DCN-500 (2.7 mmol/g)⁵⁰, etc] including other O-containing CTFs⁵¹⁻⁵⁴.

Table 4. 1. BET Surface Areas, Pore Volumes, CO₂ and H₂ Adsorption Uptakes, CO₂ Isosteric Heat of adsorption (Q_{st}), and CO₂/N₂ selectivity of the presented CTFs.

CTF	S_{ABET}^a (m ² /g)	V_{tot}^b (cm ³ /g)	V_{micro}^c (cm ³ /g)	V_{micro}/V_{tot}	N (%) ^d	O (%) ^d	CO ₂ (mmol/g)		Q_{st}^e (kJ/mol)	CO ₂ /N ₂ ^f	H ₂ uptake (wt%)
							273 K	298 K			
acac-CTF-5-400	1131	0.90	0.77	85	5.442	3.225	2.87	1.89	23.0	38	1.51
acac-CTF-10-400	1150	0.95	0.77	80	3.908	4.929	3.06	1.96	25.5	20	1.18
acac-CTF-5-500	1556	1.20	1.10	91	5.070	5.021	3.30	1.97	28.6	46(50 ^g)	1.53
acac-CTF-10-500	1626	1.60	1.23	77	4.227	4.395	3.16	1.91	23.6	21	1.44

^a BET surface area was calculated over the relative pressure range of 0.05-0.3 at 77 K. ^b V_{tot} , total pore volume was calculated at $P/P_0 = 0.98$. ^c V_{micro} , micropore volume was calculated by N₂ adsorption isotherms using the t -plot method. ^d Percentage of nitrogen content calculated from elemental analysis. ^e Calculated isosteric heat of adsorption of CO₂ using Clausius-Clapeyron equation. ^f The selectivity of material for CO₂ adsorption over N₂ at 298 K was calculated by the Henry model, ^g Selectivity at 273 K.

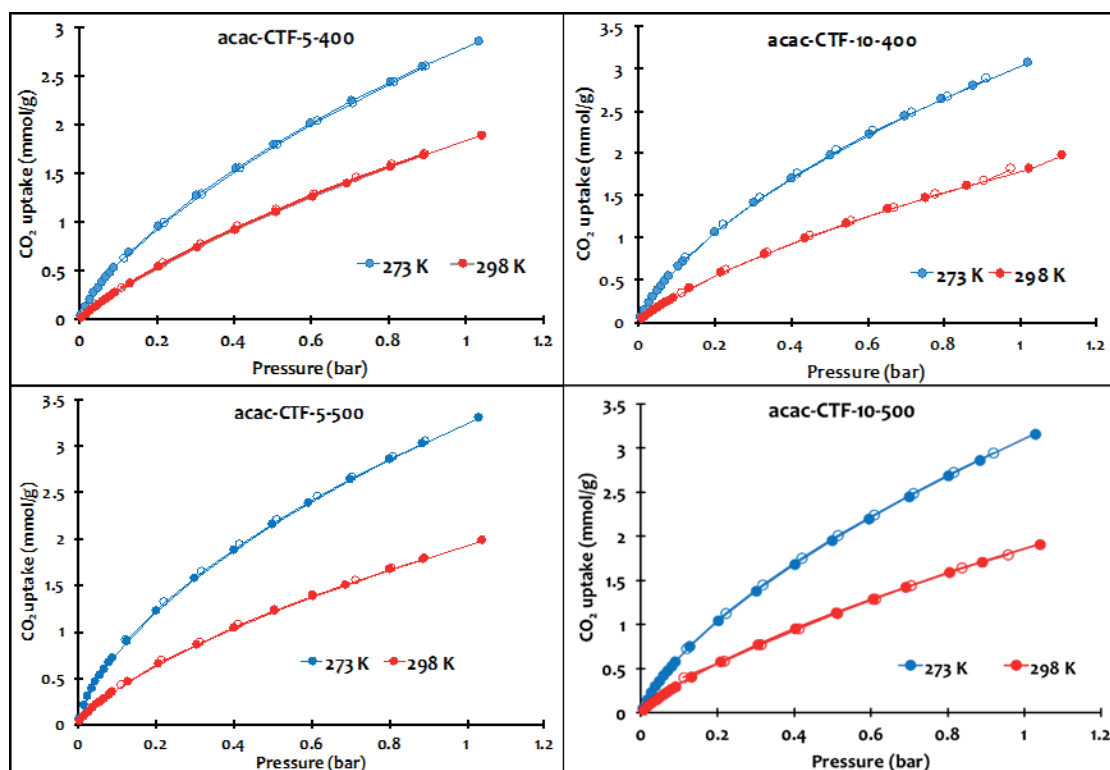


Figure 4. 3. CO₂ adsorption (closed symbols) and desorption (open symbols) isotherms of the studied acac-CTFs measured up to 1 bar at 273 K and 298 K.

Furthermore, the isosteric adsorption heat (Q_{st}) of CO₂ was calculated using the Clausius-Clapeyron equation, considering CO₂ adsorption isotherms at 273 K and 298 K. The obtained result was plotted as Q_{st} vs adsorbed amount of CO₂ (Figure S4.3). The exact values are included in Table 4.1. When comparing the acac-CTFs, it was observed that acac-CTF-5-500 shows the largest Q_{st} value (28.6 kJ/mol). This supports our statement that the acac-CTF-5-500 CO₂ uptake ranks first indeed. Moreover, all calculated acac-CTFs Q_{st} values fall within a range of 23-28 kJ/mol, a range much higher than the liquefaction heat of bulk CO₂ (17 kJ/mol)⁵⁵ and activated carbon at low CO₂ pressure (17.8 kJ/mol)⁵⁶ and are also comparable with O-containing CTFs (16 – 36 kJ/mol)⁵¹⁻⁵⁴

In addition to adsorption, the materials' selectivity to CO₂ over other gases makes up a crucial factor for carbon capture and storage as well. It has been reported that a higher reaction temperature affords a more defective CTF structure with less N content and hence lower selectivity. Therefore, to explore the impact of N content on the selectivity behavior of acac-CTFs, CO₂/N₂ selectivity was estimated using the ratio of the slopes in the Henry region of the CO₂ (< 0.05 bar) and N₂ (< 0.1 bar) adsorption isotherms at 298 K (Figure S4.4). The calculated values (Table 4.1) represent moderate to good CO₂ selectivity and are in accordance with the N/O content of the respective materials. The acac-CTF-5-400 (38) / acac-CTF-5-500 (46) showed higher selectivity than the other two. This is because higher O content and higher number ratio of V_{micro}/V_{tot} pores are less favorable for nitrogen adsorption.⁵¹

From this study, it can be concluded that not only high temperatures but also larger amounts of ZnCl₂ generate more defective acac-CTF structures with low N content and hence low CO₂ uptake as well as lower CO₂/N₂ selectivity.

After the above study concerning CO₂ adsorption and selectivity (over N₂) study, acac-CTFs materials were further tested on their H₂ storage properties. Like electricity, H₂ is considered as a potential clean energy carrier. However, safely storing large amounts of H₂ remains challenging. Anticipating better storage capacities, MOFs and COFs have recently been explored as H₂ storage materials.¹²⁻¹⁵ Therefore, to explore the H₂ storage properties of acac-CTF materials, adsorption measurements were taken at 77 K and 1 bar (Figure 4.4) and included in Table 4.1. Notably, acac-CTF-10-400/500 showed lower storage properties than acac-CTF-5-400/500. Since acac-CTF-5-400 and acac-CTF-5-500 have comparably high N content, they show a similar amount of H₂ storage of 1.51 wt% and 1.53 wt% respectively. This result signifies that materials with high N content have higher interaction and show the ability to store more H₂. The hydrogen

uptake of acac-CTF-5-400/500 is comparable to several other CTF materials and higher than the reported O-containing CTFs.⁵⁰⁻⁵³ However, the value is slightly smaller compared to that of fl-CTF-400 (1.95 wt%)²⁴ and caCTF-1-700 (2.26 wt %)⁵⁷ at 77 K and 1 bar of H₂. This allows us to conclude that the H₂ storage ability of CTFs does not necessarily only depend on the surface area but also on the N content.

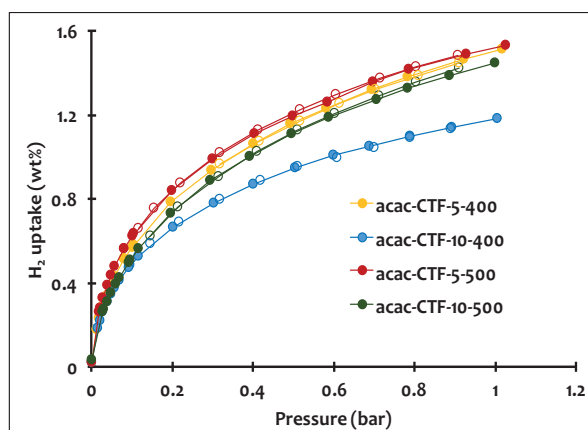


Figure 4. 4. H₂ adsorption (closed symbols) and desorption (open symbols) isotherms for acac-CTFs measured at 77 K.

4.2.3. Catalytic properties

To explore these materials as a heterogeneous support, VO(acac)₂ was anchored onto the material, as the latter was previously used as a suitable homogenous catalyst in the modified Mannich reaction.⁴⁰ However, it was reported that even after long reaction times, VO(acac)₂ showed low reactivity for substrates like 1-naphthol, phenol, and ester substituted 2-naphthol. This might be due to low intrinsic catalytic activity. Also, the separation of soluble catalyst from the reaction mixture and the production of vanadium-based waste limits the protocol. In the present case, a strong metalation between the CTF's acac functional group and VO(acac)₂ is expected because of their strong cooperativity.⁴²⁻⁴⁵ This can not only reduce the chance of catalyst deactivation during the reaction but also facilitates easy separation, increases catalyst reusability, and minimizes waste formation.

As inferred from the elemental analysis (Table S4.2), the oxygen content of acac-CTF-10-400 and acac-CTF-5-500 is similar and higher than in the other two acac-CTFs. The strong carbonyl stretching band of the acac functional group (Figure 4.1) combined with the lowest C/O ratio in acac-CTF-10-400 results in the largest number of available acac-functional sites when compared to the other three. Moreover, the pore size and surface

area of acac-CTF-10-400 is sufficient to efficiently diffuse 2-naphthol, NMO and the target Mannich product during the catalytic reactions. Therefore, acac-CTF-10-400 was chosen to act as catalytic support to anchor VO(acac)₂ and explore the latter's catalytic activities for the targeted Mannich reaction. Before these catalytic reactions, the stability of acac-CTF was determined and found stable in air, moisture and insoluble in common organic solvents such as dichloromethane, tetrahydrofuran, acetone, ethanol, methanol, diethyl ether, chloroform, dimethylformamide and dimethyl sulfoxide.

The V@acac-CTF catalyst was synthesized via the post-synthetic metalation method, where VO(acac)₂ was used as the metal source and toluene as solvent. In a typical experiment, 144 mg (0.54 mmol) of VO(acac)₂ was dissolved in 50 mL of anhydrous toluene to which 500 mg (1.8 mmol) of acac-CTF was added under argon. The mixture was stirred under reflux overnight, filtered under vacuum and dried. Further, the catalyst was first washed thoroughly using Soxhlet extraction with toluene to remove weakly bound VO(acac)₂, then filtered and dried under vacuum. Finally, the catalyst was dried under vacuum at 120 °C for 12 h to remove the solvent and used for further experiments. From the CHNO analysis of V@acac-CTF, the decrease of the C content and increase of the O content confirmed the incorporation of VO(acac)₂ in the framework (Table S4.2). To determine the exact amount of metal ions present in fresh V@acac-CTF catalyst, an ICP-OES measurement was undertaken and the sample contained 0.306 mmol/g (1.6%) of vanadium ions. The absence of zinc ion confirmed that all the accessible residual zinc was replaced by vanadium ion. However, the remaining residual amount can be assigned to the trapped metal salts or anions in the pores that are impossible to remove.^{17, 23, 49}

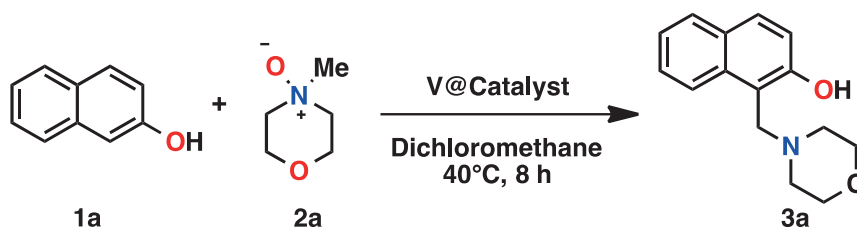
In preliminary screening, V@acac-CTF was used as the catalyst for the Mannich reaction between 2-naphthol (**1a**) and three equivalents of *N*-methylmorpholine *N*-oxide (NMO) (**2a**) in dichloromethane (DCM) at 40 °C for 24 h (Table 4.2, entry 2). The reaction mixture was analyzed at different time intervals using ¹H NMR-spectroscopy. 15% of the target product 1-(morpholinomethyl)naphthalen-2-ol (**3a**) was obtained within 30 minutes (Figure S4.5). The yield increased up to 95% after 8 h of reaction time. However, even after 24 h, the reaction yield no longer improved.

To eliminate the role of residual zinc, blank catalytic tests were performed using pristine acac-CTFs. From the ¹H NMR analysis, **3a** was not detected in any cases, which ruled out the interference of zinc in the catalytic reaction. To further explore the performance of other acac-CTFs, acac-CTF-10-500 was chosen because it has a relatively low zinc content (Table S4.2) and it exhibits mesopore (Figure 4.1). It has been reported that

mesopores might speed up the diffusion of the reactants to the catalytic center and hence better reactivity can be expected.²⁶ Therefore, V@acac-CTF-10-500 was synthesized using a similar method and used as a catalyst for the Mannich reaction under similar conditions. From ¹H NMR analysis of the reaction mixture, it was observed that the reaction was completed after only 8h with similar reactivity as the V@acac-CTF-10-400. This further confirmed that residual zinc has no interference on the reactivity and the surface area as well as pore volume of acac-CTFs are sufficient to allow easy substrate diffusion to the vanadium center.

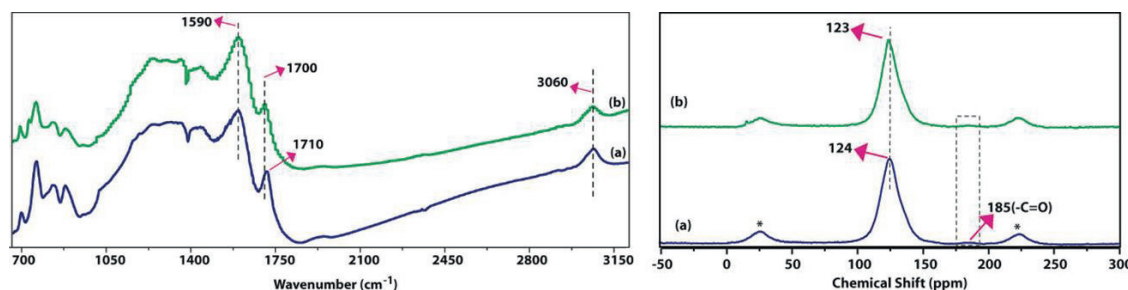
Further, to explore the probability of vanadium ions leaching from the support, hot filtration techniques were performed. The catalyst was removed from the mother liquor after 4 h and the reaction allowed to proceed for further 8 h (Figure S4.6). Notably, the reaction did not proceed at all which rules out leaching of active species. In addition, ICP-OES measurement of recovered catalyst confirmed no change in vanadium content after the first cycle of the catalytic reaction. After the first cycle, the turnover number (TON = 213) of the catalyst was calculated and found to be 23 times greater than the homogeneous catalyst. This large TON combined with its recyclability adds great value to the V@acac-CTF and hence proves that acac-CTF is likely to be used as catalytic support for the fabrication of greener heterogeneous catalysts. Furthermore, to avoid using excess oxidant (three equivalents of NMO⁴⁰), the reactions were repeated using two equivalents (Table 4.2, entry 3) and one equivalent (Table 4.2, entry 4) of NMO under the same reaction conditions. To our delight, 95% of **3a** was isolated in both cases. This further added to the novelty of V@acac-CTF over homogeneous catalysts. Additionally, the reusability of the V@acac-CTF was explored using the same catalyst for successive reactions. The catalyst retains similar reactivity over at least four reaction cycles.

To understand the coordinative interaction, an FT-IR analysis of V@acac-CTF was performed and compared with the pristine acac-CTF (Figure 4.5). The observed shifting of C=O stretching frequency of the acac group from 1710 cm⁻¹ to 1700 cm⁻¹ confirmed the coordination of vanadium ions towards O^O binding sites. The observed no changes at 1590 cm⁻¹ ruled out the possible coordination of vanadium ions to the triazine-Ns. Thus, a strong coordination of the vanadium species on the acac-CTF resulted in a greater reactivity of V@acac-CTF compared to its homogenous counterpart.

Table 4. 2. Catalytic activity of V@acac-CTF catalysts for Mannich reaction.

Entry	Catalyst	1a:2a	3a (%) ^a
1 ^b	VO(acac) ₂	1:3	100 (92)
2 ^c	V@acac-CTF	1:3	100 (95)
3 ^c	V@acac-CTF	1:2	100 (95)
4 ^c	V@acac-CTF	1:1	100 (95)

^aConversion (yield) was calculated from ¹H NMR analysis using mesitylene as internal standard, ^b10 mol%, ^c0.306 mmol/g of vanadium ion calculated from ICP-OES analysis.

**Figure 4. 5.** FT-IR spectra comparison between pristine and ¹³C CP-MAS ssNMR spectral comparison between (a) pristine acac-CTF and (b) fresh V@acac-CTF catalyst.

Additionally, to support the coordinative interaction between VO(acac)₂ and pristine acac-CTF, ¹³C-CP-MAS-ss-NMR spectroscopic analyses were carried out on both the pristine CTF and V@acac-CTF catalyst and compared. As shown in Figure S4.5, the peak at 124 ppm corresponds to the aromatic C. In addition, the small peak at 185 ppm indicates the presence of a C=O entity in the acac group.

The slight decrease in intensity of the C=O bond in the acac group and shift in aromatic carbon towards a lower chemical shift (123 ppm) further support the metalation. Surprisingly, peaks corresponding to triazine-C and CH₂ were not observed which might

be due to their relatively lower concentration. A similar observation was also noticed recently.^{49, 59}

To explore the surface area properties after anchoring of VO(acac)₂, the N₂ adsorption isotherm of V@acac-CTF catalyst was measured and compared with the pristine acac-CTF (Figure S4.7). As expected, both the BET surface area (900 m²/g) and pore volume (0.65 cm³/g) rank lower when compared to pristine acac-CTF corroborating to the successful coordination. Bright-field scanning transmission electron microscopy (BF-STEM; Figures S4.8-S4.9) analysis shows a homogeneous distribution of C, N, O and vanadium elements in acac-CTF as well as in V@acac-CTF.

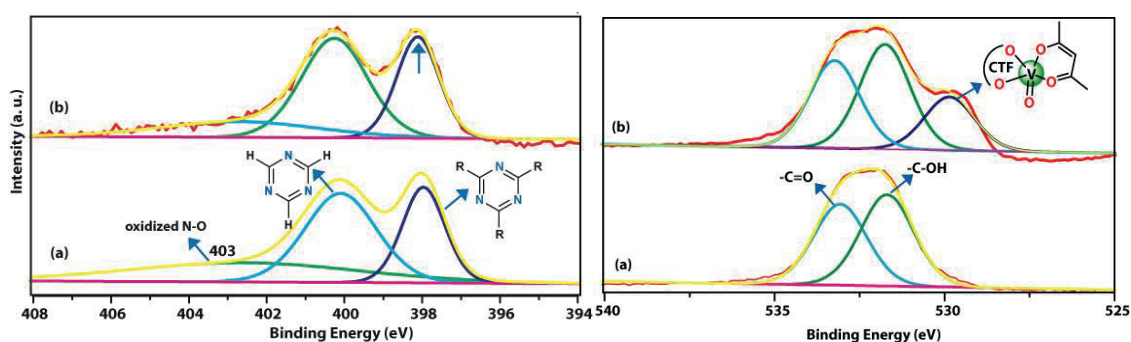


Figure 4. 6. Deconvoluted XPS N 1s spectra (left) and O 1s spectra (right) of (a) pristine acac-CTF (b) V@acac-CTF.

Furthermore, to explore the elements' nature and their binding energy as well as the nature of catalysts and the amount of catalytic active center, X-ray photoelectron spectroscopy (XPS) analysis was performed. To study the coordinative interaction, XPS spectra of pristine acac-CTF and V@acac-CTF were analyzed by fitting the respective atoms to their binding energies. The observed XPS C 1s (deconvoluted) peaks at 284, 285, and 288 eV can be assigned to C-C/C-H, C-N, and C=O species respectively present in pristine acac-CTF (Figure S4.10). A similar observation was obtained for V@acac-CTF, apart from the decrease of C=O intensity and peak broadening due to the coordinative interaction of acac group with the vanadium center. The N 1s spectrum of acac-CTF showed three peaks at 398, 400 and 403 eV (Figure 4.6(a), left) which can respectively be assigned to the phenyl functionalized triazine unit, the non-functionalized triazine and the oxidized N-O species.⁵⁸

As expected, no changes were observed in fresh V@acac-CTF (Figure 4.6(b), left) emphasizing the absence of any sort of coordination towards triazine-N.⁵⁸ The XPS O 1s spectra of acac-CTF showed two peaks at 533 and 531 eV which can be assigned to C=O

and -C-OH due to the tautomerization of acac group in both keto and enol form (Figure 4.6(a), right). Moreover, O 1s spectra of V@acac-CTF showed an additional peak at 529 eV which can be assigned to the V=O bond present in the catalyst (Figure 4.6(b), right).

In addition, to confirm the oxidation state of vanadium ions, the XPS spectrum of V@acac-CTF in the V2p region (Figure 4.7) was measured. The observed peak at binding energy of vanadium ion 516 eV can be assigned to the characteristic V 2p_{3/2} peak, as the previously reported VO(acac)₂, SB-V and VO(acac)₂ anchored on PMO as well.⁴⁴ The, binding energy at 523 eV can be assigned to V 2p_{1/2} peak. This clearly indicates the presence of V(IV) in the V@acac-CTF.

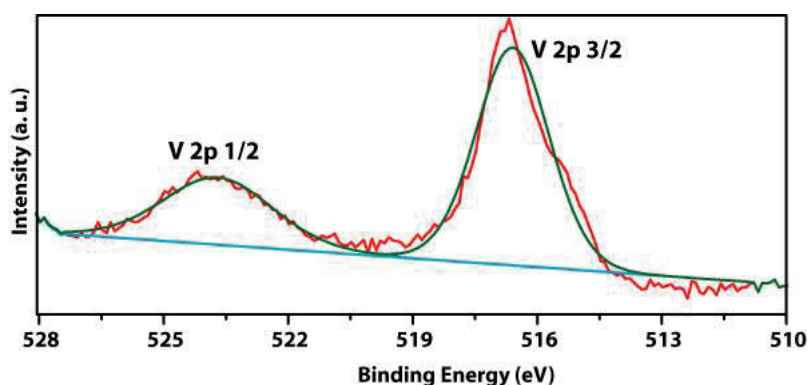


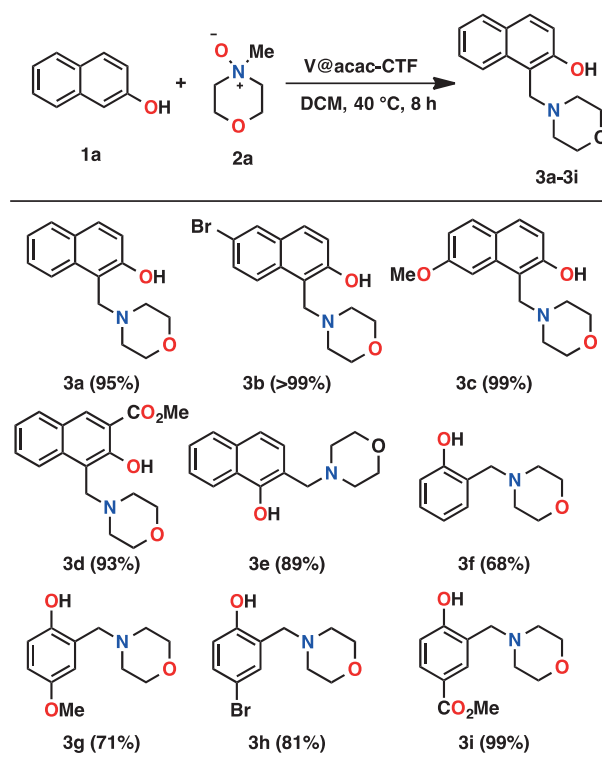
Figure 4. 7. Deconvoluted XPS spectra of vanadium in the V 2p region for V@acac-CTF catalyst.

The above experimental evidence and discussion confirmed that the strong interaction between acac-CTF and V(IV) ion leads to the excellent reactivity of the catalyst.

After complete characterization of the catalyst, a plausible mechanism was proposed which involves similar steps as reported by Uang *et al.*⁴⁰ (Scheme S4.3). In brief, the coordination of NMO to the V(IV) center followed by intramolecular elimination facilitates a six-membered transition state (A) which results in the formation of iminium ion (B). The abstraction of a proton from 2-naphthol by [V(OH)(O⁻)] generates a lone pair electron on the oxygen which migrates to the aromatic ring to generate acidic C that subsequently attacks the iminium ion to form the target Mannich base (**3a**). Further [V(OH)₂] releases one water molecule to generate the catalyst. Since the surface area of the catalyst is very high, many substrates diffuse into the pores of the materials and have more access to the catalytic reactive center. This increases the interaction of the naphtholate ion with the iminium ion and hence shows higher reactivity. This further supported the importance of the materials for the *in-situ* formation of iminium ion from

amine-oxide catalyzed heterogeneous catalysts which have never been reported yet. In addition, the robustness of the support increases the stability of the catalyst for multiple reaction cycles.

Table 4. 3. Substrate scope for Mannich reaction using V@acac-CTF.



^aYields are calculated from ¹H NMR using mesitylene as a internal standard

The reactivity of V@acac-CTF with different substituted 2-naphthol, 1-naphthol, phenol derivatives was also examined (Table 4.3) and compared to the homogeneous reaction. Surprisingly, bromo- (**3b**), methoxy- (**3c**), ester-substituted 2-naphthol (**3d**) showed above 90% of yield in 8 h, whereas in the homogenous reaction system, <90% of **3b** and **3c** and only 61% of **3d** was reported even after 72 h of reaction. In addition, 1-naphthol, phenol, and phenol derivate showed moderate to good yield under optimized reaction conditions. The excellent reactivity of V@acac-CTF compared to that of VO(acac)₂ can be attributed to the robustness of the CTF support, its large surface area, sufficient pore volume that facilitates efficient substrate and product diffusion and importantly, the presence of a catalytic binding site. Therefore, upon acac functionalization, the CTF offers a strong coordinative interaction to the V(IV) center by O[^]O coordination sites and minimized catalytic deactivation.

4.3. Conclusion

In conclusion, for the first time, a family of acetyl acetone functionalized Covalent Triazine Framework materials were synthesized under ionothermal conditions. The obtained CTF materials showed tunable surface areas and porosities based on variations in the synthesis temperature and molar equivalents of ZnCl_2 used. Among them, the acac-CTF synthesized using 5 equivalents of ZnCl_2 at 500 °C showed both the best CO_2 uptake at 273 K (3.30 mmol/g) and 298 K (1.97 mmol/g) at 1 bar as well as the highest H_2 storage uptake (1.53 wt%) at 77 K and 1 bar. In addition, a heterogeneous catalyst (V@acac-CTF) was prepared by anchoring VO(acac)_2 on pristine acac-CTF that showed excellent reactivity in a modified Mannich reaction with a TON of 213 and a wide substrate scope. Significantly, the heterogeneous catalyst showed excellent activity with the substrate where the homogenous VO(acac)_2 catalyst failed instead. Characterization of V@acac-CTF revealed that coordinative interaction between V(IV) with the O^O site of the acetyl acetone group, high surface area, the robustness of the material, and efficient diffusion of substrate and products caused such high reactivity. V@acac-CTF not only showed excellent reactivity but also allowed reusability, making the reaction more sustainable. Furthermore, the expected *in situ* formation of iminium ions from tertiary amine oxides in presence of V(IV) anchored on acetyl acetone functionalized CTF facilitates the potential application in modified Mannich type reactions. The above results signify the importance of catalytic binding site on the porous supports for efficient coordinative interaction and hence greater reactivity. Creating heterogeneity showed promising results in the catalytic reactivity compared to the homogeneous catalyst. These results show the potential of customized-CTFs with in-built catalytic active sites for sustainable chemistry.

4.4. Experimental section

4.4.1. Materials and Methods

The required chemicals were purchased from Sigma-Aldrich and used without further purifications. The ^1H and ^{13}C NMR analysis of the nitrile linker and all Mannich reaction products was performed on a Bruker Advance 300 MHz spectrometer using mesitylene as an internal standard. Elemental analyses (C, H, N, and O) were carried out on a Thermo Scientific Flash 2000 CHNS-O analyzer equipped with a TCD detector. Fourier Transform Infrared Spectroscopy (FT-IR) in the region of 4000-650 cm^{-1} was performed with a Thermo Nicolet 6700 FT-IR spectrometer equipped with a nitro-gen-cooled MCT detector and a KBr beam splitter. Dinitrogen (N_2) adsorption isotherms were obtained

using a Belsorp Mini apparatus measured at 77 K. Carbon dioxide (CO₂) and dihydrogen (H₂) adsorption measurements were carried out on a Quantachrome iSorb-HP gas sorption analyzer. X-ray powder diffraction (XRPD) patterns were collected on a Thermo Scientific ARL X'Tra diffractometer, operated at 40 kV, 30 mA using Cu-K α radiation ($\lambda = 1.5406 \text{ \AA}$). Thermogravimetric analysis (TGA) was performed on a Netzsch STA-449 F3 Jupiter-simultaneous TG-DSC analyzer within a temperature range of 20 – 800 °C, under N₂ atmosphere and heating rate of 2 °C/min. ¹³C MAS NMR spectra were acquired at 125.69 MHz using a 4 mm MAS NMR probe with a spinning rate of 8 kHz and a pulse width of 2.5 μ s for a $\pi/4$ pulse. 1800-2700 scans were further accumulated with a 4s recycle delay. The X-ray photoelectron spectroscopy (XPS) measurements were performed on a Thermo Fisher Scientific Escalab 250 Xi. The vanadium loading was determined by an Inductively Coupled Plasma (ICP) measurement Optima 8000 atomic Emission Spectrometer (ICP-OES). Bright-field Scanning Transmission Electron Microscopy (BF-STEM) was performed on a JEOL JEM-2200FS high-resolution scanning transmission electron microscope with a spatial resolution of 0.13 nm, an image lens spherical aberration corrector, an electron energy loss spectrometer (filter) and an emission field gun (FEG) operating at 200 KeV.

4.5. References

- (1) M. H. Sun, S. Z. Huang, L. H. Chen, Y. Li, x. Y. Yang, Z. Y. Yuan, B. L. Su, *Chem. Soc. Rev.* 2016, 45, 3479-3563.
- (2) J. Liang, Z. B. Liang, R. Q. Zou, Y. L. Zhao, *Adv. Mat.* 2017, 29, 1701139.
- (3) S. M. J. Rogge, A. Bavykina, J. Hajek, H. Garcia, A. L. Olivos-Suarez, A. Sepulveda-Escribano, A. Vimont, G. Clet, P. Bazin, F. Kapteijn, M. Daturi, Ramos-Fernandez, F. X. L. I. Xamena, V. Van Speybroeck, J. Gascon, *Chem. Soc. Rev.* 2017, 46, 3134-3184.
- (4) C. S. Diercks, O. M. Yaghi, *The Atom, the Molecule, and the Covalent Organic Framework*, *Science* 2017, 355, 6328.
- (5) H. Furukawa, K. E. Cordova, M. O’Keeffe, O. M. Yaghi, *The Chemistry and Applications of Metal-Organic Frameworks*, *Science* 2013, 341, 6149.
- (6) S. Das, P. Heasman, T. Ben, S. L. Qiu, *Chem. Rev.* 2017, 117, 1515-1563.
- (7) N. Huang, P. Wang, D. L. Jiang, *Nat. Rev. Mater.* 2016, 1, 16068.

- (8) P. J. Waller, F. Gandara, O. M. Yaghi, *Acc. Chem. Res.* 2015, 48, 3053-3063.
- (9) S. T. Meek, J. A. Greathouse, M. D. Allendorf, *Adv. Mat.* 2011, 23, 249-267.
- (10) P. Kaur, J. T. Hupp, S. T. Nguyen, *ACS Catal.* 2011, 1, 819-835.
- (11) Q. Sun, Z. Dai, X. Meng, L. Wang, F-S. Xiao, *ACS Catal.* 2015, 5, 4556-4567.
- (12) S. N. Zhao, X. Z. Song, S. Y. Song, H. J. Zhang, *Coord. Chem. Rev.* 2017, 337, 80-96.
- (13) C. D. Wu, M. Zhao, *Adv. Mat.* 2017, 29, 1605446.
- (14) Z. Q. Wang, S. M. Cohen, *Chem. Soc. Rev.* 2009, 38, 1315-1329.
- (15) S. Y. Ding, W. Wang, *Chem. Soc. Rev.* 2013, 42, 548-568.
- (16) K. Sakaushi, M. Antonietti, *Acc. Chem. Res.* 2015, 48, 1591-1600.
- (17) P. Kuhn, M. Antonietti, A. Thomas, *Angew. Chem. Int. Ed.* 2008, 47, 3450-3453.
- (18) P. Kuhn, A. Forget, D. Su, A. Thomas, M. Antonietti, *J. Am. Chem. Soc.* 2008, 130, 13333-13337.
- (19) S. Ren, M. J. Bojdys, R. Dawson, A. Laybourn, Y. Z. Khimyak, D. J. Adams, A. I. Cooper, *Adv. Mat.* 2012, 24, 2357-2361.
- (20) W. Huang, Z. J. Wang, B. C. Ma, S. Ghasimi, D. Gehrig, F. Laquai, K. Landfester, K. A. I. Zhang, *J. Mat. Chem. A* 2016, 4, 7555-7559.
- (21) P. Puthiaraj, Y. Lee, S. Q. Zhang, W. S. J. Ahn, *J. Mat. Chem. A* 2016, 4, 16288-16311.
- (22) A. Bhunia, D. Esquivel, S. Dey, *J. Mater. Chem. A* 2016, 4, 13450-13457.
- (23) S. Hug, L. Stegbauer, H. Oh, M. Hirscher, B. V. Lotsch, *Chem. Mat.* 2015, 27, 8001-8010.
- (24) S. Hug, M. B. Mesch, H. Oh, N. Popp, M. Hirscher, J. Senker, B. V. Lotsch, *J. Mater. Chem. A* 2014, 2, 5928-5936.
- (25) X. Zhu, C. Tian, G. M. Veith, C. W. Abney, J. Dehaudt, D. Sheng, *J. Am. Chem. Soc.* 2016, 138, 11497-11500.
- (26) J. Roeser, K. Kailasam, A. Thomas, *ChemSusChem* 2012, 5, 1793-1799.
- (27) J. Artz, S. Mallmann, R. Palkovits, *ChemSusChem* 2015, 8, 672-679.
- (28) J. Artz, R. Palkovits, *ChemSusChem* 2015, 8, 3832-3838.

- (29) C. E. Chan-Thaw, A. Villa, D. Wang, V. D. Santo, A. O. Biroli, G. M. Veith, A. Thomas, L. Prati, *ChemCatChem* 2015, 7, 2149-2154.
- (30) W. Huang, B. C. Ma, H. Li, R. Li, L. Wang, K. Landfester, K. A. I. Zhang, *ACS Catal.* 2017, 7, 5438-5442.
- (31) P. Sudakar, G. H. Gunasekar, I. Baek, S. Yoon, *Green Chem.* 2016, 18, 6456-6461.
- (32) K. Park, G. H. Gunasekar, N. Prakash, K. D. Jung, S. Yoon, *ChemSusChem* 2015, 8, 3410-3413.
- (33) T. He, L. Liu, G. Wu, P. Chen, *J. Mater. Chem. A* 2015, 3, 16235-16241.
- (34) A. V. Bavykina, H. H. Mautscke, F. Kapteijn, J. Gascon, I. Llabres F. X. Xamena, *CrystEngComm* 2017, 19, 4166-4170.
- (35) Z. Li, T. He, L. Liu, W. Chen, M. Zhang, G. Wu, P. Chen, *Chem. Sci.* 2017, 8, 781-788.
- (36) Z. Wang, C. Liu, Y. Hu, B. Zhang, *Chem. Commun.* 2016, 52, 2960-2963.
- (37) S. Hug, M. E. Tauchert, S. Li, U. E. Pachmayr, B. V. Lotsch, *J. Mat. Chem.* 2012, 22, 13956-13964.
- (38) G. H. Gunasekar, K. Park, V. Ganesan, L. Lee, N. K. Kim, K. D. Jung, S. Yoon, *Chem. Mat.* 2017, 29, 6740-6748.
- (39) P. Kaswan, A. Porter, K. Pericherla, M. Simone, S. Peters, A. Kumar, B. Deboef, *Org. Lett.* 2015, 17, 5208-5211.
- (40) D-R. Hwang, B-J. Uang, *Org. Lett.* 2002, 4, 463-466.
- (41) Y.-F. Wang, S. Chiba, *J. Am. Chem. Soc.*, 2009, 131, 12570-12572.
- (42) A. R. Hajipour, G. Azizi, *Green Chem.*, 2013, 15, 1030-1034.
- (43) A. Hajipour, G. Azizi, *Appl. Organometal. Chem.* 2015, 29, 247-253.
- (44) P. Borah, X. Ma, K. T. Nguyen, Y. Zhao, *Angew. Chem. Int. Ed.* 2012, 51, 7756-776.
- (45) B. Lai, Z. Huang, Z. Jia, R. Bai, Y. Gu, *Catal. Sci. Technol.* 2016, 6, 1810-1820.
- (46) L. Carlucci, G. Ciani, S. Maggini, D. M. Proserpio, M. Visonti, *Chem. Eur. J.* 2010, 16, 12328-12341.
- (47) S. Abdolhosseinzadeh, H. Asgharzadeh, H. S. Kim, *Sci. Rep.* 2015, 5, 10160.

- (48) G. Wang, G.; Leus, K.; Zhao, S.; Van Der Voort, P. Newly Designed Covalent Triazine Framework Based on Novel N-Heteroaromatic Building Blocks for Efficient CO₂ and H₂ Capture and Storage, *ACS Appl. Mater. Interfaces*, 2018, 10, 1244-1249.
- (49) G. Wang, K. Leus, H. Jena, C. Krishnaraj, S. Zhao, H. Depauw, N. Tahir, Y. Liu, P. Van Der Voort, *Journal of Materials Chemistry A*, 2018, 6, 6370-6375.
- (50) Y. Zhao, K. X. Yao, B. Teng, T. Zhang, Y. Han, *Energy Environ. Sci.* 2013, 6, 3684-3692.
- (51) K. Yuan, C. Liu, J. Han, G. Yu, J. Wang, H. Duan, Z. Wang, X. Jian, *RSC Adv.*, 2016, 6, 12009-12020.
- (52) M. G. Rabbani, T. Islamoglu, H. M. El-Kaderi, *J. Mater. Chem. A* 2017, 5, 258-265.
- (53) K. Yuan, C. Liu, L. Zong, G. Yu, S. Cheng, J. Wang, Z. Weng, X. Jian, *ACS Appl. Mater. Interfaces* 2017, 9, 13201-13212.
- (54) S. Wu, Y. Liu, G. Yu, J. Guan, C. Pan, Y. Du, X. Xiong, Z. Wang, *Macromolecules* 2014, 47, 2875-2882.
- (55) S. Keskin, T. M. van Heest, D. S. Sholl, *ChemSusChem* 2010, 3, 879-891.
- (56) S. Himeno, T. Komatsu, S. Fujita, *J. Chem. Eng. Data* 2005, 50, 369-376.
- (57) Y. J. Lee, S. N. Talapaneni, A. Coskun, *ACS Appl. Mater. Interfaces* 2017, 9, 30679-30685.
- (58) D. Y. Osadchii, A. I. Olivos-Suarez, A. V. Bavykina, J. Gascon, *Langmuir* 2017, 33, 14278-14285.
- (59) K. Wang, H. Huang, D. Liu, C. Wang, J. Li, C. Zhong, *Environmental Science & Technology*, 2016, 50, 4869-4876.

4.6. Supporting Information

Synthesis of linker 4,4'-malonyldibenzonitrile (acac-CN):

A 1.66 g (41.51 mmol) of NaH (60% in mineral oil) was dispersed in 50 mL of anhydrous tetrahydrofuran (THF) under argon atmosphere and stirred for 30 minutes. The heterogeneous mixture was transferred to ice bath and to that solid 4-acetylbzenzonitrile (2.0 g, 13.7 mmol) was added. Once the mixture become slightly yellow in color, a solution of methyl 4-cyanobenzoate (2.42 g, 15.03 mmol) in anhydrous THF (10 mL) was then added dropwise over a period of 30 min under Ar. The whole mixture was stirred for 1 h in ice bath followed by 1 h in room temperature. The mixture was refluxed for 24 h under Ar and then quenched with ice. The pH of the reaction mixture was adjusted to neutral by the slow addition of 1 N of HCl and linker was recovered by filtration and washed with distilled H₂O. The sticky yellow solids were washed with hot EtOH several times to afford pure linker as a pale-yellow solid. Yield: 85%; ¹H NMR (400 MHz, CDCl₃): d = 8.11 (d, *J*=8.7, 4 H), 7.844 (d, *J*=8.4, 4 H), 6.878 (s, 1 H); IR (KBr, cm⁻¹): 3460, 3100, 3060, 3050, 2230, 1700, 1610, 1570, 1510, 1430, 1320, 1290, 1180, 1120, 1020, 935, 862, 769, 744, 692.

Table S4.1. Synthetic conditions and abbreviations used for acac-CTFs.^a

Sl. No	acac Linker : ZnCl ₂	Temperature (°C)	Yield (%)	abbreviations
1	1:5	400	55	acac-CTF-5-400
2	1:10	400	54	acac-CTF-10-400
3	1:5	500	45	acac-CTF-5-500
4	1:10	500	40	acac-CTF-10-500
^a 48 h				

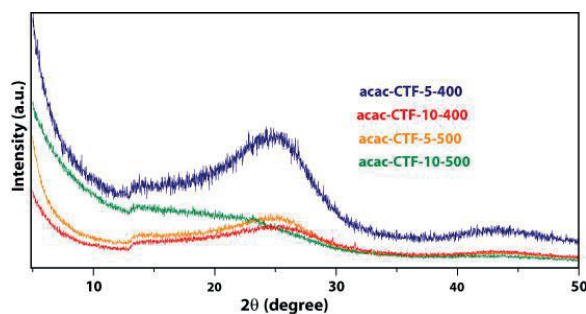
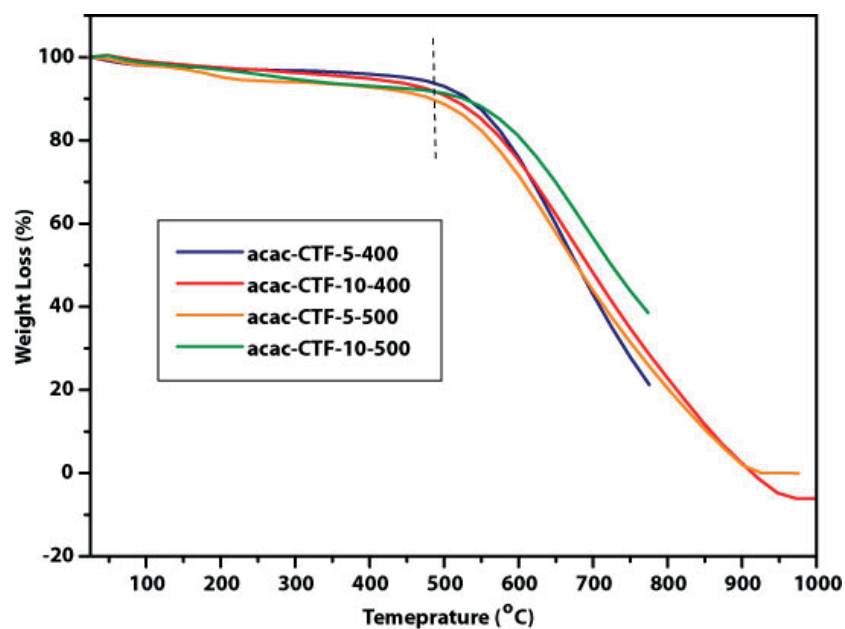
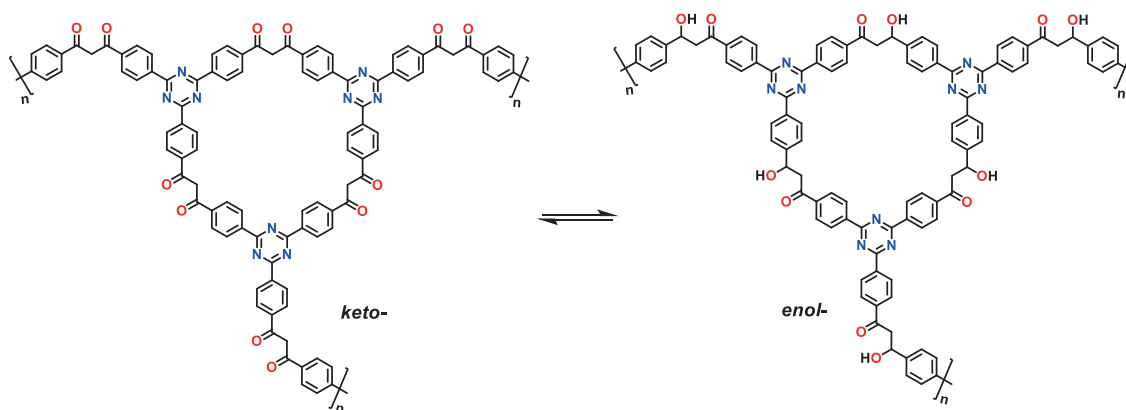


Figure S4.1. Powder X-ray diffraction (PXRD) spectra of acac-CTFs.

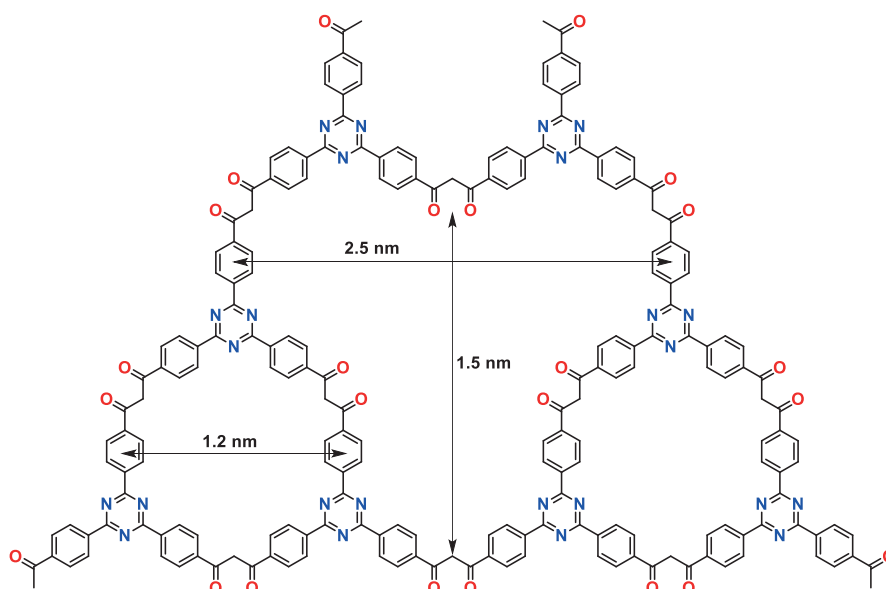
Table S4.2. Elemental Analysis of all the acac-CTFs and V@acac-CTF-10-400.

Element	acac-CTFs					V@acac-CTF	
	Calculated (%)	Found (%)				Calculated (%)	Found (%)
		5-400	10-400	5-500	10-500		
C	74.44	83.256	80.231	82.501	83.619	59.87	65.670
H	3.68	2.923	2.678	1.449	1.125	4.11	2.756
N	10.21	5.442	3.908	5.070	4.227	6.35	3.028
O	11.67	3.225	4.929	5.021	4.395	18.13	16.273
C/N	7.290	15.298	20.529	16.272	19.550	9.428	21.687
C/O	6.378	25.518	16.227	16.431	19.550	3.302	4.035

**Figure S4.2.** Thermogravimetric analysis spectra of acac-CTFs.



Scheme S4.1. Possible keto-enol tautomer formation during the CTF synthesis.



Scheme S4.2. Schematic representation of supermicropores (1.2 nm) and mesopores (2.5 nm) present in acac-CTF material.

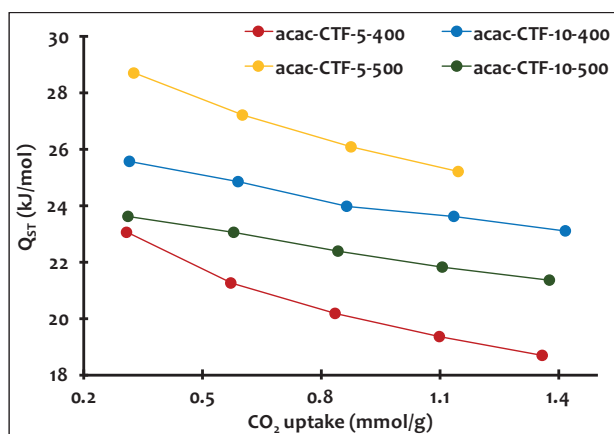


Figure S4.3. Isosteric heat (Q_{st}) of CO₂ adsorption for all acac-CTFs.

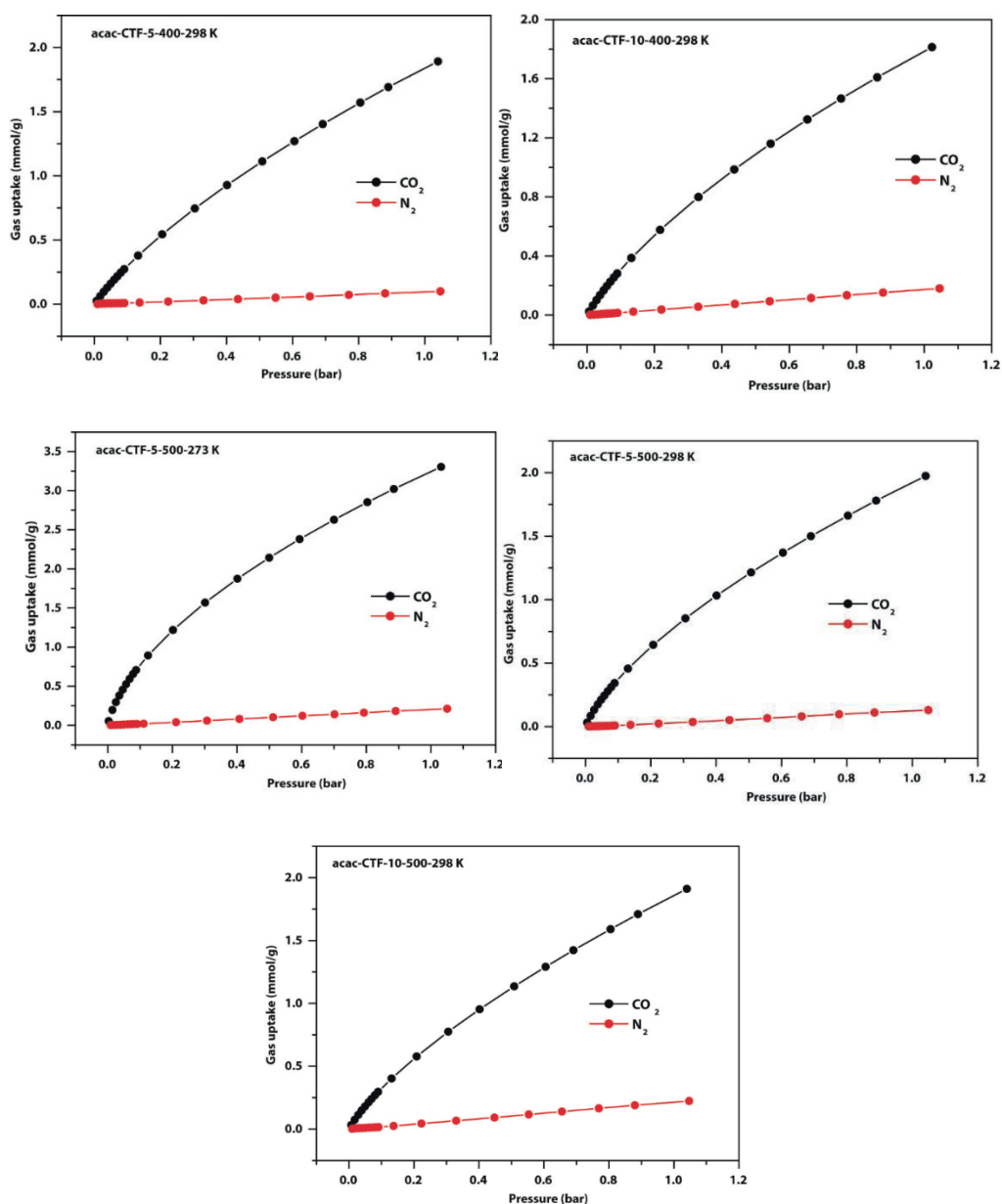


Figure S4.4. CO₂ and N₂ adsorption isotherms of acac-CTFs measured at 298 K and 1 bar.

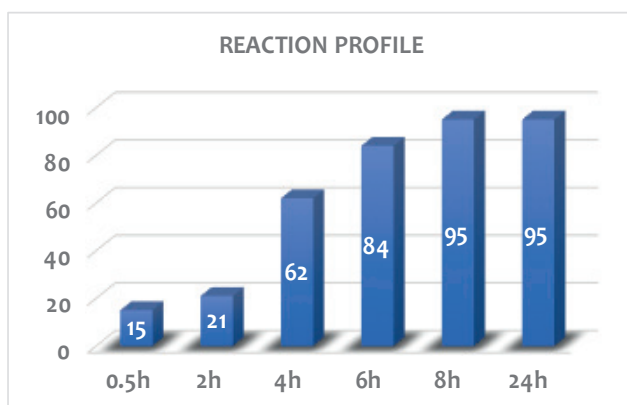


Figure S4.5. Time dependent yield of the modified Mannich reactions using V@acac-CTF catalyst (Yields are calculated using Mesitylene as internal standard).

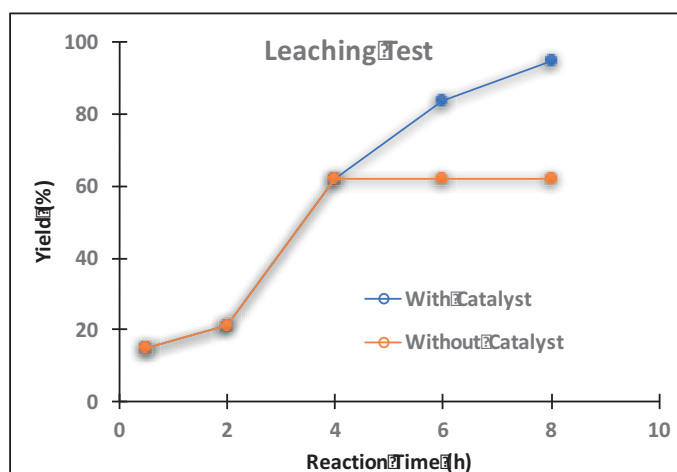


Figure S4.6. Reaction profile with or without the catalyst (after separating the catalyst from the reaction mixture via hot-filtration technique).

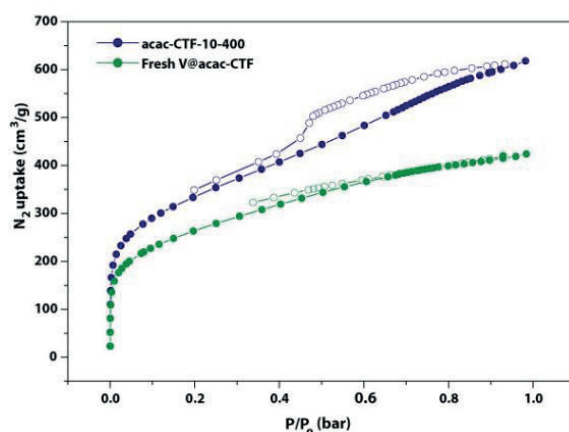


Figure S4.7. Nitrogen adsorption/desorption isotherms of acac-CTF, fresh V@acac-CTF and recovered V@acac-CTF measured at 77 K, filled and empty symbols represent adsorption and desorption, respectively.

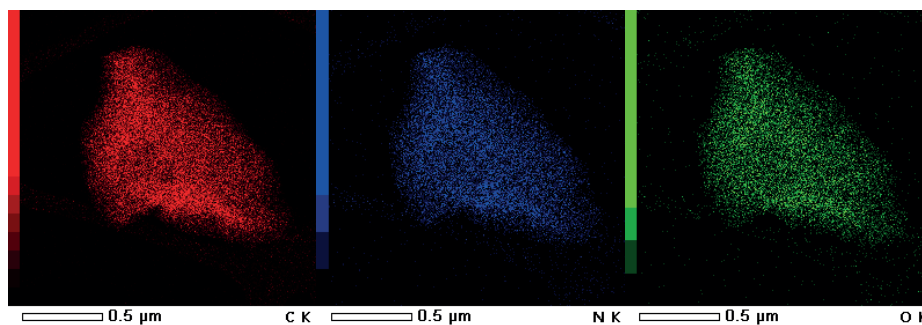


Figure S4.8. Bright-field scanning transmission electron microscopy of acac-CTF showing uniform distribution of C, N, O elements on the pristine acac-CTF.

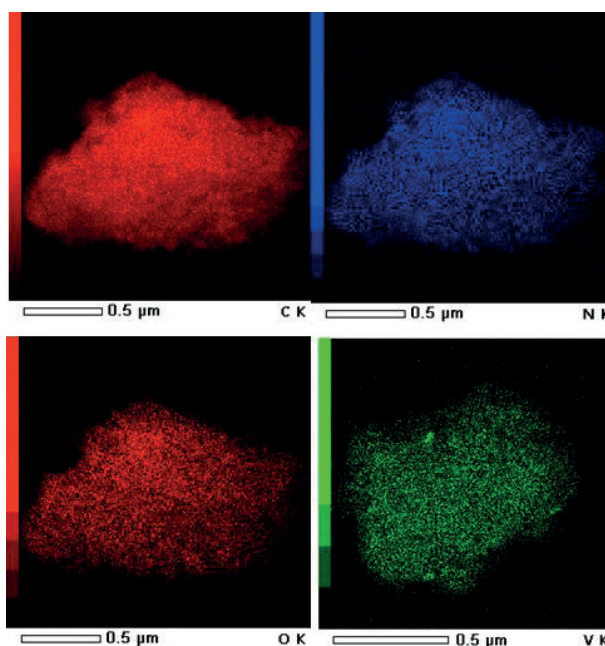


Figure S4.9. Bright-field scanning transmission electron microscopy of V@acac-CTF showing uniform distribution of C, N, O and V elements.

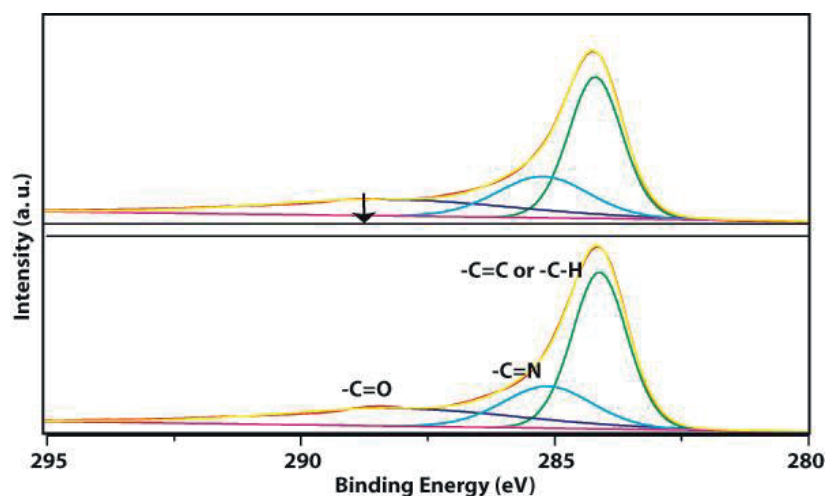
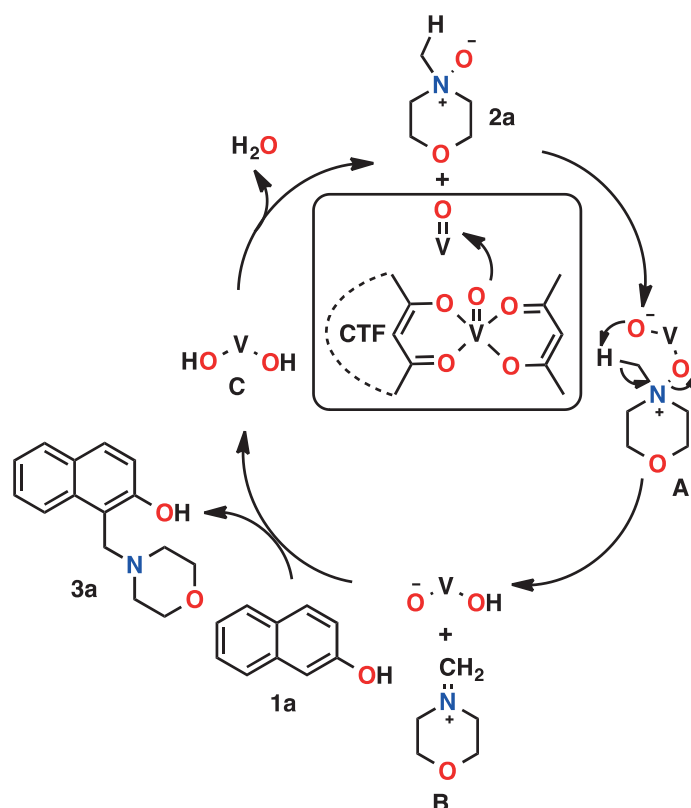


Figure S4.10. Deconvoluted XPS spectra of C 1s for (a) fresh V@acac-CTF catalyst (b) recovered V@acac-CTF catalyst after the five-catalytic cycle (c).

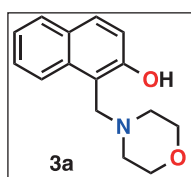


Scheme S4.3. Proposed mechanism of modified Mannich reaction.

General procedure for the modified Mannich reaction.

40 mg of V@acac-CTF, 2-naphthol (396 mg, 2.75 mmol) and NMO (322 mg, 22.75 mmol) were transferred to a schlenk flask and evacuated for 30 mins followed by Ar filling. To that 10 mL of dichloromethane (anhydrous) and mesitylene (0.382 mL, 2.75 mmol) were added and the mixture could stir at 40°C for 8 h. After the completion of reaction, the heterogeneous mixture could cool to room temperature. It gave a clear solution with black catalysts and the latter was filtered out. The solution was evaporated to dryness to afford pure Mannich base (**3a**) in quantitative yield. **3b-3i** were obtained by following same procedure. In some cases, where complete conversion was not obtained, the pure products were separated by column chromatography (hexane/ethylacetate (1:1) mixture).

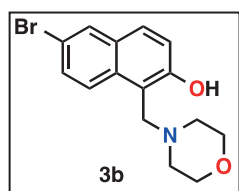
1-(morpholinomethyl)naphthalen-2-ol (**3a**):



^1H NMR (300 MHz, CDCl_3): δ 7.86 (d, $J = 8.7$ Hz, 1H), 7.79 (d, $J = 7.5$ Hz, 1H), 7.73 (d, $J = 9.0$ Hz, 1H), 7.50-7.45 (m, 1H), 7.34-7.28 (m, 1H), 7.14 (d, $J = 9.0$ Hz, 1H), 4.16 (s, 2H), 3.8 (br, 4H), 2.68 (br, 4H). ^{13}C

NMR (75.4 MHz, CDCl_3): δ 156.1, 132.7, 129.4, 128.9, 128.6, 126.4, 122.5, 120.9, 119.0, 110.3, 66.9, 56.7, 53.1.

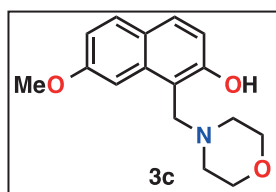
6-bromo-1-(morpholinomethyl)naphthalen-2-ol (3b):



^1H NMR (300 MHz, CDCl_3): δ 7.98 (d, $J = 2.4$ Hz, 1H), 7.77 (d, $J = 9.0$ Hz, 1H), 7.68 (d, $J = 9.0$ Hz, 1H), 7.60 (dd, $J = 9.0, 2.4$ Hz, 1H), 7.21 (d, $J = 9.0$ Hz, 1H), 4.17 (s, 2H), 3.88 (br, 4H), 2.72 (br, 4H).

^{13}C NMR (75.4 MHz, CDCl_3): δ 156.2, 132.4, 129.8, 129.19, 129.14, 126.2, 123.9, 123.66, 123.6, 111.6, 64.8, 53.3, 52.5.

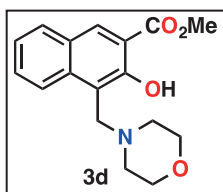
7-methoxy-1-(morpholinomethyl)naphthalen-2-ol (3c):



^1H NMR (300 MHz, CDCl_3): δ 7.66 (d, $J = 8.6$ Hz, 1H), 7.73 (d, $J = 4.5$ Hz, 1H), 7.69 (s, 1H), 7.19 (d, $J = 2.7$ Hz, 1H), 7.06 (d, $J = 2.4$ Hz, 1H), 4.17 (s, 2H), 4.01 (s, 3H), 3.90 (br, 4H), 2.76 (br, 4H).

^{13}C NMR (75.4 MHz, CDCl_3): δ 158.3, 156.7, 133.9, 130.4, 129.1, 123.9, 116.5, 114.2, 109.3, 100.7, 66.8, 56.9, 55.2, 53.1.

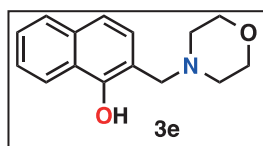
Methyl 3-hydroxy-4-(morpholinomethyl)-2-naphthoate (3d):



^1H NMR (300 MHz, CDCl_3): δ 8.53 (s, 1H), 7.84 (d, $J = 7.8$ Hz, 1H), 7.73 (d, $J = 8.4$ Hz, 1H), 7.56-7.51 (m, 1H), 7.38-7.33 (m, 1H), 4.06 (s, 5H), 3.81-3.72 (m, 4H), 2.57-2.51 (m, 4H).

^{13}C NMR (75.4 MHz, CDCl_3): δ 169.0, 156.4, 131.2, 131.0, 130.7, 128.8, 127.9, 123.5, 122.8, 116.8, 114.9, 68.5, 53.2, 53.0, 51.0.

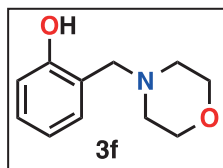
2-(morpholinomethyl)naphthalen-1-ol (3e):



^1H NMR (300 MHz, CDCl_3) δ 8.30-8.26 (m, 1H), 7.76-7.74 (m, 1H), 7.49-7.43 (m, 2H), 7.30 (d, $J = 8.2$ Hz, 1H), 7.04 (d, $J = 8.2$ Hz, 1H), 4.02 (s, 2H), 3.80-3.76 (m, 4H), 2.56 (br, 4H).

^{13}C NMR (75.4 MHz, CDCl_3) δ 152.7, 133.6, 127.2, 126.4, 125.7, 125.6, 124.5, 122.1, 118.2, 112.7, 66.4, 59.2, 54.5.

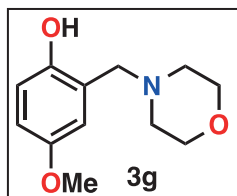
2-(morpholinomethyl)phenol (3f):



^1H NMR (300 MHz, CDCl_3): δ 7.18 (d, $J = 8.2$, 1H), 6.97 (t, $J = 8.2$ Hz, 1H), 6.82-6.79 (m, 1H), 6.76 (d, $J = 7.6$ Hz, 1H), 3.72 (s, 2H), 3.56 (br, 4H), 2.56 (br, 4H).

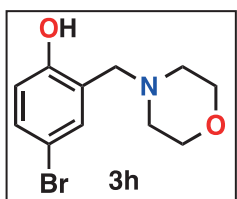
^{13}C NMR (75.4 MHz, CDCl_3): δ 158.2, 129.4, 128.6, 121.9, 120.1, 115.8, 66.8, 58.9, 54.9.

4-methoxy-2-(morpholinomethyl)phenol (3g):



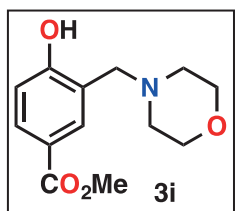
^1H NMR (300 MHz, CDCl_3) δ 6.89 (d, J = 8.6 Hz, 1H), 6.84 (d, J = 7.4 Hz, 1H), 6.74 (d, J = 8.2 Hz, 1H), 3.74 (s, 2H), 3.54 (br, 4H), 2.48 (br, 4H). ^{13}C NMR (75.4 MHz, CDCl_3) δ 158.4, 156.2, 124.2, 116.5, 114.6, 114.2, 66.4, 59.8, 54.2.

4-bromo-2-(morpholinomethyl)phenol (3h)



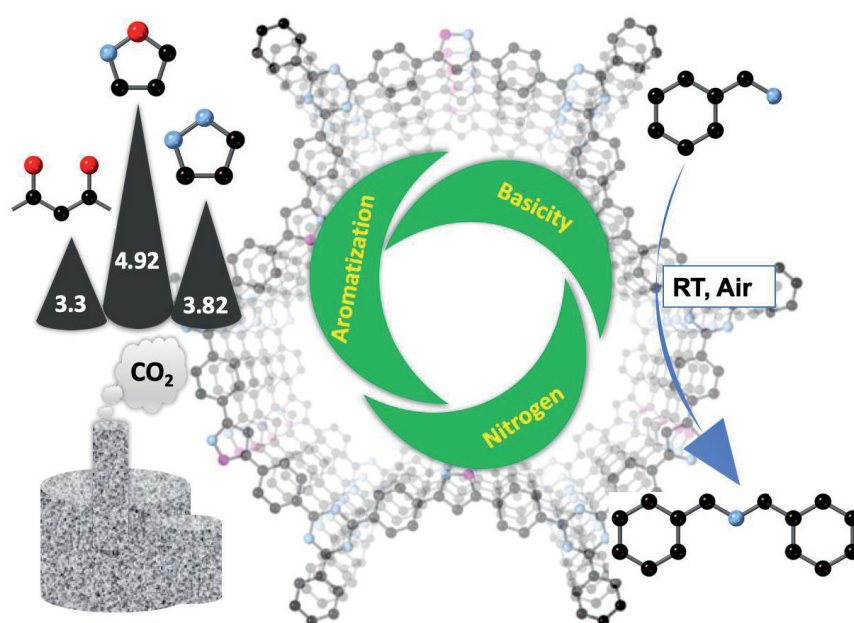
^1H NMR (300 MHz, CDCl_3) δ 7.58 (s, 1H), 7.24 (d, J = 7.6 Hz, 1H), 6.72 (d, J = 8.4 Hz, 1H), 3.70 (s, 2H), 3.56 (br, 4H), 2.42 (br, 4H). ^{13}C NMR (75.4 MHz, CDCl_3) δ 158.2, 132.4, 126.2, 122.8, 120.7, 112.2, 68.2, 57.8, 55.6.

Methyl 4-hydroxy-3-(morpholinomethyl)benzoate (3i)



^1H NMR (300 MHz, CDCl_3): δ 7.78 (d, J = 8.2 Hz, 1H), 7.72 (d, J = 6.8 Hz, 1H), 7.42 (d, J = 8.2 Hz, 1H), 3.90 (s, 3H), 3.74 (s, 2H), 3.62 (br, 4H), 2.52 (br, 4H). ^{13}C NMR (75.4 MHz, CDCl_3): δ 166.0, 162.6, 130.2, 128.4, 122.2, 122.2, 115.5, 66.4, 60.2, 55.6, 50.2.

5 EFFECT OF BUILDING BLOCK TRANSFORMATION IN CTFs FOR CO₂ UPTAKE AND METAL-FREE HETEROGENEOUS CATALYSIS



The results of this chapter were published in:

HS Jena¹, **C Krishnaraj¹**, J Schmidt, K Leus, K Van Hecke, P Van Der Voort. Effect of Building Block Transformation in Covalent Triazine Based Frameworks for Enhanced CO₂ Uptake and Metal Free Heterogeneous Catalysis. **Chemistry – A European Journal** 26 (7), **2020**, 1548-1557.

Abstract

Covalent Triazine Frameworks (CTFs) have provided a unique platform in functional material design for a wide range of applications. Herein, a series of new CTFs with two new heteroaromatic building blocks (pyrazole and isoxazole groups) are synthesized through building block transformation approach aiming for carbon capture and storage (CCS) and catalysis. The CTFs were synthesized from their respective building blocks [(4,4'-(1H-pyrazole-3,5-diyl)dibenzonitrile (pyz) and 4,4'-(isoxazole-3,5-diyl)dibenzonitrile (isox))] under ionothermal conditions using ZnCl_2 . Both of the building blocks were designed by organic transformations of acetylacetone containing dinitrile linker to pyrazole and isoxazole groups respectively. Due to this organic transformation, (i) linker aromatization; (ii) higher surface areas and nitrogen contents; (iii) higher aromaticity; and (iv) higher surface basicity was achieved. These CTFs were explored for CO_2 uptake and metal free heterogeneous catalysis. Among all, the isox-CTF, synthesized at 400 °C, showed the highest CO_2 uptake (4.92 mmol/g at 273 K and 2.98 mmol/g at 298 K at 1 bar). Remarkably, these CTFs showed excellent metal-free catalytic activity for the aerobic oxidation of amine under mild reaction conditions. On studying the properties of the CTFs, it was observed that organic transformations and ligand aromatization of the materials are crucial factor to tune the important parameters that influence the CO_2 uptake and the catalytic activity. Overall, this work highlights the substantial effect of designing new CTF materials by building block organic transformations resulting in better properties for CCS applications and heterogeneous catalysis.

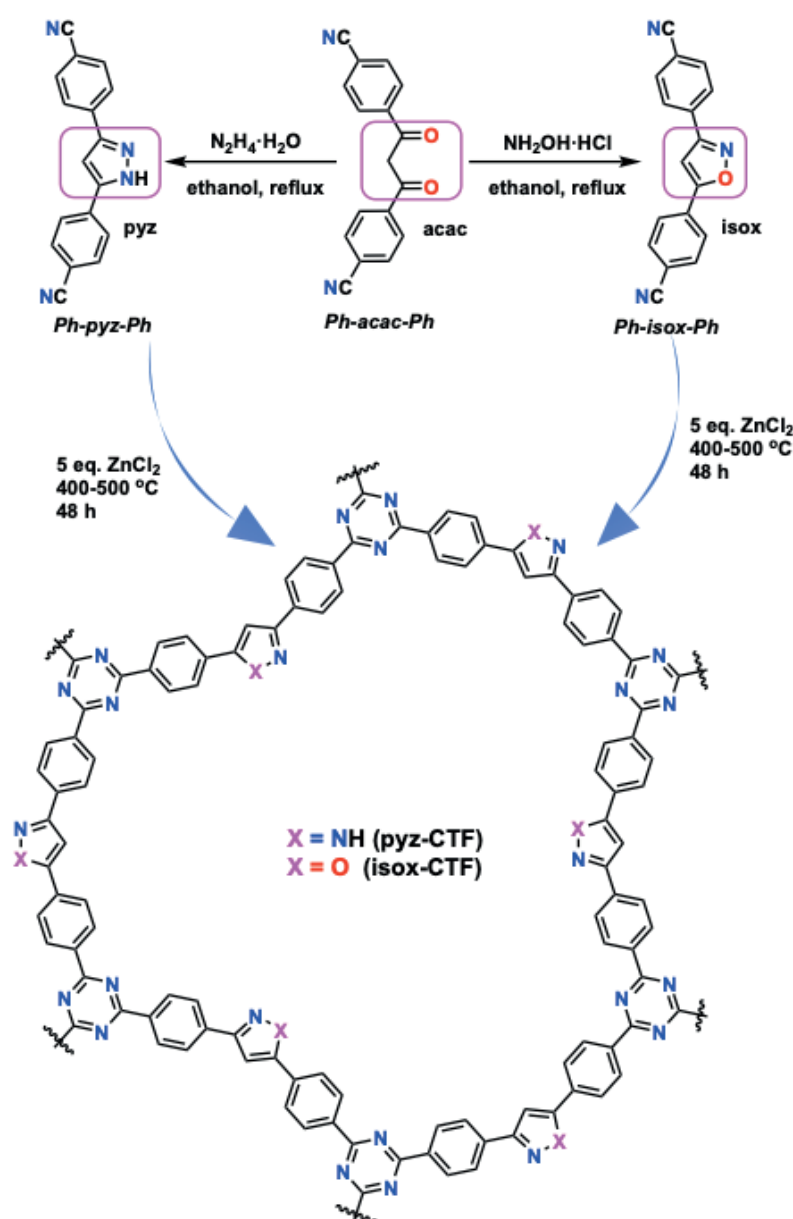
5.1. Introduction

Over the past few years, tremendous efforts have been devoted to the development of porous organic polymers (POPs).¹ This sort of polymeric materials are potential candidates for carbon capture storage (CCS)² and carbon capture utilization (CCU)¹ applications. CCS and CCU are considered as potential technologies that can tackle one of the current biggest scientific challenges and have a positive impact on the environment as well as the economy. In the view of the growing population and fulfilling energy demands, it is also necessary to develop more efficient, greener and more sustainable chemical industries by designing renewable solid catalysts.³ For these two important applications, POPs are considered as smart materials due to their unique characteristics (large surface area, tunable pore volume, functionalities and high stability).

Covalent triazine frameworks (CTFs)⁴ have proven to be a highly promising class of materials because of their easy synthesis, high stability and most importantly low-density network. In addition, they are highly reproducible and can be reused multiple times in a cost-effective way. Therefore, significant attention has been given for engineering CTFs with different heteroaromatic functional groups for CCS and heterogeneous catalysis.^{4a-c} Particularly, to achieve enhanced CO₂ uptake, CTFs have been developed with different CO₂-philic aromatics like pyridine, bipyridine,⁵ benzimidazole,⁶ fluorene,⁷ carbazole,⁸ porphyrin, perfluorinated⁹ and triazole¹⁰ backbones to enhance the Lewis acid–base interactions. Incorporation of heteroatoms (N, O, S) is another potential route to achieve enhanced CO₂ uptake because of higher dipole-quadrupole interactions.¹¹ CTFs also showed promising applications in supported metal ion or nanoparticle based heterogeneous catalysis.¹² Additionally, CTFs have also been used as metal free catalysts for the cycloaddition of CO₂ to various epoxides,¹³ oxidative cleavage of lignin model compounds¹⁴ and also as organocatalysts¹⁵ in carbene catalyzed conjugated umpolung reactions. So far, the excellent catalytic properties of CTF are claimed to be due to the presence of different types of nitrogen (pyridinic, pyrrolic, quaternary and pyridinic N-oxide) even though it is still unclear which specific type of nitrogen is responsible in a particular reaction. Recently, chemical activation of CTF by KNO₃ and KOH were used to obtain enhanced CO₂ uptake¹⁶ and high reactivity in the oxidation of methylene compounds¹⁷ respectively. It was shown that KOH and KNO₃ activation enhanced the basicity of CTF materials resulting in improved properties. Also, Giambastiani et al., reported that the gas adsorption capacity and organocatalytic activity of CTFs can be

modulated through an appropriate selection of the building blocks.¹⁸ Their results showed that neither purely microporous samples (highly N-rich) nor mesoporous and N-poor CTFs were ideal candidates for the CO₂ capture and storage. However, a balanced combination of surface area, N content and micro-mesoporous morphology of CTFs are necessary to obtain highest CO₂ uptake.

Herein, the effect of organic transformations and ligand aromatization to tune the surface area, N content, pore characteristics and surface basicity of CTFs to achieve enhanced CO₂ uptake and metal free catalytic activity are described.



Scheme 5.1. Scheme illustrating linker synthesis and their respective Covalent Triazine Frameworks synthesized under ionothermal conditions.

5.2. Results and discussion

5.2.1. Synthesis of CTFs

So far, four synthetic methods have been used for CTF synthesis; ionothermal synthesis,^{5c} room temperature and microwave synthesis using CF₃SO₃H,²² polycondensation of aldehydes and amidines at 120 °C²³ and direct synthesis using P₂O₅-catalyzed condensation of aromatic amides.²⁴ However, most of the reported CTFs are synthesized using the ionothermal method as it is less stringent on linkers and is highly reproducible. Using this method, herein two sets of CTFs were synthesized from their respective dinitrile linkers (4,4'-(1H-pyrazole-3,5-diyl)dibenzonitrile (pyz) and 4,4'-(isoxazole-3,5-diyl)dibenzonitrile (isox) (Scheme 5.1). Details about the synthesis and characterization of both the dintrile linkers/building units are described in the supporting information (Figure S5.1-S5.7). Further on, they are referred to as pyz-CTF-x-y and isox-CTF-x-y, where, x-ZnCl₂ equivalents and y-synthesis temperature (Table S5.1). Notably, these two linkers (pyz and isox) were easily obtained from 4,4'-malonyldibenzonitrile (acac) upon simple condensation reactions, with hydrazine hydrate and hydroxylamine hydrochloride, respectively. As shown in Scheme 5.1, the organic transformation resulted in extended fused aromatic rings (phenyl-pyrazole-phenyl and phenyl-isoxazole-phenyl) with polar functional sites (N[^]N and N[^]O) from a flexible phenyl-acac-phenyl containing dinitrile linker. The new sets of CTF materials are characterized well and explored for gas adsorption, separation and metal-free heterogeneous catalysis. The results were compared with acac-CTF^[11f] and CTF-1^{5b, 5c} and other CTFs were included wherever necessary.

5.2.2. Characterization of CTFs

For the preliminary characterization, FT-IR measurements were undertaken to confirm the complete trimerization of the nitrile group to a triazine ring (Figure S5.7). Notably, the absence of a -CN band at 2229 cm⁻¹ and presence of a -C=N (triazine) band at 1598cm⁻¹ confirmed the complete conversion of the nitrile groups to triazine rings ensuring the CTF formation. In all the CTFs, two sharp peaks observed at around 2850 and 2900 cm⁻¹ are the C-H stretching bands of the ligand.^{9b, 11f, 25} From the elemental analysis (Table 5.1 and Table S5.2), the observed increase in N content from acac-CTF^{11f} to pyz-CTF and isox-CTF confirmed the formation of both CTFs with the respective functional groups. However, the obtained results indicate a lower number of heteroatoms and a higher C content than the expected value. To obtain a more detailed picture, the

degree of carbonization was calculated. 9-12% carbonization was found in the CTFs. As can be seen from Table 5.1, the C/N ratio slightly increases with increase in the synthesis temperature which is comparable to the reported CTF materials.

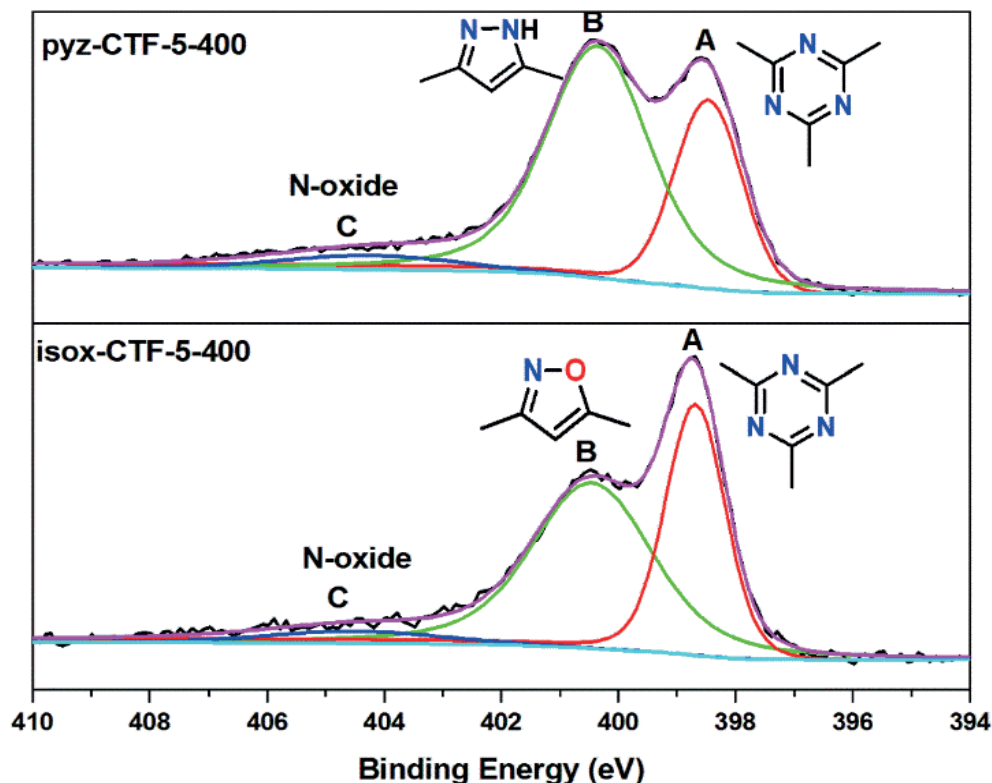


Figure 5. 1. Deconvoluted XPS N 1s spectra of pyz-CTF-5-400 and isox-CTF-5-400.

Further, the nature of elements corresponding to the functional groups and their binding energy were characterized by X-ray photoelectron spectroscopy (XPS) measurements. XPS spectra of pyz-CTF-5-400 and isox-CTF-5-400 were measured and analyzed by fitting the respective atoms to their binding energies.²⁶ For pyz-CTF-5-400, in the obtained XPS spectra, C 1s (deconvoluted) peaks at 284 eV and 285 eV can be assigned to C-C/C-H and C-N species respectively (Figure S5.8). The N 1s spectrum of pyz-CTF-5-400 showed two peaks at 398 eV (A) and 400 eV (B) which can be assigned to the phenyl functionalized triazine (A) and pyrrolic-NH species (B) respectively (Figure 5.1). For isox-CTF-5-400, the C 1s spectra are very similar to pyz-CTF-5-400 (Figure S5.8), however in the N 1s spectra, a significant decrease in intensity of the peak at 400 eV with respect to 398 eV was noticed. This is due to the absence of pyrrolic-NH function in the isoxazole unit which was replaced by an oxygen atom. Even in the absence of pyrrolic N-species for isox-CTF, a peak at ~400 eV appears. It is common to observe pyrrolic NH for almost all CTF materials under ionothermal conditions rearrangements despite of their

functional groups. However, the decrease in intensity clearly confirmed the transformation of pyrazole and isoxazole and retention of the respective groups even after ionothermal synthesis.

Table 5. 1. BET Surface areas, Pore volumes, CO₂ and H₂ uptakes, CO₂ Isosteric Heat of adsorption (Q_{st}), and CO₂/N₂ selectivity of the CTFs.

No	CTF	SA _{BET} [a] (m ² /g)	V _t ^[b] (cm ³ /g)	N(%) [c]	C/N	CO ₂ uptake (mmol/g)		Q_{st} ^[d] (kJ/mol)	CO ₂ /N ₂ [e]	H ₂ (wt%)	Ref.
						273 K	298 K				
1	pyz-CTF-5-400	1605	0.81	10.888	7.23	3.82	2.19	27	26	1.78	-
2	pyz-CTF-5-500	1405	0.85	8.914	7.96	3.31	1.96	27	18	1.31	
3	isox-CTF-5-400	1683	0.70	7.467	7.18	4.92	2.86	29	29	1.60	
4	isox-CTF-5-500	1537	0.72	7.917	8.99	4.23	2.69	25	18	1.32	
5	acac-CTF-5-500	1556	1.20	5.070	16.27	3.30	1.97	28	46	1.53	11f
6	CTF-1-400	610	0.98	18.60	3.77	2.83	1.52	33.7	59	-	5a
7	bipy-CTF-600	2479	1.24	13.61	4.96	5.58	2.95	34.4	37	2.10	5a
8	F-DCBP-CTF-400	1574	1.50	11.3	5.28	5.98	3.82	33.1	31	1.77	9b

9	HAT-CTF-450/600	1090	0.263 ^[f]	32.8 ^[g]	-	6.3	4.80	27.1	126	-	11b
10	df-TzCTF-600	1720	1.12	8.26	7.05	6.9	4.60	34	21	2.50	10a
11	Tz-df-CTF-600	2106	1.43	6.15	7.86	7.65	5.08	20.0	21.1	2.91	10b

^[a]BET surface area was calculated over the relative pressure range of 0.01–0.05 at 77 K. ^[b]V_t, total pore volume was calculated at P/P₀ = 0.98. ^[c]Percentage of nitrogen content calculated from elemental analysis, ^[d]Calculated isosteric heat of adsorption of CO₂ using the Clausius-Clapeyron equation, ^[e]The selectivity of material for CO₂ adsorption over N₂ was calculated by the Henry model, ^[f]estimated from CO₂ isotherm, ^[g]XPS analysis.

To explore the phase purity and nature of the CTF materials, powder X-ray diffraction (PXRD) measurements were undertaken (Figure S5.9). Based on the results, all the CTFs showed a very broad peak in the range of $2\theta = 20\text{--}24^\circ$ corresponding to the two-dimensional layers stacked on each other by $\pi\cdots\pi$ interactions.^{5c} The stability of all the CTFs was verified by TGA analysis under N₂ atmosphere which showed that they are robust like other reported CTFs and are stable up to 500 °C (Figure S5.10).

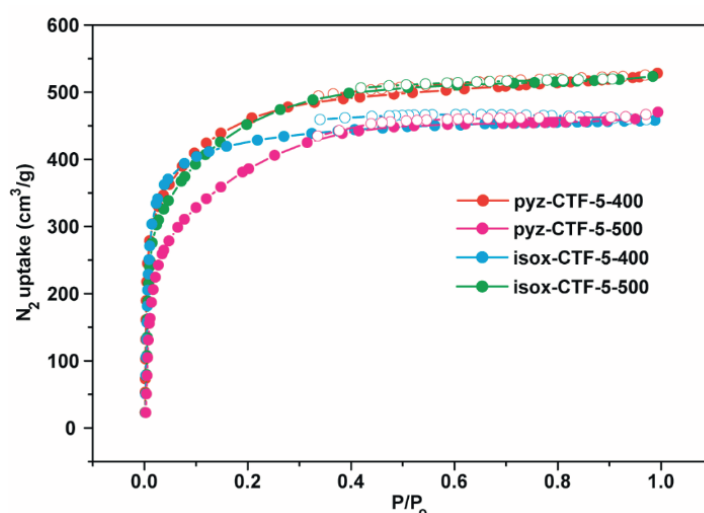


Figure 5. 2. Nitrogen adsorption/desorption isotherms of pyz-CTFs and isox-CTFs measured at 77 K, filled and empty symbols represent adsorption and desorption, respectively.

5.2.3. Gas Sorption Properties.

For gas sorption analysis, the CTF materials were activated under vacuum at 150 °C overnight. The surface area properties of all these activated CTF materials were determined from N₂ sorption measurements at 77 K (Figure 5.2). The respective surface areas and total pore volumes (V_t) calculated at $P/P_0 = 0.98$ are displayed in Table 5.1. As shown in Figure 5.2, the obtained isotherms for all these CTF materials resemble type-I adsorption isotherm. As summarized in Table 5.1, the BET surface area (S_{BET}) of both set of CTFs decreases upon increase in temperature. However, in both sets of materials, the total pore volume (V_{tot}) increases with respect to temperature (entry 1-4; Table 5.1). Notably, the observed S_{BET} and V_t of pyz-CTFs and isox-CTFs significantly differencing from acac-CTF (entry 5). From XPS, TGA and N₂ sorption analysis, it was confirmed that both sets of CTF materials are robust with large surface area and different kind of N-sites (due to triazine and pyrazole/isoxazole groups) uniformly distributed over the materials. In general, these kinds of N-sites interact strongly with CO₂ due to dipolar interactions. Therefore, these materials were used to evaluate their CO₂ adsorption and selectivity over N₂.

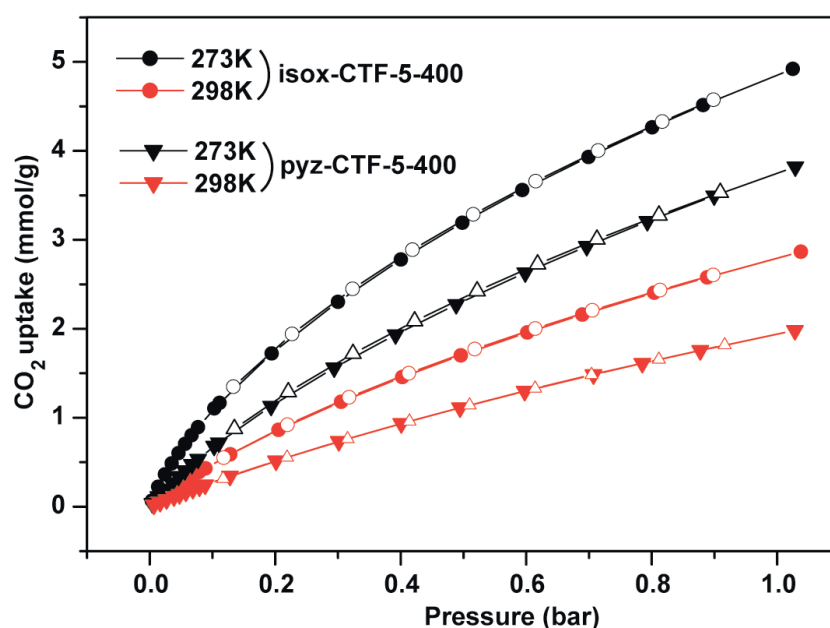


Figure 5. 3. CO₂ adsorption/desorption isotherms of pyz-CTF-5-400 and isox-CTF-5-400 measured at 1 bar, filled and empty symbols represent adsorption and desorption, respectively.

CO₂ adsorption/desorption isotherms were recorded at 273 K and 298 K at 1 bar of pressure (Figure 5.3). The uptake of both sets of CTF materials at respective temperatures

are included in Table 5.1. The best CO₂ uptake was obtained for isox-CTF-5-400 with values of 4.92 mmol/g at 273 K and 2.86 mmol/g at 298 K and 1 bar respectively (entry 3; Table 5.1). In general, for previously reported CTFs, larger surface area, greater number of heteroatoms and high amount of microporosity collectively resulted in high CO₂ uptake. When comparing the two sets of CTF materials (entry 1-4), it was found that isox-CTF-5-400 with highest surface area and lowest total pore volume (0.70 cm³/g) showed the best CO₂ uptake.

In order to compare the observed CO₂ uptake properties with reported values, few representative CTFs with different surface area, pore volume, nitrogen content and C/N ratio were included in Table 5.1 (entry 5-11). On comparison, it can be stated that CO₂ capacities of the present new sets of CTF materials are higher than acac-CTFs, DCI-CTF, CTF-1 and comparable with many other CTFs with different heteroaromatic groups.^{5a, 6-7, 9d, 11f, 18, 25, 27} However, they are lower than observed in bipy-CTF-600 (5.58 mmol/g)^{5a}, F-DCBP-CTF^{9b} (5.98 mmol/g), HAT-CTF-450/600^{11b} (6.3 mmol/g) and triazole containing CTFs¹⁰ (7.65 mmol/g) (entry 7-12). In order to gain more insight, the CO₂ uptake of each CTF was plotted with respect to its surface area and nitrogen content per 1000 m²/g surface area into a bar graph (Figure 5.4). The overall CO₂ uptake increases with increase in the nitrogen content, but also sufficient surface area of the CTF is required for improving overall storage capacity. With some exceptions, it can be concluded that both parameters (surface area and nitrogen contents) have significant role in CCS application.^{2c, 18, 28} In order to further investigate the difference in CO₂ capacities of isox-CTF and pyz-CTFs, the isosteric heats of adsorptions (Q_{st}) of CO₂ were calculated using the Clausius-Clapeyron equation (Figure S5.11). From the obtained values in Table 5.1, it was found that isox-CTF-5-400 showed the highest Q_{st} value (29 kJ/mol), confirming that the former exhibited the strongest interaction with CO₂ among these four CTFs and corroborated with the highest CO₂ value. Notably, the calculated Q_{st} values are higher than the heat of liquefaction of CO₂ (17 kJ/ mol)²⁹ and are comparable to most of the reported CTFs at similar conditions^{4a, c}.

In addition to the CO₂ storage, CTFs are promising materials for CO₂ separation from a mixture of gases. In particular, they showed promising application in CO₂/N₂ separation because of their robustness, large surface areas and high N content (Table 5.1). Therefore, to explore the potential of pyz-CTF and isox-CTF materials in CO₂/N₂ separation, the selectivity was calculated using the Henry law by using the ratio of the slopes of the CO₂

adsorption isotherms (<0.06 bar) and N₂ (<0.1 bar) at 298 K (Figure S5.12 and S5.13). The obtained values in Table 5.1, represent moderate CO₂/N₂ selectivity of these materials. The best value was 29 for isox-CTF-5-400. The obtained selectivity is directly correlated to the synthesis temperature. The CTF materials synthesized at 500 °C showed lower CO₂/N₂ selectivity than 400 °C. The obtained values are comparable with most of the CTFs^[4c] but far below those of HAT-CTF-450/600^{11b}(entry 9; Table 5.1).

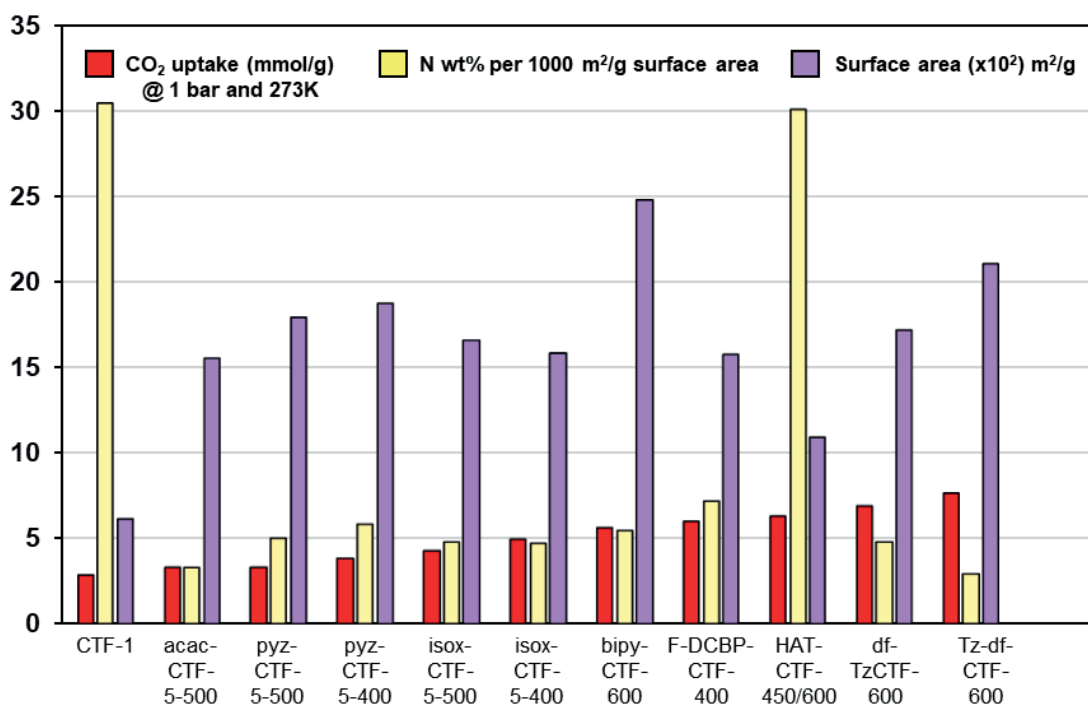


Figure 5. 4. CO₂ uptake of CTF materials vs their BET surface area and nitrogen content per 1000 m²/g surface area, measured at 273 K and 1 bar.

From the above discussed CO₂ uptake studies, it is concluded that modifications in the building units (conversion of acetylacetone to pyrazole and isoxazole) resulted in a significant enhancement of CO₂ uptake (Figure 5.4; inset). Although these new CTFs do not achieve the best amount of CO₂ storage, this work emphasizes the impact of a simple transformation of functional groups on the carbon capture properties. Further, to prove the structural properties (surface area and number of heteroatoms) and its correlation with the enhanced CO₂ uptake, single crystal X-ray analysis of (4,4'-(1H-pyrazole-3,5-diyl)dibenzonitrile was performed (Figure S5.14). As expected, the dihedral angle between two appended benzonitrile groups is increased from 135° (acac) to 151°(pyz/isox). As shown in Scheme S5.1, this difference in dihedral angle resulted in completely different ideal structure with high surface area and increase in number of

heteroatoms. Therefore, the obtained higher CO₂ uptake can be corroborated with both parameters.

Apart from the surface properties, basicity of porous materials is considered as an important parameter to achieve higher CO₂ uptake.^{17, 30} In general, the basicity of metal free carbon-based materials is linked to the nature of the nitrogen-based dopant. Particularly in CTFs, four different N-sites/N-dopants e.g. pyridinic-N, pyrrolic-N, quaternary-N and N-oxides are uniformly distributed over the surface. Therefore, the overall basicity of CTF materials is linked to these four different N-sites, including chemically accessible or unreachable basic N-sites.³⁰

In particular, surface basicity is an open matter of debate and has a significant influence on CCS and base catalysed heterogeneous catalysis.^{3b, c, 11e, 30} In order to further corroborate the observed CO₂ uptake with surface basicity, temperature programmed desorption (TPD) of CO₂ analysis of isox-CTF, pyz-CTF, acac-CTF and CTF-1 were performed. As shown in Figure 5.5, mainly two desorption peaks of CO₂ in the temperature range of 68-160 °C and 190-350 °C were observed (Table 5.2). These two-desorption peaks signify weak and moderate basic sites respectively. This observance is quite consistent with similar sort of reported materials.³¹ The total basicity corresponds to the total amount of CO₂ desorbed from the materials and therefore it is calculated by taking the weight as well as the surface area of the respective materials into consideration (Table 5.2).

From the TPD-CO₂ analysis, it is revealed that the basicity of the CTF materials changed with synthesis temperature and nature of building blocks. As represented in Table 5.2, CTF-1 showed the highest degree of basicity. Among the new sets of CTF materials, isox-CTF-5-400 showed a higher degree of basicity than the other pyz-CTFs, isox-CTF and acac-CTFs. This result clearly substantiates that CTF materials with higher basicity can show high CO₂ uptake. From this study, it can be concluded that, simple organic transformation of acetyl acetone to pyrazole and isoxazole groups also influenced the basicity of respective CTFs to a greater extent. Overall, the surface basicity including surface area, pore volume and number of heteroatoms of any CTF materials have significant influence on their CO₂ uptake capacities.

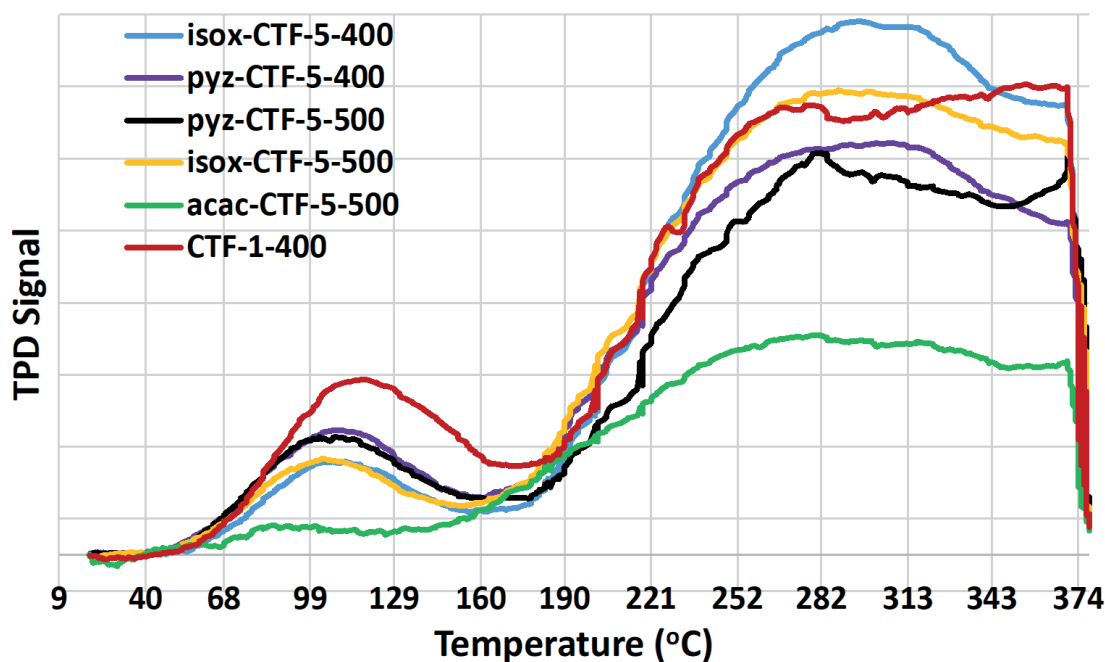


Figure 5. 5. CO₂-TPD of pyz-CTF, isox-CTF, acac-CTF and CTF-1.

Motivated by the enhanced CO₂ uptake and moderate CO₂/N₂ selectivity, H₂ storage properties of these CTF materials were also explored. Recently, CTF materials showed potential to store large amounts of H₂ (bipy-CTF-600, 2.10wt%; df-TzCTF-600, 2.50wt%; Tz-df-CTF-600, 2.91wt%) at 77 K and 1 bar (entry 7,10,11; Table 5.1).^{5a, 10a,b} In order to explore the hydrogen storage properties, the hydrogen adsorption measurements of pyz-CTF and isox-CTF were performed at 77 K (Figure 5.6) and a hydrogen storage amount of 1.31-1.78wt% at 1 bar was obtained (entry 1-4; Table 5.1). Notably, at low hydrogen pressure (0.12 bar), isox-CTF-5-400 showed the highest storage amount (0.9 wt%) but the isotherm was saturated at 0.7 bar of pressure with 1.6 wt% of hydrogen storage (Figure 5.6, insert). However, in pyz-CTF-5-400, the isotherm was not saturated even at 1 bar and hence exhibited the highest hydrogen storage capacity (1.78wt%). As noted in Table 5.1, pyz-CTF-5-400 exhibited slightly higher pore volume and 3.4 wt% higher N content than isox-CTF-5-400. Both of these parameters might be responsible for the higher amount of H₂ storage. Additionally, the obtained values are comparable with most of the CTFs obtained from building blocks with pyridine, bipyridine, benzimidazole, carbazole and other functional groups.^{4c, d}

Table 5. 2. Distribution of basicity and correlation with CO₂ uptake.

CTF	Basicity (mmol/g)			CO ₂ ^[b]
	Weak	Moderate	Total ^[a]	
pyz-CTF-5-400	1.021	28.837	29.85 (0.016)	3.82
pyz-CTF-5-500	1.289	26.988	28.27 (0.015)	3.31
isox-CTF-5-400	1.141	30.560	31.70 (0.020)	4.92
isox-CTF-5-500	1.926	24.442	26.36 (0.016)	4.23
acac-CTF-5-500	0.076	14.637	14.71 (0.009)	3.30
CTF-1-400	3.973	31.912	35.88 (0.059)	2.83

^[a]Values in the parentheses represent the basicity of respective materials with respect to their surface area (mmol/m²), ^[b]uptake in mmol/g at 273 K and 1 bar.

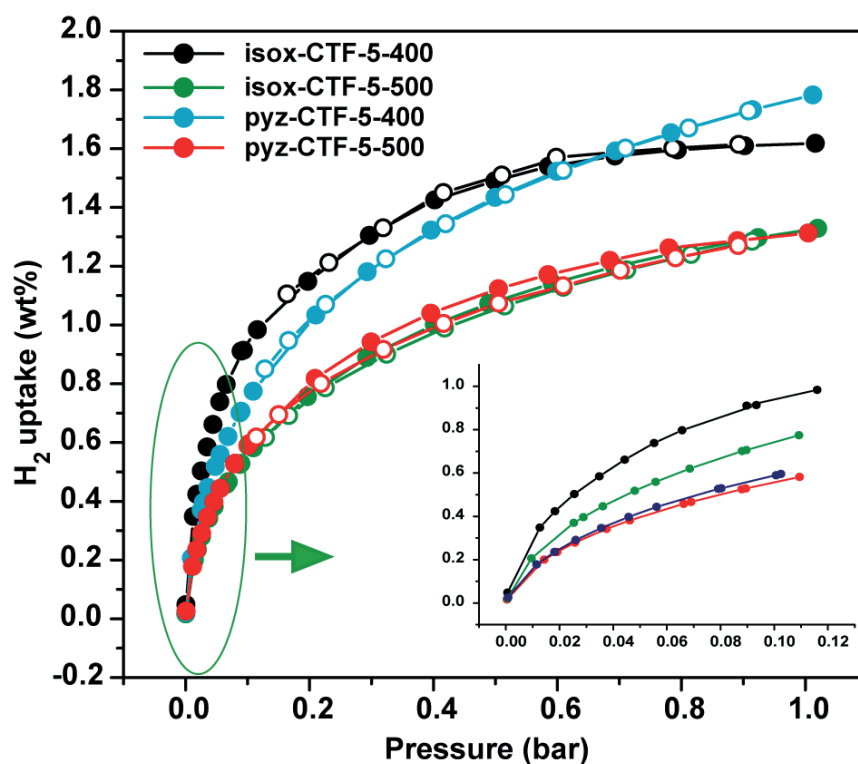


Figure 5. 6. Hydrogen adsorption isotherms of pyz-CTF and isox-CTF at 77K and 1 bar.

5.2.4. Catalytic Properties

The enhanced properties, presence of different N-sites and surface basicity of these new CTFs prompted us to explore their catalytic activity as solid heterogeneous metal-free catalysts. Recently, development of porous solid bases from simple and efficient methods are attracting interest in green chemistry and heterogeneous catalysis. In general, traditional inorganic bases suffer from many important disadvantages, despite their low cost and easy availability, i.e. they often deteriorate the catalytic activity, worsen the separation process and produce waste.¹⁷ Recently, CTFs have shown significant promise as porous solid base and have been used in base free Ru-catalyzed aqueous phase oxidation^{12h} and Ir-catalyzed transfer hydrogenation^{12a}, and metal-free cycloaddition reaction of CO₂ and epoxides,^{13a} oxidation of methylene compounds¹⁷, alcohol oxidations^{12b} and oxidative cleavage of lignin model compounds.¹⁴


Herein, we explored these new CTFs as metal free heterogeneous catalysts for the aerobic oxidative dimerization of benzyl amine to N-benzyl-1-phenylmethanimine as proof-of-concept catalysis. Selective oxidative dimerization of amine to imine, is regarded as an important electrophilic intermediate in organic synthesis.³² Although it can be achieved by stoichiometric number of organic bases, effort has been devoted to developing catalysts using simple oxygen/air as terminal oxidant. Different sets of metal based-, metal-free catalysts and photo catalysts have shown good activity for the reaction (Table 5.3, entry 10-17).³²⁻³³ However, the key challenge is to avoid formation of two key side products, aldehyde and nitriles, due to the hydrolysis of imine and dehydrogenation of amine, respectively. Therefore, the development of highly selective heterogeneous metal-free catalysts for selective synthesis of imine under mild conditions (at room temperature and solvent free) using simple air is highly desirable.

CTFs, owing their large surface area, different N-sites and surface basicity might be efficient solid base catalysts for highly selective formation of imine from the oxidative dimerization of amines. To explore this, the oxidative coupling of benzyl amine (**1a**) was chosen as a model reaction using pyz-CTF-5-500 CTF as catalyst under 1 atm of O₂ as green oxidant in different solvents at 40 °C for 12 h (Table S5.3, entry 1-4). To our delight, CH₃CN was found to be the best solvent giving 60% of conversion of **1a** (from the ¹H NMR analysis). Furthermore, allowing the same reaction for 24 h, 100% conversion of **1a** was observed with 86% yield of N-benzyl-1-phenylmethanimine (**2a**). In order to further explore the effect of other CTFs, reactions were continued in the same

conditions using other CTFs as catalyst. From the ^1H NMR results (Table 5.3), it was found that isox-CTF-5-400 showed the best yield for the formation of **2a**. Notably, the catalytic activity is comparable with the other isox-CTF and pyz-CTFs (entry 1,2,4; Table 5.3), higher than acac-CTF (entry 5; Table 5.3) and slightly lower than CTF-1-400 (entry 6; Table 5.3). The observed catalytic properties are in accordance with the basicity of the respective CTFs (Table 5.2). Furthermore, the same reactions were repeated under air (entry 7), neat (no solvent, entry 8) and even at room temperature (entry 9) using CTF-1-400. Surprisingly in each case, >99% of **2a** was obtained selectively. The reactions were also repeated using isox-CTF-5-400 and >90% selectivity for **2a** was observed. On comparison with the reported solid catalyst (entry 8-15; Table 5.3), CTFs showed best catalytic activity for aerobic oxidative dimerization of benzylamine at mild reaction condition. Very recently Xu et al., used CTF-P (obtained by using 1,4-dicyanobenzene and ZnCl_2 in 1:1 ratio for 40 h) as metal free catalyst for the oxidation of amine at elevated temperature (120 °C) using methanol as solvent (entry 15, table 5.3).^{33g} However, the catalyst showed low reactivity at ambient temperature (<100 °C). Surprisingly, in the present case using CTF-1 in CH_3CN , a high reactivity is observed even at ambient condition (entry 6, Table 5.3). This might be due to the nature of solvent that enables high dispersion of substrate and catalyst in the reaction medium. In addition, synthesis conditions of CTF-1-400 (entry 6; 1,4-dicyanobenzene and ZnCl_2 in 1:10 ratio for 48 h) and reported CTF-P are different resulting CTF materials with varying their surface areas, pore volumes and surface basic properties. Therefore, in the present case, synthesis conditions of CTF, characteristics of catalyst and solvent played important role to obtain high reactivity at ambient conditions.

To investigate the reaction performance with CTF-1-400 in detail, progress of the reaction was supervised via in-situ ^1H NMR analysis using CD_3CN as solvent. As shown in Figure 5.7, **2a** was the sole product during the whole reaction. Surprisingly, the reaction started immediately unlike MOF-253^{33d} (entry 14, Table 5.3) where an induction period was noticed. To gain more insight into the radical mechanism of the reaction, TEMPO (2,2,6,6-tetramethylpiperidin-1-yl)oxidanyl) as free radical scavenger was added into the reaction. However, from the ^1H NMR analysis, it was found that TEMPO did not affect the formation of **2a** (entry 16, Table 5.3), and hence radical mechanism of the reaction can be ruled out.

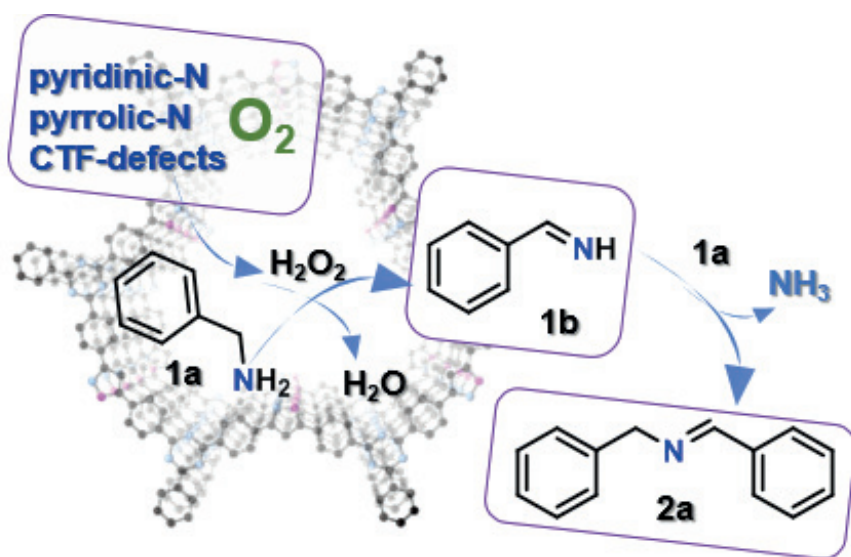
Table 5. 3. Catalytic test using CTF in the aerobic oxidative dimerization of benzylamine to N-benzyl-1-phenylmethanimine.^[a]

			
Entry	Catalyst	Conversion of 1a (%) ^[b]	Selectivity of 2a (%) ^[b]
1	pyz-CTF-5-400	100	92
2	pyz-CTF-5-500	100	86
3	isox-CTF-5-400	100	98
4	isox-CTF-5-500	100	90
5	acac-CTF-5-500	38	35
6	CTF-1-400	100	>99
7 ^[c,d,e]	CTF-1-400	100	91
8 ^[f]	Graphite oxide ^[33a]	99	98
9 ^[g]	Silica templated mesoporous carbon ^[33b]	100	94.2
10 ^[h]	N-doped carbon ^[33c]	98	98
11 ^[i]	mpg-C ₃ N ₄ ^[32]	99	99
12 ^[j]	WS ₂ nanosheets ^[33e]	92	95
13 ^[k]	CF-HCP based POPs ^[33f]	100	91
14 ^[f]	MOF-253 ^[33d]	>99	>99
15 ^[l]	CTF-P ^[33g]	94	91
16 ^[m]	CTF-1-400	100	>99
17 ^[n]	CTF-1-400	<1	-

^[a]Reaction conditions: **1a** (2 mmol), CTF catalyst (10 mg), 1 atm of O₂, 24 h, 40 °C and CH₃CN as solvent, ^[b]Determined from ¹H NMR analysis using mesitylene as internal standard, ^[c]air, ^[d]solvent free, ^[e]at room temperature, ^[f]100 °C, 5 atm of O₂, ^[g]100 °C, ^[h]110 °C, ^[i]60 °C, 5 atm of O₂ and λ > 420 nm, ^[j]80 °C, 60 W white LED lamp, ^[k]35 W green LED lamp (520 nm),

^[l]110 °C, 60 mg catalyst for 1mmol of substrate, no clear mechanism ^[m]in presence of TEMPO, ^[n]in presence of benzoquinone.

Therefore, it can be proposed that different N-sites, surface basicity and defects of CTF easily activate substrate **1a** and O₂ to initiate the reaction.^{33b} Furthermore, these N-sites can serve as reversible adsorption sites for the substrate **1a** and the product **2a** to obtain higher conversion and selectivity. A proposed reaction mechanism is shown in Scheme 5.2. In the beginning of the reaction, substrate **1a** and O₂ were activated by CTF and subsequently transformed into benzylimine (**1b**) and H₂O₂ as intermediate respectively. In-situ ¹H NMR analysis was performed to detect the formation of H₂O₂. However, the absence of a peak at around 10.95 ppm^{33e} clearly indicates that H₂O₂ was immediately consumed by another **1a** to form **1b**. Further, upon use of benzoquinone as superoxide scavenger, the reaction stopped immediately and **2a** was not noticed from the NMR analysis (entry 17, Table 5.3). This observation clearly confirmed the formation of H₂O₂ in the reaction mixture. Finally, the intermediate **1b** owing to its highly unstable nature, immediately reacts with another molecule of **1a** to form product **2a**. Notably, during the reaction, the peak corresponding to the formation benzaldehyde^{32-33, 33c-g} was not noticed from the NMR analysis. This ruled out the hydrolysis of **1b** to aldehyde and its reaction with **1a** to form **2a**. This observation strongly suggests benzylimine (**1b**) as a sole intermediate during this whole reaction.



Scheme 5.2. Proposed reaction pathway for CTF catalyzed oxidative dimerization of **1a** to **2a**.

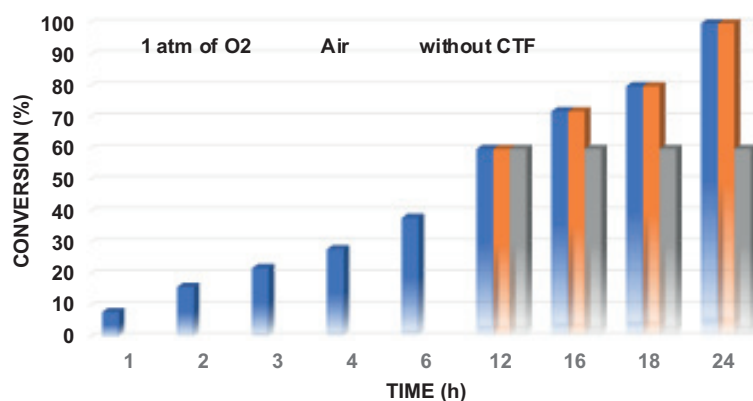


Figure 5. 7. Conversion of 1a using CTF-1-400 with reaction times using 1 atm of O₂. After 12h the reaction was split into two - (i) pure O₂ removed and reaction continued (Air), and (ii) CTF-1-400 was filtered out and reaction continued under pure (without CTF).

Further to explore the effect of heterogeneity and O₂, the reaction was stopped after 12 h of reaction time, cap of the vial was opened to remove all O₂ and further stirred for 12 h. Notably the reaction, did not stop even in the absence of O₂. This result again supported the fact that oxidation of amine to imine can be achieved simply under air (Figure 5.7; entry 7, Table 5.3). However, when the CTF is filtered out of the reaction after 12 h, the reaction stops immediately (Figure 5.7). This clearly indicates that CTF has a significant role in the oxidation reaction. Furthermore, the recyclability, reusability and reproducibility test - up to five cycles (Figure S5.15) - confirmed CTF as an extremely stable and solid porous base catalyst for aerobic oxidative dimerization of amine to imine under mild conditions. At the same time, larger surface area, N content, porosity and surface basicity of CTFs play important roles in achieving high reactivity and selectivity.

5.3. Conclusion

In this study, a simple chemical transformation of one dinitrile linker (4,4'-malonyldibenzonitrile) (acac) to two other dinitrile linkers (4,4'-(1H-pyrazole-3,5-diyl)dibenzonitrile (pyz) and 4,4'-(isoxazole-3,5-diyl)dibenzonitrile (isox)) was performed. Using them, two new sets of CTF materials (pyz-CTF and isox-CTF) with different functional groups were synthesized under ionothermal conditions, thoroughly characterized and explored for carbon capture storage and metal-free heterogeneous catalysis. Among all, isox-CTF-5-400 showed the best CO₂ capture (4.9 mmol/g at 273 K

and 1 bar) and CO₂/N₂ selectivity (28). Further, TPD-CO₂ analysis confirmed that the surface basicity of CTF is equally responsible as the surface area and the pore volume for enhanced CO₂ uptake. In addition, these new CTF materials showed excellent catalytic activity as an efficient solid porous base catalyst for aerobic oxidation of amine to imine in mild conditions using simple air as terminal oxidant. The mechanism of the reaction suggested that benzylimine was the sole intermediate during the reaction and was obtained by direct activation of benzylamine and O₂ through the basic nitrogen sites present in the CTF material. CTF with the highest basicity, showed best reactivity for the oxidation reaction.

5.4. Experimental Section

Materials and Methods. The required chemicals were purchased from Sigma-Aldrich and used without further purifications. The ¹H and ¹³C NMR analysis of the dinitrile linker were measured using a 300 MHz spectrometer. Elemental analyses (C, H, N and O) were carried out on a Thermo Scientific Flash 2000 CHNS-O analyser equipped with a TCD detector. Fourier Transform Infrared Spectroscopy (FT-IR) in the region of 4000-650 cm⁻¹ were performed with a Thermo Nicolet 6700 FT-IR spectrometer equipped with a nitrogen-cooled MCT detector and a KBr beam splitter. Dinitrogen (N₂) adsorption isotherms were obtained using a Belsorp Mini apparatus measured at 77 K, whereas CO₂ and H₂ adsorption measurements were carried out on a Quantachrome iSorb-HP gas sorption analyzer at respective temperatures and 1 bar pressure. TPD-CO₂ measurements were performed in a Quantachrome Autosorb-iQ TPX with a flow of CO₂/He (5/95) mixture. Powder X-ray diffraction (PXRD) patterns were collected on a Thermo Scientific ARL X'Tra diffractometer, operated at 40 kV, 30 mA using Cu-K α radiation (λ = 1.5406 Å). Thermogravimetric analysis (TGA) were performed on a Netzsch STA-449 F3 Jupiter-simultaneous TG-DSC analyzer in a temperature range of 20 - 800 °C under N₂ atmosphere and a heating rate of 2 °C/min. The X-ray photoelectron spectroscopy (XPS) measurements were performed on a Thermo Fisher Scientific K-Alpha 250 Xi. For the structure of the 4,4'-(1H-pyrazole-3,5-diyl)dibenzonitrile (pyz), X-ray intensity data were collected on an Agilent Supernova Dual Source (Cu at zero) diffractometer equipped with an Atlas CCD detector using CuK α radiation (λ = 1.54178 Å) and ω scans. The images were interpreted and integrated with the program CrysAlisPro (Agilent Technologies).¹⁹ Using Olex2,²⁰ the structure was solved by direct methods using the ShelXS structure solution program and refined by full-matrix least-

squares on F² using the ShelXL program package.²¹ Non-hydrogen atoms were anisotropically refined and the hydrogen atoms in the riding mode and isotropic temperature factors fixed at 1.2 times U(eq) of the parent atoms.

5.5. References

- (1) a) S. Kramer, N. R. Bennedsen and S. Kegnæs, *ACS Catalysis* 2018, 8, 6961-6982; b) Y. Zhang and S. N. Riduan, *Chemical Society Reviews* 2012, 41, 2083-2094; c) P. Kaur, J. T. Hupp and S. T. Nguyen, *ACS Catalysis* 2011, 1, 819-835.
- (2) a) A.-H. Lu and S. Dai, *Porous materials for carbon dioxide capture*, Springer, 2014, p; b) L. Zou, Y. Sun, S. Che, X. Yang, X. Wang, M. Bosch, Q. Wang, H. Li, M. Smith and S. Yuan, *Advanced Materials* 2017, 29, 1700229; c) E. S. Sanz-Perez, C. R. Murdock, S. A. Didas and C. W. Jones, *Chemical reviews* 2016, 116, 11840-11876; d) Y. S. Bae and R. Q. Snurr, *Angewandte Chemie International Edition* 2011, 50, 11586-11596; e) D. M. D'Alessandro, B. Smit and J. R. Long, *Angewandte Chemie International Edition* 2010, 49, 6058-6082.
- (3) a) R. Rinaldi and F. Schüth, *Energy & Environmental Science* 2009, 2, 610-626; b) R. Palkovits, M. Antonietti, P. Kuhn, A. Thomas and F. Schüth, *Angewandte Chemie International Edition* 2009, 48, 6909-6912; c) A. Thomas, *Angewandte Chemie International Edition* 2010, 49, 8328-8344.
- (4) a) Y. Zhang and S. Jin, *Polymers* 2019, 11, 31; b) J. Artz, *ChemCatChem* 2018, 10, 1753-1771; c) M. Liu, L. Guo, S. Jin and B. Tan, *Journal of Materials Chemistry A* 2019, 7, 5153-5172; d) P. Puthiaraj, Y.-R. Lee, S. Zhang and W.-S. Ahn, *Journal of Materials Chemistry A* 2016, 4, 16288-16311.
- (5) a) S. Hug, L. Stegbauer, H. Oh, M. Hirscher and B. V. Lotsch, *Chemistry of Materials* 2015, 27, 8001-8010; b) P. Katekomol, J. r. m. Roeser, M. Bojdys, J. Weber and A. Thomas, *Chemistry of Materials* 2013, 25, 1542-1548; c) P. Kuhn, M. Antonietti and A. Thomas, *Angewandte Chemie International Edition* 2008, 47, 3450-3453.
- (6) a) L. Tao, F. Niu, C. Wang, J. Liu, T. Wang and Q. Wang, *Journal of Materials Chemistry A* 2016, 4, 11812-11820; b) J. Du, Y. Liu, R. Krishna, Y. Yu, Y. Cui, S. Wang, Y. Liu, X. Song and Z. Liang, *ACS applied materials & interfaces* 2018, 10, 26678-26686.

- (7) S. Hug, M. B. Mesch, H. Oh, N. Popp, M. Hirscher, J. Senker and B. V. Lotsch, *Journal of Materials Chemistry A* 2014, 2, 5928-5936.
- (8) W. Yu, S. Gu, Y. Fu, S. Xiong, C. Pan, Y. Liu and G. Yu, *Journal of Catalysis* 2018, 362, 1-9.
- (9) a) S. H. Je, H. J. Kim, J. Kim, J. W. Choi and A. Coskun, *Advanced Functional Materials* 2017, 27, 1703947; b) G. Wang, K. Leus, H. S. Jena, C. Krishnaraj, S. Zhao, H. Depauw, N. Tahir, Y.-Y. Liu and P. Van Der Voort, *Journal of Materials Chemistry A* 2018, 6, 6370-6375; c) F. Xu, S. Yang, G. Jiang, Q. Ye, B. Wei and H. Wang, *ACS applied materials & interfaces* 2017, 9, 37731-37738; d) Y. Zhao, K. X. Yao, B. Teng, T. Zhang and Y. Han, *Energy & Environmental Science* 2013, 6, 3684-3692.
- (10) a) S. Mukherjee, M. Das, A. Manna, R. Krishna and S. Das, *Journal of Materials Chemistry A* 2019, 7, 1055-1068; b) S. Mukherjee, M. Das, A. Manna, R. Krishna and S. Das, *Chemistry of Materials* 2019, 31, 3929-3940.
- (11) a) O. Buyukcakil, S. H. Je, S. N. Talapaneni, D. Kim and A. Coskun, *ACS applied materials & interfaces* 2017, 9, 7209-7216; b) X. Zhu, C. Tian, G. M. Veith, C. W. Abney, J. r. m. Dehaut and S. Dai, *Journal of the American Chemical Society* 2016, 138, 11497-11500; c) K. Park, K. Lee, H. Kim, V. Ganesan, K. Cho, S. K. Jeong and S. Yoon, *Journal of Materials Chemistry A* 2017, 5, 8576-8582; d) K. Yuan, C. Liu, L. Zong, G. Yu, S. Cheng, J. Wang, Z. Weng and X. Jian, *ACS applied materials & interfaces* 2017, 9, 13201-13212; e) M. J. Bojdys, J. Jeromenok, A. Thomas and M. Antonietti, *Advanced materials* 2010, 22, 2202-2205; f) H. S. Jena, C. Krishnaraj, G. Wang, K. Leus, J. Schmidt, N. Chaoui and P. Van Der Voort, *Chemistry of Materials* 2018, 30, 4102-4111.
- (12) a) A. Bavykina, H.-H. Mautscke, M. Makkee, F. Kapteijn, J. Gascon and F. L. i Xamena, *CrystEngComm* 2017, 19, 4166-4170; b) C. E. Chan-Thaw, A. Villa, L. Prati and A. Thomas, *Chemistry—A European Journal* 2011, 17, 1052-1057; c) T. He, L. Liu, G. Wu and P. Chen, *Journal of Materials Chemistry A* 2015, 3, 16235-16241; d) A. V. Bavykina, E. Rozhko, M. G. Goesten, T. Wezendonk, B. Seoane, F. Kapteijn, M. Makkee and J. Gascon, *ChemCatChem* 2016, 8, 2217-2221; e) A. V. Bavykina, A. I. Olivos-Suarez, D. Osadchii, R. Valecha, R. Franz, M. Makkee, F. Kapteijn and J. Gascon, *ACS applied materials & interfaces* 2017, 9, 26060-26065; f) G. H. Gunasekar, K. Park, V. Ganesan, K. Lee, N.-K. Kim, K.-D. Jung

- and S. Yoon, *Chemistry of Materials* 2017, 29, 6740-6748; g) A. K. Beine, A. J. Krüger, J. Artz, C. Weidenthaler, C. Glotzbach, P. J. Hausoul and R. Palkovits, *Green Chemistry* 2018, 20, 1316-1322; h) J. Artz and R. Palkovits, *ChemSusChem* 2015, 8, 3832-3838; i) Q.-Q. Dang, C.-Y. Liu, X.-M. Wang and X.-M. Zhang, *ACS applied materials & interfaces* 2018, 10, 27972-27978; j) C. E. Chan-Thaw, A. Villa, D. Wang, V. D. Santo, A. Orbelli Biroli, G. M. Veith, A. Thomas and L. Prati, *ChemCatChem* 2015, 7, 2149-2154; k) X. Lan, C. Du, L. Cao, T. She, Y. Li and G. Bai, *ACS applied materials & interfaces* 2018, 10, 38953-38962; l) N. Tahir, F. Muniz-Miranda, J. Everaert, P. Tack, T. Heugebaert, K. Leus, L. Vincze, C. V. Stevens, V. Van Speybroeck and P. Van Der Voort, *Journal of Catalysis* 2019, 371, 135-143.
- (13) a) T. T. Liu, R. Xu, J. D. Yi, J. Liang, X. S. Wang, P. C. Shi, Y. B. Huang and R. Cao, *ChemCatChem* 2018, 10, 2036-2040; b) J. Roeser, K. Kailasam and A. Thomas, *ChemSusChem* 2012, 5, 1793-1799.
- (14) L. Zhao, S. Shi, M. Liu, G. Zhu, M. Wang, W. Du, J. Gao and J. Xu, *Green Chemistry* 2018, 20, 1270-1279.
- (15) E. Troschke, K. D. Nguyen, S. Paasch, J. Schmidt, G. Nickerl, I. Senkovska, E. Brunner and S. Kaskel, *Chemistry—A European Journal* 2018, 24, 18629-18633.
- (16) Y. J. Lee, S. N. Talapaneni and A. Coskun, *ACS applied materials & interfaces* 2017, 9, 30679-30685.
- (17) G. Zhu, S. Shi, M. Liu, L. Zhao, M. Wang, X. Zheng, J. Gao and J. Xu, *ACS applied materials & interfaces* 2018, 10, 12612-12617.
- (18) G. Tuci, A. Iemhoff, H. Ba, L. Luconi, A. Rossin, V. Papaefthimiou, R. Palkovits, J. Artz, C. Pham-Huu and G. Giambastiani, *Beilstein Journal of Nanotechnology* 2019, 10, 1217-1227.
- (19) R. O. Diffraction in CrysAlisPro Software System, Vol. Rigaku Corporation Oxford, UK, 2018.
- (20) O. V. Dolomanov, L. J. Bourhis, R. J. Gildea, J. A. Howard and H. Puschmann, *Journal of Applied Crystallography* 2009, 42, 339-341.
- (21) G. M. Sheldrick, *Acta Crystallographica Section A: Foundations of Crystallography* 2008, 64, 112-122.

- (22) S. Ren, M. J. Bojdys, R. Dawson, A. Laybourn, Y. Z. Khimyak, D. J. Adams and A. I. Cooper, *Advanced Materials* 2012, 24, 2357-2361.
- (23) K. Wang, L. M. Yang, X. Wang, L. Guo, G. Cheng, C. Zhang, S. Jin, B. Tan and A. Cooper, *Angewandte Chemie International Edition* 2017, 56, 14149-14153.
- (24) S. Y. Yu, J. Mahmood, H. J. Noh, J. M. Seo, S. M. Jung, S. H. Shin, Y. K. Im, I. Y. Jeon and J. B. Baek, *Angewandte Chemie International Edition* 2018, 57, 8438-8442.
- (25) G. Wang, K. Leus, S. Zhao and P. Van Der Voort, *ACS applied materials & interfaces* 2017, 10, 1244-1249.
- (26) D. Y. Osadchii, A. I. Olivos-Suarez, A. V. Bavykina and J. Gascon, *Langmuir* 2017, 33, 14278-14285.
- (27) C. Krishnaraj, H. S. Jena, K. Leus, H. Freeman, L. G. Benning and P. Van Der Voort, *Journal of Materials Chemistry A* 2019.
- (28) H. Naims, *Environmental Science and Pollution Research* 2016, 23, 22226-22241.
- (29) S. Keskin, T. M. van Heest and D. S. Sholl, *ChemSusChem* 2010, 3, 879-891.
- (30) G. Tuci, M. Pilaski, H. Ba, A. Rossin, L. Luconi, S. Caporali, C. Pham-Huu, R. Palkovits and G. Giambastiani, *Advanced Functional Materials* 2017, 27, 1605672.
- (31) S. K. Das, S. Mondal, S. Chatterjee and A. Bhaumik, *ChemCatChem* 2018, 10, 2488-2495.
- (32) F. Su, S. C. Mathew, L. Möhlmann, M. Antonietti, X. Wang and S. Blechert, *Angewandte Chemie International Edition* 2011, 50, 657-660.
- (33) a) H. Huang, J. Huang, Y.-M. Liu, H.-Y. He, Y. Cao and K.-N. Fan, *Green Chemistry* 2012, 14, 930-934; b) B. Chen, L. Wang, W. Dai, S. Shang, Y. Lv and S. Gao, *ACS Catalysis* 2015, 5, 2788-2794; c) P. Yang, J. Zhang, D. Liu, M. Liu, H. Zhang, P. Zhao and C. Zhang, *Microporous and Mesoporous Materials* 2018, 266, 198-203; d) X. Qiu, C. Len, R. Luque and Y. Li, *ChemSusChem* 2014, 7, 1684-1688; e) F. Raza, J. H. Park, H.-R. Lee, H.-I. Kim, S.-J. Jeon and J.-H. Kim, *ACS Catalysis* 2016, 6, 2754-2759; f) Y. Zhi, K. Li, H. Xia, M. Xue, Y. Mu and X. Liu, *Journal of Materials Chemistry A* 2017, 5, 8697-8704; g) H. Zheng, S. Shi, X. Wang, L. Zhao, G. Zhu, M. Liu, J. Gao and J. Xu, *ChemistrySelect* 2019, 4, 5073-5080

5.6. Supporting Information

Synthesis of linkers

[(4,4'-(1H-pyrazole-3,5-diyl)dibenzonitrile)] (pyz) and [4,4'-(isoxazole-3,5-diyl)dibenzonitrile] (isox)

Both linkers (pyz and isox) were successfully obtained from the reaction of 4,4'-malonyldibenzonitrile (acac) with hydrazine hydrate and hydroxylamine hydrochloride respectively in refluxing ethanol. Detail procedure with NMR and FT-IR analysis are described as follows. NMR, LC-MS spectra and FT-IR spectra are shown in Figure S1 to Figure S7.

pyz: 1g (3.64 mmol) of acac was dispersed in 50 mL of absolute ethanol and to the mixture hydrazine hydrate (0.5 mL) was added dropwise. After sometimes, the reaction mixture gave a clear solution and precipitates slowly deposited in the flask. After 4h ensuring fully conversion, the reaction brought to room temperature and flited. The residues were washed in hot ethanol and dried under vacuum. Yield: 95%; ¹H NMR (300 MHz, DMSO-d₆): d = 13.83(s, 1H, NH), 7.87-7.98 (dd, J=6, J=9, 8H, ArH), 7.50 (s, 1 H, =CH); ¹³C NMR (75 MHz, DMSO-d₆): 132.9, 125.8, 118.7, 102.37; LC-MS(ES⁺): 271.1; IR (KBr, cm⁻¹): 3839, 3600, 3500, 3410, 3182, 3131, 3073, 2918, 2867, 1609, 1588, 1561, 1501, 1450, 1424, 1407, 1389, 1313, 1267, 1230, 1183, 1114, 1090, 1018, 975, 960,844, 816, 791, 614.

isox: 1g (3.64 mmol) of acac was dispersed in a mixture of 50 mL of water and absolute ethanol each and stirred for 10 mints. To the mixture hydroxylamine hydrochloride (0.5 g, 0.7 mmol) was added batch wise. After sometimes, color of the precipitates slowly turned to off-white. After 4h ensuring fully conversion, the reaction brought to room temperature and flited. The residues were washed in hot ethanol and dried under vacuum. Yield: 80%; ¹H NMR (300 MHz, DMSO-d₆): d = 8.10-8.02(m, 8H, ArH), 7.93 (s, 1 H, =CH); ¹³C NMR (75 MHz, DMSO-d₆): 168.46, 161.67, 133.32, 133.19, 132.39, 130.25, 127.39, 126.24, 118.31, 118.22, 112.90, 112.90, 101.24; LC-MS(ES⁺): 272.1, IR (KBr, cm⁻¹): 3837, 3411, 3099, 3068, 2918, 2855, 2230, 1613, 1593, 1556, 1493, 1294, 1225, 1120, 1051, 1017, 959, 854, 833, 787, 711, 692.

General CTF synthesis

For CTF synthesis, respective linkers and 5 equivalents of ZnCl_2 were taken together with glass ampoules and dried under vacuum for 1 h. Glass ampoules with materials were then vacuum sealed and heated to desired temperatures in a Nabertherm oven in $1^\circ\text{C}/\text{min}$ for 48 h. After the oven reached room temperature, black materials were removed from the ampoules and dispersed in 1H HCl overnight, followed by reflux in water. The isolated shiny black materials were cleaned with THF by stirring overnight, filtered, washed with excess THF and dried under vacuum at 150°C . Detail synthesis conditions, yields and CHNS details are included in Table S1 and Table S2.

CTF-1 was synthesized using 1,4-dicyanobenzene and ZnCl_2 in 1:10 ratio for 48 hours at 400°C . The cleaning procedure was the same as for other CTFs.

Table S5.1. Synthetic conditions and abbreviations used for all the new CTFs.

Linker	Linker: ZnCl_2	Temperature ($^\circ\text{C}$) and 48 h	Yield (%)	abbreviations
pyz	1:5	400	72	pyz-CTF-5-400
	1:5	500	70	pyz -CTF-5-500
isox	1:5	400	69	isox-CTF-5-400
	1:5	500	68	isox-CTF-5-500

Table S5.2. Elemental Analysis of all the obtained acac-CTFs and V@acac-CTF-10-400.

	pyz-CTFs			isox-CTFs		
Element	Calculated (%)	Found (%)		Calculated (%)	Found (%)	
		5-400	5-500		5-400	5-500
C	75.54	78.761	70.968	75.27	53.650	71.227
H	3.73	2.188	1.250	3.34	3.369	1.665
N	20.73	10.888	8.914	15.49	7.467	7.917
C/N	3.64	7.23	7.96	4.85	7.18	8.99

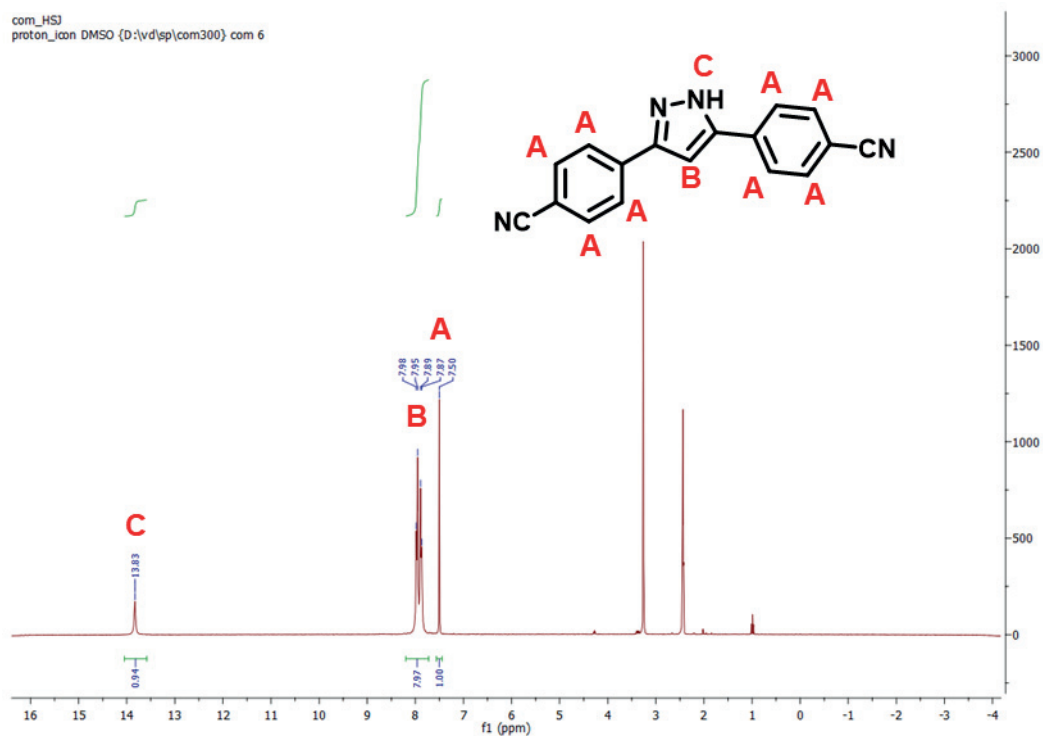


Figure S5.1. ¹H NMR spectrum of pyz in DMSO-d₆.

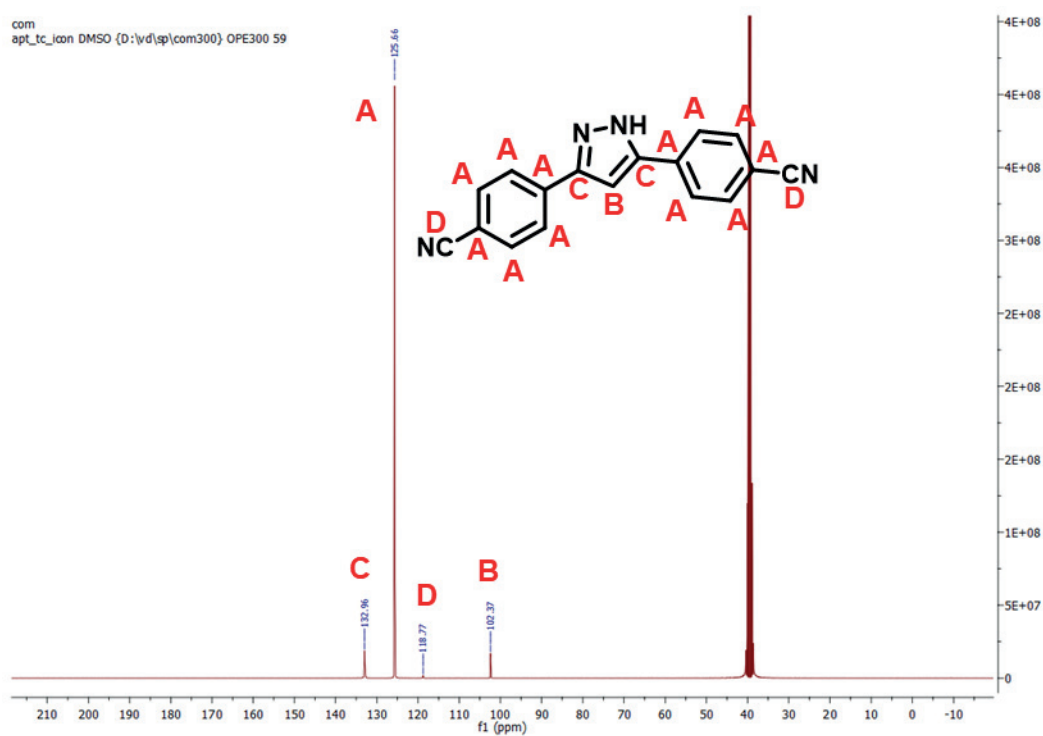


Figure S5.2. ¹³C NMR spectrum of pyz in DMSO-d₆.

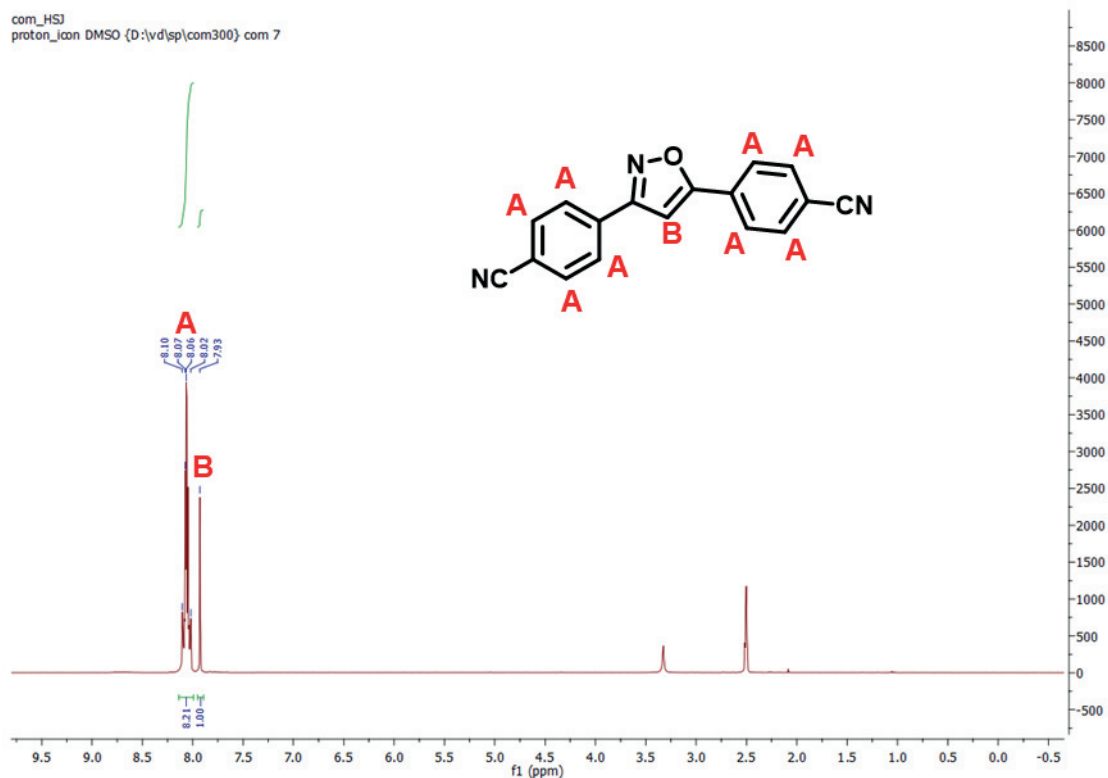


Figure S5.3. ^1H NMR spectrum of isox in DMSO-d_6 .

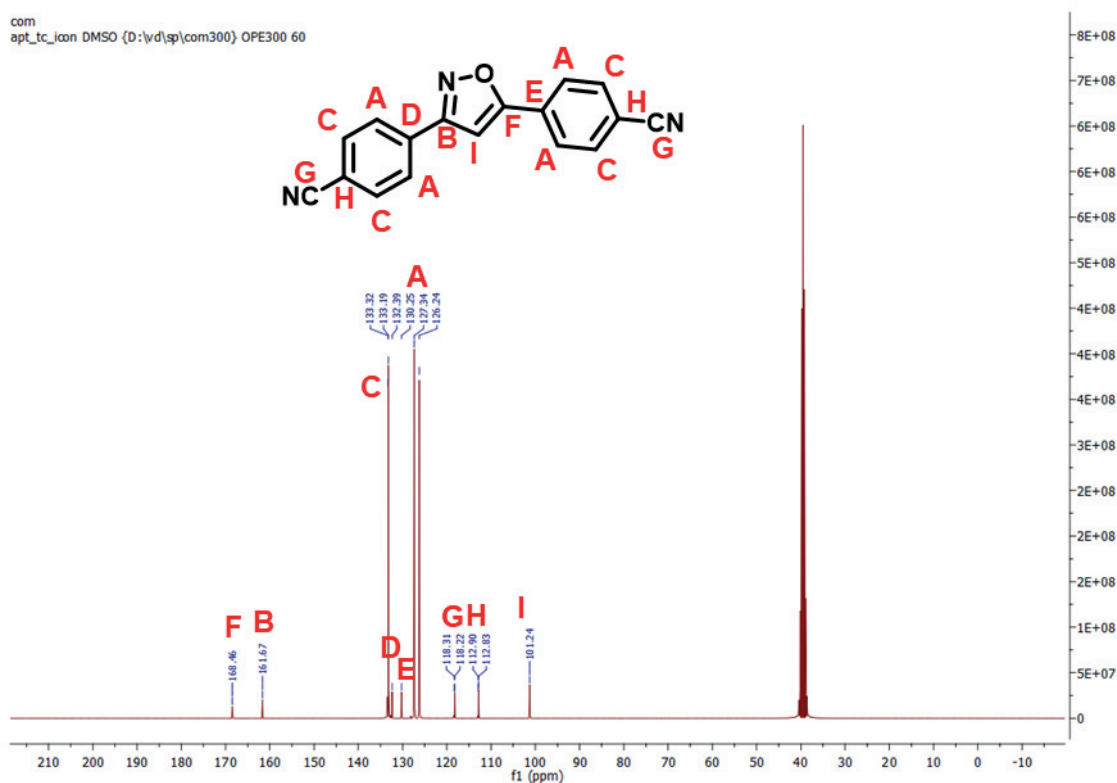


Figure S5.4. ^{13}C NMR spectrum of isox in DMSO-d_6 .

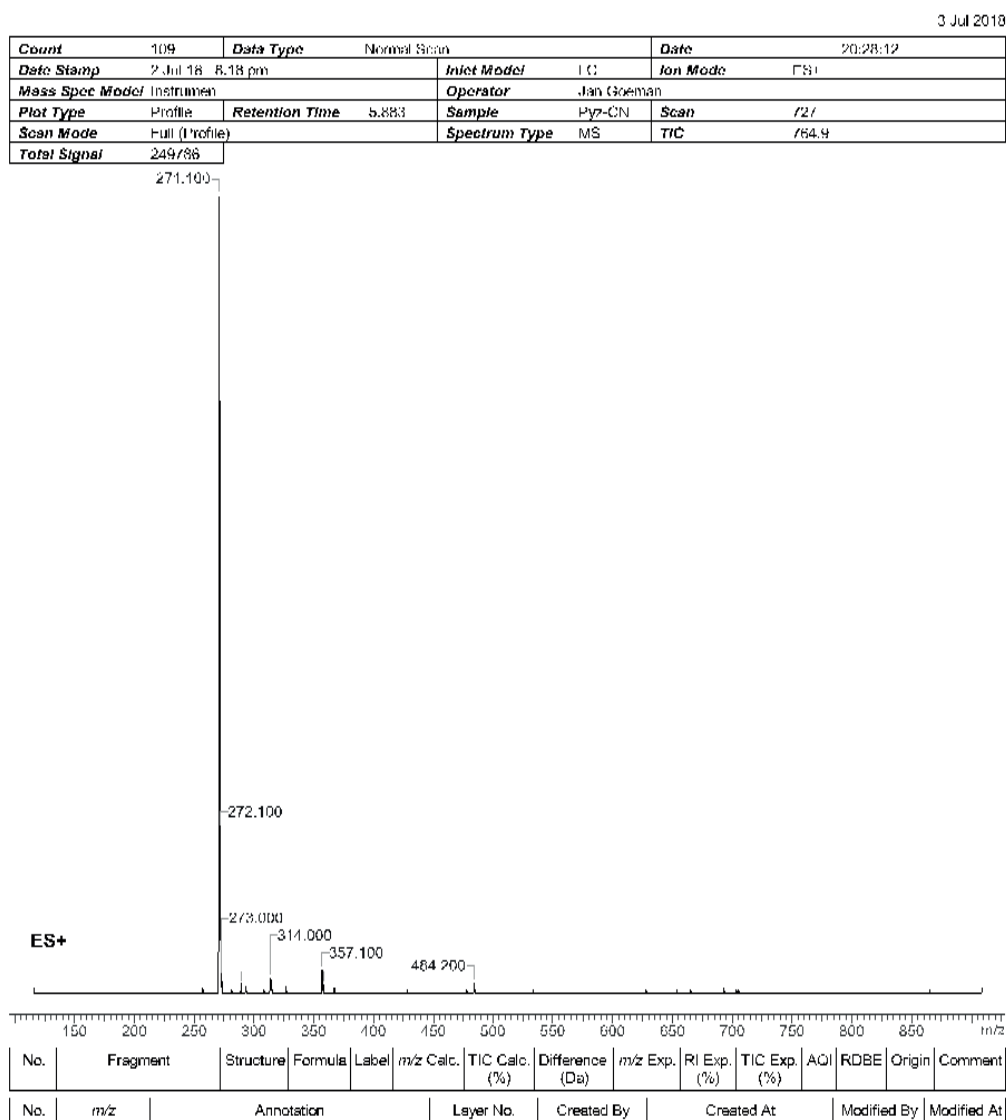


Figure S5.5. LC-MS spectrum of pyz.

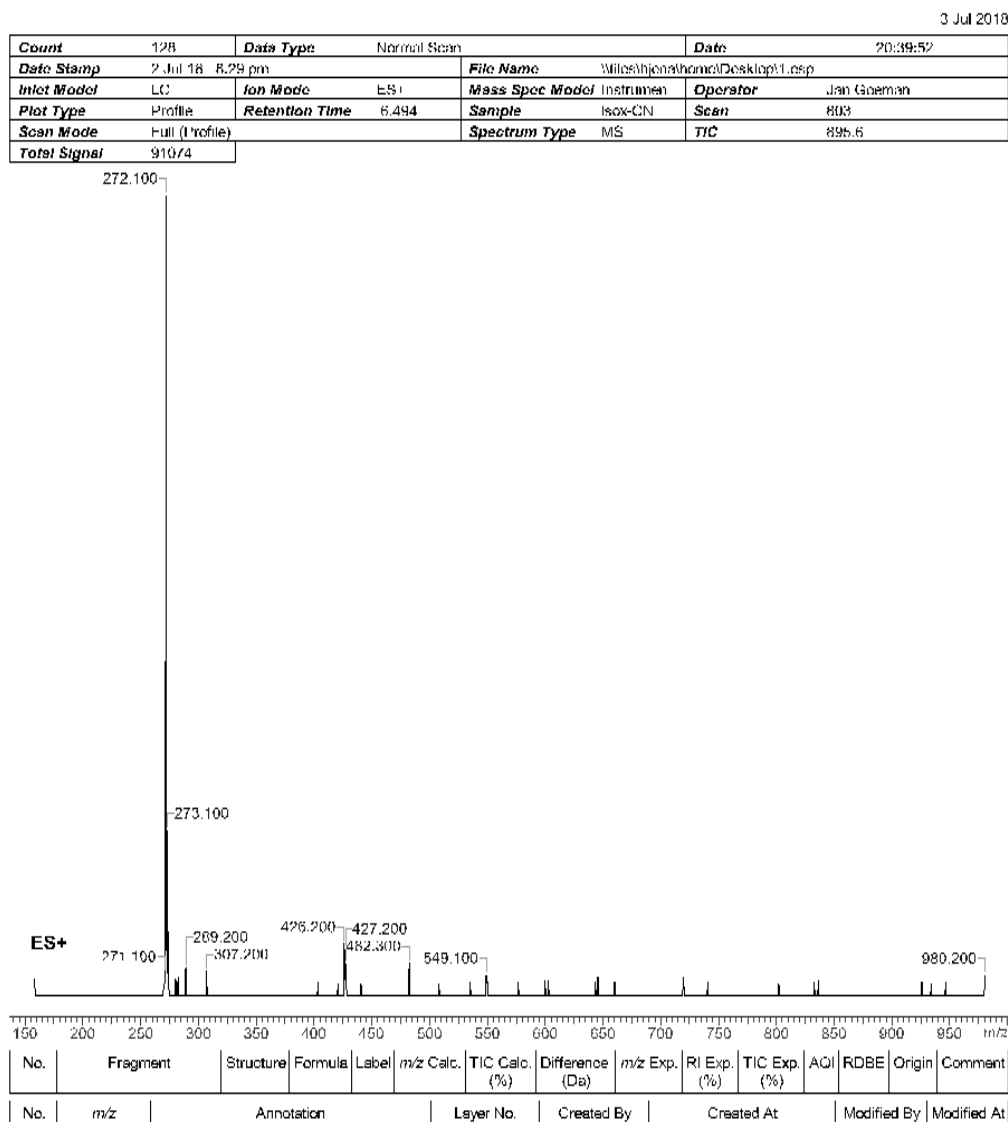


Figure S5.6. LC-MS spectrum of isox.

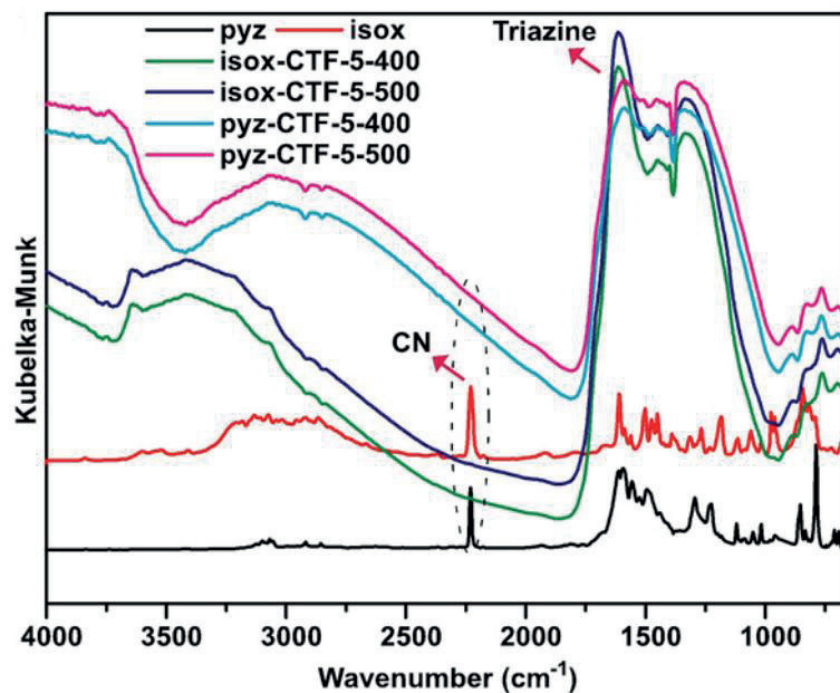


Figure S5.7. FT-IR spectral comparison between linkers and respective CTFs.

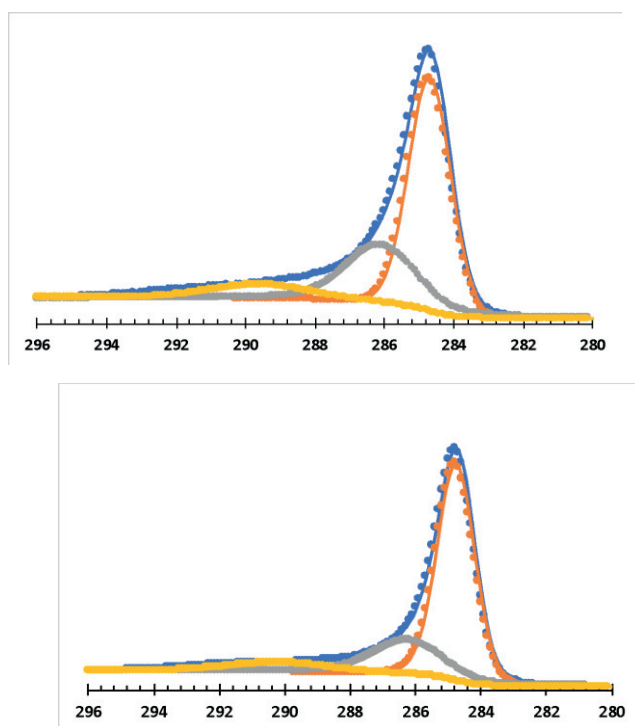


Figure S5.8. Deconvoluted XPS spectra of C 1s for pyz-CTF-5-400 (left) and isox-CTF-5-400 (right).

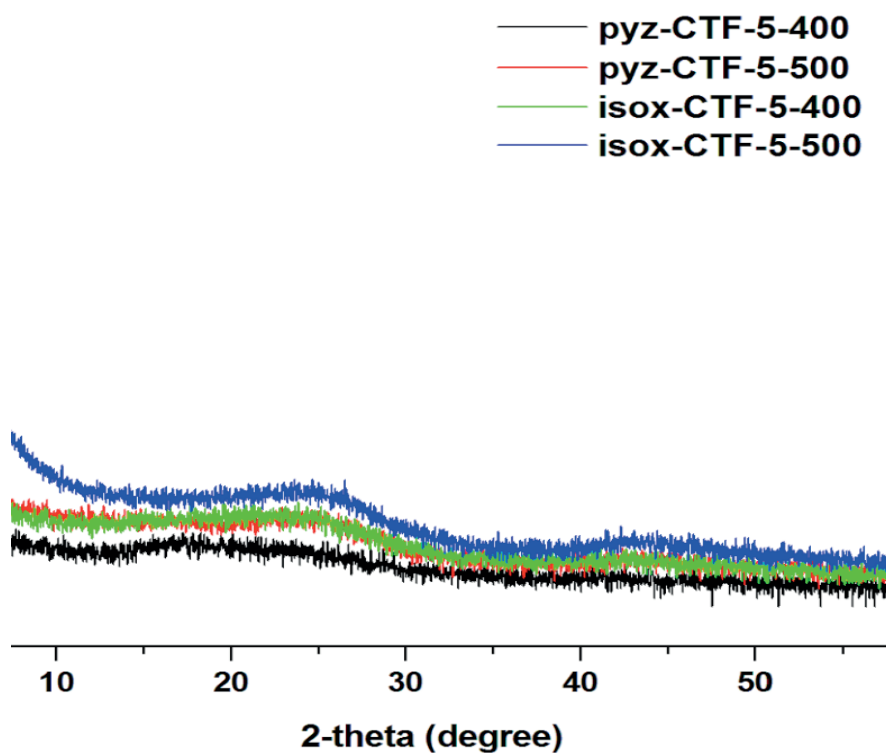


Figure S5.9. Powder X-ray diffraction (PXRD) spectra of all CTFs.

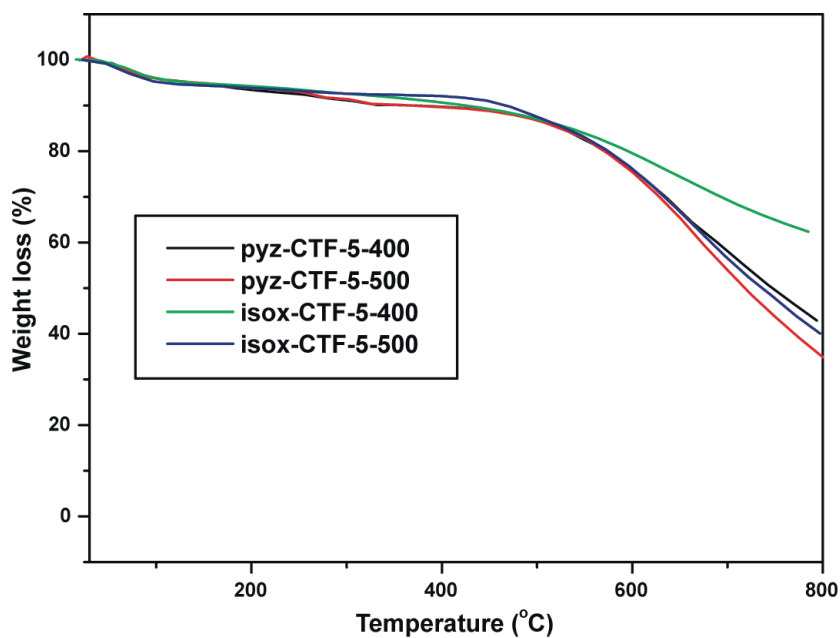


Figure S5.10. Thermogravimetric analysis spectra of all the CTFs.

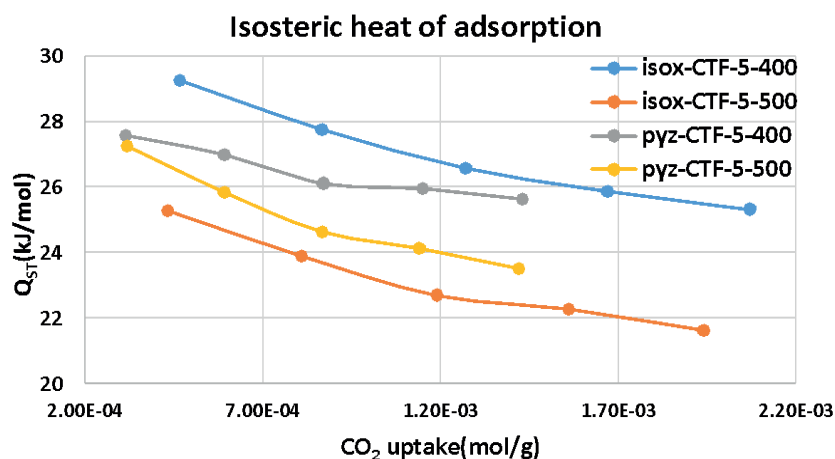


Figure S5.11. Isosteric heat (Q_{st}) of CO₂ adsorption for all CTFs.

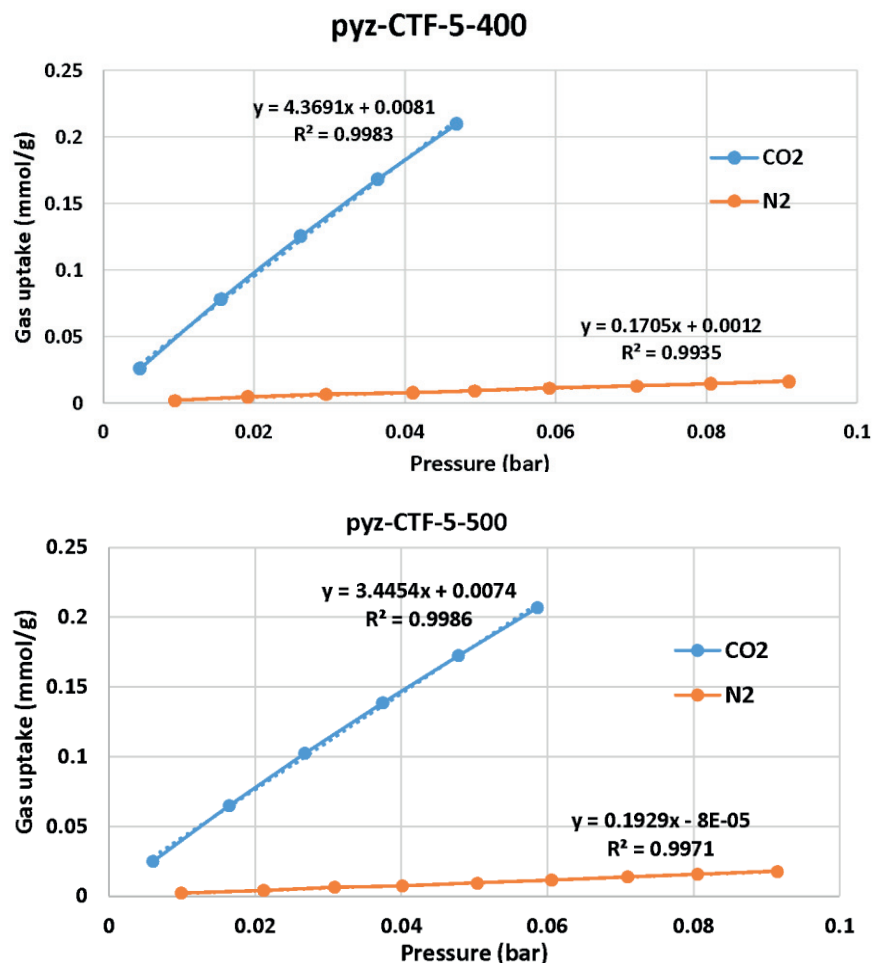


Figure S5.12. Henry plots of pyz-CTF-5-400 (top) and pyz-CTF-5-500(bottom) as obtained from CO₂ and N₂ isotherms at 298K.

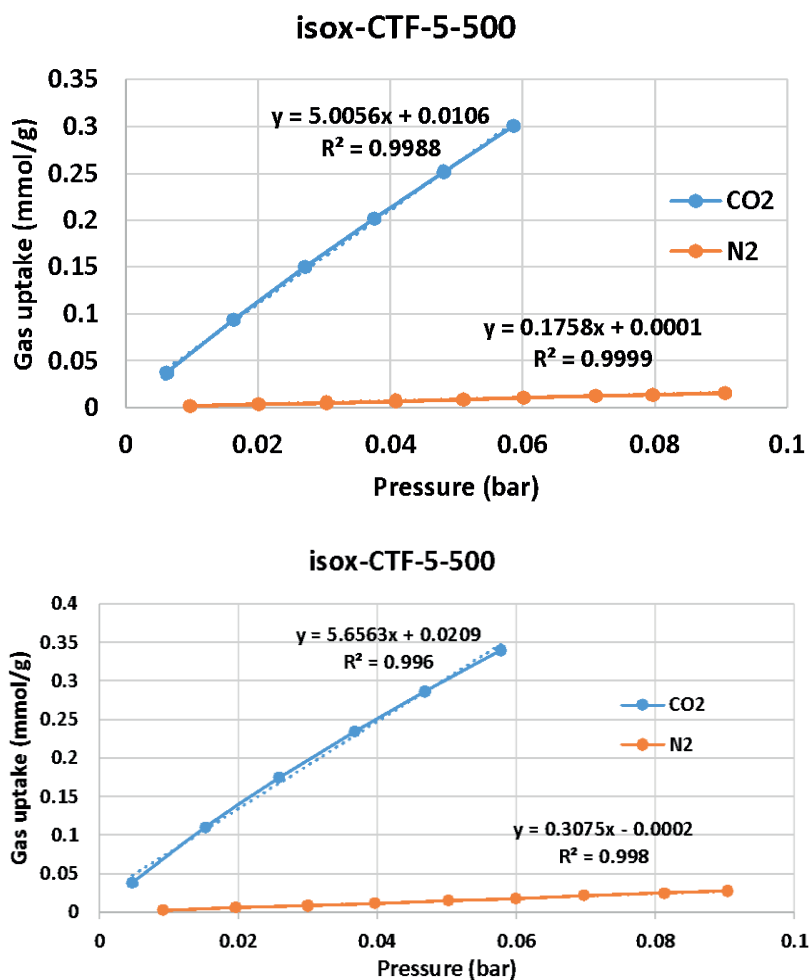


Figure S5.13. Henry plots of iso-CTF-5-400 (top) and iso-CTF-5-500 (bottom) as obtained from CO₂ and N₂ isotherms at 298K.

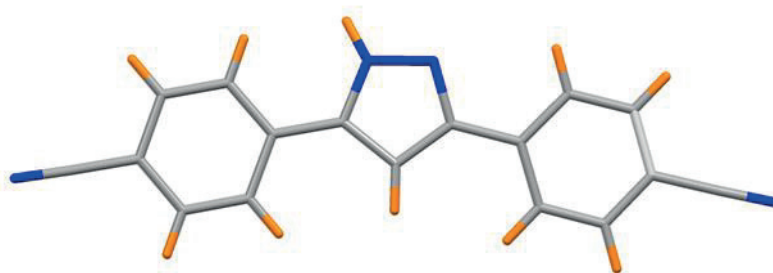


Figure S5.14. Stick-model of the crystal structure of 4,4'-(1*H*-pyrazole-3,5-diyl)dibenzonitrile (pyz). The dihedral angle of 151° between the planes containing two appended phenyl rings.

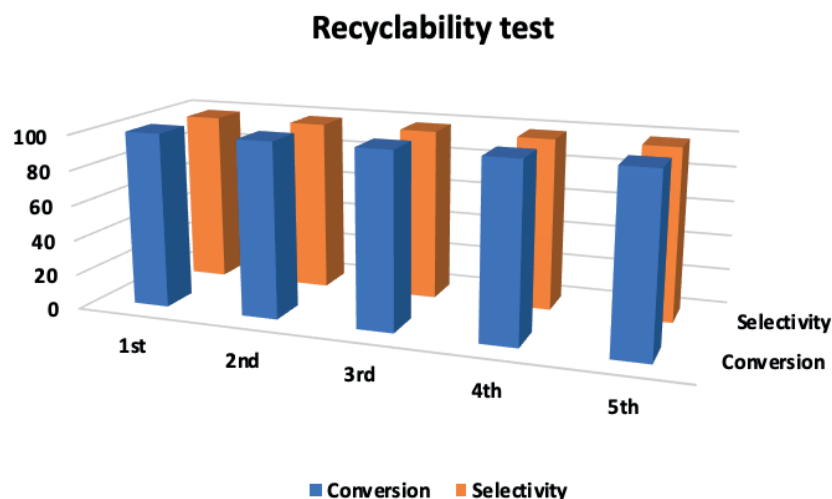
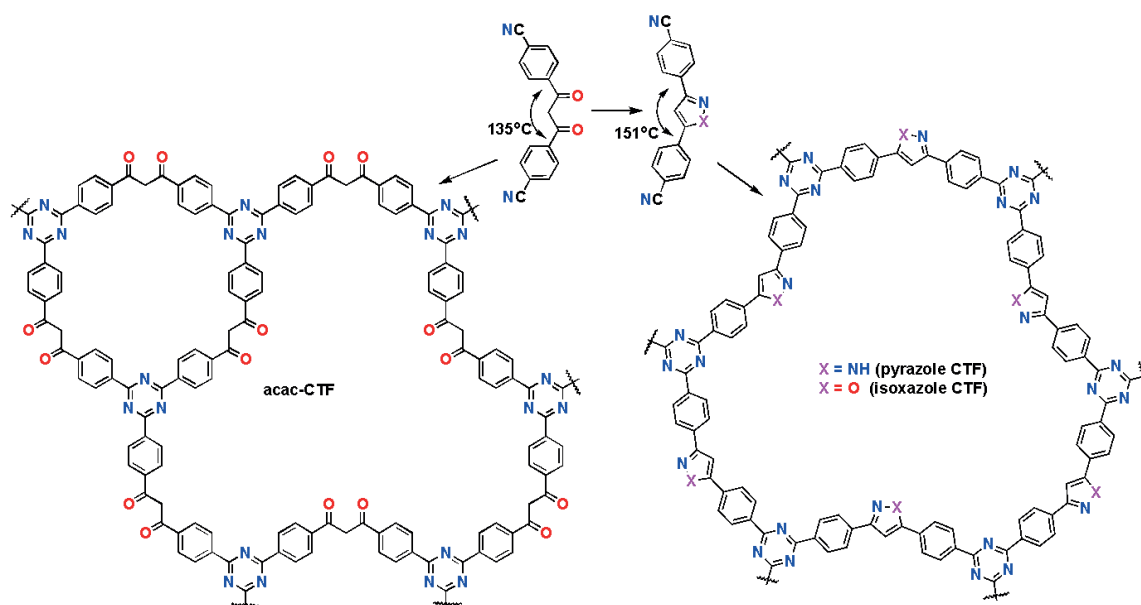


Figure S5.15. Recyclability test up to 5th cycle of catalysis using isox-CTF-5-400 as catalyst.



Scheme S5.1. Schematic representation of two different ideal structures of acac-CTF and pyz-/isox-CTF due to difference in dihedral angles and aromaticity.

General procedure for the amine oxidation reaction.

For the preliminary reactions, 10 mg of respective CTF (activated at 150°C prior to catalysis), benzylamine (**1a**, 2 mmol), mesitylene (2 mmol), and CH₃CN (3 mL) were transferred to 20 mL glass vials and evacuated for 30 mins followed by filling with oxygen. The mixture was allowed to stir at 40°C for 12 h. After the completion of

reaction, the heterogeneous mixture was allowed cool to room temperature. After 10 mins, all the CTF catalysts were settled down and a clear solution separated out. The solution was evaporated to dryness to afford pure imine (**2a**) as included in Table S3. Isolated imine was analyzed from ^1H NMR analysis using mesitylene as internal standard which was well matched with the reported literature¹⁻⁷. All the reactions included in Table 3 in the main article were repeated similarly according to the conditions noted respectively.

Table S5.3. Preliminary catalytic test.

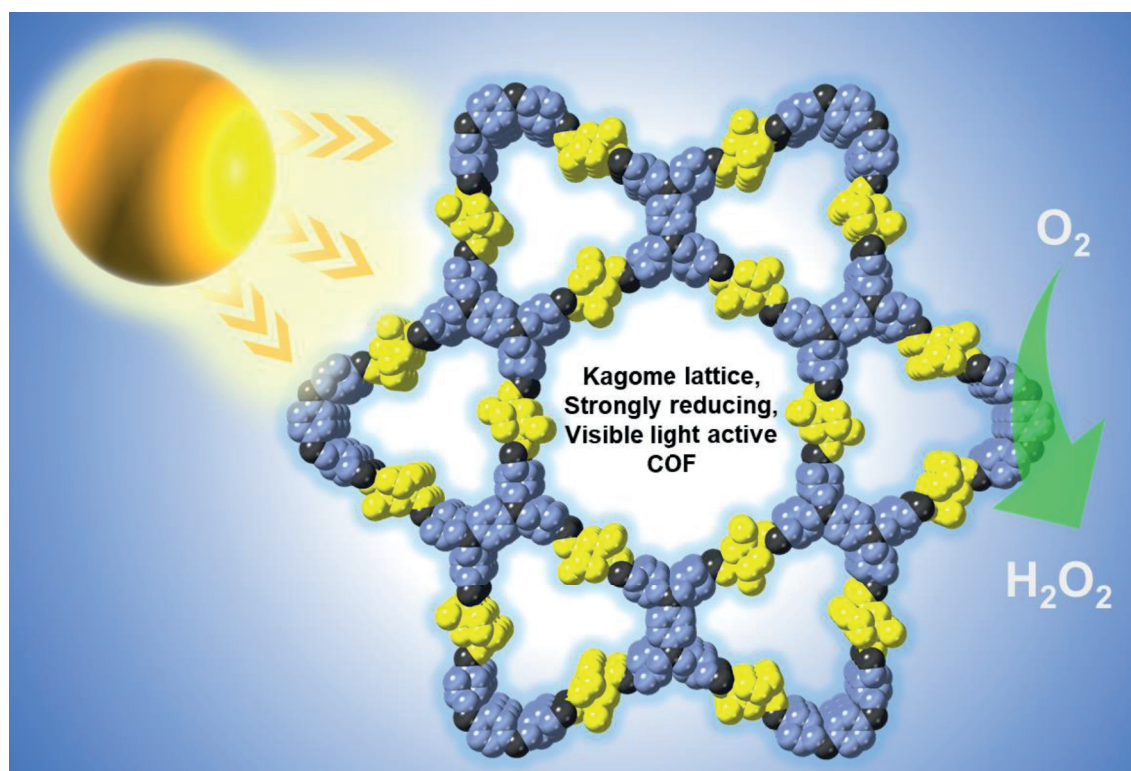
Entry	Catalyst	Solvent	Time (h)	Conditions	Conversion (%)
1	Pyz-CTF-5-500	CH ₃ CN	12	40°C/1 atm O ₂	60
2	Pyz-CTF-5-500	Dichloromethane	12	40°C/1 atm O ₂	18
3	Pyz-CTF-5-500	THF	12	40°C/1 atm O ₂	38
4	Pyz-CTF-5-500	Toluene	12	40°C/1 atm O ₂	35

References

- (S1) F. Su, S. C. Mathew, L. Möhlmann, M. Antonietti, X. Wang, S. Blechert, Aerobic Oxidative Coupling of Amines by Carbon Nitride Photocatalysis with Visible Light. *Angewandte Chemie International Edition* 2011, 50 (3), 657-660.
- (S2) H. Huang, J. Huang, Y.-M. Liu, H.-Y. He, Y. Cao, K.-N. Fan, Graphite oxide as an efficient and durable metal-free catalyst for aerobic oxidative coupling of amines to imines. *Green Chemistry* 2012, 14 (4), 930-934.
- (S3) B. Chen, L. Wang, W. Dai, S. Shang, Y. Lv, S. Gao, Metal-Free and Solvent-Free Oxidative Coupling of Amines to Imines with Mesoporous Carbon from Macrocyclic Compounds. *ACS Catalysis* 2015, 5 (5), 2788-2794.

- (S4) P. Yang, J. Zhang, D. Liu, M. Liu, H. Zhang, P. Zhao, C. Zhang, Facile synthesis of porous nitrogen-doped carbon for aerobic oxidation of amines to imines. *Microporous and Mesoporous Materials* 2018, 266, 198-203.
- (S5) X. Qiu, C. Len, R. Luque, Y. Li, Solventless Oxidative Coupling of Amines to Imines by Using Transition-Metal-Free Metal–Organic Frameworks. *ChemSusChem* 2014, 7 (6), 1684-1688.
- (S6) F. Raza, J. H. Park, H.-R. Lee, H.-I. Kim, S.-J. Jeon, J.-H. Kim, Visible-Light-Driven Oxidative Coupling Reactions of Amines by Photoactive WS₂ Nanosheets. *ACS Catalysis* 2016, 6 (5), 2754-2759.
- (S7) Y. Zhi, K. Li, H. Xia, M. Xue, Y. Mu, X. Liu, Robust porous organic polymers as efficient heterogeneous organo-photocatalysts for aerobic oxidation reactions. *J. Mater. Chem. A* 2017, 5 (18), 8697-8704.

6 (DIARYLAMINO) BENZENE BASED COF FOR METAL-FREE VISIBLE LIGHT PHOTOCATALYTIC H₂O₂ GENERATION



The results of this chapter were published in:

C Krishnaraj, HS Jena, L Bourda, A Laemont, P Pachfule, J Roeser, CV Chandran, S Borgmans, SMJ Rogge, K Leus, CV Stevens, JA Martens, V Van Speybroeck, E Breynaert, A Thomas, P Van Der Voort. Strongly Reducing (Diarylamino)benzene-Based Covalent Organic Framework for Metal-Free Visible Light Photocatalytic H₂O₂ Generation. **Journal of the American Chemical Society** 142(47), 2020, 20107-20116.

Abstract

Photocatalytic reduction of molecular oxygen is a promising route towards sustainable production of hydrogen peroxide (H₂O₂). This challenging process requires photoactive semiconductors enabling solar energy driven generation and separation of electrons and holes with high charge transfer kinetics. Covalent organic frameworks (COFs) are an emerging class of photoactive semiconductors, tuneable at a molecular level for high charge carrier generation and transfer. Herein, we report two newly designed 2D COFs based on (diarylamino)benzene linker that forms a kagome (**kgm**) lattice and shows strong visible light absorption. Their high crystallinity and large surface areas (up to 1165 m²·g⁻¹) allow efficient charge transfer and diffusion. The diarylamine (donor) unit promotes strong reduction properties, enabling these COFs to efficiently reduce oxygen to form H₂O₂. Overall, the use of a metal-free, recyclable photocatalytic system allows efficient photocatalytic solar transformations.

6.1. Introduction

Covalent Organic Frameworks (COFs) are an emerging class of crystalline porous organic materials, built up from covalently linked organic molecules.¹ Tuning the reticular chemistry leading to these structures enables synthesis of crystalline, photoactive, porous, and highly stable materials, providing an optimal platform for photocatalysis.² The main factors required for an efficient photocatalyst are: (i) suitable bandgap, (ii) proper band position alignments, (iii) strong light absorption, (iv) efficient charge carrier generation, (v) high charge transfer kinetics, (vi) low recombination, and (vii) efficient diffusion and active sites.³⁻⁵ By modifying the starting linker, COFs can be functionalized at a molecular level to optimize these properties. Functionalities such as triazine, porphyrin and, benzothiadiazole have been incorporated into COFs to improve charge transfer kinetics and charge carrier separation.^{2,6} By incorporating alternating donor-acceptor moieties into an extended framework, several COFs have been rendered suitable for photocatalysis.^{7,8} There remains however, extensive potential to design COFs optimized for photocatalysis by tweaking their structures at a molecular level.

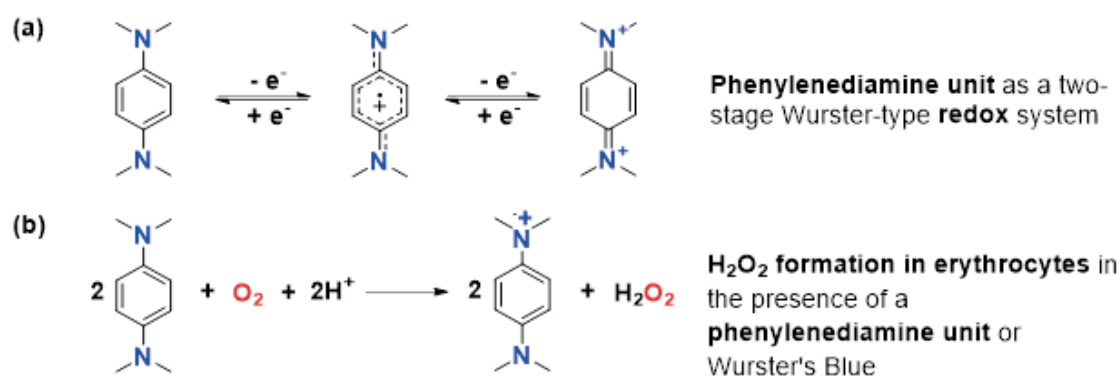


Figure 6. 1. (a) *N,N,N',N'*-Tetramethyl-*p*-phenylenediamine (TMPD) as a two-stage Wurster-type redox system. (b) Generation of hydrogen peroxide in erythrocytes in the presence of TMPD.²³

In photocatalysis, COFs have been mainly limited to hydrogen evolution reaction through water splitting,⁹ CO₂ reduction,¹⁰ degradation of organic pollutants,¹¹ oxidative hydroxylation of arylboronic acids to form phenols,¹² oxidation of anisoles to sulfoxides,¹³ reductive dehalogenation of phenacyl bromide,¹⁴ oxidative coupling of amines to imines,¹⁵ etc. To the best of our knowledge, COFs enabling photocatalytic reduction of molecular oxygen to produce H₂O₂ have not yet been reported.

Hydrogen peroxide (H₂O₂) is a widely used chemical with applications as antiseptic, disinfectant, bleaching agent, and as an oxidizer in synthetic pathways. It is produced on a large scale through multistep hydrogenation of anthraquinone moiety using H₂, followed by oxidation using O₂.¹⁶ Direct production of H₂O₂ with Au-Pd bimetallic catalysts using H₂ and O₂ gas mixtures was also investigated.¹⁷ Alternative approaches involving electrochemical, photocatalytic, and photoelectrochemical processes were also studied for this purpose.^{18,19} Recently, Yamashita and co-workers have developed a two-phase system for the photocatalytic H₂O₂ production. The photocatalyst is dispersed in one phase (benzyl alcohol) where oxidation reaction takes place, whereas in the other phase (water) reduction of O₂ to form H₂O₂ occurs.^{20,21} This promoted separation and avoided catalytic decomposition of H₂O₂. Photocatalytic pathways provide a sustainable route for H₂O₂ synthesis as they involve (i) a one-step reaction, (ii) utilization of green reagents, and (iii) light as the source of energy. Especially, the use of only visible light for the production of H₂O₂ is considered to be particularly sustainable.²² Photocatalytic H₂O₂ synthesis is performed by irradiating water saturated with oxygen in the presence of a semiconductor, using alcohols as the electron and proton donor. Excitation of the semiconductor produces electron (e⁻) and hole (h⁺) pairs. The holes oxidize the alcohol and produce aldehyde and protons (eq.6.1). Simultaneously, the electrons promote a two-electron reduction of oxygen to give H₂O₂ (eq.6.2).²² A side reaction, detrimental to the desired two-electron reduction of oxygen, involves one-electron reduction to produce a superoxide anion. Hence an efficient system to selectively perform the two-electron reduction is required.



Wurster-type systems are classic examples of phenylenediamine units displaying redox activity (Figure 6.1a).^{23,25} Phenylenediamine units are found in several dyes and are relevant in several biological processes. In erythrocytes, they can react with molecular O₂ to form superoxide radicals and Wurster salts, which can further react to generate hydrogen peroxide (Figure 6.1b).²⁵ For example, *N,N,N',N'*-tetramethyl-*p*-phenylenediamine (TMPD) undergoes autoxidation to generate ‘active oxygen’ species

which could be responsible for toxic changes in the erythrocytes. In a similar molecular system, Ito et al. reported 1-electron oxidation of 9,10-bis(di(*p*-anisyl)amino)anthracene inducing formation of the mixed-valence species, i.e., a delocalized cationic radical species, $[D-\pi-D]^+$.²⁴ Recently, diarylamine scaffolds (derivative of phenylenediamine) have been used for metal-free molecular photocatalytic fluoroalkylation.²⁶ The diarylamine (donor) moiety acts as a strong reducing agent and promotes reduction. These studies encouraged us to design COFs based on diarylamine/diaminobenzene units for exploiting their strong reduction properties in photocatalysis.

Herein, we report the synthesis of two novel, highly crystalline COFs: TAPD-(Me)₂ and TAPD-(OMe)₂. Both COFs are highly stable (chemically and thermally) and form a Kagome lattice as a result of the C4+C2 linkage. There are only a limited number of COFs with Kagome lattices²⁷⁻²⁹ and the new *N,N,N',N'*-Tetrakis(4-aminophenyl)-1,4-phenylenediamine (TAPD) linker expands the inventory of C4 linkers which can be used to form Kagome lattices. Considering the high charge-transfer transitions in COFs, for the first time, TAPD-(Me)₂ and TAPD-(OMe)₂ COFs have been applied for photocatalytic production of H₂O₂ through oxygen reduction. This photocatalytic system is completely metal-free and green solvents are used for the reaction, thus paving way for a sustainable pathway.

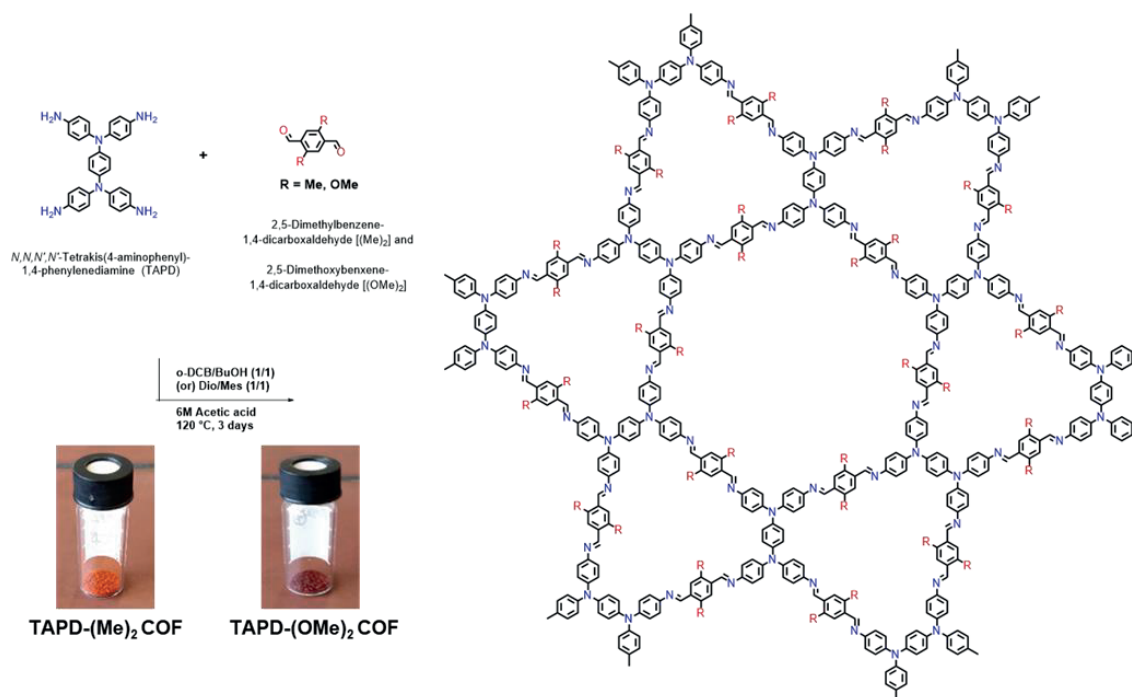


Figure 6. 2. Synthesis of TAPD-(Me)₂ and TAPD-(OMe)₂ COFs forming dual pore Kagome lattice.

6.2. Results and discussion

6.2.1. Synthesis of COFs

TAPD-(Me)₂ and TAPD-(OMe)₂ COFs are synthesized in the presence of 6 M acetic acid (0.1 ml) by reacting N,N,N',N'-Tetrakis(4-aminophenyl)-1,4-phenylenediamine (TAPD, 23.6 mg, 0.5 mmol) with 2,5-dimethylbenzene-1,4-dicarboxaldehyde ((Me)₂, 16.2 mg, 1 mmol) or 2,5-dimethoxybenzene-1,4-dicarboxaldehyde ((OMe)₂, 19.4 mg, 1 mmol), in the presence of 1:1 o-dichlorobenzene/butanol (0.6 ml) or 1:1 dioxane/mesitylene (0.6 ml) respectively (Figure 6.2, Section S6.2). For the synthesis of the COFs, the TAPD linker was deliberately utilized because of the possibility of internal charge-transfer transitions leading to strong absorption bands in the visible light region. In similar molecular systems (diarylamino(anthracene)), Konishi et al. showed that distorted donor planes induces interchromophoric conjugation rather than conjugation within the local structure which promotes charge-transfer between the diarylamine and anthracene moieties.³⁰ Contrary to the general expectation, Bredas et al. have shown that the strength of electronic interaction is higher in benzene than anthracene for such diarylamino systems due to the dependence on steric interactions.³¹ This led us to using diarylamino(benzene) as the COF linker to promote strong electronic interactions.

6.2.2. Characterization of COFs

The imine (C=N) bond formation was confirmed through Fourier Transform Infra-red (FT-IR) spectroscopy. Stretching vibrations at 1616 and 1612 cm⁻¹ correspond to imine linkages in TAPD-(Me)₂ and TAPD-(OMe)₂ COFs respectively (Figures S6.4, S6.5). ¹H direct excitation MAS NMR (35 kHz MAS; 800 MHz) confirmed the presence of phenyl, N=CH-Ph and methyl and methoxy protons for TAPD-(Me)₂ and TAPD-(OMe)₂ COFs, respectively. ¹³C{¹H} CPMAS (Figures 6.3g-3j) revealed 9 different carbon signals for TAPD-(Me)₂ COF and TAPD-(OMe)₂ COF. All carbon resonances can be assigned to the local chemical structure forming the Kagome sheets. Note that both ¹H MAS NMR and ¹³C{¹H} CPMAS NMR reveal the presence of methoxy and methyl substitutions in the structure. Combining ¹H DQ-SQ and ¹³C{¹H} CP HETCOR spectra allows to confirm the local chemical environments occurring in the COF structures (Figures 6.3c-3f). While ¹³C{¹H} CP HETCOR reveals the substitution of the C_A and C_B of the phenyl moiety with methyl and methoxy groups respectively, ¹H DQ-SQ MAS NMR reveals a strong correlation between the respective methyl/methoxy protons and the HCa of the phenyl

group (Figures S6.6-S6.9). Elemental analyses were performed to reveal the elemental composition of the COFs. The obtained C/N and C/H ratios were 7.23/13.49 for TAPD-(Me)₂ and 7.42/13.90 for TAPD-(OMe)₂ COFs, respectively. These values matched well with the theoretically calculated values (Table S6.2).

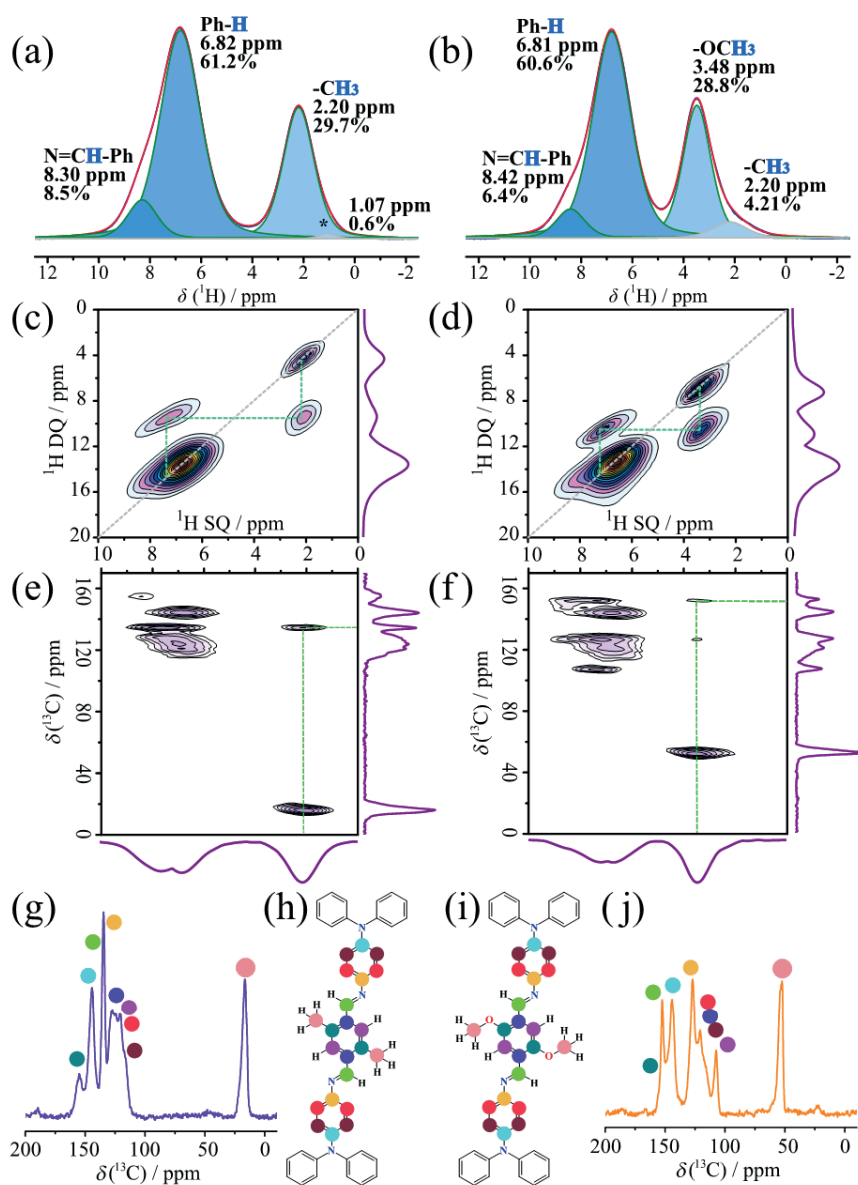


Figure 6. 3. Solid-state NMR spectra of TAPD-(Me)₂ (left column) and TAPD-(OMe)₂ (right column). Sections a and b show ¹H MAS (35 kHz) NMR spectra and decompositions which yielded the chemical shifts and fractions. Sections c and d show ¹H DQ-SQ 2D correlations indicating the proximity of one of the phenyl protons to the methyl and methoxy protons. Sections e and f show ¹H-¹³C CP HETCOR 2D correlations indicating the proximity of one type of carbon atoms at the phenyl rings to the attached methyl and methoxy protons. The ¹³C{¹H} CPMAS spectrum (g) corresponds to the structure (h) and the spectrum (j) corresponds to the structure (i).

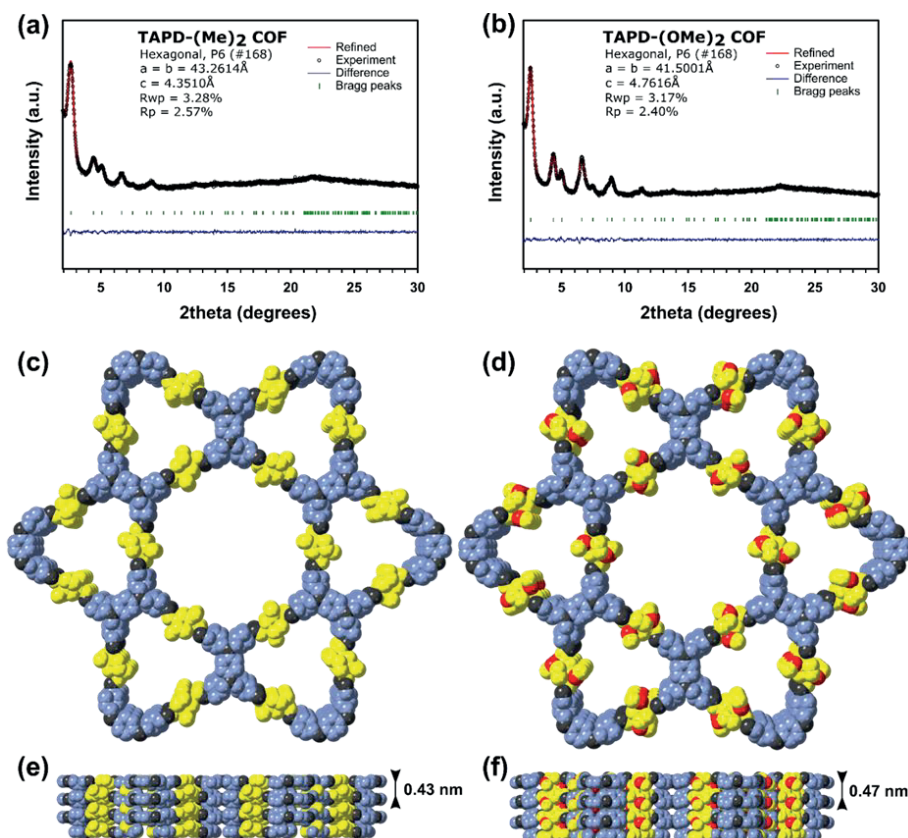


Figure 6. 4. PXRD pattern and Pawley refinement of (a) TAPD-(Me)₂ and (b) TAPD-(OMe)₂ COFs, Top view of (c) TAPD-(Me)₂ and (d) TAPD-(OMe)₂ COFs showing the ideal eclipsed (AA) structures. Side views of (e) TAPD-(Me)₂ and (f) TAPD-(OMe)₂ COFs. *H atoms are omitted for clarity.

Powder X-ray diffraction (PXRD) analyses were performed to determine the structural features of the synthesized COFs. Both TAPD-(Me)₂ and TAPD-(OMe)₂ COFs exhibited an intense reflection in the low-angle region at 2.3 and 2.4 degrees 2θ (*d* spacing = ~3.8 and 3.7 nm) respectively. An additional set of lower symmetry reflections that could not be assigned to the starting monomers are also obtained in the low angle region, indicating the formation of crystalline frameworks (Figures 6.4, S6.21 and S6.24). Indexing of the PXRD patterns in primitive hexagonal lattices and the presence of a broad diffraction peaks at ~20.4 and 18.6 degrees 2θ suggest the formation of a 2D layered material stacking in the *c* direction through π - π interactions. According to the symmetry of the linkers, the structural models for TAPD-(Me)₂ and TAPD-(OMe)₂ COFs were constructed by generating the expected 2D layers with **kgm** topology and modeling stacking sequences with eclipsed (AA) and staggered (AB) arrangement (Figure 6.4(c-f), section S6.4, Figures S6.21-S6.26). The models were geometrically optimized, and their corresponding theoretical PXRD patterns were compared to the experimentally measured

patterns. Pawley fitting over the full profile was carried out to refine the final unit cell parameters (TAPD-(Me)₂: $a=b=43.26\text{Å}$, $c=4.35\text{Å}$, $R_{\text{wp}}=3.28\%$; TAPD-(OMe)₂: $a=b=41.50\text{Å}$, $c=4.76\text{Å}$, $R_{\text{wp}}=3.17\%$), resulting in low residual values and acceptable profile differences (Figures 6.4a and 6.4b)).

To further elucidate the atomic structure of the synthesized COFs, molecular dynamics (MD) simulations were performed at 300 K and 1 bar to include peak broadening effects. These MD results are obtained without fitting or refining any model parameter, using *ab initio* derived force fields for the TAPD-(Me)₂ and TAPD-(OMe)₂ COFs using our QuickFF protocol^{32,33} (Section S5). Furthermore, as our dynamic simulations intrinsically take into account the movement of adjacent layers, no separate AA and AB models need to be considered. However, given that the functional groups in adjacent layers can either be in a parallel or an inverted conformation, both possibilities were explicitly modelled (Figure S6.28). As illustrated in Figure 6.5 and S6.30, the MD simulations provide similar unit cell parameters for both COFs in line with the expectations for the almost identical building units used in both materials and indicate that the COFs display only limited deviations from a perfect AA stacking, showcasing the strong interlayer interactions. Furthermore, our MD simulations indicate that the most likely ordering of the functional groups is inverted for both COFs and allow us to uniquely index the experimentally observed PXRD peaks, as shown in Figure 6.5.

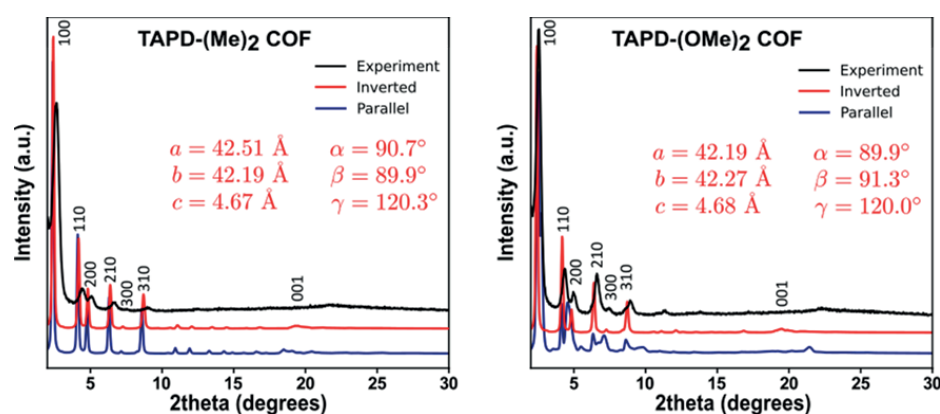


Figure 6. 5. Comparison between the experimentally observed and MD calculated PXRD patterns for TAPD-(Me)₂ and TAPD-(OMe)₂, averaged over the course of a 400 ps MD simulation at 300 K and 1 bar using an *ab initio* derived system-specific force fields. The resulting unit cell parameters and peak positions have been indicated.

The permanent porosity of TAPD-(Me)₂ and TAPD-(OMe)₂ COFs was assessed by argon sorption measurements at 87 K and N₂ sorption measurements at 77 K (Figures 6.6, S6.32

and S6.33). Both COFs display a steep uptake in the low-pressure region ($P/P_0=0-0.01$), corresponding to permanent microporosity. In addition, a step is observed in the isotherm around $P/P_0=0.22$. This feature represents the filling of the second type of bigger pores. The overall isotherm is a combination of type I and type IV isotherms indicating both microporous and mesoporous characteristics as expected in the Kagome type structures. Using Ar sorption, Brunauer-Emmett-Teller (BET) surface area values of 1105 and 1165 $\text{m}^2\cdot\text{g}^{-1}$ were observed for TAPD-(Me)₂ and TAPD-(OMe)₂ COFs, respectively. Using N₂ sorption the BET surface area values were calculated as 1083 and 1153 $\text{m}^2\cdot\text{g}^{-1}$ for TAPD-(Me)₂ and TAPD-(OMe)₂ COFs, respectively. Pore size analysis shows two different pore sizes as expected from the Kagome type COF structures. The experimental and theoretical average pore sizes for TAPD-(Me)₂ and TAPD-(OMe)₂ COFs were 1.7/2.7nm (theoretical: 1.5/2.5nm) and 1.3/2.5nm (theoretical: 1.4/2.4nm) respectively (Figure 6.6 inset), thus confirming the formation of 2D layers with **kgm** topology stacking in an eclipsed AA stacking mode. We used an Argon sorption based quenched solid density functional theory (QSDFT) carbon kernel for cylindrical type pores. These characterizations prove the successful formation of the expected structure of TAPD-(Me)₂ and TAPD-(OMe)₂ COFs.

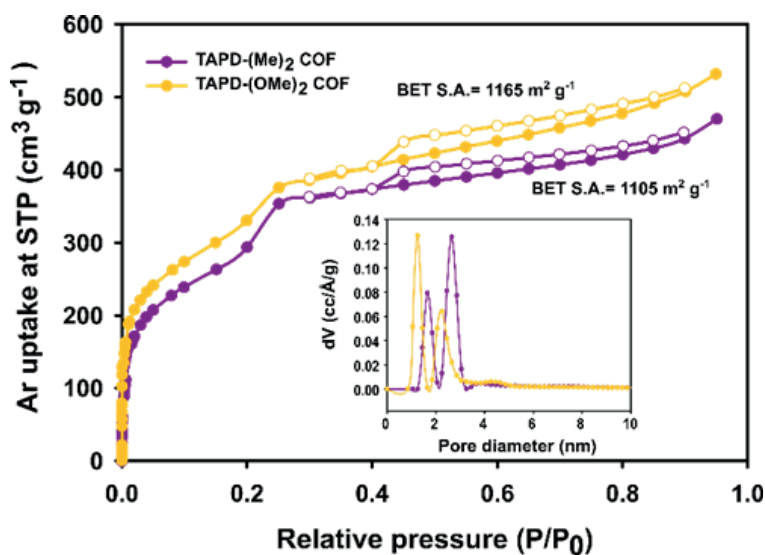


Figure 6. 6. Ar sorption isotherms and pore size distributions (inset) of TAPD-(Me)₂ COF and TAPD-(OMe)₂ COF.

Transmission electron microscopy (TEM) images of both COFs revealed crystalline features with domain sizes in the range of >50nm (Figure 6.7(a, c), Figures S6.14 and S6.16). Scanning electron microscopy (SEM) analyses show rough spherical morphologies of both COFs (Figure 6.7(b, d), Figures S6.15, S6.17). To analyze the

structural integrity, the chemical and thermal stability of the COFs was tested. Both COFs (20 mg each) were immersed in 1M HCl (acidic) and 1M NaOH (basic) solutions for 72 h and were washed with water and acetone before further analysis. PXRD patterns collected after these treatments show that the COFs retain their crystallinities and remain stable (Figure S6.18, S6.19). The yields of the COFs after treatment with acid and base were >90%. Additionally, both COFs remain insoluble in common organic solvents like acetone, methanol, ethanol, hexane, tetrahydrofuran, diethyl ether, and dichloromethane. Furthermore, after soaking the COFs in dimethyl formamide for 8 days, the crystallinity was retained (Figure S6.18, S6.19). In addition to the chemical stability, no significant loss in mass of COFs was observed when heating up to 450°C as shown through thermogravimetric analyses (Figure S6.20).

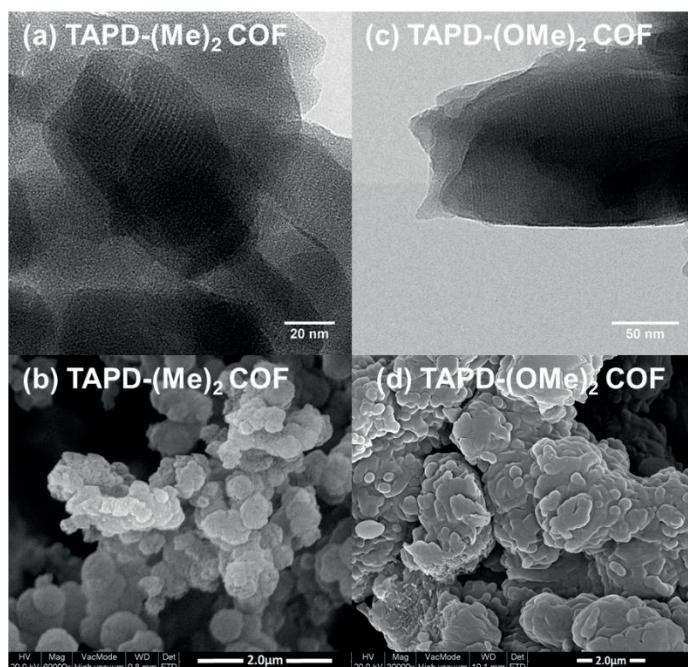


Figure 6. 7. TEM and SEM images of (a, b) TAPD-(Me)₂ and (c, d) TAPD-(OMe)₂ COFs showing crystalline domains and the morphology of COF crystallites.

6.2.3. Photocatalytic studies

By integrating functionalized units or groups such as triazine,² diacetylene,⁹ sulfone,³⁴ etc., in the COF backbone, several photocatalytic conversions have been achieved successfully. For efficient photocatalytic activity, the COF needs to generate electron-hole pairs and avoid recombination. The (diaryl-amino)benzene unit in the TAPD-(Me)₂ and TAPD-(OMe)₂ COFs is a strong donor and has strong reducing properties.²⁶ Moreover, high crystallinity of the COFs can enhance the charge transfer kinetics.³⁴

Diffuse reflectance ultraviolet-visible (UV-vis) spectroscopy was used to analyze the optical properties of the COFs, where it was observed that the COFs exhibit a broad and strong absorbance peak in the visible region (Figure 6.8a). The optical bandgaps calculated from Tauc plots are 2.61 and 2.63 eV, respectively for TAPD-(Me)₂ and TAPD-(OMe)₂ COFs, respectively (Figure 6.8b). This makes them ideal materials for visible light activation and photocatalytic H₂O₂ generation.

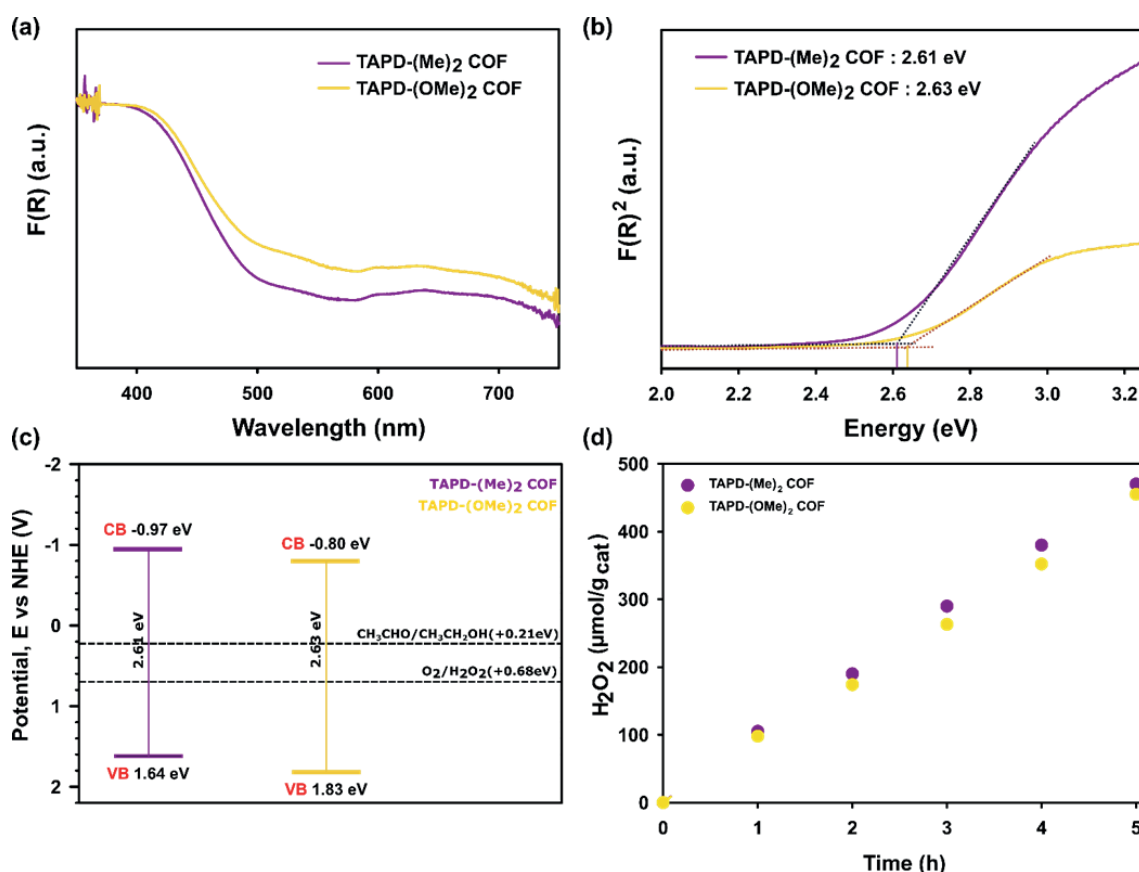


Figure 6. 8. (a) Solid state UV-Vis spectra, (b) Tauc plot analyses for bandgap calculations, (c) band potential alignments of the COF vs NHE (V) at pH=0, and (d) H₂O₂ production per gram catalyst over 5 hours of reaction time of TAPD-(Me)₂ and TAPD-(OMe)₂ COFs.

The positions of the conduction band (CB) and valence band (VB) of both COFs were estimated based on linear sweep voltammetry measurements under chopped illumination.^{35,36} A photocatalyst-coated FTO substrate was used as the working electrode in a three electrode setup, together with an Ag/AgCl (3M NaCl) reference electrode and a Pt coil counter electrode. Under an applied bias of +0.4 V vs. Ag/AgCl and chopped white light illumination, an anodic photocurrent was measured. As the bias voltage was swept in the negative direction from +0.4 V to -0.4 V at a scan rate of 4 mV/s, the

photocurrent decreased in magnitude and then changed sign. The potential at which the sign change of the photocurrent occurred, allows to calculate a good estimate of the conduction band minimum (Figures S6.35, S6.36 and S6.37). The CB band positions were determined in three different alkaline buffers, displaying a Nernstian dependence of the CB position with pH. From these values, the CB positions at pH=0 were extrapolated (Figure S6.38). In combination with the optical bandgaps as derived from the Tauc-plots, the band structure was derived for TAPD-(Me)₂ (CB=-0.97eV, VB=1.64eV) and TAPD-(OMe)₂ (CB=-0.80eV, VB=1.83eV) COF as shown in Figure 6.8c. The band positions are very well under the requirements for oxygen reduction to hydrogen peroxide (0.68 V vs NHE), hence the COFs were utilized further for H₂O₂ generation.

Table 6. 1. Photocatalytic production of H₂O₂.

No	Material	H ₂ O ₂ produced rate	Irradiation conditions	Solvent system	Ref
1.	g-C ₃ N ₄	63 $\mu\text{mol h}^{-1} \text{g}_{\text{cat}}^{-1}$	$\lambda = 420\text{-}500 \text{ nm}$	H ₂ O:EtOH (1:9)	22
2.	g-C ₃ N ₄ /PDI-BN0.2-rGO _{0.05}	30.8 $\mu\text{mol h}^{-1} \text{g}_{\text{cat}}^{-1}$	$\lambda > 420 \text{ nm}$	H ₂ O	37
3.	PEI/C ₃ N ₄	208.1 $\mu\text{mol h}^{-1} \text{g}_{\text{cat}}^{-1}$	Solar simulator (AM=1.5)	H ₂ O	38
4.	Si/TiO ₂ -Au	14.8 $\mu\text{mol h}^{-1}$	$\lambda = 365 \text{ nm}$	0.01M HCl, Y ³⁺ co-catalyst	39
5.	g-C ₃ N ₄ /AQ-COOH	361 $\mu\text{mol h}^{-1} \text{g}_{\text{cat}}^{-1}$	$\lambda > 400 \text{ nm}$	Propan-2-ol/H ₂ O (1:9)	40
6	g-C ₃ N ₄ /rGO (10 wt%)	74.3 $\mu\text{mol h}^{-1} \text{g}_{\text{cat}}^{-1}$	$\lambda > 400 \text{ nm}$	Propan-2-ol/H ₂ O (1:9)	40
7.	Boron nitride quantum dots - carbon nitride (BNQD/UPCN)	72.3 $\mu\text{mol h}^{-1} \text{g}_{\text{cat}}^{-1}$	$\lambda > 420 \text{ nm}$	Propan-2-ol/H ₂ O (1:9)	41
8.	C-N-g-C ₃ N ₄	0.98 $\mu\text{mol h}^{-1} \text{g}_{\text{cat}}^{-1}$	$420 < \lambda < 700 \text{ nm}$	H ₂ O	42

9.	OPA/Zr _{92.5} Ti _{7.5} -MOF	9700 $\mu\text{mol L}^{-1} \text{h}^{-1}$	$\lambda > 420 \text{ nm}$	Benzyl alcohol:H ₂ O (2.5:1)	20
10.	Resorcinol-formaldehyde resins	$\sim 40^* \mu\text{mol h}^{-1}$	$\lambda > 420 \text{ nm}$	H ₂ O	43
11.	TAPD-(Me) ₂ COF	97 $\mu\text{mol h}^{-1} \text{g}_{\text{cat}}^{-1}$	$\lambda = 420\text{-}700 \text{ nm}$	H ₂ O:EtOH (9:1)	This work
12.	TAPD-(OMe) ₂ COF	91 $\mu\text{mol h}^{-1} \text{g}_{\text{cat}}^{-1}$	$\lambda = 420\text{-}700 \text{ nm}$	H ₂ O:EtOH (9:1)	This work
13.	TAPD-(Me) ₂ COF	234.52 $\mu\text{mol h}^{-1} \text{g}_{\text{cat}}^{-1}$	$\lambda = 420\text{-}700 \text{ nm}$	H ₂ O:EtOH (1:9)	This work

Photocatalytic H₂O₂ generation experiments were performed in sealed glass vials with water:ethanol (9:1), where ethanol acts as the electron and proton donor. Under visible-light (420-700 nm) irradiation, long term (16 h) reactions were carried at room temperature (condenser) using 20 mg of COF as photocatalyst. H₂O₂ concentration was determined through iodometric titration.⁴⁴ After 16 h of reaction, the TAPD-(Me)₂ and TAPD-(OMe)₂ COFs produced 25.3 and 22.6 $\mu\text{mol H}_2\text{O}_2$ respectively, when irradiated under 250W light (5.46 W m⁻²). This is quite comparable to pure carbon nitride, which produced 30 $\mu\text{mol H}_2\text{O}_2$ but used 2kW light source and with 9 times higher ethanol content.²² Also, in case of TAPD-(Me)₂ COF when using higher amount of ethanol (water:ethanol - 1:9), 57.2 $\mu\text{mol H}_2\text{O}_2$ was produced, which is almost twice more than pure carbon nitride.²² Moreover, compared to a TiO₂ photocatalyst, the TAPD-(Me)₂ COF performed >120 times better.²² We acknowledge that it is difficult to compare the activities of different materials due to different reaction conditions (irradiation wavelength, light intensity, sacrificial agent, reaction time etc.). Besides, most of the catalysts used in literature (Table 6.1) for H₂O₂ production involve the assistance of a metal (Cu, Au, TiO₂ etc.), whereas the COFs provide a completely metal-free platform. H₂O₂ production vs time profile was recorded for the photocatalytic reaction over 5 h (Figure 6.8d). The overall H₂O₂ production rates of $97 \pm 10 \mu\text{mol h}^{-1} \text{g}_{\text{cat}}^{-1}$ and $91 \pm 10 \mu\text{mol h}^{-1} \text{g}_{\text{cat}}^{-1}$ were obtained for TAPD-(Me)₂ and TAPD-(OMe)₂ COFs, respectively. The following reaction mechanism is proposed (figure S6.39). The reaction proceeds with the formation of electron-hole carriers through visible light irradiation on the COF. The holes are utilized by ethanol to produce acetaldehyde and two protons along with it. Molecular

oxygen utilizes the electrons from the COF and the protons from the alcohol transformation to produce H_2O_2 . Electron and hole trapping experiments were performed using silver nitrate (AgNO_3) and triethylamine (TEA) respectively (table S6.3; entries 7 and 8). In case of electron trapping experiment there was a drastic decrease in the formation of H_2O_2 whereas in case of hole trapping experiment there was no formation of H_2O_2 . This emphasizes the role of photocatalytic electron-hole carriers in the overall reaction. Further, benzoquinone was used as a radical scavenger in the reaction system to determine the role of radicals in the reaction (table S6.3; entry 9). However, the reaction proceeded without much hindrance which means the radicals formed are quickly utilized for the formation of H_2O_2 . Similar fast step was also observed in the carbon nitride photocatalyst²² where the one-electron reduction of O_2 to release superoxide ($\bullet\text{OOH}$) is suppressed. To determine the H_2O_2 selectivity, the reaction was tested with benzyl alcohol as the proton source instead of ethanol, as the quantification of benzaldehyde is more reliable than of acetaldehyde using NMR analysis. The reaction was performed with water:benzylalcohol (1:9) for 16 h at room temperature using TAPD-(Me)₂ COF. 53.7 μmol H_2O_2 was produced which is comparable to the reaction with ethanol under the same conditions. ¹H NMR analysis showed the production of benzaldehyde and correspondingly H_2O_2 was produced with 96% selectivity (Figure S6.39). In addition, this also confirms the mechanism of the reaction. As expected, alcohol to aldehyde conversion occurs which provides protons for reducing oxygen to H_2O_2 . A control reaction was performed with all substrates excluding the COF yielding no significant amount of H_2O_2 . Further, the reaction was also tested with all the substrates and the COF but in the absence of light. No H_2O_2 was produced, thus confirming the requirement of light (Table S6.3). To check the reusability of the catalyst, the reaction was performed for three consecutive cycles with TAPD-(Me)₂ COF and no significant loss of activity was observed (Figure S6.40). The PXRD patterns of the COFs after 16 h of photocatalytic reactions show that they retain crystallinity, confirming that the structure is stable under the reaction conditions (Figures S6.41 and S6.42). SEM analyses before and after catalysis of TAPD-(Me)₂ and TAPD-(OMe)₂ COFs show no changes in the overall morphologies (Figures S6.43 and S6.44). Additionally, the reaction was performed for 96h continuously and 142.3 μmol of H_2O_2 was obtained. The production was still linear compared to the overall kinetics in the short-term reactions (Figure S46). The effect of different alcohol sources in the reaction was tested by performing the photocatalytic reactions using isopropanol and methanol in addition to ethanol and benzyl alcohol. The

production of H₂O₂ was in the order iso-propanol>ethanol>methanol>benzylalcohol (Figure S47). These results imply that the COFs are active for metal-free visible light photocatalytic production of H₂O₂ by oxygen reduction.

6.3. Conclusion

Inspired by Wurster type systems, we have synthesized a new series of imine-COFs consisting of (diarylamino)benzene units. These COFs are highly crystalline and arrange into a Kagome lattice. ¹³C-¹H and ¹H-¹H NMR experiments confirmed the local chemical environments of the COFs. The COFs remained stable under various thermochemical conditions. Molecular dynamics simulations on the COF structures further confirmed the AA stacked crystalline nature. Both COFs displayed high surface areas, strong absorption in visible light region and ideal bandgaps for photocatalysis. The absolute positions of the conduction and valence bands was determined by linear sweep voltammetry under chopped illumination. Photocatalytic reactions using oxygen saturated water under visible light irradiation showed a H₂O₂ production rate that is more than 100 times better than titania. The catalysts are stable and reusable for several runs of the reaction. This study is the first example of utilizing COFs for photocatalytic H₂O₂ production and opens a new avenue towards solar driven metal-free photocatalysis.

6.4. References

- (1) C. Diercks, O. M. Yaghi, *Science* 2017, 355 (6328), eaal1585.
- (2) C. Krishnaraj, H. S. Jena, K. Leus, P. Van Der Voort, *Green Chem.* 2020, 22, 1038-1071.
- (3) S. Zhu, D. Wang, *Advanced Energy Materials* 2017, 7 (23), 1700841.
- (4) C. Xu, P. R. Anusuyadevi, C. Aymonier, R. Luque, S. Marre, *Chemical Society Reviews* 2019, 48 (14), 3868-3902.
- (5) Y. Zhi, Z. Li, X. Feng, H. Xia, Y. Zhang, Z. Shi, Y. Mu, X. Liu, *Journal of Materials Chemistry A* 2017, 5 (44), 22933-22938.
- (6) S. Li, L. Li, Y. Li, L. Dai, C. Liu, Y. Liu, J. Li, J. Lv, P. Li, B. Wang, *ACS Catalysis* 2020, 8717-8726.
- (7) K. Lei, D. Wang, L. Ye, M. Kou, Y. Deng, Z. Ma, L. Wang, Y. Kong, *ChemSusChem* 2020, 13 (7), 1725-1729.

- (8) P. Pachfule, A. Acharjya, J. Roeser, R. Sivasankaran, M. Ye, A. Brückner, J. Schmidt, A. Thomas, *Chemical Science* 2019, 10 (36), 8316-8322.
- (9) P. Pachfule, A. Acharjya, J. Roeser, T. Langenhahn, M. Schwarze, R. Schomäcker, A. Thomas, J. Schmidt, *Journal of the American Chemical Society* 2018, 140 (4), 1423-1427.
- (10) S. Yang, W. Hu, X. Zhang, P. He, B. Pattengale, C. Liu, M. Cendejas, I. Hermans, X. Zhang, J. Zhang, J. Huang, *Journal of the American Chemical Society* 2018, 140 (44), 14614-14618.
- (11) Y. Zhang, Y. Hu, J. Zhao, E. Park, Y. Jin, Q. Liu, W. Zhang, *Journal of Materials Chemistry A* 2019, 7 (27), 16364-16371.
- (12) S. Bi, P. Thiruvengadam, S. Wei, W. Zhang, F. Zhang, L. Gao, J. Xu, D. Wu, J. Chen, F. Zhang, *Journal of the American Chemical Society* 2020, 142 (27), 11893-11900.
- (13) H. Vardhan, G. Verma, S. Ramani, A. Nafady, A. Al-Enizi, Y. Pan, Z. Yang, H. Yang, S. Ma, *ACS Applied Materials & Interfaces* 2018, 11 (3), 3070-3079.
- (14) Z. Li, Y. Zhi, P. Shao, H. Xia, G. Li, X. Feng, X. Chen, Z. Shi, X. Liu, *Applied Catalysis B: Environmental* 2019, 245, 334-342.
- (15) Z. Liu, Q. Su, P. Ju, X. Li, G. Li, Q. Wu, B. Yang, *Chemical Communications* 2020, 56 (5), 766-769.
- (16) E. Shanley, *Journal of Chemical Education* 1951, 28 (5), 260.
- (17) E. Ntainjua, M. Piccinini, S. Freakley, J. Pritchard, J. Edwards, A. Carley, G. Hutchings, *Green Chem.* 2012, 14 (1), 170-181.
- (18) E. Pizzutilo, O. Kasian, C. Choi, S. Cherevko, G. Hutchings, K. Mayrhofer, S. Freakley, *Chemical Physics Letters* 2017, 683, 436-442.
- (19) H. Hou, X. Zeng, X. Zhang, *Angewandte Chemie International Edition* 2020.
- (20) X. Chen, Y. Kuwahara, K. Mori, C. Louis, H. Yamashita, *J. Mater. Chem. A* 2020, 8, 1904-1910.
- (21) Y. Isaka, Y. Kawase, Y. Kuwahara, K. Mori, H. Yamashita, *Angewandte Chemie* 2019, 58, 5402-5406.

- (22) Y. Shiraishi, S. Kanazawa, Y. Sugano, D. Tsukamoto, H. Sakamoto, S. Ichikawa, T. Hirai, *ACS Catalysis* 2014, 4 (3), 774-780.
- (23) L. Michaelis, M. Schubert, S. Granick, *Journal of the American Chemical Society* 1939, 61 (8), 1981-1992.
- (24) M. Uebe, T. Kato, K. Tanaka, A. Ito, *Chemistry - A European Journal* 2016, 22 (52), 18923-18931.
- (25) R. Munday, *Chemico-Biological Interactions* 1988, 65 (2), 133-143.
- (26) N. Noto, Y. Tanaka, T. Koike, M. Akita, *ACS Catalysis* 2018, 8 (10), 9408-9419.
- (27) Y. Tian, S. Xu, R. Liang, C. Qian, G. Jiang, X. Zhao, *CrystEngComm* 2017, 19 (33), 4877-4881.
- (28) E. Jin, K. Geng, K. Lee, W. Jiang, J. Li, Q. Jiang, S. Irle, D. Jiang, *Angewandte Chemie* 2020, 132 (29), 12260-12267.
- (29) N. Keller, T. Sick, N. Bach, A. Koszalkowski, J. Rotter, D. Medina, T. Bein, *Nanoscale* 2019, 11 (48), 23338-23345.
- (30) S. Sasaki, K. Hattori, K. Igawa, G. Konishi, *The Journal of Physical Chemistry A* 2015, 119 (20), 4898-4906.
- (31) C. Lambert, C. Risko, V. Coropceanu, J. Schelter, S. Amthor, N. Gruhn, J. Durivage, J. Brédas, *Journal of the American Chemical Society* 2005, 127 (23), 8508-8516.
- (32) L. Vanduyfhuys, S. Vandenbrande, T. Verstraelen, R. Schmid, M. Waroquier, V. Van Speybroeck, *Journal of Computational Chemistry* 2015, 36 (13), 1015-1027.
- (33) L. Vanduyfhuys, S. Vandenbrande, J. Wieme, M. Waroquier, T. Verstraelen, V. Van Speybroeck, *Journal of Computational Chemistry* 2018, 39 (16), 999-1011.
- (34) X. Wang, L. Chen, S. Chong, M. Little, Y. Wu, W. Zhu, R. Clowes, Y. Yan, M. Zwijnenburg, R. Sprick, A. Cooper, *Nature Chemistry* 2018, 10 (12), 1180-1189.
- (35) L. Stegbauer, S. Zech, G. Savasci, T. Banerjee, F. Podjaski, K. Schwinghammer, C. Ochsenfeld, B. V. Lotsch, *Adv. Energy Mater.* 2018, 8, 1703278.
- (36) A. Hankin, F. E. Bedoya-Lora, J. C. Alexander, A. Regoutz, G. H. Kelsall, *J. Mater. Chem. A* 2019, 7, 26162-26176.

- (37) Y. Kofuji, Y. Isobe, Y. Shiraishi, H. Sakamoto, S. Ichikawa, S. Tanaka, T. Hirai, *ChemCatChem* 2018, 10 (9), 2070-2077.
- (38) X. Zeng, Y. Liu, Y. Kang, Q. Li, Y. Xia, Y. Zhu, H. Hou, M. H. Uddin, T. R. Gengenbach, D. Xia, C. Sun, D. T. McCarthy, A. Delectic, J. Yu, X. Zhang, *ACS Catal.* 2020, 10(6), 3697-3706.
- (39) N. Kaynan, B. Berke, O. Hazut, R. Yerushalmi, *J. Mater. Chem. A* 2014, 2 (34), 13822-13826.
- (40) H.-I. Kim, Y. Choi, S. Hu, W. Choi, J.-H Kim, *Appl. Catal. B: Environ.* 2018, 229, 121-129.
- (41) Y. Yang, C. Zhang, D. Huang, G. Zeng, J. Huang, C. Lai, C. Zhou, W. Wang, H. Guo, W. Xue, R. Deng, M. Cheng, W. Xiong, *Appl. Catal. B: Environ.* 2019, 245, 87-99.
- (42) Y. Fu, C. Liu, M. Zhang, C. Zhu, H. Li, H. Wang, Y. Song, H. Huang, Y. Liu, Z. Kang, *Advanced Energy Materials* 2018, 8 (34), 1802525.
- (43) Y. Shiraishi, T. Takii, T. Hagi, S. Mori, Y. Kofuji, Y. Kitagawa, S. Tanaka, S. Ichikawa, T. Hirai, *Nature Materials* 2019, 18 (9), 985-993.
- (44) H. Goto, Y. Hanada, T. Ohno, M. Matsumura, *Journal of Catalysis* 2004, 225(1), 223-229.

6.5. Supporting Information

Section S6.1. General procedures

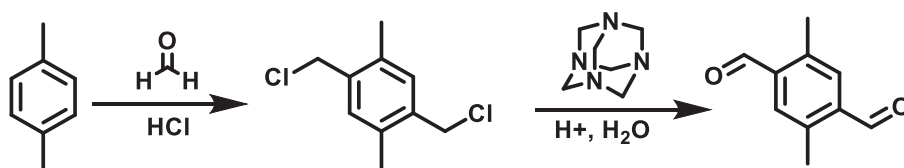
Materials. Unless stated otherwise all reagents were purchased from commercial sources and used without further purification.

Instrumentation. Fourier Transform Infrared Spectroscopy (FT-IR) in the region 4000-650 cm⁻¹ was performed with a Thermo Nicolet 6700 FTIR spectrometer equipped with a nitrogen-cooled MCT detector and a KBr beam splitter. Nitrogen adsorption-desorption isotherms were obtained using a Belsorp Mini apparatus measured at 77 K. Argon sorption was performed using micropore analyzer from 3P instruments. Elemental analyses (C, H, N and O) were carried out on a Thermo Scientific Flash 2000 CHNS-O analyzer equipped with a TCD detector. X-ray powder diffraction (XRPD) patterns were collected on a Thermo Scientific ARL X'Tra diffractometer, operated at 40 kV, 30 mA using Cu-K α radiation ($\lambda = 1.5406 \text{ \AA}$). Thermogravimetric analysis (TGA) was performed on a Neetzsch STA-449 F3 Jupiter-simultaneous TG-DSC analyzer within a temperature range of 20-800 °C, under a N₂ atmosphere and at a heating rate of 2 °C/min.

NMR spectroscopy: All the solid-state NMR experiments have been carried out in a Bruker 800 spectrometer operating at a ¹H Larmor frequency of 801.25 MHz at a magnetic field of 18.8 T equipped with a triple channel 1.9 mm magic-angle spinning (MAS) probe-head. The 1.9mm zirconia rotors were packed with the samples and spun at a MAS frequency of 35 kHz at room temperature (controlled by Bruker cooling unit). The ¹H NMR experiments were done with direct excitation with radio-frequency (RF) pulses of a strength of 140 kHz. Typically, eight transients were recorded with a recycle delay of 4 s for both samples. The ¹³C cross-polarization (CP) MAS experiments (Larmor frequency of 201.49 MHz) performed with varying contact times (1, 2, 4 and 8 ms) collected 4096 scans each. The decoupling sequence employed was SW_r-TPPM^[S1] at an RF strength of 140 kHz. The 2D ¹³C-¹H CP-HETCOR experiment used a contact time of 2 ms with 320 transients and 80 incremented slices. The rotor-synchronized ¹H double-quantum-single-quantum (DQ-SQ) correlation experiments were performed with the standard BABA^[S2, S3] sequence. The DQ excitation period was one rotor period and the duration for evolution of DQ coherence was incremented 120 times for the 2D experiment with 16 scans for each slice. The ¹H and ¹³C chemical shifts of the samples were referenced against corresponding shifts of tetramethylsilane (TMS).

Section S6.2. Synthesis of organic linkers and COFs

S6.2.1. Synthesis of 2,5-dimethylbenzene-1,4-dicarboxaldehyde [(Me)₂]



Scheme S6.1. Synthesis of 2,5-dimethylbenzene-1,4-dicarboxaldehyde [(Me)₂].

20 mL *p*-xylene (0.16 mol), 12.5 g *p*-formaldehyde (1.3 eq) and 13.6 g ZnCl (0.1 mol) were dissolved in 100 mL 37% HCl. The mixture was refluxed for 2 days at 110°C. Afterwards, the mixture was allowed to cool down to room temperature and the formed solid was filtered off to obtain 1,4-bis(chloromethyl)-2,5-dimethylbenzene as pure white needles. Yield = 25.27 g (77.8%). ¹H NMR (300 MHz, CDCl₃) δ 7.14 (s 2H), 4.55 (s 2H), 2.37 (s 6H).

1.446 g 1,4-bis(chloromethyl)-2,5-dimethylbenzene (7.1 mmol) and 2.6 g hexamine (18.6 mmol) were added to a 10 mL 50% acetic acid solution. The mixture was refluxed for 1h at 110°C, before addition of 5 mL 37% HCl. Afterwards, reflux (110°C) was continued for 1 more hour, and the clear yellow mixture was subsequently cooled in an ice bath. 2,5-dimethylbenzene-1,4-dicarboxaldehyde crystallized out and was filtered off. (white flakes, yield = 83.4 %). ¹H NMR (300 MHz, CDCl₃) δ 10.34 (s 2H), 7.69 (s 2H), 2.70 (s 6H).

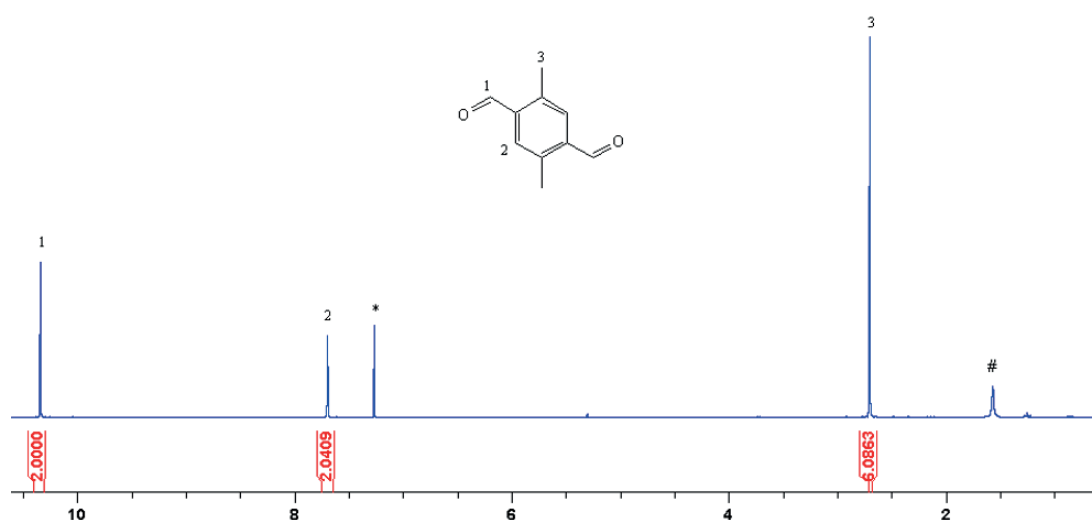
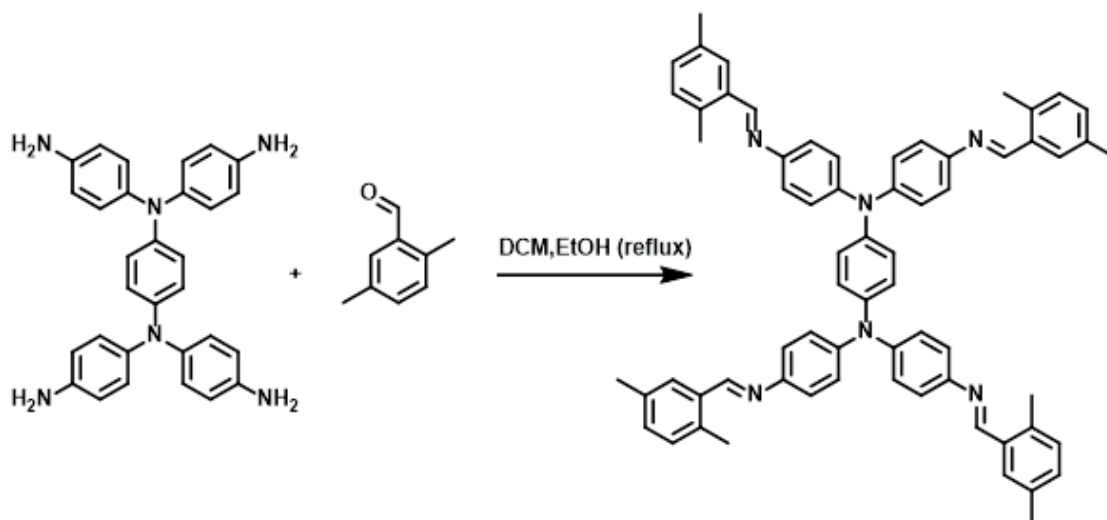


Figure S6.1. ¹H NMR spectra of 2,5-dimethylbenzene-1,4-dicarboxaldehyde, the solvent (CDCl₃) peak is depicted with *, the peak marked with # was assigned to residual H₂O in the sample.

S6.2.2. Synthesis of model compound TAPD-(Me)₂-MC



Scheme S6.2. Synthesis of model compound TAPD-(Me)₂-MC.

N,N,N',N'-Tetrakis(4-aminophenyl)-1,4-phenylenediamine (TAPD, 23.6 mg, 0.5 mmol) and 2,5-dimethylbenzaldehyde ((Me)₂, 40.2 mg, 3 mmol) were added in a round bottom flask equipped with a magnetic stirring bar. 4 ml of dichloromethane and 4 ml of absolute ethanol were added to the mixture and stirred under reflux for 5 hours. The reaction mixture was cooled to room temperature and the precipitate was filtered off. The orange-brown solid is washed thoroughly with ethanol and dried. Yield = 94%. ¹H NMR (300 MHz, CDCl₃) δ 8.71 (s 4H), 7.83 (s 4H), 6.99-7.11 (28H), 2.47 (s 12H), 2.30 (s 12H).

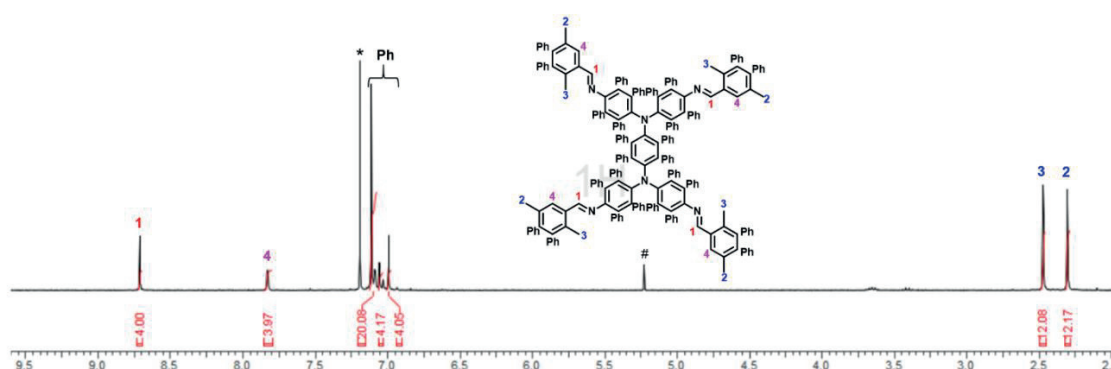
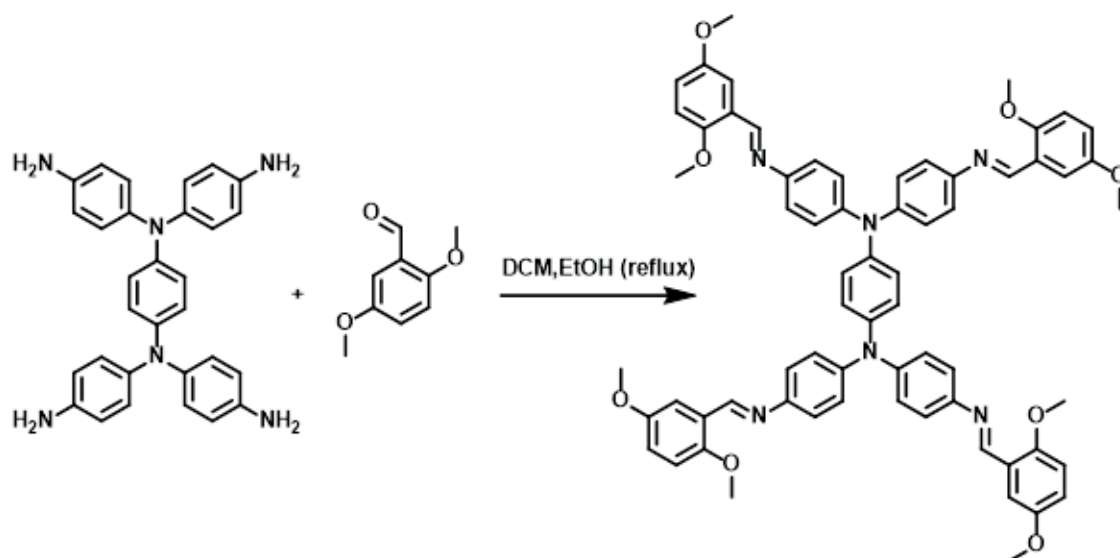


Figure S6.2. ¹H NMR spectra of model compound TAPD-(Me)₂-MC, the solvent (CDCl₃) peak is depicted with *, the peak marked with # was assigned to residual dichloromethane in the sample.

S6.2.3. Synthesis of model compound TAPD-(OMe)₂-MC



Scheme S6.3. Synthesis of model compound TAPD-(OMe)₂-MC.

N,N,N',N'-Tetrakis(4-aminophenyl)-1,4-phenylenediamine (TAPD, 23.6 mg, 0.5 mmol) and 2,5-dimethoxybenzaldehyde ((OMe)₂, 49.8 mg, 3 mmol) were added in a round bottom flask equipped with a magnetic stirring bar. 4 ml of dichloromethane and 4 ml of absolute ethanol were added to the mixture and stirred under reflux for 5 hours. The reaction mixture was cooled to room temperature and the precipitate was filtered off. The brown solid is washed thoroughly with ethanol and dried. Yield = 80%. ¹H NMR (300 MHz, CDCl₃) δ 8.86 (s 4H), 7.63 (d 4H), 6.81-7.16 (28H), 3.79 (d 24H).

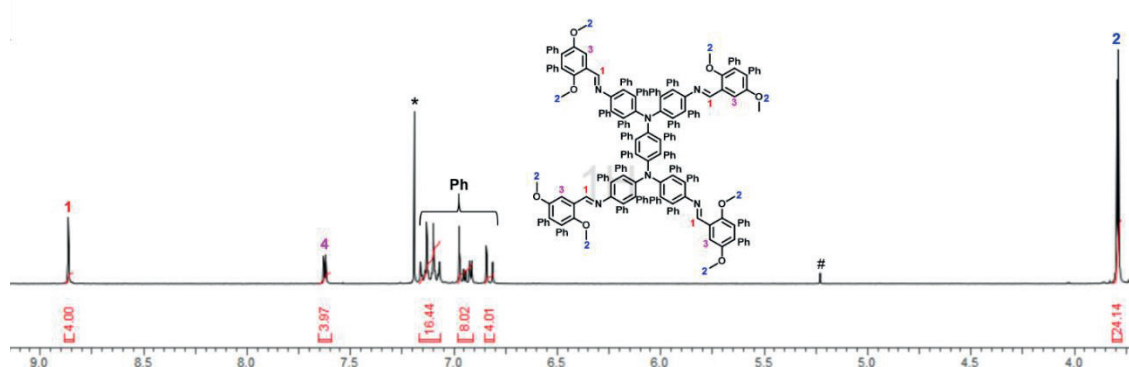


Figure S6.3. ¹H NMR spectra of model compound TAPD-(OMe)₂-MC, the solvent (CDCl₃) peak is depicted with *, the peak marked with # was assigned to residual dichloromethane in the sample.

S6.2.4. Synthesis of TAPD-(Me)₂ COF

N,N,N',N'-Tetrakis(4-aminophenyl)-1,4-phenylenediamine (TAPD, 23.6 mg, 0.5 mmol) and 2,5-dimethylbenzene-1,4-dicarboxaldehyde ((Me)₂, 16.2 mg, 1 mmol) were added in an ampoule. 0.3 ml dichlorobenzene and 0.3 ml *n*-butanol were added to the ampoule. Finally, 0.1 ml 6M acetic acid was added, and the mixture was sonicated for 5 minutes. Freeze-pump-thaw procedure for 3 cycles were repeated before sealing the ampoule. The sealed ampoule was placed in an oven at 120°C. After 72 hours, the precipitate was filtered and washed with distilled water, tetrahydrofuran (THF) and acetone. The bright red solid is then washed using Soxhlet with THF for 12 hours. After drying the materials at 90°C for 24 h under vacuum TAPD-(Me)₂ COF (~38 mg) was obtained as bright red colored solid.

S6.2.5. Synthesis of TAPD-(OMe)₂ COF

N,N,N',N'-Tetrakis(4-aminophenyl)-1,4-phenylenediamine (TAPD, 23.6 mg, 0.5 mmol) and 2,5-dimethylbenzene-1,4-dicarboxaldehyde ((Me)₂, 19.4 mg, 1 mmol) were added in an ampoule. 0.3 ml mesitylene and 0.3 ml dioxane were added to the ampoule. Finally, 0.1 ml 6M acetic acid was added, and the mixture was sonicated for 5 minutes. Freeze-pump-thaw procedure for 3 cycles were repeated before sealing the ampoule. The sealed ampoule was placed in an oven at 120°C. After 72 hours, the precipitate was filtered and washed with distilled water, tetrahydrofuran (THF) and acetone. The dark red solid is then washed using Soxhlet with THF for 12 hours. After drying the materials at 90°C for 24 h under vacuum TAPD-(OMe)₂ COF (~42 mg) was obtained as dark red colored solid.

Section S6.3: Characterization of COFs

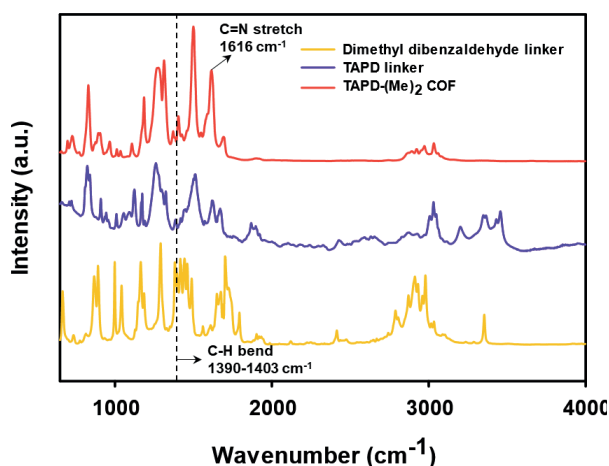


Figure S6.4. FT-IR spectra of TAPD-(Me)₂ COF, TAPD linker and (Me)₂ linker.

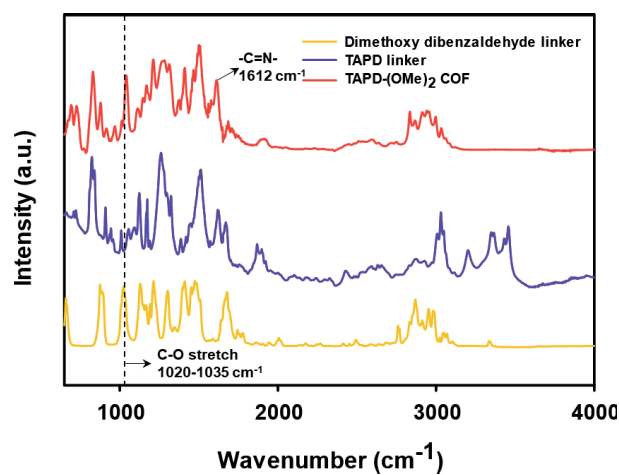


Figure S6.5. FT-IR spectra of TAPD-(OMe)₂ COF, TAPD linker and (OMe)₂ linker.

¹H DQ-SQ MAS (35 kHz) NMR

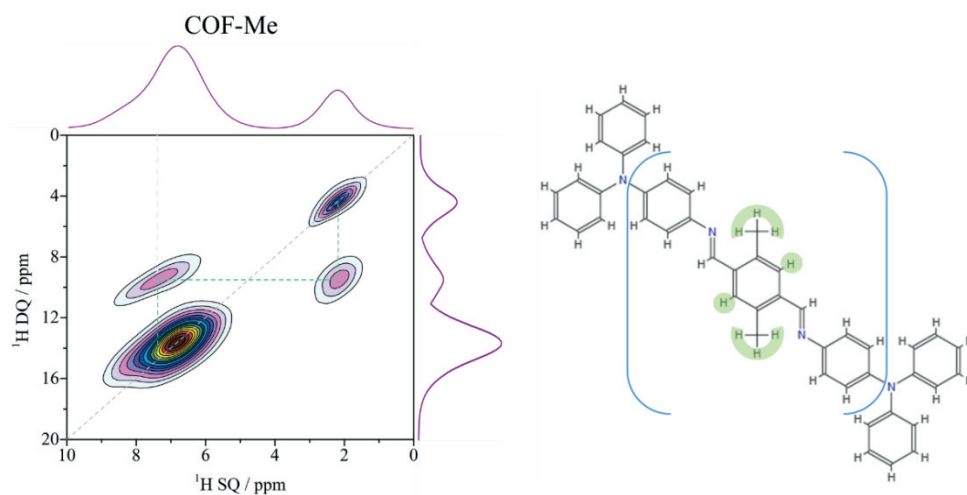


Figure S6.6. ¹H DQSQ correlation and assignment of TAPD-(Me)₂ COF.

¹H DQ-SQ MAS (35 kHz) NMR

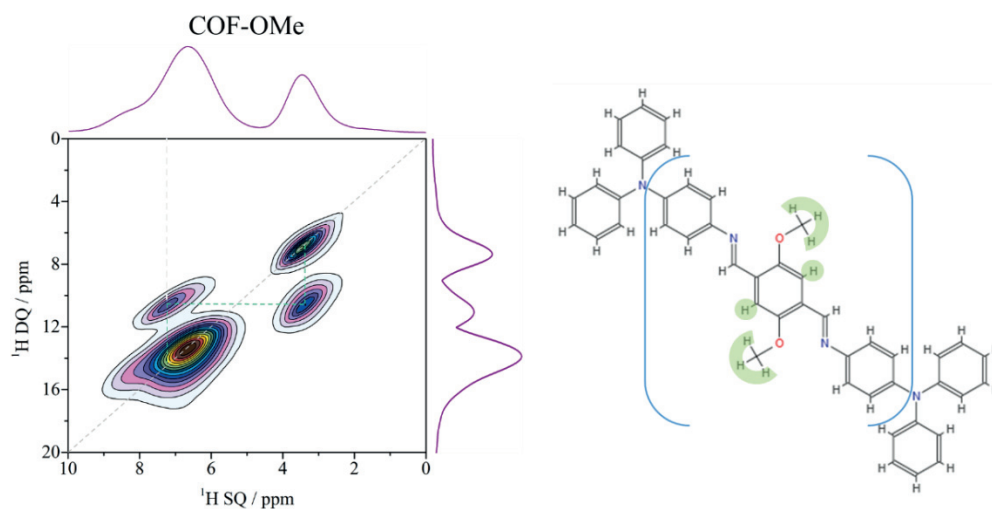


Figure S6.7. ¹H DQSQ correlation and assignment of TAPD-(OMe)₂ COF.

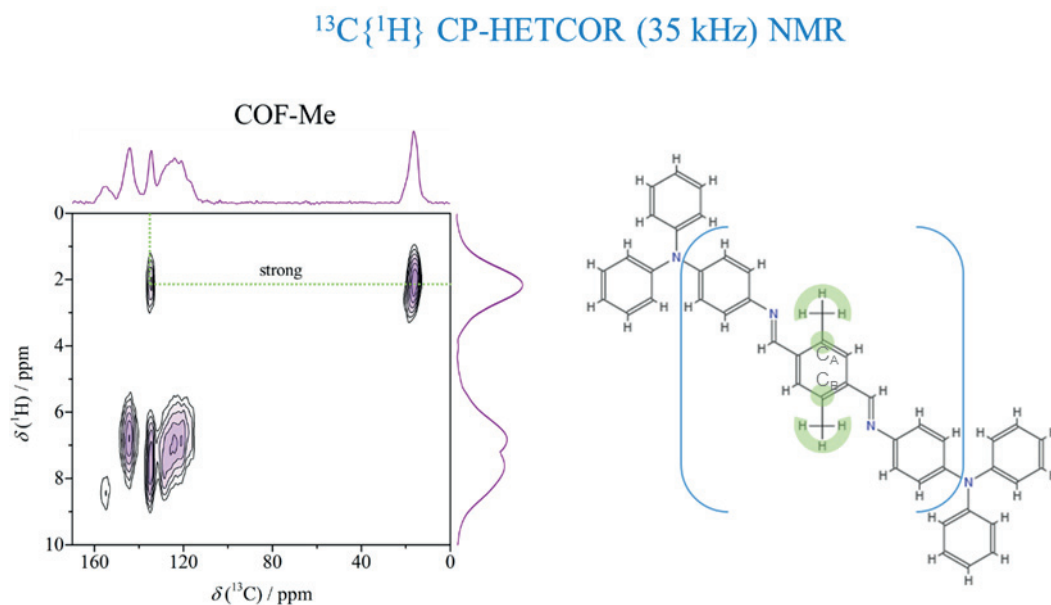


Figure S6.8. ^1H - ^{13}C CP HETCOR spectrum and assignment TAPD-(Me)₂ COF.

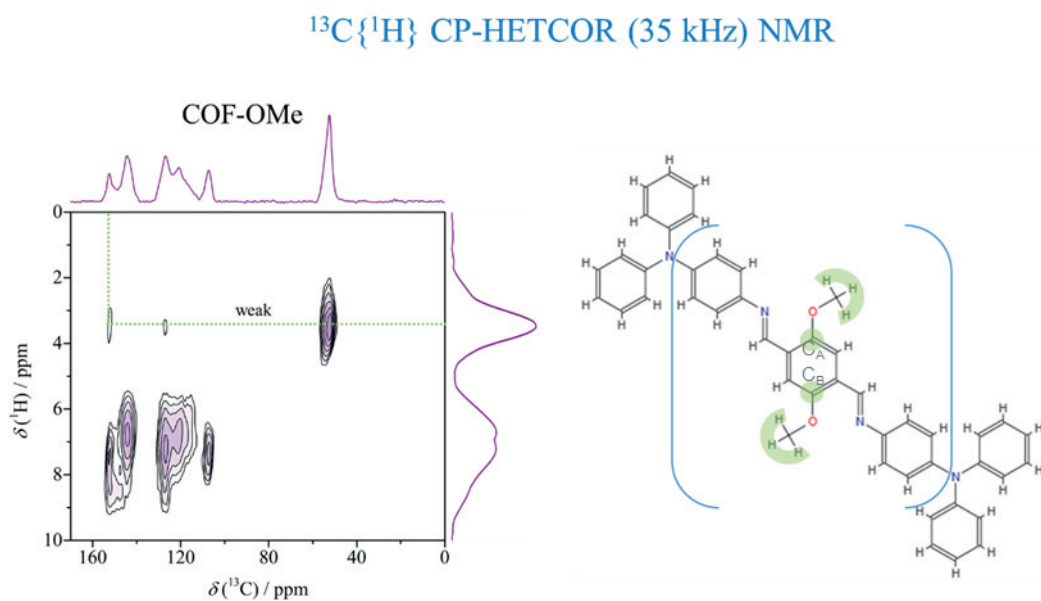


Figure S6.9. ^1H - ^{13}C CP HETCOR spectrum and assignment of TAPD-(OMe)₂ COF.

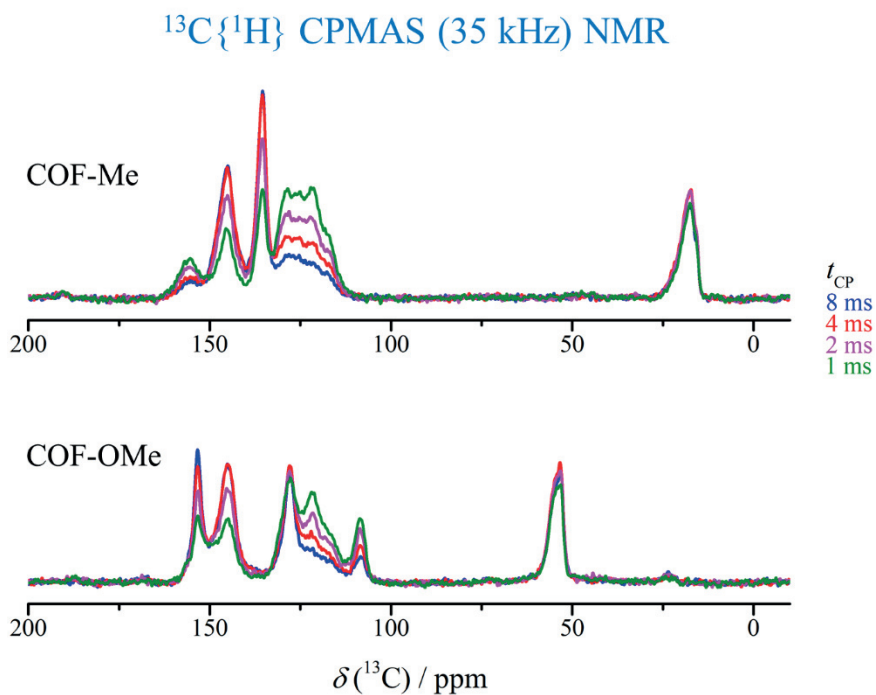


Figure S6.10. ^1H - ^{13}C variable contact time CP buildup of TAPD-(Me)₂ COF (top) and TAPD-(OMe)₂ COF (bottom).

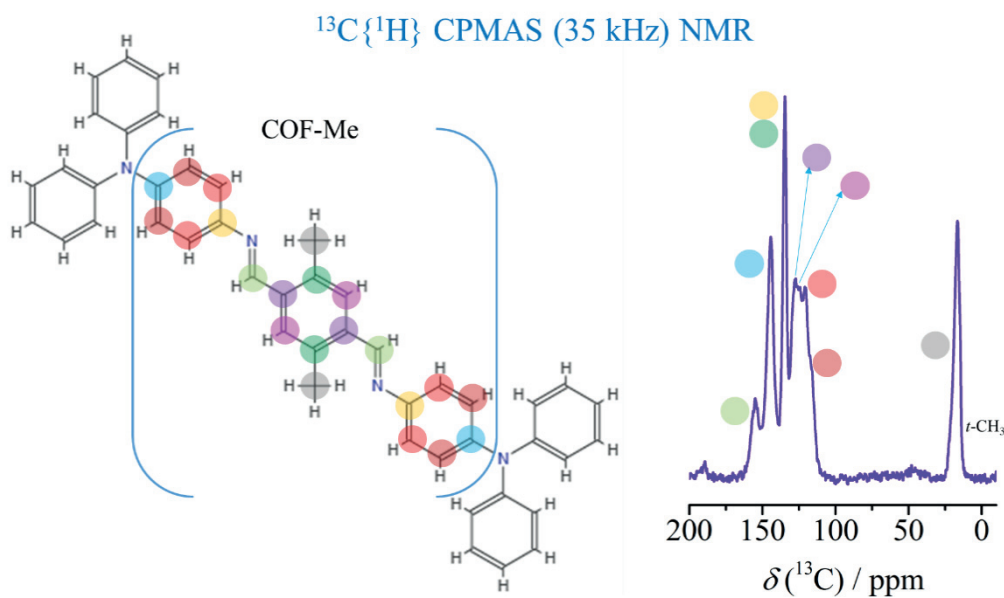


Figure S6.11. ^1H - ^{13}C CPMAS (35 kHz) NMR spectrum (contact time 2 ms) and assignment of TAPD-(Me)₂ COF.

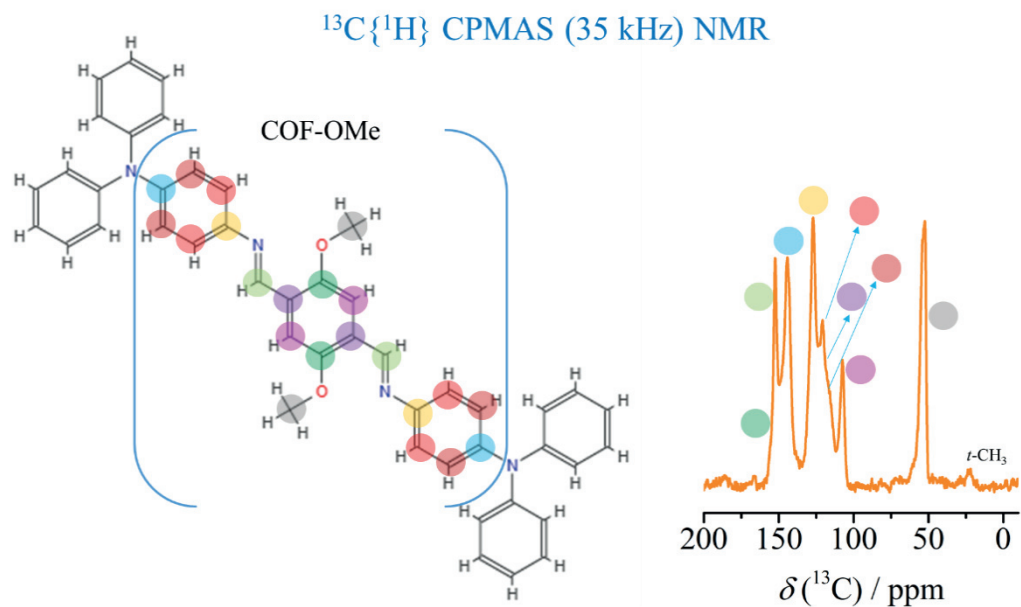


Figure S6.12. ^1H - ^{13}C CPMAS (35 kHz) NMR spectrum (contact time 2 ms) and assignment of TAPD-(OMe)₂ COF.

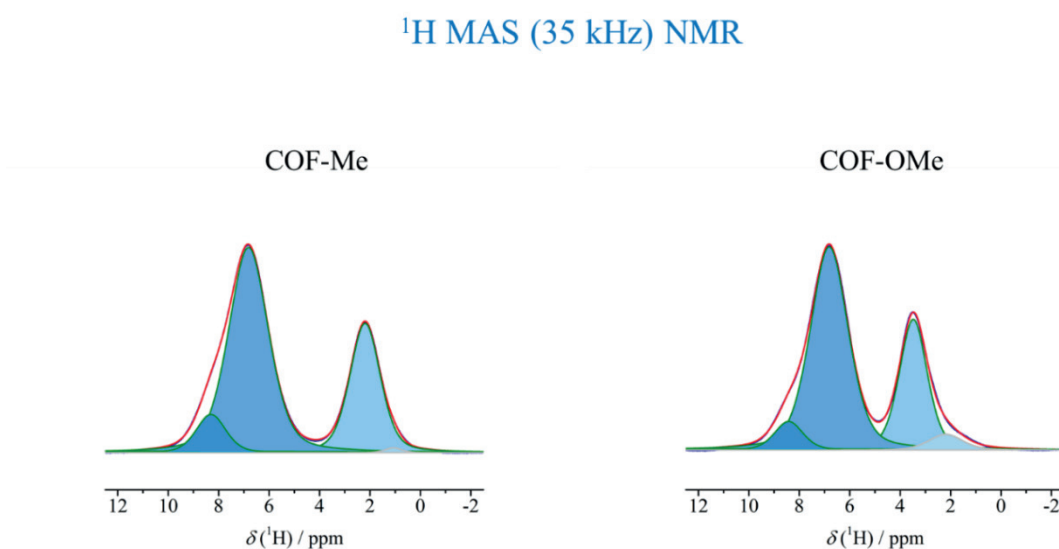


Figure S6.13. ^1H MAS (35 kHz) NMR spectra (and their decomposition) of TAPD-(Me)₂ COF (left) and TAPD-(OMe)₂ COF (right).

Table S6.1. Listed are the chemical shift, population, and assignment of TAPD-(Me)₂ COF and TAPD-(OMe)₂ COF.

Material	Chemical shift / ppm	Population (%)	Assignment
TAPD-(Me) ₂ COF	8.30	8.5	N=CH-Ph
	6.82	61.2	Ph-H
	2.20	29.7	-CH ₃
	1.07	0.6	impurity
TAPD-(OMe) ₂ COF	8.42	6.4	N=CH-Ph
	6.81	60.6	Ph-H
	3.48	28.8	-OCH ₃
	2.20	4.21	-CH ₃

Table S6.2. Elemental analysis of the TAPD COFs.

Sample	C %	N %	H %	O %	C/N ratio	C/H ratio
TAPD-(Me) ₂ COF – Exp	79.51	10.85	5.89	-	7.32	13.49
TAPD-(Me) ₂ COF – Theory	82.84	11.59	5.56	-	7.15	14.89
TAPD-(OMe) ₂ COF – Exp	72.19	9.72	5.19	-	7.42	13.90
TAPD-(OMe) ₂ COF – Theory	69.75	9.76	5.62	14.87	7.15	12.41

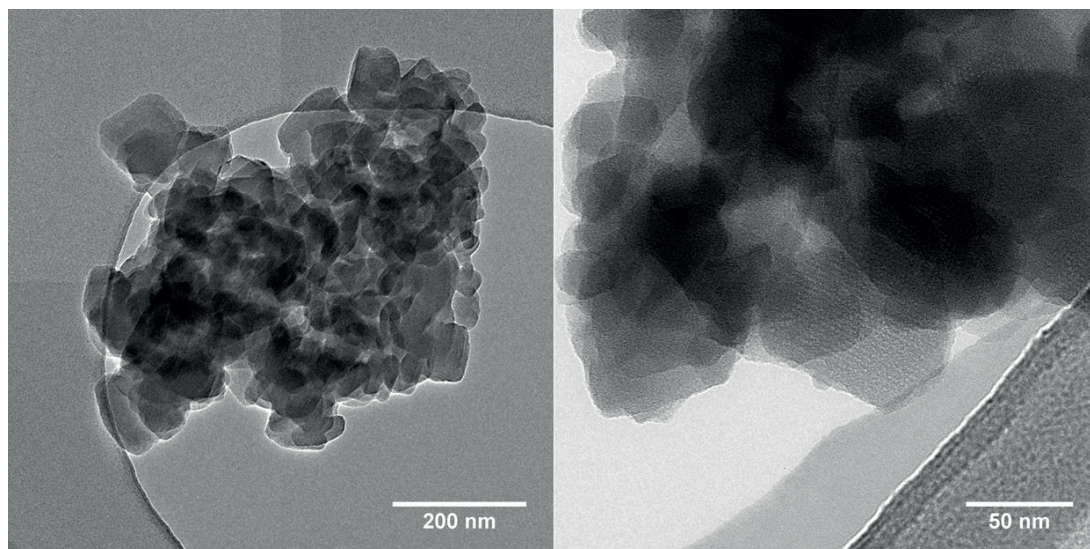


Figure S6.14. TEM images of TAPD-(Me)₂ COF showing layered structures.

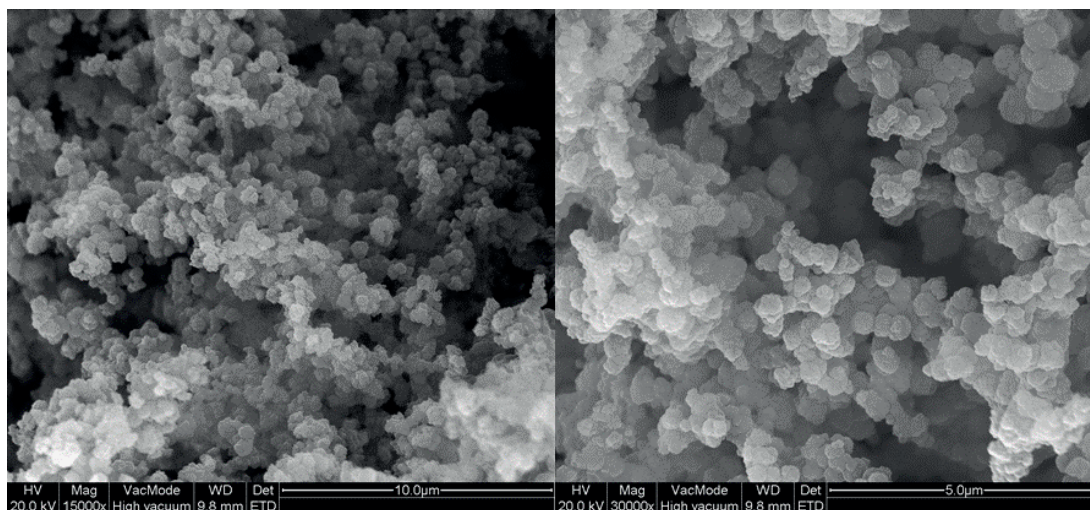


Figure S6.15. SEM images of TAPD-(Me)₂ COF showing homogeneous morphologies.

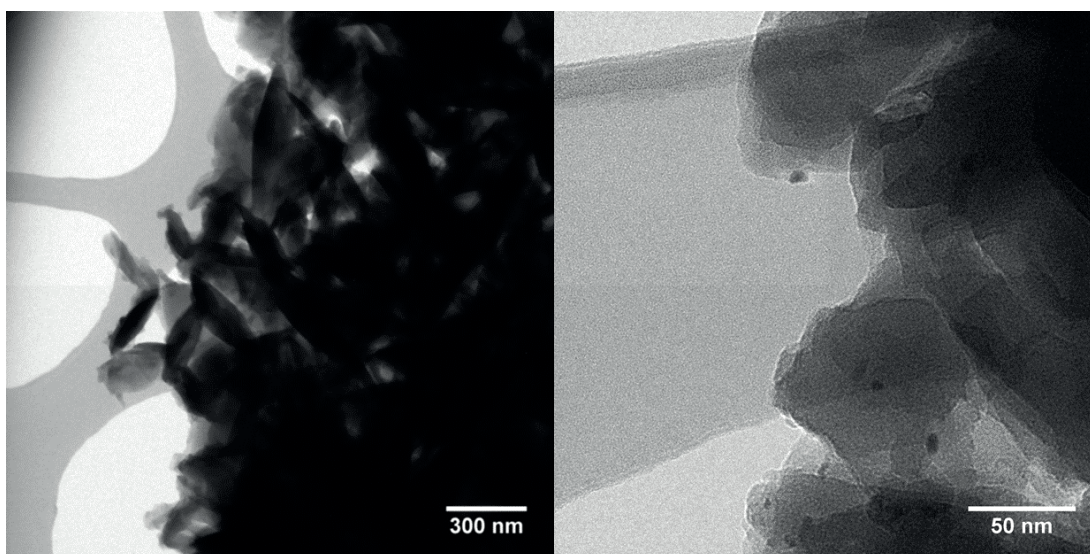


Figure S6.16. TEM images of TAPD-(OMe)₂ COF showing layered structures.

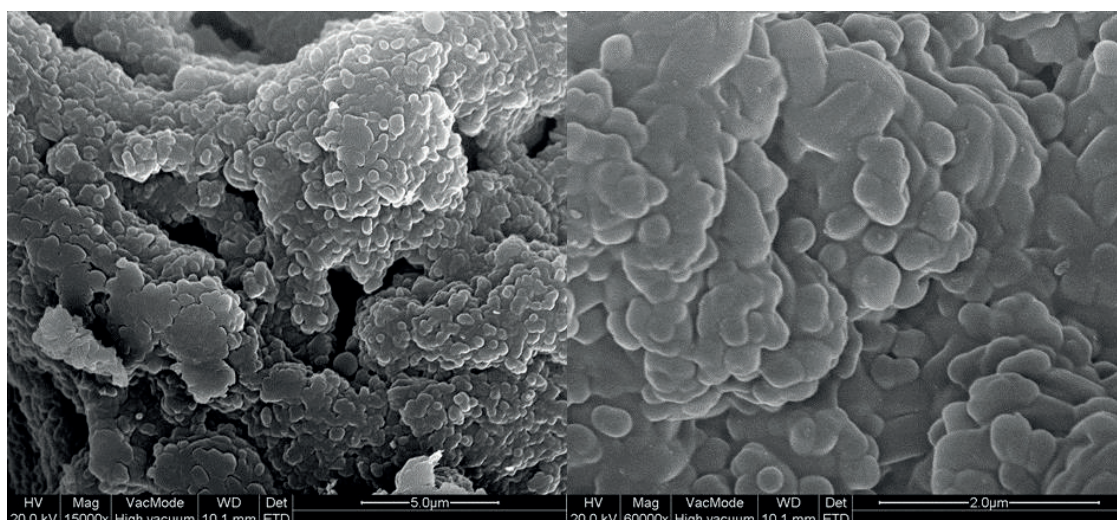


Figure S6.17. SEM images of TAPD-(OMe)₂ COF showing homogeneous morphologies.

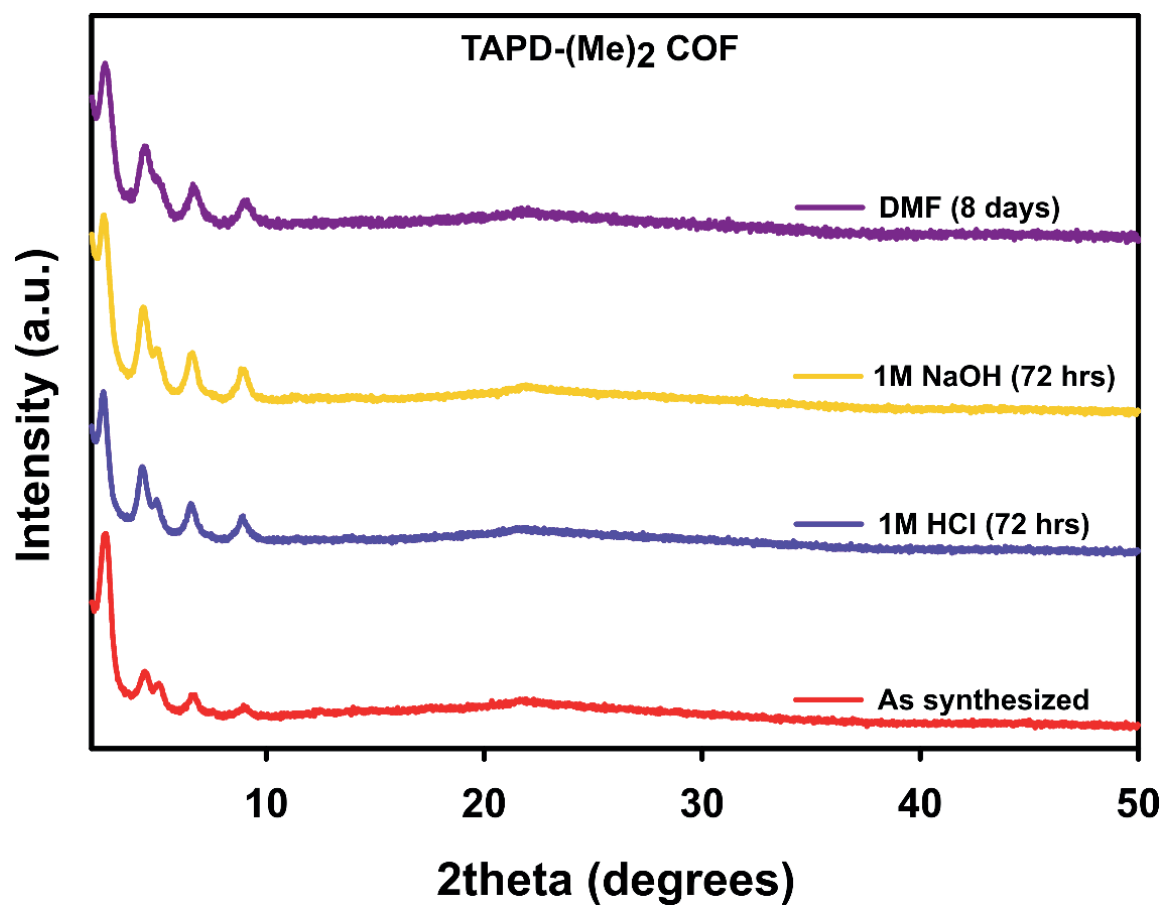


Figure S6.18. PXRD patterns of TAPD-(Me)₂ COF after treatment under different conditions.

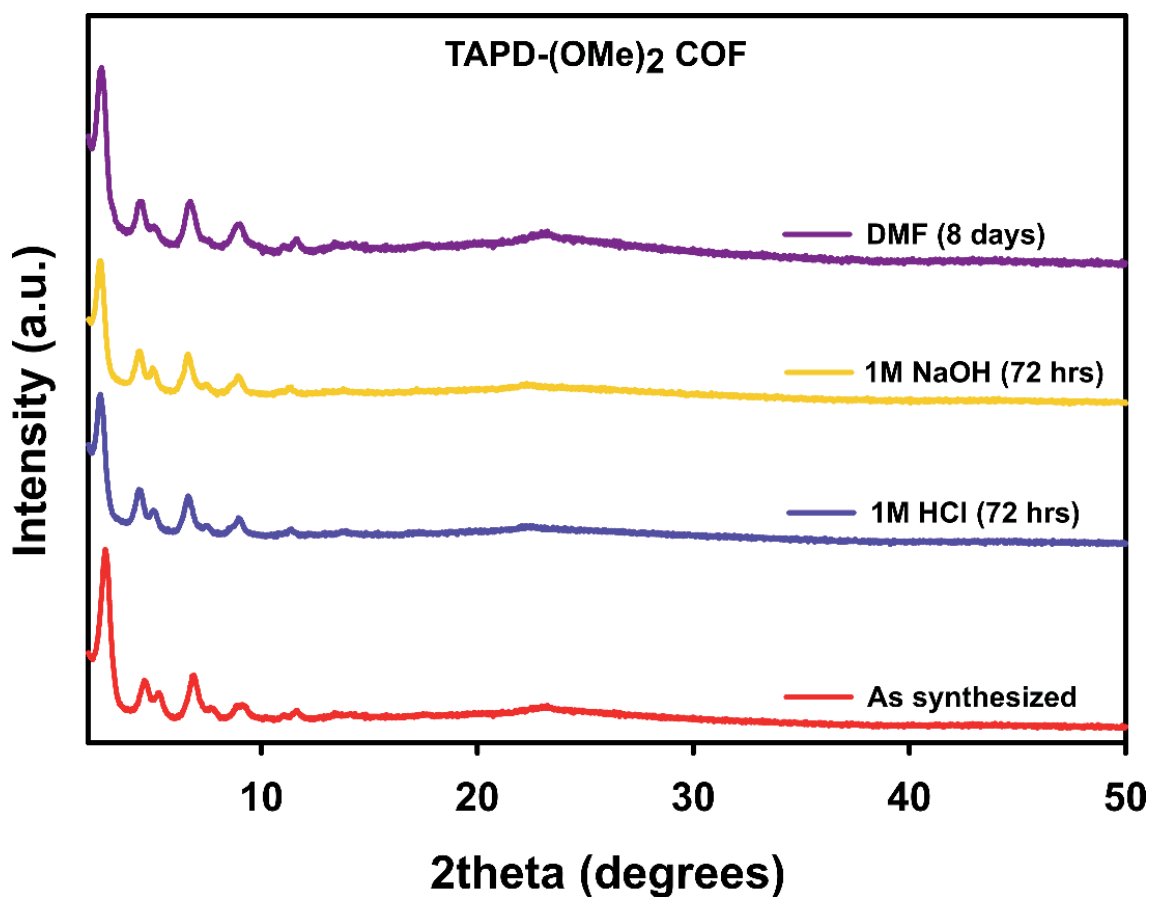


Figure S6.19. PXRD patterns of TAPD-(OMe)₂ COF after treatment under different conditions.

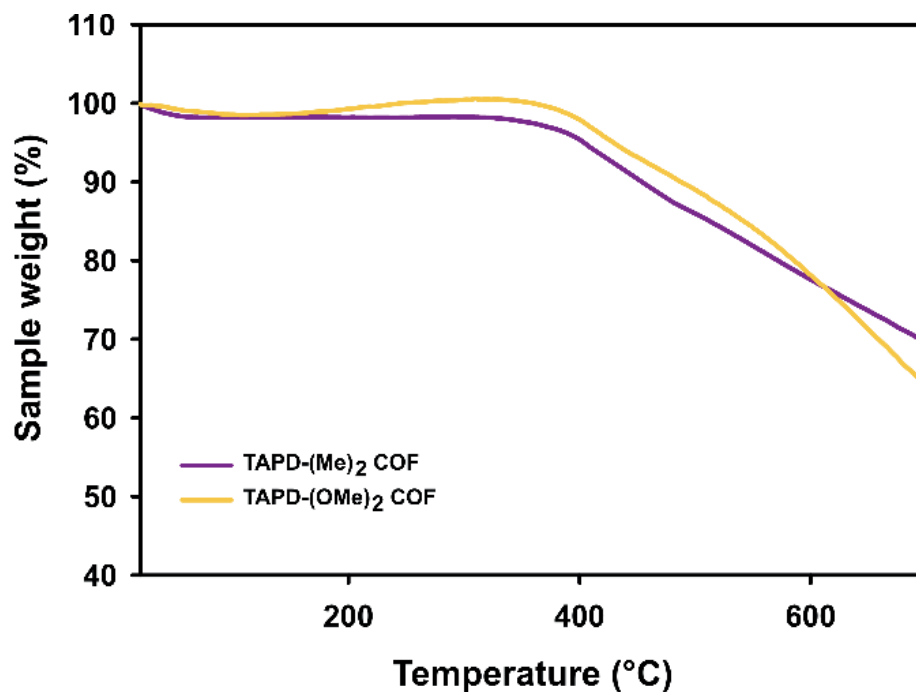


Figure S6.20. Thermogravimetric (TGA) spectra of TAPD-(Me)₂ and TAPD-(OMe)₂ COFs.

Section S6.4: Structural modelling and atomic coordinates of COFs

The structural crystal models with **kgm** topology of the TAPD-(Me)₂ and TAPD-(OMe)₂ COFs were initially constructed in a P6 primitive hexagonal unit cell in the Materials Studio suite of programs by Accelrys. Geometry optimization of the structures with Universal Force Field (UFF) led to satisfactory models whose theoretical pattern matched well the experimentally obtained patterns in terms of reflection positions and relative intensities. The Pawley profile refinements were performed using a Pseudo-Voigt profile function. The observed diffraction patterns were subjected to a polynomial background subtraction and the refined parameters included the zero point shift, the unit cell parameters, the FWHM parameters and the peak asymmetry (Berar-Baldizzone function). For both the COFs, AA stacking and AB stacking models were constructed, and their corresponding PXRD patterns were calculated.

S6.4.1. Crystal Structure Data of TAPD-(Me)₂ COF

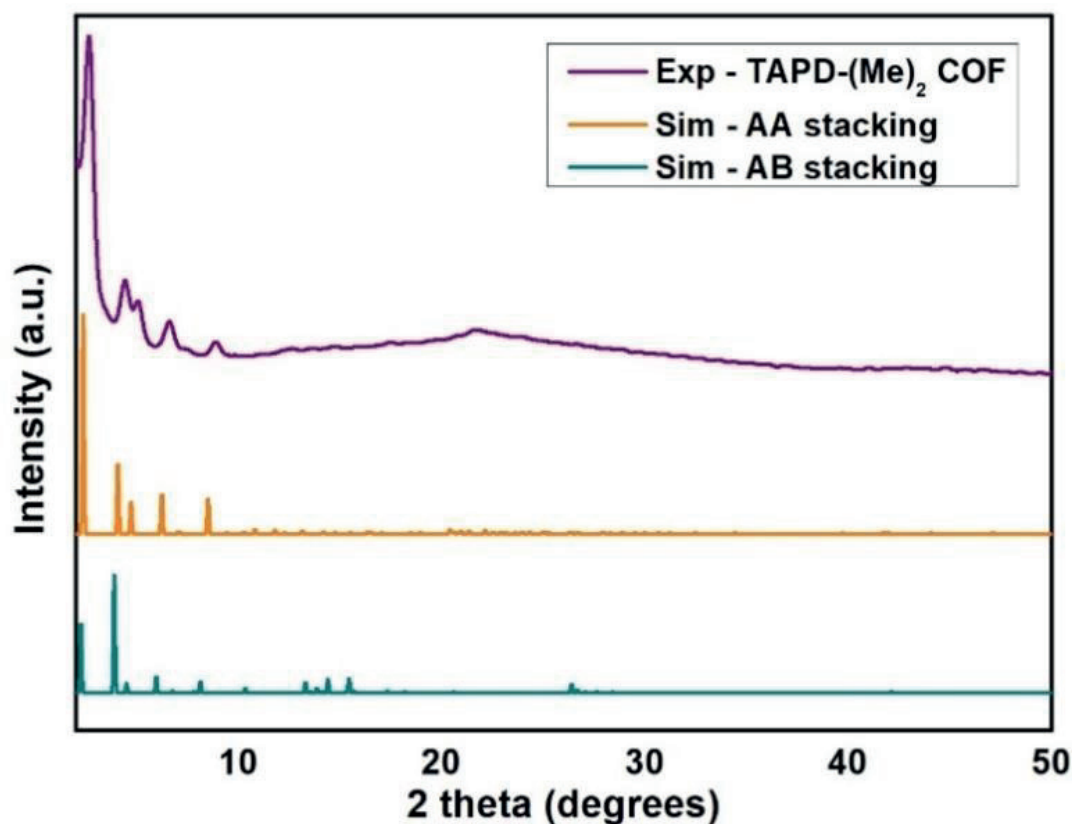


Figure S6.21. Simulated and experimental XRD patterns of TAPD-(Me)₂ COF.

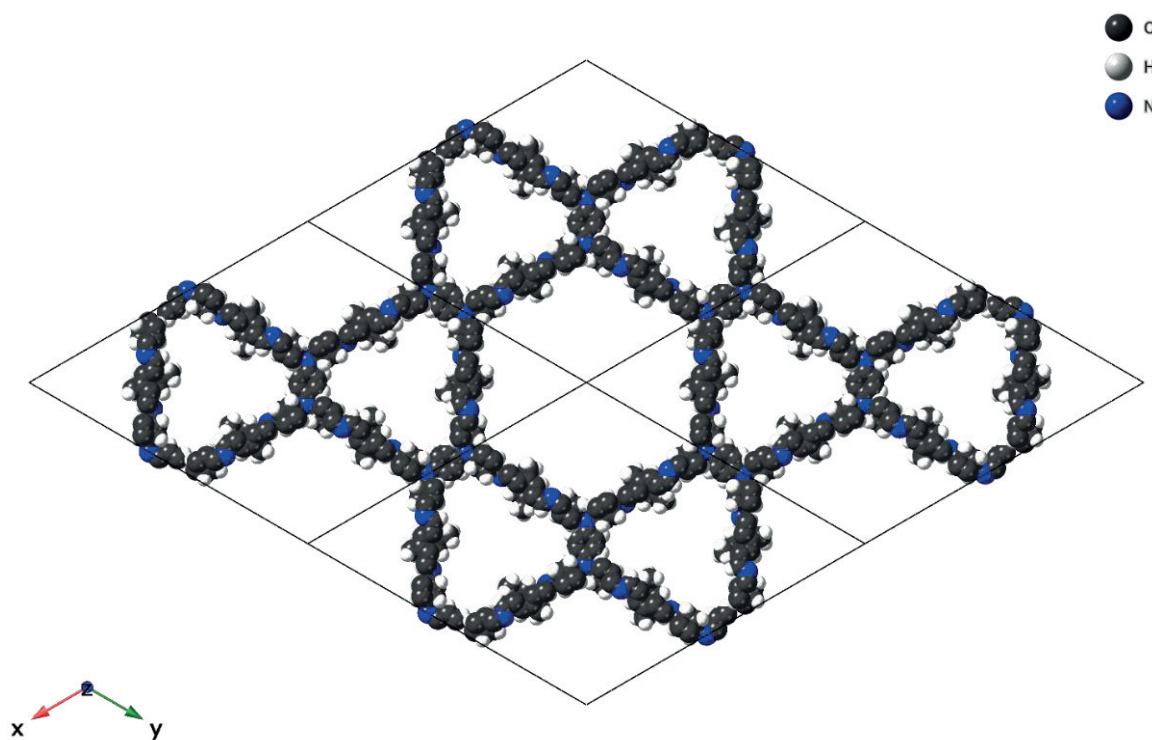


Figure S6.22. Theoretical structure of TAPD-(Me)₂ COF with eclipsed (AA) stacking arrangement.

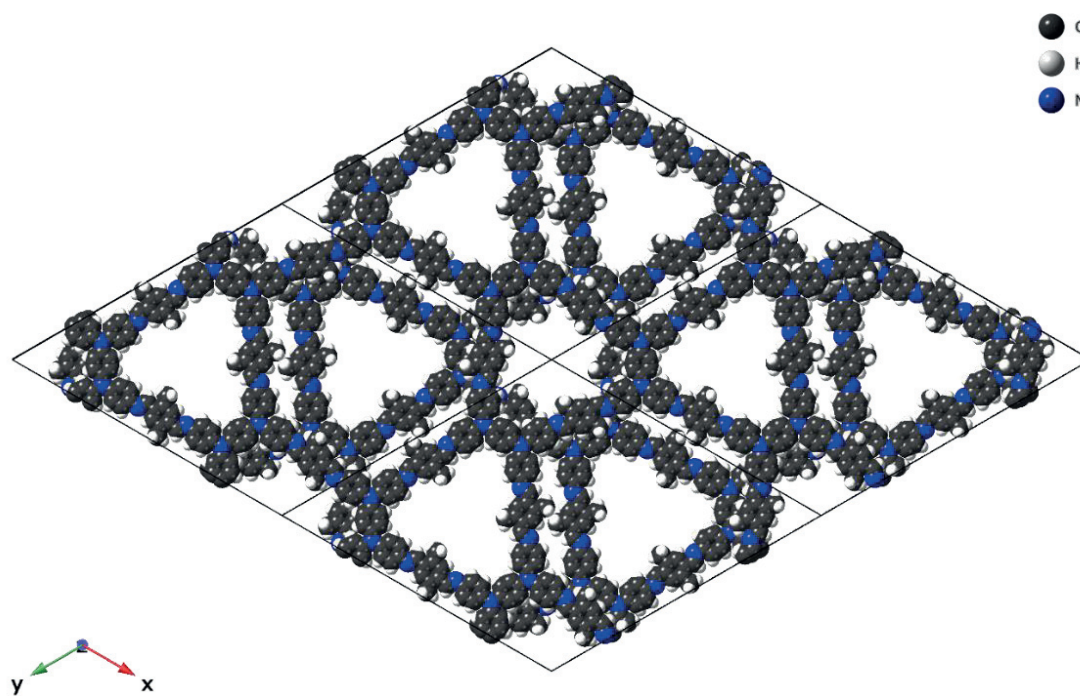


Figure S6.23. Theoretical structure of TAPD-(Me)₂ COF with eclipsed (AB) stacking arrangement.

S4.2. Crystal Structure Data of TAPD-(OMe)₂ COF

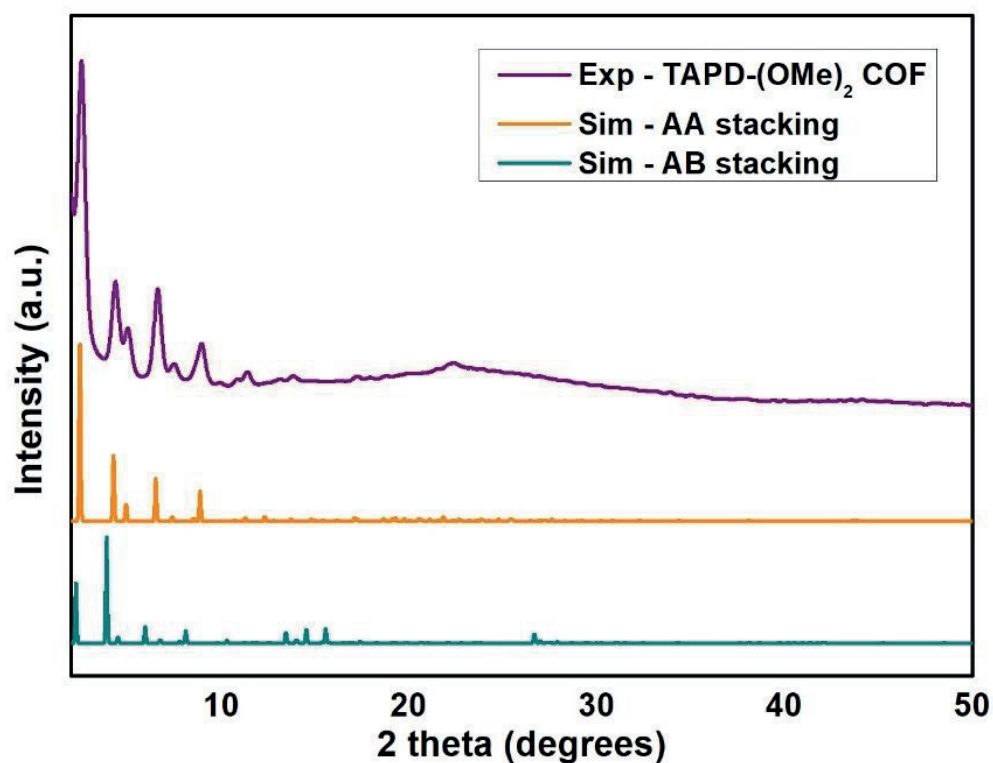


Figure S6.24. Simulated and experimental XRD patterns of TAPD-(OMe)₂ COF.

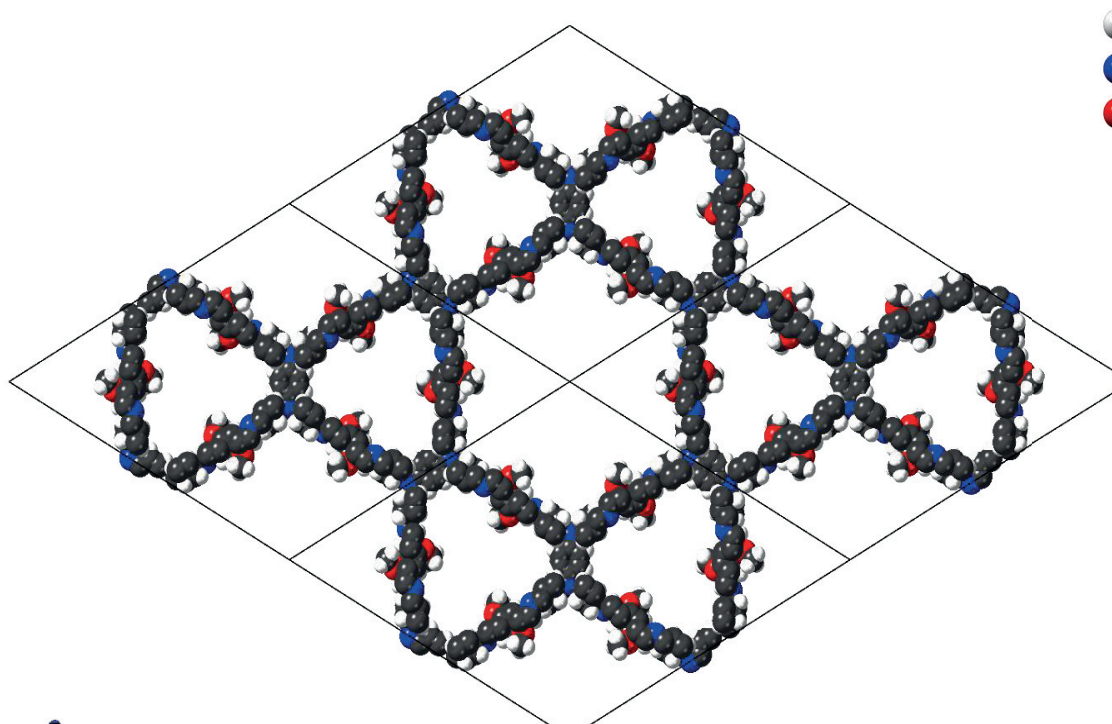


Figure S6.25. Theoretical structure of TAPD-(OMe)₂ COF with eclipsed (AA) stacking arrangement.

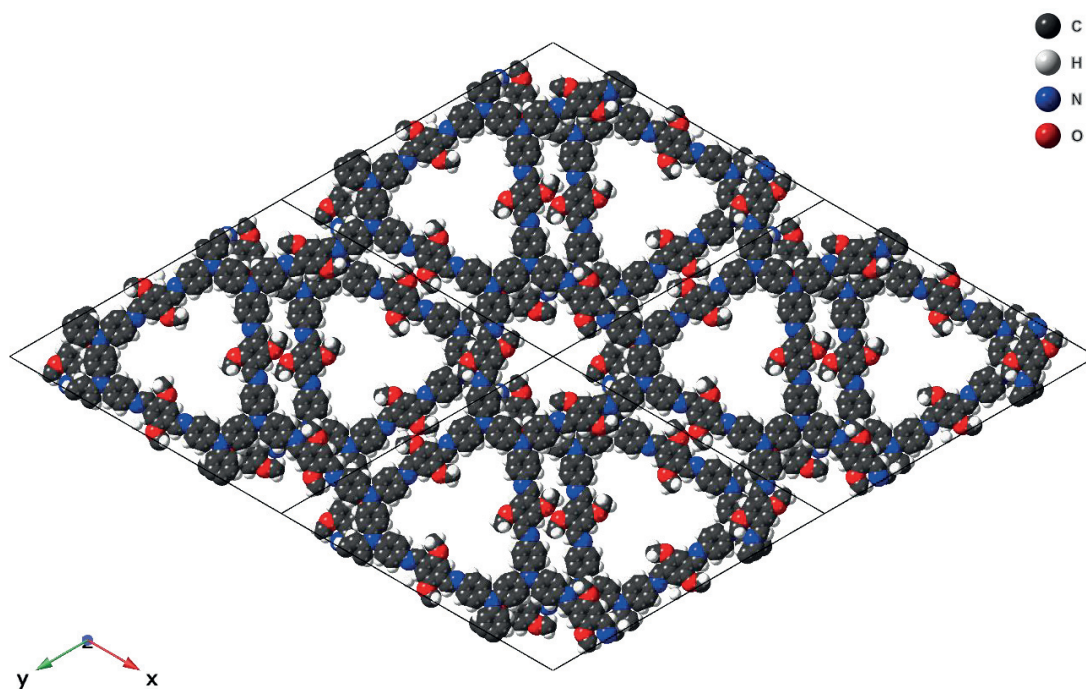


Figure S6.26. Theoretical structure of TAPD-(Me)₂ COF with eclipsed (AB) stacking arrangement.

Section S6.5: Computational modelling

S6.5.1. Constructing system-specific force fields: To derive system-specific force fields for the two periodic COF materials, *ab initio* calculations were performed on finite molecular clusters using the B3LYP [S4-S6] exchange-correlation functional and the 6-311++G(d,p) Pople basis set [S7] as implemented in the Gaussian16 suite.[S8] Furthermore, the default convergence criteria for distances and angles were adopted (maximum force=0.00045 Ha/a₀ and Ha/rad, rms force=0.00030 Ha/a₀ and Ha/rad, maximum displacement=0.00180 Ha/a₀ and Ha/rad, rms displacement=0.00120 Ha/a₀ and Ha/rad). The pairwise combinations of these molecular systems are representative of the periodic materials as shown in the insets of Figure S27. As such, four different clusters are considered: two ditopic building units corresponding to the linear linker and two tetratopic building units corresponding to the *N,N,N',N'*-Tetrakis(4-aminophenyl)-1,4-phenylenediamine linker, each with a suitable termination to mimic the environment of the moiety in the periodic framework.

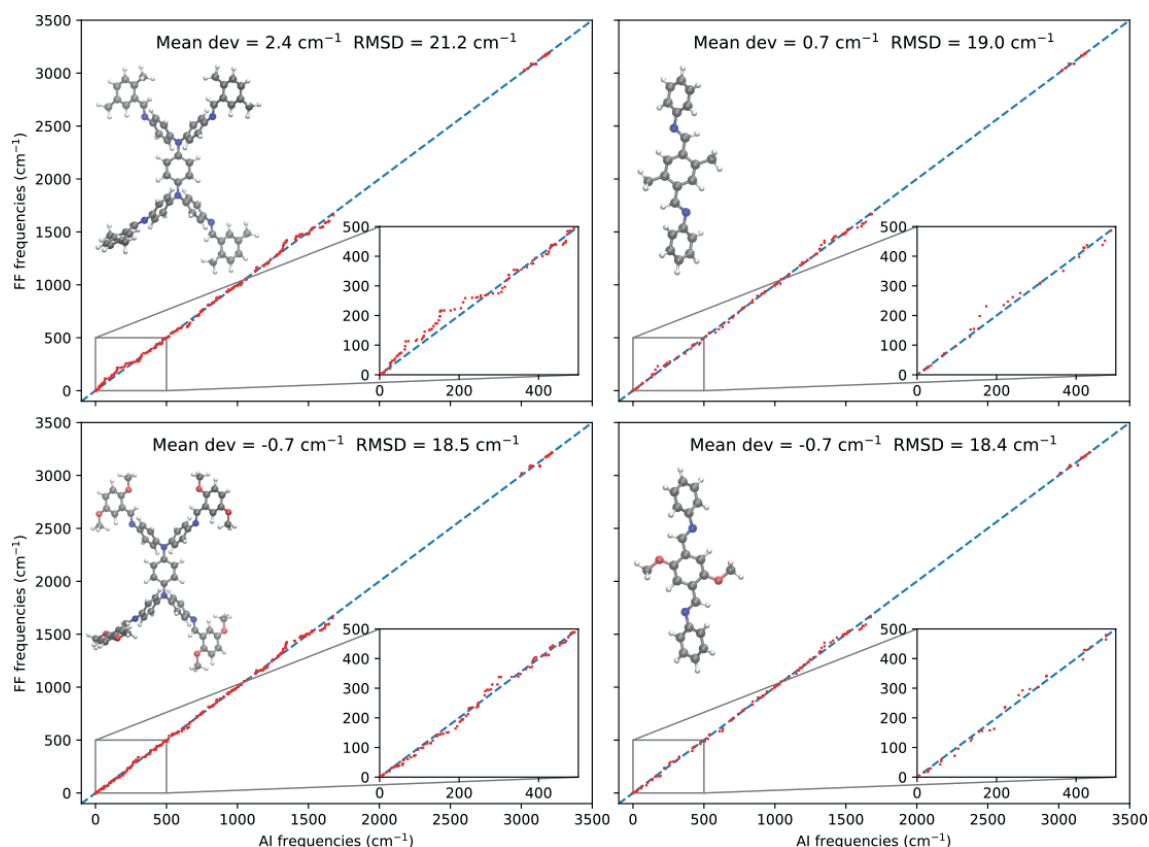


Figure S6.27. Comparison of the *ab initio* (AI) and force field (FF) normal mode frequencies for all the considered building blocks. The corresponding building block is visualized in the top left corner, with a zoomed-in picture for the low frequencies in the bottom right corner. The dashed lines indicate a perfect agreement.

After optimizing the geometry and calculating the Hessian, a normal mode analysis was performed to confirm that only positive frequencies were present, validating the geometry as a minimum on the potential energy surface. Subsequently, the atomic partial charges were derived using the MBIS partitioning scheme^[S9], as implemented in Horton.^[S10] Finally, with the optimized geometry, the Hessian and the partial charges as input, QuickFF^[S11, S12] was used to derive the covalent force field parameters for the separate clusters. The obtained force fields were then validated with respect to the *ab initio* derived Hessian using TAMkin^[S13], yielding good agreement between the force field and *ab initio* frequencies (Fig. S27). Finally, these cluster force fields were combined into force fields for the periodic structures, and a van der Waals model is added *a posteriori*, modeled by the MM3-Buckingham potential.^[S14] The resulting force fields are provided as part of the Supplementary Information.

S6.5.2. Structural models: While the AA and AB stacking models of Section S4 account for the different relative positions of adjacent layers, the relative position of the functional

groups in adjacent layers forms an additional degree of freedom that can influence the geometry of the COFs and hence their PXRD patterns. To take this into account, we constructed two different stacking models with varying locations of the functional groups across the layers, as illustrated in Figure S28. The configuration with aligned functional groups is labelled as ‘parallel’, while the configuration with alternating locations is labelled ‘inverted’. These parallel and inverted models are considered separately from the AA and AB stacking models mentioned before. As our simulations allow for layer movement, there is no need to consider the AA and offsetted AB configuration as distinct models.

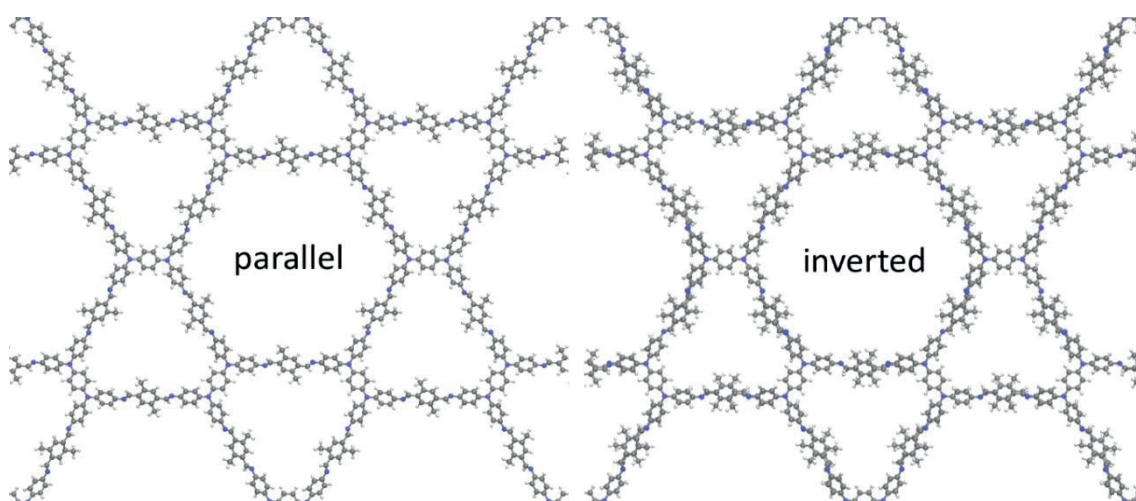


Figure S6.28. The parallel and inverted structural models used for TAPD-(Me)₂, with analogous models adopted for TADP-(OMe)₂. (Left) In the parallel model, the location of the functional groups is identical in all layers. (Right) In the inverted model, the location of the functional groups alternates across adjacent layers.

S6.5.3. Generation of computational PXRD patterns: An accurate description of the potential energy surface (PES) and its sampling are essential when calculating a computationally representative diffraction pattern. In a first approach, we followed a static approach to sample the PES by optimizing the different structural models at zero Kelvin. The resulting PXRD patterns and their relative agreement with the experimentally observed patterns are visualized in Figure S29 and show already good correspondence. The PXRD patterns were calculated employing the pyobjcryst python package, based on the ObjCryst++ Object-Oriented Crystallographic Library.^[S15] In accordance with experiment, the Cu K_α wavelength of 1.54056 Å was used. The peak shape was calculated using a pseudo-Voigt shape function, with mixing parameter $\eta = \eta_0 + \eta_1 2\theta + \eta_2 2\theta^2$ ($\eta_0 = 0.5$, $\eta_1 = 0$, $\eta_2 = 0$) which determines the ratio between Lorentzian

and Gaussian shape functions. The corresponding peak width, $H^2 = U \tan^2(\theta) + V \tan(\theta) + W$, is fixed with $W=0.02$ degrees, keeping the other parameters U , V equal to 0 degrees.

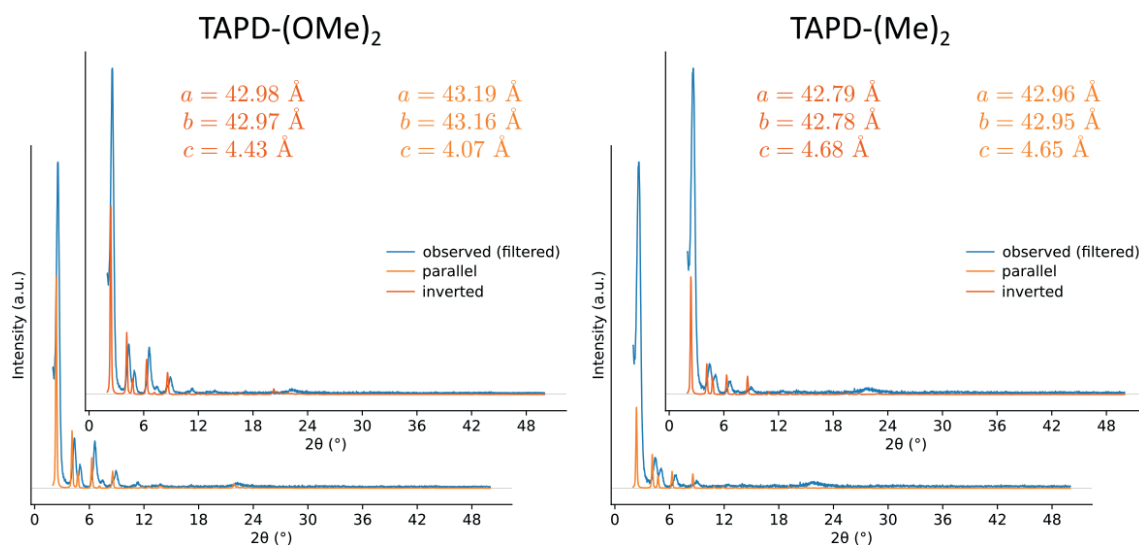


Figure S6.29. Comparison between the observed and calculated PXRD patterns, and the derived unit cell parameters, based on the force field optimized structures of TAPD-(OMe)₂ and TAPD-(Me)₂.

However, at elevated temperatures and pressures, the reflection planes will show small dynamic fluctuations over time that increase with increasing temperature due to atomic vibrations. Inherently, an XRD measurement thus provides a time-averaged view of these dynamic reflection planes at certain operando conditions. To mimic these dynamic effects, in our second approach, we performed MD simulations and took different snapshots from the resulting trajectories. Here, Yaff^[S16] was used as the MD engine and interfaced with LAMMPS^[S17] to efficiently compute the long-range interactions. A time step of 0.5 fs was used with a run time of 400 ps taking a snapshot every 0.1 ps. The MD simulations were performed in the $(N, P, \sigma_a=0, T)$ ensemble^[S18], fixing the temperature at 300 K with a Nosé-Hoover chain thermostat^[S19-S21] with three beads and a relaxation time of 100 fs. The pressure was controlled at 1 bar by a Martyna-Tuckerman-Tobias-Klein barostat^[S22, S23] with a relaxation time of 1000 fs. As a result, this second approach allows for an *ab initio* protocol to introduce average atomic displacements into the computationally derived PXRD patterns, as these snapshots are generated using an *ab initio* derived force field, accounting for temperature effects that were missing in the first approach. Time-averaging the PXRD pattern over the course of the simulation thus provides a more accurate representation of the atomic structure during measurement, generally resulting in a better correspondence with experimentally observed PXRD

patterns. This is indeed observed in Figure S30, showing excellent agreement between the experimental and the MD averaged diffraction patterns.

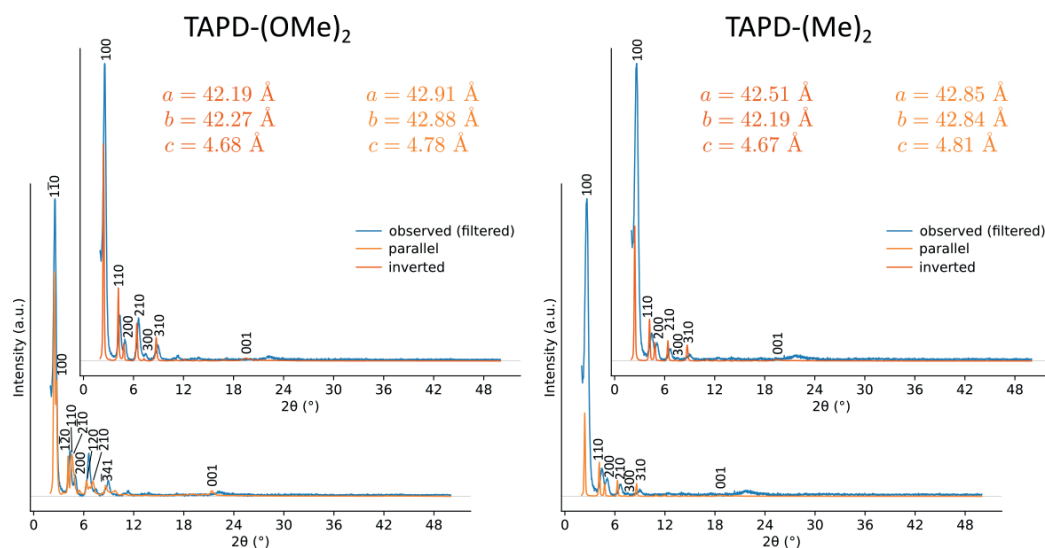


Figure S6.30. Comparison between the observed and calculated PXRD patterns, and the unit cell parameters, based on the molecular dynamics simulations of TAPD-(OMe)₂ and TAPD-(Me)₂.

S6.5.4. Stacking offset: As our MD simulations can dynamically switch between AA and AB stackings, they directly reveal the preferred alignment between adjacent layers, as quantified by their offset (Figure S31). From our MD simulations, it is apparent that, for both COFs, the offsets between adjacent layers is very limited and without directionality, such that the average structure during the MD simulation resembles a 2D COF with an eclipsed (AA) stacking (Figure S31).

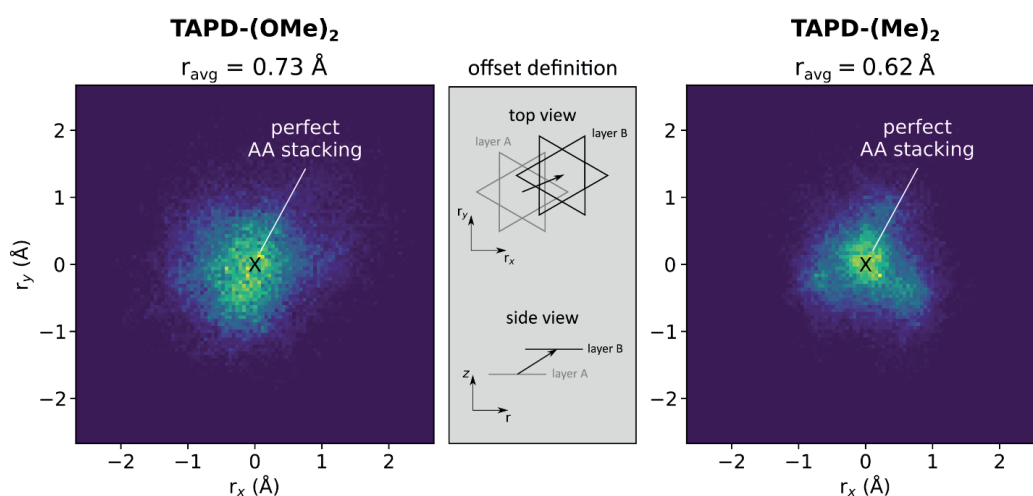


Figure S6.31. Heatmap of the offsets between adjacent layers for (Left) TAPD-(OMe)₂ and (Right) TAPD-(Me)₂. The average offset with respect to perfect AA stacking, r_{avg} , is reported at the top of each heatmap.

Section S6.6: Gas sorption

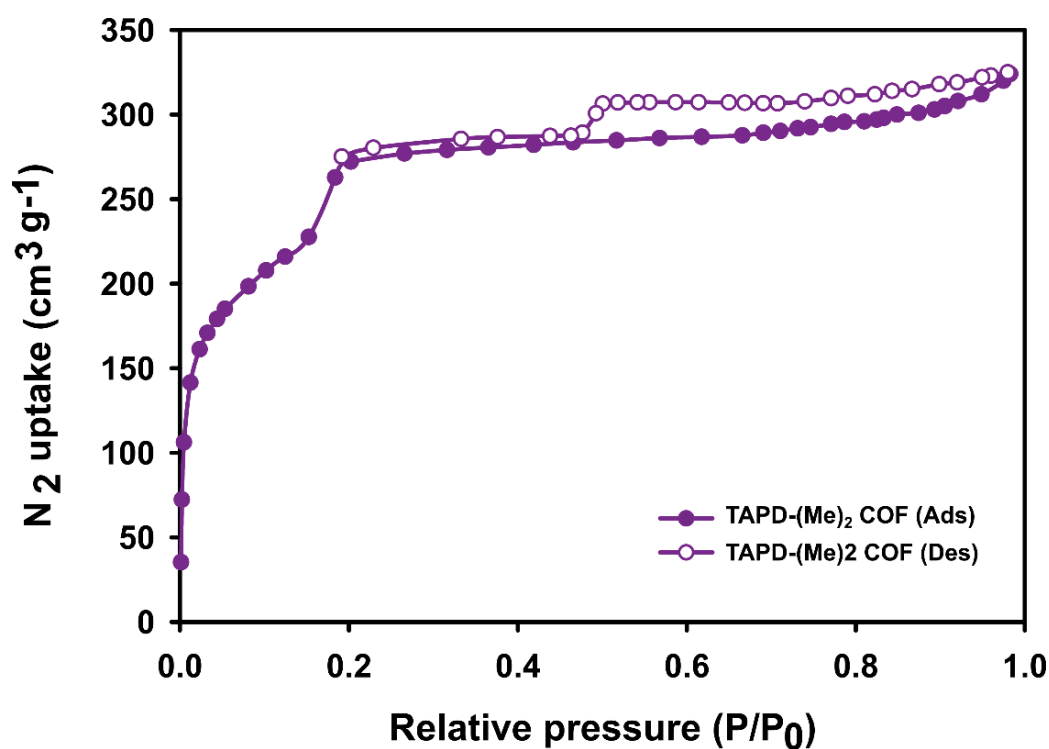


Figure S6.32. N_2 sorption isotherms of TAPD-(Me)₂ COF.

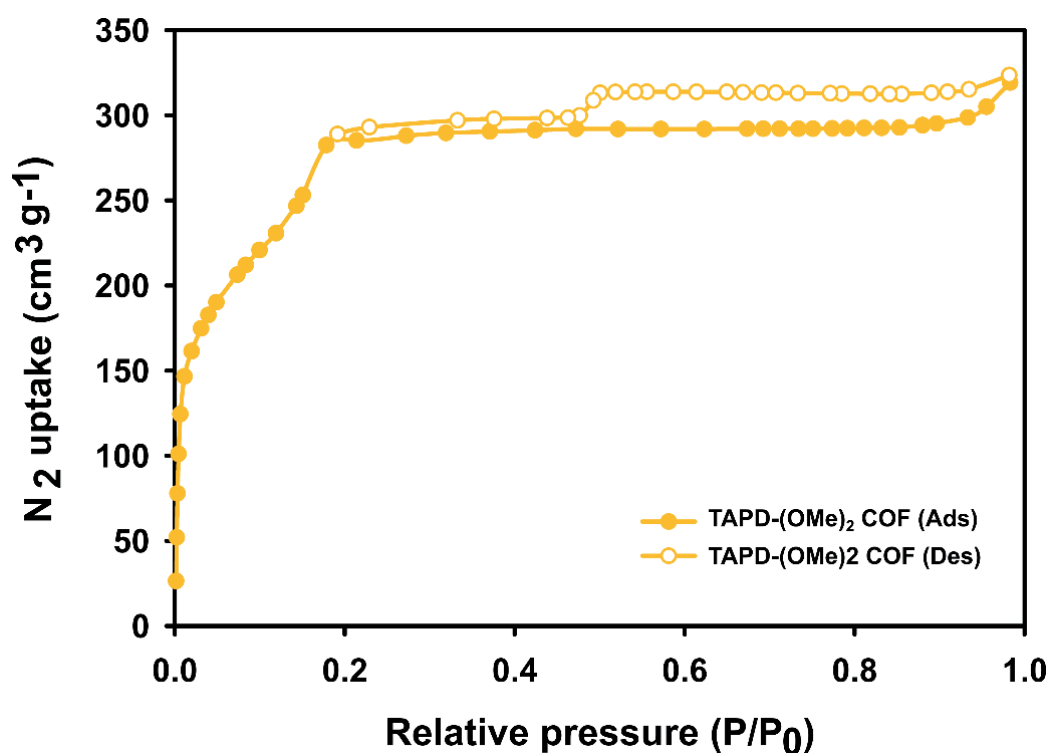


Figure S6.33. N_2 sorption isotherms of TAPD-(OMe)₂ COF.

Section S6.7: Photo(electro)chemical characterization and photocatalytic experiment details

S6.7.1. Photo(electro)chemical characterization: For the electrochemical measurements, a thin layer of COF was deposited on FTO. To this end, 2 mg of COF was dispersed in a mixture of 350 μ l acetonitrile, 150 μ l tetrahydrofuran, 100 μ l trifluoroacetic acid (TFA) and 20 μ l water. The TFA temporarily protonates the imine bonds, which positively charges the COF layers, strongly increasing their electrostatic repulsion, which in turn leads to improved dispersion behavior [S24]. The mixture was sonicated for 1 hour until a visually homogeneous dispersion was obtained. 100 μ l of this dispersion was drop-casted on a 1 cm \times 2 cm area of an FTO substrate. After drying, the coating was soaked in ethanol for two minutes, which deprotonated the COF layer. This could be visually observed as a fast change in color (Fig. S34), accompanied by the formation of small H₂ gas bubbles. The coating was left to dry under air for one hour.



Figure S6.34. The photocatalyst-coated FTO substrate before (left) and after (right) soaking in ethanol.

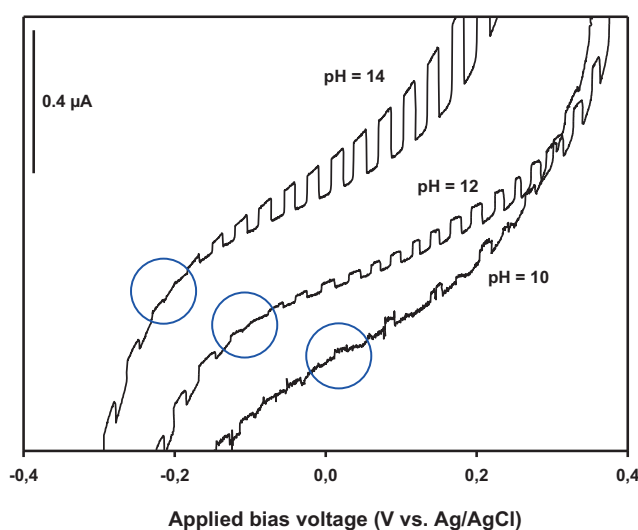


Figure S6.35. TAPD-(Me)₂ COF. Linear sweep voltammetry under chopped illumination in three electrolytes with different pH. The potential regions where the photocurrent changes its sign are marked in blue.

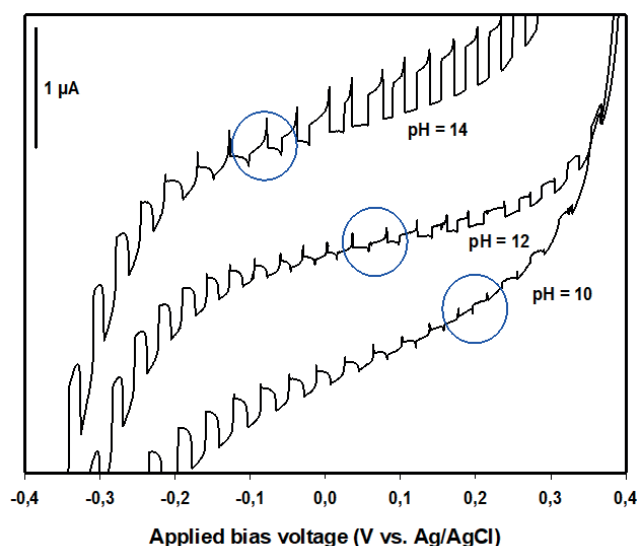


Figure S6.36. TAPD-(OMe)₂ COF. Linear sweep voltammetry under chopped illumination in three electrolytes with different pH. The potential regions where the photocurrent changes its sign are marked in blue.

Photoelectrochemical measurements were performed in either 1 M NaOH (pH = 14), 0.2 M KCl/NaOH buffer (pH = 12) or 0.06 M Na₂B₄O₇·10H₂O/NaOH buffer (pH = 10) using an ALS-Japan Ag/AgCl 3 M NaCl reference electrode (+0.195 V vs. SHE), an ALS-Japan Pt coil counter electrode and the photocatalyst-coated FTO as working electrode. 5 ml electrolyte was used, so that the entire photocatalyst-coated surface of the FTO substrate was submerged. The electrolyte was de-aerated with Ar before every measurement. We found that measurements in acidic electrolytes (pH < 7) gave less reproducible results.

Measurements were recorded using a Bio-Logic VSP potentiostat and EC-Lab software. White light was provided by a Philips Tornado T2 CFL (23 W, 1450 lumen). The voltage was swept in the negative direction from +0.4 V to -0.4 V vs. Ag/AgCl at a scanrate of 4 mV/s, whilst at the same time the white light was chopped every 3 seconds.

The potential at which the photocurrent sign change occurred was visually determined from the LSV curves, and from here on will be referred to as the Umklapppotential, E_{UK} (Fig. S35 and S36). The redox potential of the electrolyte $E_{electrolyte}$ (V vs. Ag/AgCl) was calculated from the pH according to:

$$E_{electrolyte} = -0.195 - 0.059 \times pH$$

The difference in E_{UK} and $E_{electrolyte}$ is the voltage bias that is necessary to align the electrolyte potential with the conduction band minimum (Fig. S37). Therefore, the

conduction band minimum E_{CBM} (V. vs Ag/Ag/Cl) can be found at an energy level that is $(E_{UK} - E_{electrolyte})$ volts more negative than the redox potential of the electrolyte $E_{electrolyte}$.

$$E_{CBM} = E_{electrolyte} - (E_{UK} - E_{electrolyte}) = 2E_{electrolyte} - E_{UK}$$

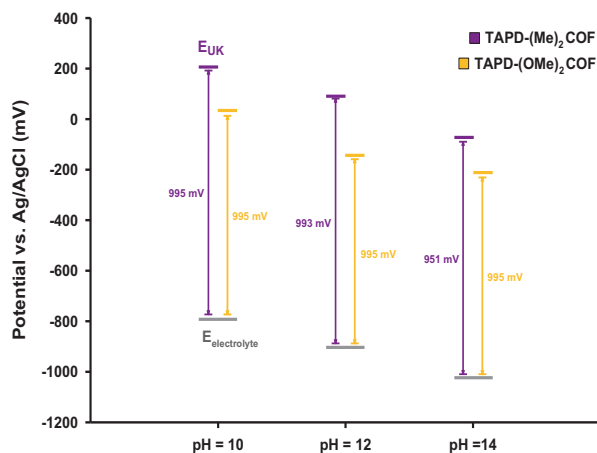


Figure S6.37. Electrolyte redox potentials $E_{electrolyte}$ and Umklappotentials E_{UK} of TAPD-(Me)₂ COF and TAPD-(OMe)₂ COF.

The calculated conduction band minima follow a Nernstian dependence in good approximation. From the values at pH 14, 12 and 10, we extrapolated a value for the conduction band minimum at pH = 0 (Fig. S38).

pH	$E_{electrolyte}$ vs. Ag/AgCl (mV)	E_{UK} vs. Ag/AgCl (mV) TAPD-(Me) ₂ COF	E_{UK} vs. Ag/AgCl (mV) (TAPD-(OMe) ₂ COF
14	-1021	-70	-210
12	-903	90	-140
10	-785	210	30
pH	E_{CBM} vs. NHE (mV) TAPD-(Me) ₂ COF		E_{CBM} vs. NHE (mV) (TAPD-(OMe) ₂ COF
14	-1777		-1637
12	-1701		-1471
10	-1585		-1405
0	-972		-796

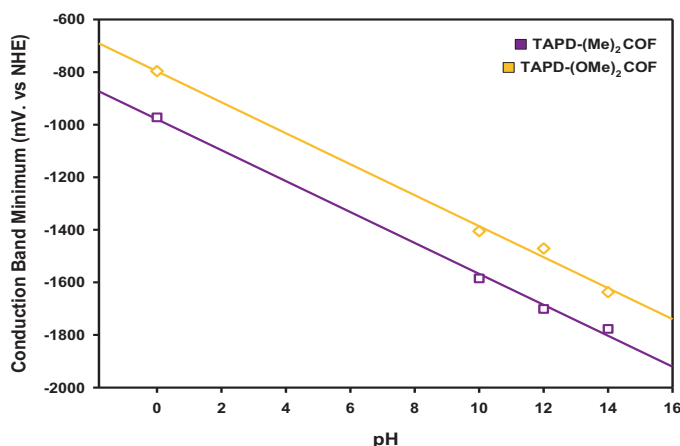


Figure S6.38. The measured conduction band minima at pH = 10, pH = 12 and pH = 14 approximately follow a Nernstian dependence. The conduction band minima at pH = 0 were extrapolated from these values.

S6.7.2. Photocatalytic experiment details: Hydrogen peroxide production was carried out in 15 ml glass vial. 20 mg of catalyst was dispersed in 5 mL water:ethanol (9:1) mixture and sonicated for 5 minutes. Oxygen gas was saturated in the mixture for 20 minutes by bubbling and vial was sealed. 250 W of light within 420-700nm wavelength was irradiated on the vial in a dark room (light intensity = 5.46 W m^{-2}). The temperature was maintained at 25°C using a condenser. The distance between the reactor and the light source was kept fixed at 5 cm and stirring speed was maintained at 900 rpm. After the reaction, the products were analyzed by iodometric titration to determine hydrogen peroxide concentration.

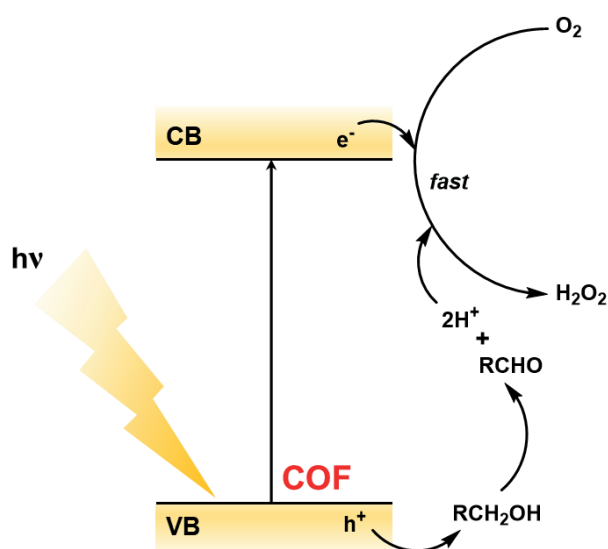


Figure S6.39. Proposed mechanism for the photocatalytic formation of hydrogen peroxide.

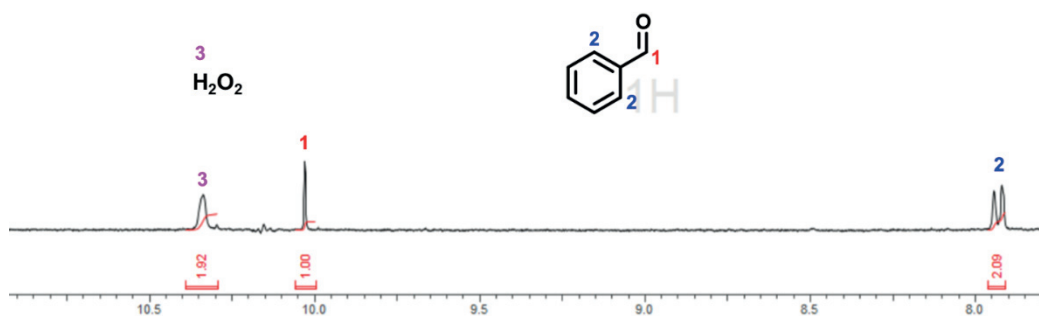


Figure S6.40. ¹H NMR spectra of the end product (crude) after 16 h reaction with water:benzylalcohol (1:9) at room temperature using TAPD-(Me)₂ COF. Mesitylene of known concentration was used to quantify the amount of benzyl alcohol and H₂O₂ produced.

Table S6.3. Photocatalytic results under various conditions

Entry	Photocatalyst	Solvent system	Gas	Irradiation conditions	H ₂ O ₂ produced (μmol)
1.	Model Compound TAPD-(Me) ₂ -MC	Water:EtOH (9:1)	O ₂ saturated	λ = 420-700 nm	7
2.	Blank	Water:EtOH (9:1)	O ₂ saturated	λ = 420-700 nm	-
3.	TAPD-(Me) ₂ COF	Water:EtOH (9:1)	O ₂ saturated	Dark	-
4.	TAPD-(Me) ₂ COF	Water:Benzyalcohol (1:9)	O ₂ saturated	λ = 420-700 nm	53.7
5.	TAPD-(Me) ₂ COF	Water:EtOH (9:1)	Ambient	λ = 420-700 nm	8
6.	TAPD-(Me) ₂ COF	Water:EtOH (9:1), 4 days	O ₂	λ = 420-700 nm	142.3
7.	TAPD-(Me) ₂ COF	Water:EtOH (9:1)	Triethylamine (TEA):	λ = 420-700 nm	-

			h^+ trapping agent		
8.	TAPD-(Me) ₂ COF	Water:EtOH (9:1)	AgNO ₃ : e^- trapping agent	$\lambda = 420-700$ nm	2
9.	TAPD-(Me) ₂ COF	Water:EtOH (9:1)	Benzoquinone: Radical scavenger	$\lambda = 420-700$ nm	22

S6.7.3. Recyclability test: TAPD-(Me)₂ COF was collected after each run through filtration and washed thoroughly with acetone and THF. Before performing the second run, it was dried under vacuum at 120°C for 12 hours.

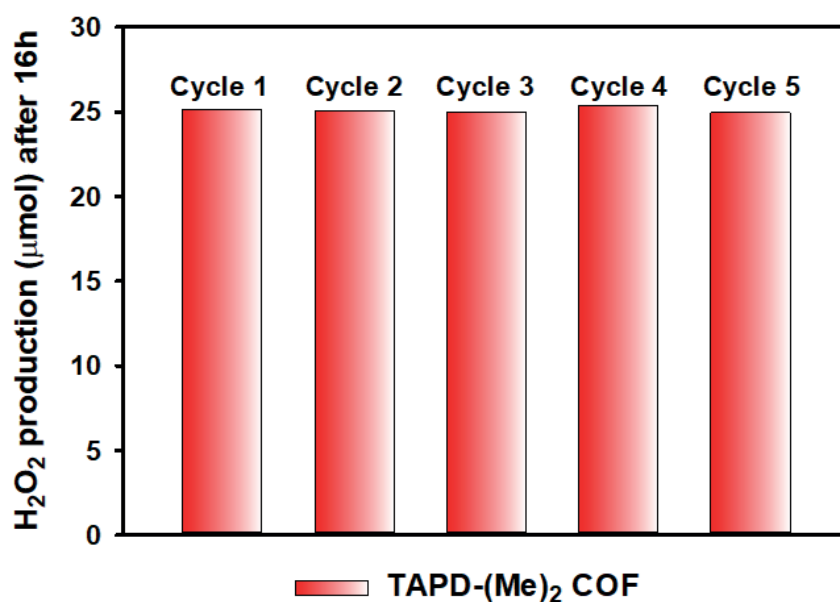


Figure S6.41. H₂O₂ production for 5 consecutive cycles using TAPD-(Me)₂ COF.

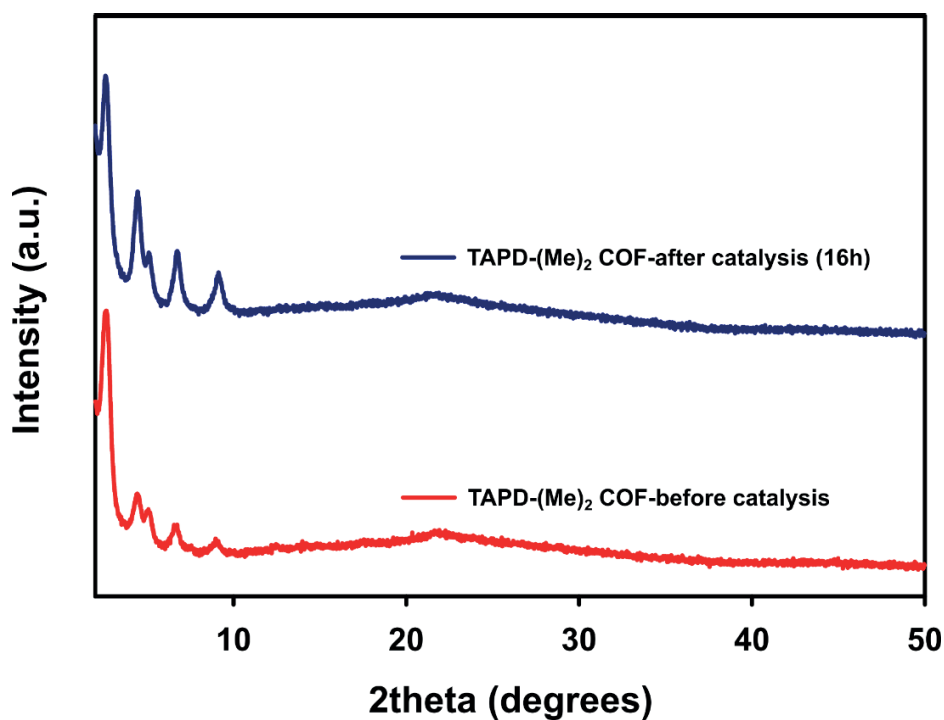


Figure S6.42. PXRD patterns of TAPD-(Me)₂ COF before and after catalysis showing that the crystallinity is retained.

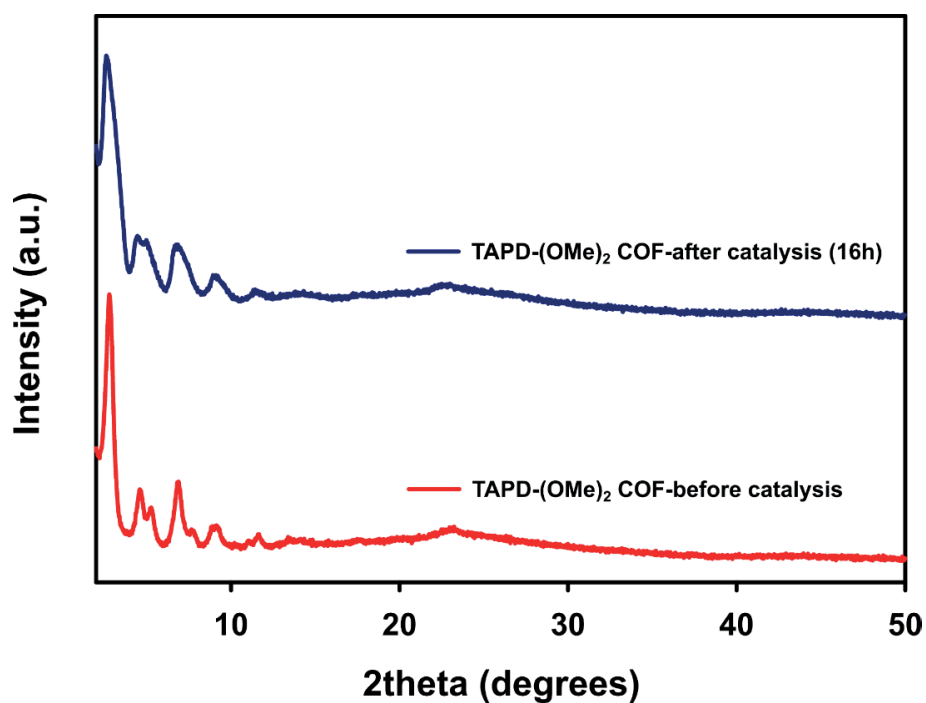


Figure S6.43. PXRD patterns of TAPD-(OMe)₂ COF before and after catalysis showing that the crystallinity is retained.

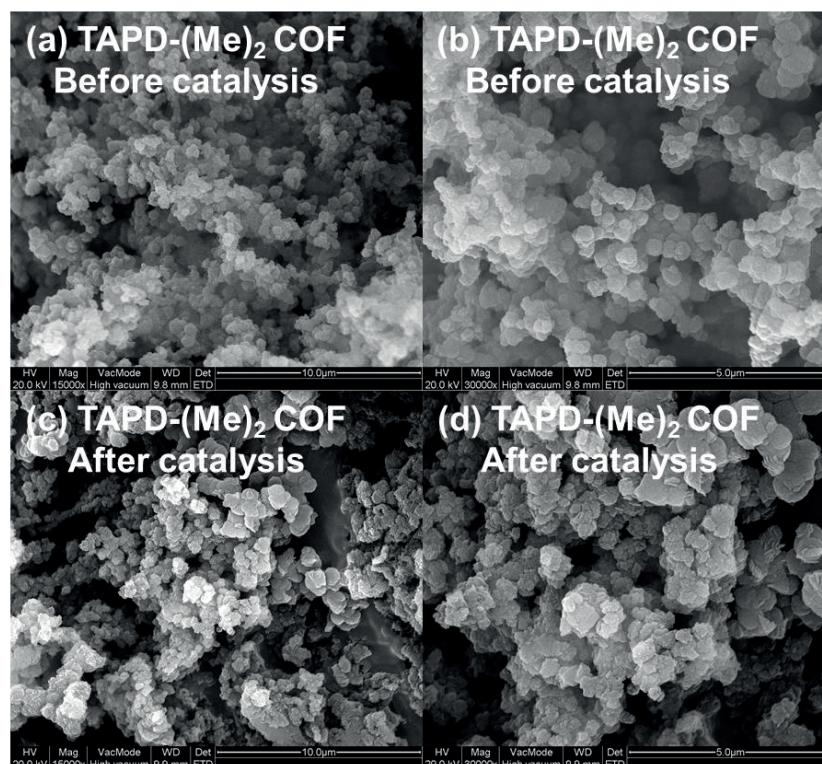


Figure S6.44. SEM images of TAPD-(Me)₂ COF before and after catalysis.

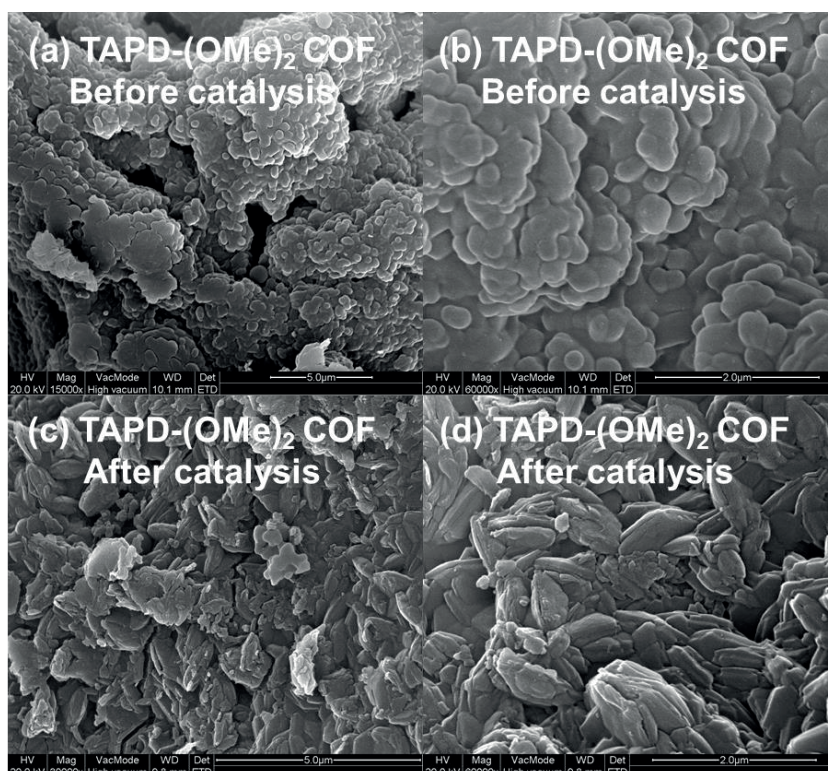


Figure S6.45. SEM images of TAPD-(OMe)₂ COF before and after catalysis.

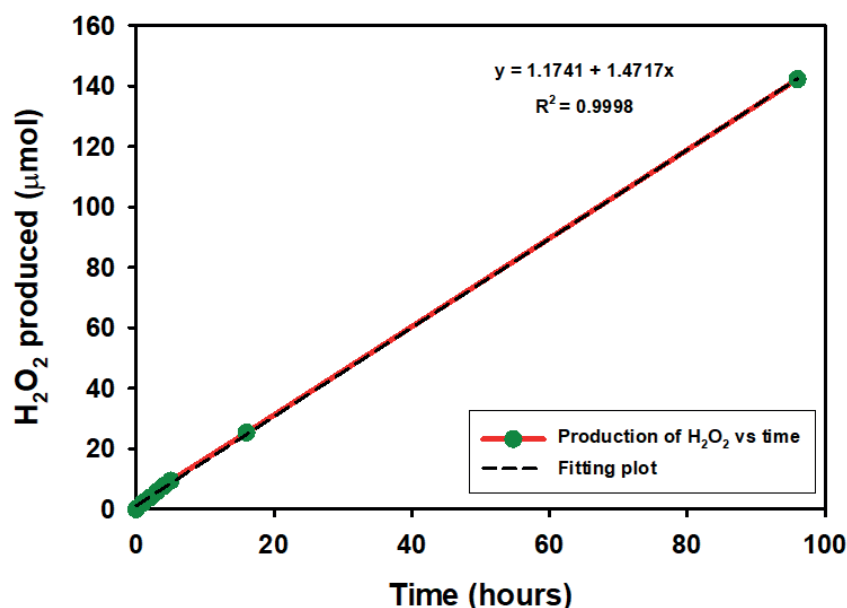


Figure S6.46. Production of H₂O₂ vs time.

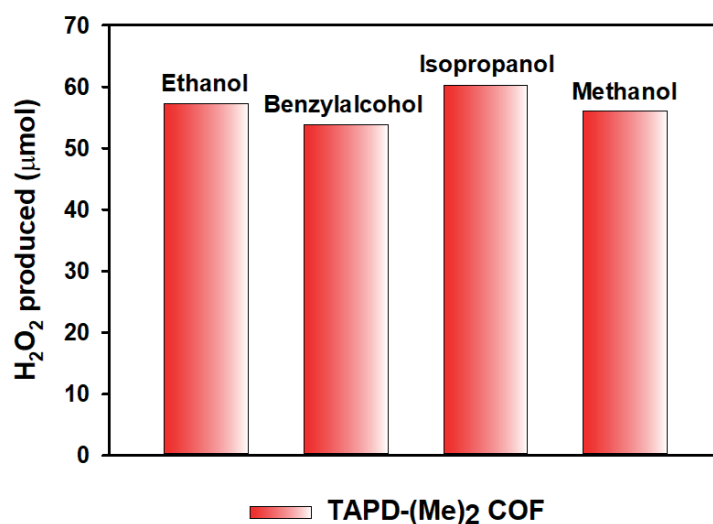


Figure S6.47. Effect of different proton donors in the overall production of H₂O₂.

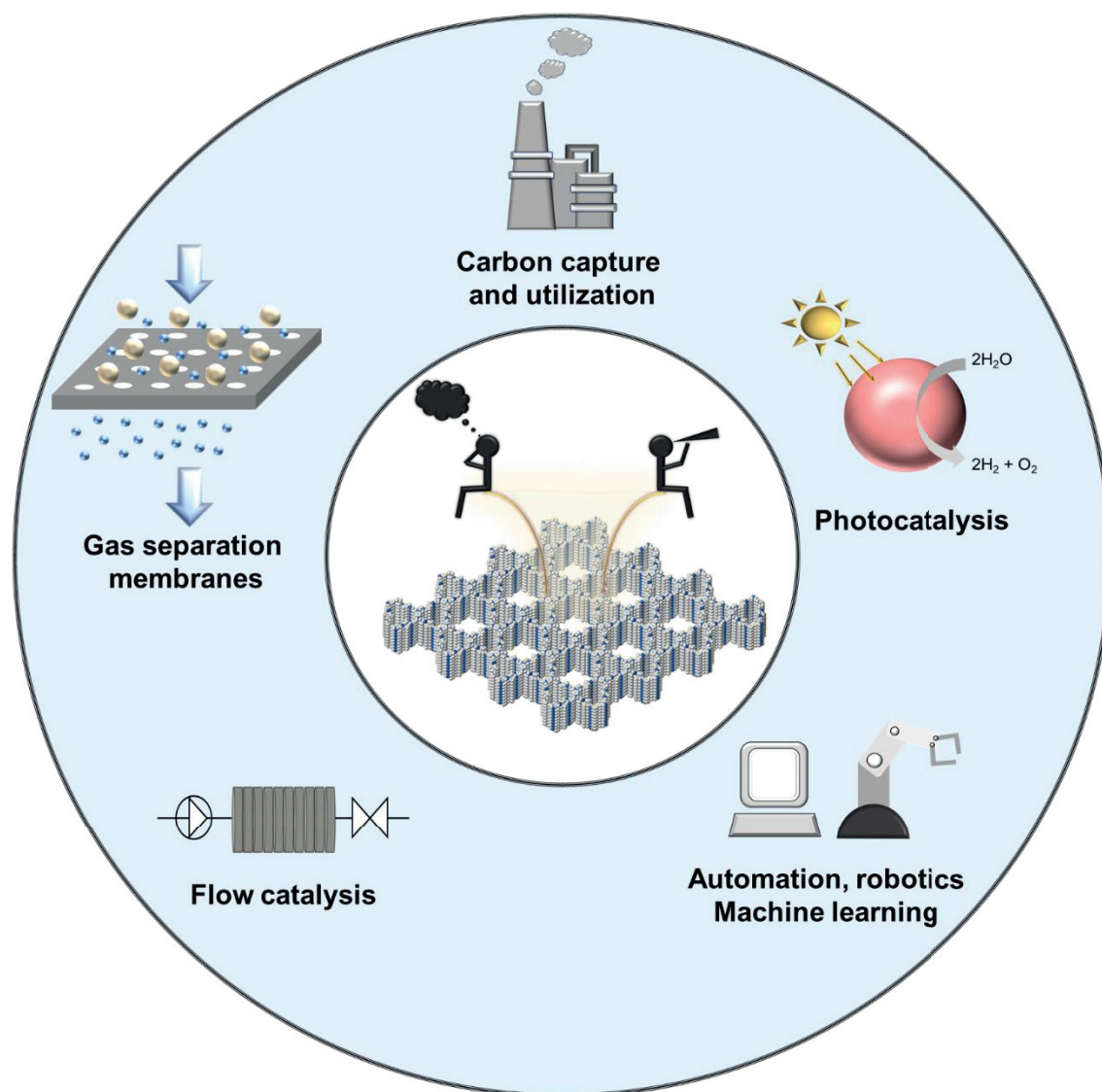
References

- (S1) C. V. Chandran, P. K. Madhu, N. D. Kurur, T. Bräuniger, Swept-frequency two-pulse phase modulation (SWf-TPPM) sequences with linear sweep profile for heteronuclear decoupling in solid-state NMR. *Magn. Reson. Chem.* 2008, 46(10) 943-947.
- (S2) M. Feike, D. E. Demco, R. Graf, J. Gottwald, S. Hafner, H. W. Spiess, Broadband multiple-quantum NMR spectroscopy. *J. Magn. Reson. Ser. A* 1996, 122(2), 214-221.

- (S3) R. Graf, D. E. Demco, J. Gottwald, S. Hafner, H. W. Spiess, Dipolar couplings and internuclear distances by double-quantum nuclear magnetic resonance spectroscopy of solids. *J. Chem. Phys.* 1997, 106(3), 885-895.
- (S4) A. D. Becke, Density-functional thermochemistry. III. The role of exact exchange. *J. Chem. Phys.* 1993, 98, 5648–5652.
- (S5) C. Lee, W. Yang, R. G. Parr, Development of the Colle-Salvetti correlation-energy formula into a functional of the electron density. *Phys. Rev. B* 1988, 37, 785–789.
- (S6) P. J. Stephens, F. J. Devlin, C. F. Chabalowski, M. J. Frisch, Ab initio calculation of vibrational absorption and circular dichroism spectra using density functional force fields. *J. Chem. Phys.* 1994, 98, 11623–11627.
- (S7) M. J. Frisch, J. A. Pople, J. S. Binkley, Self-consistent molecular orbital methods 25. Supplementary functions for Gaussian basis sets. *J. Chem. Phys.* 1984, 80, 3265–3269.
- (S8) M. J. Frisch, et al. Gaussian 16 Revision A.03. 2016; Gaussian Inc. Wallingford CT.
- (S9) T. Verstraelen, S. Vandenbrande, F. Heidar-Zadeh, L. Vanduyfhuys, V. Van Speybroeck, M. Waroquier, P. W. Ayers, Minimal Basis Iterative Stockholder: Atoms in Molecules for Force-Field Development. *J. Chem. Theory Comput.* 2016, 12, 3894–3912.
- (S10) T. Verstraelen, P. Tecmer, F. Heidar-Zadeh, K. Boguslawski, M. Chan, Y. Zhao, T. D. Kim, S. Vandenbrande, D. Yang, C. E. González-Espinoza, S. Fias, P. A. Limacher, D. Berrocal, A. Malek, P. W. Ayers, HORTON 2.0.0. 2015; <http://theochem.github.com/horton/>.
- (S11) L. Vanduyfhuys, S. Vandenbrande, T. Verstraelen, R. Schmid, M. Waroquier, V. Van Speybroeck, QuickFF: A program for a quick and easy derivation of force fields for metal-organic frameworks from ab initio input. *J. Comput. Chem.* 2015, 36, 1015–1027.
- (S12) L. Vanduyfhuys, S. Vandenbrande, J. Wieme, M. Waroquier, T. Verstraelen, V. Van Speybroeck, Extension of the QuickFF force field protocol for an improved accuracy of structural, vibrational, mechanical and thermal properties of metal-organic frameworks. *J. Comput. Chem.* 2018, 39, 999–1011.
- (S13) A. Ghysels, T. Verstraelen, K. Hemelsoet, M. Waroquier, V. Van Speybroeck, TAMkin: a versatile package for vibrational analysis and chemical kinetics. *J. Chem. Inf. Model.* 2010, 50, 1736–1750.

- (S14) N. L. Allinger, Y. H. Yuh, J.-H. Lii, Molecular mechanics. The MM3 force field for hydrocarbons. 1. *J. Am. Chem. Soc.* 1989, 111, 8551–8566.
- (S15) V. Favre-Nicolin, R. Černý, FOX, 'free objects for crystallography': a modular approach to ab initio structure determination from powder diffraction. *J. Appl. Cryst.* 2002, 35, 734–743.
- (S16) T. Verstraelen, L. Vanduyfhuys, S. Vandenbrande, S. M. J. Rogge, Yaff, yet another force field. <http://molmod.ugent.be/software/>.
- (S17) S. Plimpton, Fast Parallel Algorithms for Short-Range Molecular Dynamics. *J. Comput. Phys.* 1995, 117, 1–19.
- (S18) S. M. J. Rogge, L. Vanduyfhuys, A. Ghysels, M. Waroquier, T. Verstraelen, G. Maurin, V. Van Speybroeck, A Comparison of Barostats for the Mechanical Characterization of Metal-Organic Frameworks. *J. Chem. Theory Comput.* 2015, 11, 5583–5597.
- (S19) S. Nosé, A molecular dynamics method for simulations in the canonical ensemble. *Mol. Phys.* 1984, 52, 255–268.
- (S20) W. G. Hoover, Canonical dynamics: Equilibrium phase-space distributions. *Phys. Rev. A* 1985, 31, 1695–1697.
- (S21) G. J. Martyna, M. L. Klein, M. Tuckerman, Nosé-Hoover chains: The canonical ensemble via continuous dynamics. *J. Chem. Phys.* 1992, 97, 2635–2643.
- (S22) G. J. Martyna, D. J. Tobias, M. L. Klein, Constant pressure molecular dynamics algorithms. *J. Chem. Phys.* 1994, 101, 4177–4189.
- (S23) G. J. Martyna, M. E. Tuckerman, D. J. Tobias, M. L. Klein, Explicit reversible integrators for extended systems dynamics. *Mol. Phys.* 1996, 87, 1117–1157.
- (S24) D. W. Burke, C. Sun, I. Castano, N. C. Flanders, A. M. Evans, E. Vitaku, D. C. Mcleod, R. H. Lambeth, L. X. Chen, N. C. Gianneschi, W. R. Dichtel, Acid Exfoliation of Imine-linked Covalent Organic Frameworks Enables Solution Processing into Crystalline Thin Films. *Angew. Chemie Int. Ed.* 2020, 59, 5165–5171.

7 CONCLUSIONS AND OUTLOOK



The discussion in this chapter can hopefully inspire research in future.

In this thesis, the prospect of synthesizing new Covalent Triazine Frameworks (CTFs) and Covalent Organic Frameworks (COFs) was investigated. Since the first reports on COFs and CTFs in 2005 and 2008 respectively, a fair amount of research has been carried out in this field. This is clearly seen through the increase in the number of publications with the keywords “Covalent Organic Frameworks” and “Covalent Triazine Frameworks” (Figure 7.1). Reticular chemistry is the key feature in these materials. Moreover, tunable porosity, high surface areas, variable functionalities, long-term stabilities are other advantages of these materials which are beneficial for several applications.

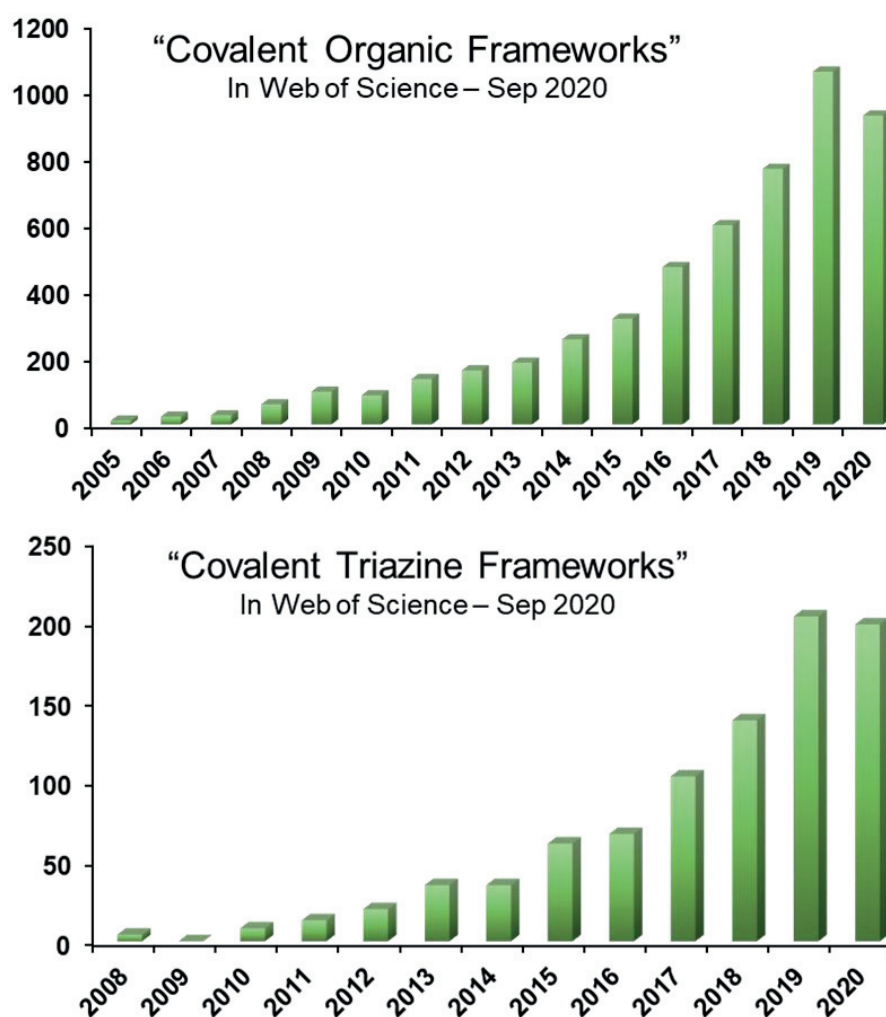


Figure 7. 1. Number of publications in web of science (till September 2020) based on the key words (top) “Covalent Organic Frameworks” (bottom) “Covalent Triazine Frameworks”.

7.1. Gas storage, separation, and utilization

In this thesis, Hexene-CTFs based on triazine linkage were synthesized, characterized, and utilized for C₂/C₁ separation, which was previously not done using similar materials. The obtained adsorption capacities and selectivities were good compared to other porous organic materials of similar standard. On one hand, inorganic materials such as Metal-Organic Frameworks (MOFs) have shown better performance due to the presence of abundant open metal sites. However, on the other hand, CTFs provide the benefit of being more stable due to strong covalent linkages. Further work in this direction must focus on increasing selectivities in C₂/C₁ separation. This can be achieved through molecular control over the microporosity and functionalities in the CTFs. Additionally, such materials must be tested in breakthrough experiments to prove their worth under real conditions. For example, testing their performance under mixed gas systems (mimicking real conditions) can provide a consolidated proof of their usage in industries.

In terms of carbon storage, families of three CTFs based on similar starting linkers (acetylacetonate, pyrazole, isoxazole) were synthesized. Initially, acac-CTFs were developed with a goal of increasing the oxygen content in addition to the ubiquitous nitrogen in CTFs. The resulting polar (N-/O-) sites of acac-CTFs enabled stronger interaction with CO₂ molecules over N₂. To further improve the material-CO₂ interaction, the acac unit was aromatized by linker modification to form pyz and isox units. The overall CO₂ uptake was observed to be ~1.5 folds higher using the isoxazole-CTF. This was a direct consequence of the increased basicity in the material. Also, pyrazole-CTF showed better CO₂ uptake capacity than the acac-CTF. Nonetheless, all these CTFs showed excellent selectivities over N₂. In future, further improvement in CO₂ storage can be targeted through the introduction of heteroatoms (such as S, O, F, etc.). Additionally, flue gas consists of 2-3% water and hence, increasing hydrophobicity can also work in favor of stronger CO₂ interaction over water. A good approach for gas separation is through the utilization of gas permeable membranes fabricated from porous materials displaying selective gas sorption capabilities. In conventional polymeric membranes, Robeson limit has been holding back the overall separation performance.¹ Robeson limit describes the relation between permeability and selectivity in a gas separation process, i.e., selectivity must be sacrificed for permeability and vice versa. CTFs can prove to be a material which can overcome these issues. Hence research in the direction of fabricating gas permeable membranes containing CTFs could lead to breakthroughs.

Ideally, carbon capture and storage (CCS) is less favored in comparison to carbon capture and utilization (CCU) due to the involved costs and expected returns. According to the International Energy Agency (IEA)² reports, two large-scale CCUS (carbon capture, utilization, and storage) power projects are in operation currently with a total capture capacity of 2.4 MtCO₂ per year. The 2030 Sustainable Development Scenario (SDS) targets 310 MtCO₂ per year. Since 2017 more than 30 new integrated CCUS facilities have been announced with the majority in the United States and Europe. If these projects proceed according to plans, the overall global CO₂ capture capacity would be more than triple, to around 130 Mt per year. Hence, materials that can perform both CCS and CCU should be developed simultaneously to accelerate the SDS target. Preliminary studies on such applications have been performed using CTFs, such as epoxide ring-opening reaction using CO₂. CTFs have also shown good CO₂ reduction activities. But these just scratch the surface based on the number of available CO₂ transformation reactions. Due to the currently increasing CO₂ concentration in the world, such CCU based processes require urgent attention as they can help mitigate global warming issues.

7.2. Heterogeneous catalysis

The usage of catalysts for production of goods of economic values can be classified into four sectors, (i) the polymer industry (21%), (ii) coal, oil, and gas refining (22%), (iii) chemical manufacturing, and (iv) environmental applications (30%).³ While both homogeneous and heterogeneous catalysis are currently in use, heterogeneous catalysis provides benefits in product separation and better processability in flow setups. However, the challenge is to produce heterogeneous catalysts which are both stable and as well as active for a desired reaction. To this end, the use of CTFs as scaffolds for metal coordination has been explored in this thesis. Especially when literature is filled with nitrogen coordinating ligands such as bipyridine, pyridine, phenanthroline, etc., we showed that oxygen-containing porous structures can also assist in coordinating metals. The acac-CTF containing oxygen groups could support Vanadium complex which acts as the active site for modified Mannich reaction. Excellent heterogeneous catalytic activity was observed even after several runs without loss in activity showing the recyclable capacity of the CTFs. Apart from vanadium, oxygen can bind to several other transition metals which can in turn catalyze other organic transformations. For example, iron can coordinate strongly to oxygen and iron(acac) could be heterogenized using acac-CTF to perform reaction such as regio/site-selective acylation of diols and carbohydrates.

However, performing these reactions under flow conditions should be targeted in future work. Not only acac based CTFs, but other CTFs that have been proved to be excellent support materials for anchoring metals could also be used in flow setups. This can enable technology transfer from lab scale to industrial scales.

Additionally, since the CTFs contain different nitrogen sites, they have an intrinsic basicity associated with them. This helps them to act as an organo-catalyst for several organic transformations. One such reaction was successfully performed in this thesis where benzyl amines were transformed into imines under aerobic conditions using CTFs. Such reactions (albeit limited) show the capability of these materials to be utilized as a green alternative to industrially used homogenous complexes. Though such reactions have been performed using nitrogen-containing materials such as carbon nitride, N-doped carbon, CTFs, etc., the active site for the catalysis remains elusive. Only speculations about the mechanisms are currently present as it remains hard to conclude the mechanism through experimental studies alone. Hence to overcome this barrier, the use of computational studies must be incorporated. Such theoretical calculations will assist in determining the mechanism of these organocatalytic reactions.

Heterogeneous catalysis using CTFs have mostly been at liquid-solid interfaces. Several gas phase reactions are industrially relevant but are challenging to achieve due to high temperature requirements. Hence heterogeneous catalysts which can remain stable at these conditions need to be studied. As a result of their high stabilities, CTFs can be a potential choice in this direction.

7.3. Photocatalysis

The synthesis of two new COFs which formed kagome lattices (containing dual pores) is described in this thesis. These COFs were highly crystalline and contained strongly reducing groups (diarylamino benzene). Moreover, the bandgaps and band positions were aligned well for photocatalysis under visible light irradiation. The TAPD-COFs showed good activity for photocatalytic H_2O_2 production and acted as a metal-free platform. Hence the overall reaction can be considered entirely green both in terms of materials as well as reaction conditions. However, a better approach would be the production of H_2O_2 from water (without proton donors such as alcohol). This reaction is more challenging as the COF must perform water splitting to produce protons which an uphill reaction. Especially, at a given instance, COFs have only been used to perform half-reactions of

the water splitting (i.e., either hydrogen evolution or oxygen evolution). Overall water splitting is a difficult target to obtain with only a single COF as photocatalyst. To achieve this, a composite material can be utilized. Formation of heterojunctions such as Z-scheme has proven to be beneficial for charge separation and low energy utilization. COFs can be used to make such heterojunctions that can be rendered suitable for such photocatalytic reactions. Several photoactive building blocks can be interesting for the development of COFs for efficient photocatalysis. Porphyrins, phthalocyanines, tetraxetan are some of the interesting units which can act as both light harvesters and as support for catalytic active metal species. The combination of theoretical and experimental chemistry can be crucial for this purpose. It would be ideal if a computational screening could be performed on these linkers with different metal species for any targeted photocatalytic reaction (e.g., water-splitting or CO₂ reduction to sustainable fuels). Theoretical prediction of the electronic structures could be used as starting point for experimental chemists. Apart from these, other interesting units to study could be donor and acceptor units and their combined influence in the semiconducting properties of COFs. On a broader perspective, photochemistry has its genesis dating back to the early 1900s. Several landmark advancements have been obtained since then including the TiO₂ catalyzed water splitting by Fujishima and Honda in 1970,⁴ and development of polymeric carbon nitride as metal-free visible-light active photocatalyst in 2009.⁵ However, even after the tremendous efforts of “academic” research witnessed over the years, the commercialization of photocatalysis has just seen its onset. One of the main challenges regarding the commercialization is the upscaling process. Quite often reactions performed under small scale do not translate directly into large scale setups. Moreover, not having standard benchmarks for comparing “figure of merits” of these catalysts makes this translation furthermore troublesome.⁶ On a positive note, there have been strides made in applications like photocatalytic self-cleaning surfaces, wastewater treatment, and air purifiers.⁷ Very recently, photocatalysis in flow has been achieved for chemical product manufacturing.⁸ The commercial market for photocatalysis is just seeing its dawn and gives hope for a brighter and greener future.

7.4. General outlook

Though there have been quite a few reports on COFs and CTFs, the opportunity in this field is enormous. It has become clear throughout these chapters that both CTFs and COFs can still be considered to be at its infancy. Especially from the design perspective several

topologies are yet to be identified. Particularly, 3D COFs are scarce due to the limited number of 3D directing starting linkers. However, other approaches such as woven COFs can be utilized to further expand on this. Inspiration from hybrid materials can be taken to produce inorganic-organic 3D COFs. In addition, single crystal COFs are also limited. Hence, research in this direction will surely be appreciated by the research community.

In CTFs, the limiting factor has been the chemical and structural characterization. In most cases CTFs are made through ionothermal route which results in carbonization and produces black colored materials that are difficult to characterize. Though strides towards this target has been made (for example: mild synthesis of CTFs), a concrete method to characterize these materials is yet to be developed. A synthetic method to produce crystalline and porous CTF using mild methods which can be characterized through existing techniques such as PXRD, FT-IR and ss-NMR should be developed. However, in my personal experience, CTFs have proven to be quite a stable material. They are quite resistant to acidic and basic conditions as well as thermal conditions. The reproducibility factor of CTFs is also remarkable. Hence from a synthetic point of view, these materials can be transferred easily to industrial applications.

Last but not the least, toxicity tests on these materials are important if they need to be employed for large scale applications. Such tests on all available CTFs and COFs from literature would be a herculean task. However, considering the advantages of these materials, this is still beneficial and viable through a coordinated approach.

Finally, I wanted to highlight an important paradigm shift in the chemistry research which is the introduction of ‘automation and robotics’. The synthesis of any new material (CTF, COF or any porous material) requires extensive experimental optimizations. What works for one COF might not work for another COF! The adaptation of automation for extensive experimental work can decrease the manual labor and accelerate the development of novel materials. Another important technological advancement is ‘machine learning’. It is a branch of artificial intelligence which allows computers to automatically learn and adapt from experience without the requirement of explicit programming. The existence of literature containing thousands of synthetic conditions can be utilized to predict parameters for synthesis of new materials through machine learning.⁹ Ideally, if machine learning is combined with automation, computers will predict synthesis conditions and robots will perform the synthesis. Though this seems to be a stretch, in the future such development is highly likely.

7.5. References

1. X. Zhu, C. Tian, C.-L. Do-Thanh, S. Dai, Two-dimensional materials as prospective scaffolds for mixed-matrix membrane-based CO₂ separation, *ChemSusChem*, 2017, 10 (17), 3304-3316.
2. IEA, CCUS in Clean Energy Transitions, 2020, Paris <https://www.iea.org/reports/ccus-in-clean-energy-transitions>.
3. J. Heveling, Heterogeneous catalytic chemistry by example of industrial applications, *J. Chem. Educ.*, 2012, 89 (12), 1530-1536.
4. A. Fujishima, K. Honda, Electrochemical photolysis of water at a semiconductor electrode, *Nature*, 1972, 238 (5358), 37-38.
5. X. Wang, K. Maeda, A. Thomas, K. Takanabe, G. Xin, J. M. Carlsson, K. Domen, M. Antonietti, *Nature Materials*, 2009, 8 (1), 76-80.
6. M. Melchionna, P. Fornasiero, Updates on the roadmap for photocatalysis, *ACS Catal.*, 2020, 10 (10), 5493-5501.
7. E. Hiolski, *Chemical & Engineering News (C&EN)*, 2019, 97 (36).
8. G. Laudadio, Y. Deng, K. van der Wal, D. Ravelli, M. Nuño, M. Fagnoni, D. Guthrie, Y. Sun, T. Noël, C(sp³)-H functionalizations of light hydrocarbons using decatungstate photocatalysis in flow, *Science*, 2020, 369 (6499), 92-96.
9. S. M. Moosavi, A. Chidambaram, L. Talirz, M. Haranczyk, K. C. Stylianou, B. Smit, Capturing chemical intuition in synthesis of metal-organic frameworks, *Nature Communications*, 2019, 10, 539.

